Highly Efficient Inductive Power Transfer Across Wide Operating Range

Zhu, G.

DOI
10.4233/uuid:3b05acf6-5a55-4d77-8d4d-5df8248f53d8

Publication date
2024

Document Version
Final published version

Citation (APA)
Zhu, G. (2024). *Highly Efficient Inductive Power Transfer Across Wide Operating Range*. [Dissertation (TU Delft), Delft University of Technology]. https://doi.org/10.4233/uuid:3b05acf6-5a55-4d77-8d4d-5df8248f53d8

HIGHLY EFFICIENT INDUCTIVE POWER TRANSFER ACROSS WIDE OPERATING RANGE

HIGHLY EFFICIENT INDUCTIVE POWER TRANSFER ACROSS WIDE OPERATING RANGE

Dissertation

for the purpose of obtaining the degree of doctor
at Delft University of Technology,
by the authority of the Rector Magnificus Prof. dr. ir. T.H.J.J van der Hagen,
chair of the Board for Doctorates,
to be defended publicly on
Wednesday 27 November 2024 at 10:00 o'clock

by

Gangwei ZHU

Master of Science in Electrical Engineering, Shanghai Jiao Tong University, China
born in Hunan, China.

This dissertation has been approved by the promotors.

Composition of the doctoral committee:

Rector Magnificus,	chairperson
Prof. dr. ir. P. Bauer,	Delft University of Technology, promotor
Dr. J. Dong,	Delft University of Technology, copromotor

Independent members:

Dr. A. Coraddu	Delft University of Technology
Prof. dr. P. Mitcheson,	Imperial College London, United Kingdom
Prof. dr. ing. A. Neto,	Delft University of Technology
Prof. dr. ir. A.H.M. Smets,	Delft University of Technology
Dr. ir. P. Venugopal,	University of Twente

ISBN 978-94-6366-974-0

An electronic version of this dissertation is available at
http://repository.tudelft.nl/.

CONTENTS

SUMMARY

The electric vehicle (EV) market has experienced significant expansion in recent years, underscoring the pressing need for advanced EV charging infrastructures. In addition to conductive charging, wireless EV charging has proven to be a promising charging solution as it provides safe, convenient, and automated charging for EVs.

The most commonly adopted technology for wireless EV charging is inductive power transfer (IPT). Moreover, in wireless EV charging systems, achieving a wide operating range is imperative due to several contributing factors. Firstly, EV battery loads vary significantly during the constant current-constant voltage (CC-CV) charging process. Secondly, coil misalignment and capacitance drift lead to notable deviations in the parameters of resonant circuits. Thirdly, accommodating diverse EV models to enhance interoperability introduces significant variations in air gaps, receiver coil configurations, and nominal EV battery voltages. These factors collectively expand the operating range requirements for wireless EV charging systems. Nevertheless, ensuring highly-efficient and wide-range operation under these varying conditions is challenging. This thesis aims to address this challenge by implementing advanced control and modulation techniques for power converters and compensation networks in wireless EV charging systems. Specifically, the content of this thesis is divided into three main parts, as illustrated below.

PART I-HYBRID MODULATION AND CONTROL

The CC and CV charging profiles of EV batteries require wireless EV charging systems to have a wide output power regulation capability. However, existing power regulation methods result in significant efficiency drops under considerable load variations. In this context, Part I aims to enable wide output power regulation while maintaining high transmission efficiency under significantly varying loads.

Chapter 2 introduces a mode-switching-based phase shift control (MS-PSC) method for achieving wide output power regulation while maintaining high efficiency under load variations. In this MS-PSC method, both the inverter and active rectifier are modulated and controlled to achieve wide power regulation, maximum efficiency tracking (also known as optimal load tracking), and wide zero-voltage switching (ZVS) operations simultaneously. This approach eliminates the front-end and back-end DC-DC converters used in conventional IPT systems, allowing power to be directly transferred from the power factor correction (PFC) output to the battery. More importantly, hybrid operating modes—including half-bridge (HB), mixed-bridge (MB), and full-bridge (FB) modes—are implemented. By transitioning modes of both the inverter and rectifier, the MS-PSC method ensures wide-range ZVS with minimized reactive power circulation. Experimental validation of the MS-PSC method shows significant efficiency improvements over the conventional triple-phase-shift (TPS) method, particularly in the 10%-63% rated power range, with efficiency gains ranging from 1.5% to 6%. As a result, the

proposed system achieves DC-to-DC efficiency between 93.5% and 96.1% in the 1-10 kW power range.

In Chapter 3, a hybrid modulation (HM) technique is proposed to facilitate secondary side control in wireless EV charging systems. The secondary-side control technique enables communication-less power regulation, significantly reducing the control complexity. Conventional phase shift modulation (PSM), also known as pulse width modulation (PWM), suffers from significant efficiency drops under light-load conditions in secondary-side controlled IPT systems. Existing pulse density modulations (PDMs) lead to considerable current and voltage ripples. To address this, an optimal discrete PDM (DPDM) is proposed for active rectifier modulation. By symmetrically and uniformly distributing pulses, the optimal D-PDM eliminates even-subharmonics in the rectifier input voltage, thereby reducing current distortions and output voltage ripple while removing capacitor DC blocking voltages. Additionally, pulse width regulation is incorporated into the optimal D-PDM, enabling continuous output tuning and further minimizing voltage subharmonics. Experimental results show that the proposed HM technique significantly reduces current and voltage ripples while allowing continuous tuning compared to existing PDMs. Furthermore, compared to PWM, the HM technique shows notable efficiency improvements within the 10%-60% power range, achieving a maximum efficiency enhancement of up to 5.5%.

PART II-PARAMETER IDENTIFICATION AND IMPEDANCE TUNING

In practical wireless EV charging applications, coil misalignment and capacitance drift inevitably cause parameter deviations within resonant circuits, leading to non-resonant operating conditions, decreased transmission efficiency, and a lower power factor. To this end, Part II investigates technical solutions to effectively address parameter deviations in practical scenarios.

To mitigate significant parameter deviations, Chapter 4 introduces a parameter identification method to determine unknown parameters of the resonant circuits. This approach involves measuring only the RMS values of the coil currents, eliminating the need for phase-detection circuits and auxiliary measurement coils. Additionally, based on the identified parameters, an impedance tuning technique is proposed to address system detuning caused by these parameter deviations. This involves minimizing undesirable reactance in the resonant circuits by adjusting the system frequency and phase shift angles of the active rectifier. Experimental results demonstrate accurate recognition of unknown parameters in the proposed identification approach, with average relative errors all less than 3%. Furthermore, implementing the proposed impedance tuning method improves the DC-to-DC efficiency of the IPT system by 4.3% to 15% in experiments.

PART III-VARIABLE DLCC COMPENSATION

To enhance the compatibility of public wireless EV chargers with the variety of EV models available in the market, it is preferable for these chargers to accommodate diverse vehicle types. The diversity of EV models results in distinct configurations of receiver coils, leading to asymmetry in primary and secondary parameters. Additionally, public wireless EV chargers should ideally accommodate varying air gaps and differing nominal battery voltages across various EV models. Part III aims to enhance the interoperabil-

ity of wireless EV chargers under these conditions based on variable double-sided LCC (DLCC) compensation.

In Chapter 5, an optimal multivariable control (OMC) strategy is introduced to manage the asymmetric parameters of the IPT system, specifically focusing on the DLCC compensation network. This network ensures constant coil currents even under poor coupling conditions, significantly enhancing system robustness against varying air gaps and coil misalignment. Chapter 5 begins by identifying the limitations of existing methods under asymmetric parameters, which exhibit increased reactive power and reduced efficiency under varying load conditions. To address these issues, the proposed OMC method incorporates dual-side hybrid modulation and primary-side switch-controlled-capacitor (SCC) tuning into the triple-phase-shift (TPS) control. By collaboratively modulating and controlling the inverter, rectifier, and SCC, the OMC method reduces the RMS values of circulating currents and minimizes turn-off currents for the converters, thereby improving efficiency in both light and heavy load conditions. This approach enables wide output regulation and full-range efficiency optimization simultaneously. Experimental results confirm the superiority of the proposed OMC method, achieving higher DC-to-DC efficiency in the power range of 0.2-2.2 kW, with a maximum efficiency improvement of up to 6.3%.

Furthermore, Chapter 6 proposes a dual-side capacitor tuning and cooperative control strategy to manage wide output voltage variations while maintaining high overall efficiency. This chapter introduces a reconfigurable DLCC compensation network by incorporating two switch-controlled capacitors (SCCs) on both the primary and secondary sides. Optimal capacitor tuning factors are derived to reduce the RMS values of inductor currents and minimize turn-off currents across the semiconductors. Additionally, a dual-side cooperative control strategy is proposed, leveraging collaborative control of the inverter, rectifier, and SCCs to achieve dual-side optimal zero-voltage switching (ZVS), wide power regulation, and maximum efficiency tracking simultaneously. Experimental results demonstrate notable efficiency improvement over a wide input-to-output DC voltage gain range (0.5-1.5) without requiring additional DC-DC converters, with a maximum efficiency enhancement of up to 1.9%.

SAMENVATTING

De markt voor elektrische voertuigen (EV) heeft de afgelopen jaren een aanzienlijke groei doorgemaakt, wat de dringende behoefte aan geavanceerde oplaadinfrastructuren voor EV's benadrukt. Naast geleid laden is draadloos laden van EV's een veelbelovende oplossing gebleken, omdat het veilig, handig en geautomatiseerd laden van EV's mogelijk maakt.

De meest gebruikte technologie voor draadloos laden van EV's is inductieve kracht overdracht (IPT). Bovendien is het in draadloze EV-laadsystemen van cruciaal belang om een groot werkingsbereik te bereiken vanwege verschillende bijdragende factoren. Ten eerste variëren de EV-batterijladingen aanzienlijk tijdens het constant stroom-constant voltage (CC-CV) laadproces. Ten tweede leiden spoelverplaatsing en capacitantieveranderingen tot aanzienlijke afwijkingen in de parameters van resonante circuits. Ten derde introduceert het accommoderen van diverse EV-modellen om de interoperabiliteit te verbeteren aanzienlijke variaties in luchtspleten, ontvangerspoelconfiguraties en nominale EV-batterijspanningen. Deze factoren samen vergroten de vereisten voor het werkingsbereik van draadloze EV-laadsystemen. Desalniettemin is het een uitdaging om een zeer efficiënte en breed bereikende werking onder deze variërende omstandigheden te waarborgen. Dit proefschrift heeft tot doel deze uitdaging aan te pakken door geavanceerde controle- en modulatietechnieken voor vermogensomvormers en compensatienetwerken in draadloze EV-laadsystemen te implementeren. Specifiek is de inhoud van dit proefschrift verdeeld in drie hoofdonderdelen, zoals hieronder geïllustreerd.

DEEL I-HYBRIDE MODULATIE EN CONTROLE

De CC- en CV-laadprofielen van EV-batterijen vereisen dat draadloze EV-laadsystemen een brede output vermogensregeling hebben. Bestaande vermogensregelmethode resulteren echter in aanzienlijke efficiëntieverliezen bij aanzienlijke variaties in de belasting. In deze context heeft Deel I tot doel brede output vermogensregeling mogelijk te maken terwijl een hoge transmissie-efficiëntie wordt behouden onder sterk variërende belastingen.

Hoofdstuk 2 introduceert een op modus wisselende faseverschuivingscontrole (MS-PSC) methode voor het bereiken van brede output vermogensregeling met behoud van hoge efficiëntie onder belasting variaties. In deze MS-PSC-methode worden zowel de omvormer als de actieve gelijkrichter gemoduleerd en gecontroleerd om brede vermogensregeling, maximale efficiëntietracking (ook bekend als optimale belastingstracking) en brede zero-voltage switching (ZVS) operaties tegelijkertijd te bereiken. Deze benadering elimineert de voor- en achterkant DC-DC omvormers die in conventionele IPT-systemen worden gebruikt, waardoor vermogen direct van de vermogensfactorcorrectie (PFC) output naar de batterij kan worden overgebracht. Belangrijker nog, hybride bedrijfsmodi – inclusief half-bridge (HB), mixed-bridge (MB) en full-bridge (FB) modi – worden geïmplementeerd. Door het overgaan van modi van zowel de omvormer als

de gelijkrichter zorgt de MS-PSC-methode voor brede-range ZVS met geminimaliseerde reactieve vermogenscirculatie. Experimentele validatie van de MS-PSC-methode toont aanzienlijke efficiëntieverbeteringen ten opzichte van de conventionele triple-phase-shift (TPS) methode, vooral in het 10%-63% van het nominale vermogensbereik, met efficiëntiewinsten variërend van 1,5% tot 6%. Hierdoor bereikt het voorgestelde systeem DC-naar-DC-efficiëntie tussen 93,5% en 96,1% in het vermogensbereik van 1-10 kW.

In Hoofdstuk 3 wordt een hybride modulatie (HM) techniek voorgesteld om secundaire zijde controle in draadloze EV-laadsystemen te vergemakkelijken. De secundaire zijde controle techniek maakt communicatie-loze vermogensregeling mogelijk, wat de controlecomplexiteit aanzienlijk vermindert. Conventionele faseverschuivingsmodulatie (PSM), ook bekend als pulsbreedtemodulatie (PWM), lijdt onder aanzienlijke efficiëntie drops onder lichte belastingomstandigheden in IPT-systemen met secundaire zijde controle. Bestaande pulsdichtheidsmodulaties (PDMs) leiden tot aanzienlijke stroom- en spanningsrimpels. Om dit aan te pakken, wordt een optimale discrete PDM (DPDM) voorgesteld voor actieve gelijkrichtermodulatie. Door pulsen symmetrisch en gelijkmatig te verdelen, elimineert de optimale D-PDM even-subharmonischen in de gelijkrichteringangsspanning, waardoor stroomvervormingen en outputspanningsrimpels worden verminderd, terwijl DC-blokkeringsspanningen van condensatoren worden verwijderd. Bovendien wordt pulsbreedteregeling opgenomen in de optimale D-PDM, waardoor continue outputafstemming mogelijk is en spanningssubharmonischen verder worden geminimaliseerd. Experimentele resultaten tonen aan dat de voorgestelde HM-techniek stroom- en spanningsrimpels aanzienlijk vermindert terwijl continue afstemming mogelijk is vergeleken met bestaande PDM's. Bovendien toont de HM-techniek aanzienlijke efficiëntieverbeteringen binnen het 10%-60% vermogensbereik, met een maximale efficiëntieverbetering tot 5,5% vergeleken met PWM.

DEEL II - PARAMETER IDENTIFICATIE EN IMPEDANTIE AFSTEMMING

In praktische draadloze EV-laadtoepassingen veroorzaken spoelverplaatsing en capacitantieveranderingen onvermijdelijk parameterafwijkingen binnen resonante circuits, wat leidt tot niet-resonante bedrijfsomstandigheden, verminderde transmissie-efficiëntie en een lagere vermogensfactor. Daartoe onderzoekt Deel II technische oplossingen om parameterafwijkingen in praktische scenario's effectief aan te pakken.

Om aanzienlijke parameterafwijkingen te beperken, introduceert Hoofdstuk 4 een parameteridentificatiemethode om onbekende parameters van de resonante circuits te bepalen. Deze aanpak omvat het meten van alleen de RMS-waarden van de spoelstromen, waardoor de behoefte aan fase-detectie circuits en hulpmiddelingsspoelen wordt geëlimineerd. Daarnaast wordt op basis van de geïdentificeerde parameters een impedantie afstemmingstechniek voorgesteld om systeemontstemming veroorzaakt door deze parameterafwijkingen aan te pakken. Dit omvat het minimaliseren van ongewenste reactantie in de resonante circuits door de systeemfrequentie en faseverschuivingshoeken van de actieve gelijkrichter aan te passen. Experimentele resultaten tonen een nauwkeurige herkenning van onbekende parameters in de voorgestelde identificatiebenadering, met gemiddelde relatieve fouten allemaal minder dan 3%. Bovendien verbetert de implementatie van de voorgestelde impedantie afstemmingsmethode de DC-naar-DC efficiëntie van het IPT-systeem met 4,3% tot 15% in experimenten.

DEEL III-VARIABELE DLCC COMPENSATIE

Om de compatibiliteit van openbare draadloze EV-laders met de verscheidenheid aan EV-modellen op de markt te verbeteren, is het wenselijk dat deze laders verschillende voertuigtypes kunnen accommoderen. De diversiteit aan EV-modellen resulteert in verschillende configuraties van ontvangerspoelen, wat leidt tot asymmetrie in primaire en secundaire parameters. Bovendien zouden openbare draadloze EV-laders idealiter verschillende luchtspleten en verschillende nominale batterijspanningen van diverse EV-modellen moeten accommoderen. Deel III heeft tot doel de interoperabiliteit van draadloze EV-laders onder deze omstandigheden te verbeteren op basis van variabele dubbelzijdige LCC (DLCC) compensatie.

In Hoofdstuk 5 wordt een optimale multivariabele controle (OMC) strategie geïntroduceerd om de asymmetrische parameters van het IPT-systeem te beheren, met speciale aandacht voor het DLCC compensatienetwerk. Dit netwerk zorgt voor constante spoelstromen, zelfs onder slechte koppeling omstandigheden, waardoor de systeem robuustheid tegen variërende luchtspleten en spoelverplaatsing aanzienlijk wordt verbeterd. Hoofdstuk 5 begint met het identificeren van de beperkingen van bestaande methoden onder asymmetrische parameters, die verhoogde reactieve kracht en verminderde efficiëntie vertonen onder variërende belastingomstandigheden. Om deze problemen aan te pakken, omvat de voorgestelde OMC-methode dual-side hybride modulatie en primaire-zijde switch-gecontroleerde-condensator (SCC) afstemming in de triple-phase-shift (TPS) controle. Door samen de omvormer, gelijkrichter en SCC te moduleren en te controleren, vermindert de OMC-methode de RMS-waarden van circulerende stromen en minimaliseert het afschakelstromen voor de omvormers, waardoor de efficiëntie wordt verbeterd in zowel lichte als zware belastingomstandigheden. Deze benadering maakt brede outputregeling en volledige efficiëntieoptimalisatie tegelijkertijd mogelijk. Experimentele resultaten bevestigen de superioriteit van de voorgestelde OMC-methode, met een hogere DC-naar-DC efficiëntie in het vermogensbereik van 0,2-2,2 kW, met een maximale efficiëntieverbetering tot 6,3%.

Verder stelt Hoofdstuk 6 een dual-side condensator afstemmings- en coöperatieve controle strategie voor om brede outputspanningsvariaties te beheren terwijl een hoge algehele efficiëntie wordt behouden. Dit hoofdstuk introduceert een reconfigureerbaar DLCC compensatienetwerk door twee switch-gecontroleerde condensatoren (SCC's) op zowel de primaire als secundaire zijden op te nemen. Optimale condensator afstemfactoren worden afgeleid om de RMS-waarden van spoelstromen te verminderen en afschakelstromen over de halfgeleiders te minimaliseren. Daarnaast wordt een dual-side coöperatieve controlestrategie voorgesteld, die gebruik maakt van collaboratieve controle van de omvormer, gelijkrichter en SCC's om dual-side optimale zero-voltage switching (ZVS), brede vermogensregeling en maximale efficiëntietracking tegelijkertijd te bereiken. Experimentele resultaten tonen aanzienlijke efficiëntieverbetering over een breed input-naar-output DC spanningsverhouding bereik (0,5-1,5) zonder aanvullende DC-DC omvormers, met een maximale efficiëntieverbetering tot 1,9%.

LIST OF FIGURES

LIST OF TABLES

1

INTRODUCTION

1.1. OVERVIEW OF WIRELESS POWER TRANSFER

1.1.1. WIRELESS POWER TRANSFER TECHNOLOGIES

WIRELESS power transfer technologies have become pivotal solutions in our increasingly interconnected world, enabling the transmission of electrical energy without the need for physical connections [6–17]. As described in [18], WPT technologies can be broadly classified into two main categories based on the distance between the transmitting and receiving antennas with respect to the wavelength of the electromagnetic field (EMF): the near-filed and far-field WPT technologies. The classifications of the WPT technologies are outlined in Fig. 1.1.

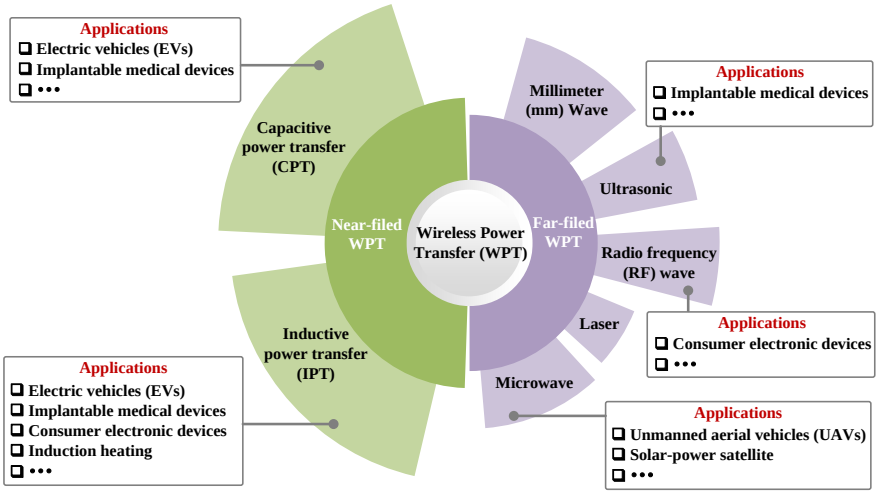

Figure 1.1: Classifications and example applications of the WPT technologies.

As demonstrated in Fig. 1.1, the far-field WPT technologies utilize various types of waves, including radio frequency (RF) waves [19], microwaves[18, 20, 21], laser beams[22], millimeter (mm) wave beams [21], and ultrasonic waves [23]. According to [24], the far-field WPT technologies can operate over considerable distances, e.g., in the range of up to 10 kilometers. However, in most far-field WPT applications, only low power can be transferred due to the stringent exposure limits imposed for the safety of humans and electrical devices. Additionally, given the long distances between the transmitter and receiver, the overall power transfer efficiency is typically quite low in far-field WPT systems.

On the other hand, the near-field WPT technologies operate at relatively short transmission distances (normally shorter than 10 meters) [25–28]. The near-field WPT occurs either in the form of inductive power transfer (IPT), which relies on the magnetic field exchange between coupled coils, or as capacitive power transfer (CPT), which is based on the electric field exchange between coupled metallic plates [29–32].

Although CPT provides benefits such as power transfer through metallic surfaces without inducing eddy currents and exhibiting good misalignment tolerance, it suffers from considerably lower surface power density at larger air gaps [32]. Conversely, the IPT systems can use inductive coupling to achieve power delivery over a relatively long distance (ranging from a few centimeters to several meters) [33–36]. By integrating compensation networks and operating the IPT systems at the resonant state, it is feasible to minimize the circulating reactive power at low coupling factors ($k < 0.4$) and enable considerably high power transfer efficiencies (for instance, exceeding 97% [3]). Additionally, this technology is capable of transferring high power levels, reaching into the range of several hundred kilowatts (kW) [37–39].

The WPT technologies can be applied to numerous industrial applications to eliminate the cable connections between power transmitting devices and receivers [40–62]. In Fig. 1.1, several example applications of WPT technologies are demonstrated to emphasize the significance of this technology in various aspects of human life.

1.1.2. INDUCTIVE POWER TRANSFER FOR WIRELESS EV CHARGING

The electric vehicle (EV) market has seen significant expansion, highlighting the urgent requirement for advanced EV charging infrastructures [63]. Presently, EVs primarily employ conductive charging technology, which demands manual handling and connection of charging cables by drivers [64, 65]. To simplify the process of connecting bulky, high-gauge cables, wireless charging technology emerges as a more user-friendly alternative. This innovative approach eliminates the inconvenience of cables, particularly in adverse weather conditions [66–68]. More importantly, with the increasing emphasis on autonomous driving technologies in recent years, wireless EV charging has become imperative, especially for fully autonomous EVs. Given that these vehicles operate without drivers, they require automated charging processes that do not rely on human intervention [69, 70].

Wireless EV charging primarily employs IPT technologies [71–86]. In recent years, extensive academic research has been conducted at prestigious universities and research institutes, such as University of Auckland [87–91], Oak Ridge National Laboratory(ORNL) [92–94], Korea Advanced Institute of Science and Technology (KAIST) [95–97], ETH Zurich

(ETHz)[98–100], and Delft University of Technology (TU Delft) [3, 101–104]. Furthermore, several companies have successfully commercialized EV wireless charging products, such as WiTricity, Plugless Power, Momentum Dynamics, ElectReon, WAVE, and Tesla [105]. In response to the growing industrial interest in this technology, standards, and regulations have been established since 2015, including SAE J2954, the IEC 61980 series, and ISO 19363 [106]. These standards define key characteristics of EV wireless charging systems, such as power classes, allowable relative positions between the charging station and EV, operating frequency range, minimum communication requirements, and electromagnetic compatibility (EMC) limits. Specifically, the current standards address static wireless charging systems for light-duty EVs [1]. SAE J2954 categorizes three power classes (WPT1, WPT2, and WPT3), each with maximum grid input power limits of 3.7 kVA, 7.7 kVA, and 11.1 kVA, respectively. Additionally, the operating frequency range of the IPT system is constrained between 79 kHz and 90 kHz, while the air gap between the transmitter (Tx) and receiver (Rx) coils is specified to range from 10 cm to 25 cm.

In wireless EV charging systems, the transmitting coil is typically placed on the ground or embedded as part of the ground assembly (GA), while the receiving coil is mounted on the chassis of the EV as part of the vehicle assembly (VA) [1]. These coils form a loosely coupled transformer due to their relatively large distance [107]. To compensate for significant leakage inductances of these loosely coupled coils, compensation networks are essential [108]. Additionally, in wireless EV charging applications, achieving a wide operating range is crucial due to several contributing factors. Firstly, EV battery loads undergo significant variations during the constant current (CC) and constant voltage (CV) charging stages. Secondly, coil misalignment and capacitance drift result in notable deviations in the parameters of resonant circuits. Thirdly, accommodating diverse EV models to enhance interoperability introduces significant variations in air gaps, receiver coil configurations, and nominal EV battery voltages. These factors significantly expand the operating range of wireless EV charging systems. In this context, ensuring highly-efficient and wide-range operation under significantly varying conditions poses a challenging yet important task.

1.2. TECHNICAL CHALLENGES IN WIRELESS EV CHARGING

1.2.1. HIGH EFFICIENCY UNDER WIDE-RANGE LOAD VARIATIONS

In wireless EV charging, batteries serve as the loads of the system. Given the noticeable variations in battery profiles during charging, it is crucial for the system to regulate power across a wide range of load variations effectively. Specifically, as illustrated in Fig. 1.2(a), EV battery charging typically involves two main stages: the CC charging stage and the CV charging stage. Therefore, a wireless EV charging system needs to be capable of delivering both CC and CV outputs [109]. Furthermore, as demonstrated in Fig. 1.2(b), significant variations in charging power and equivalent load resistance occur during the CC and CV charging processes. Consequently, it is also imperative for the system to achieve broad power regulation under wide-range load variations.

Over the past decades, extensive research has been conducted to address wide-range load variations in wireless EV charging. These efforts can be broadly categorized into three approaches: 1) cascading DC-DC converters, 2) modulating the inverter and/or

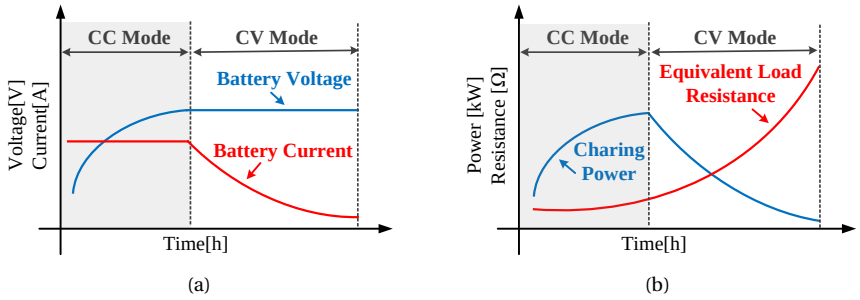

Figure 1.2: Qualitative illustrations of (a) the CC-CV charging profile in wireless EV charging systems, and (b) variations in charging power and equivalent load resistance during the CC-CV charging process. Here, the charging power is defined by multiplying the system's DC output voltage by the DC output current, while the equivalent load resistance is determined by dividing the DC output voltage by the DC output current.

rectifier, and 3) tuning the system frequency. Detailed discussions of these techniques are presented as follows.

(1) DC-DC CONVERTERS

To enable broad-range output power regulation for the wireless EV charging systems, a commonly adopted approach is to cascade DC-DC converters in the front- and/or back-end of the system [110]. Fig. 1.3 demonstrates the incorporation of front-end and back-end DC-DC converters in wireless EV charging systems. As it can be observed, by adjusting the output voltages of the DC-DC converters, the system output power can be regulated accordingly. Nevertheless, the introduction of DC-DC converters results in additional power losses. Moreover, DC-DC converters require extra components and power switches, which raise manufacturing costs and decrease the power density of the system.

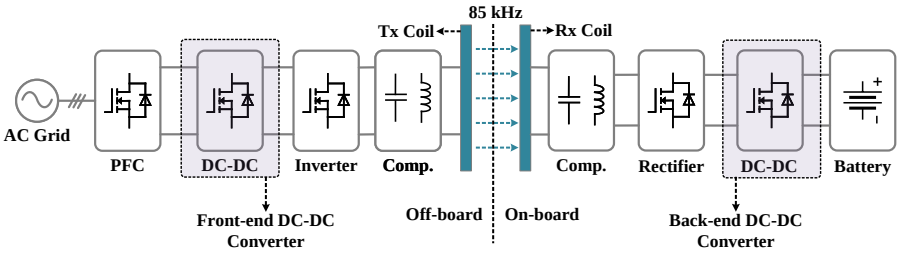

Figure 1.3: Incorporation of front-end and back-end DC-DC converters in wireless EV charging systems. In this figure, "Comp." refers to the compensation network; "PFC" denotes the power factor correction converter; "Tx coil" and "Rx coil" represent the transmitter coil and receiver coil, respectively. The same description also applies to Fig. 1.4, Fig. 1.5, Fig. 1.9.

(2) MODULATION OF THE INVERTER AND/OR RECTIFIER

Alternatively, to eliminate the need for additional DC-DC converters, another well-known method for output power regulation is to optimize modulation techniques for the inverter and/or rectifier. Fig. 1.4 demonstrates typical modulation techniques for wireless EV charging systems.

On the one hand, existing power control strategies for wireless EV charging systems can be roughly categorized into three groups: primary-side control, secondary-side control, and dual-side cooperative control. In the primary-side control, as illustrated in Fig. 1.4, the output voltage of the inverter is adjusted for power regulation [111, 112]. Additionally, according to [113], power regulation can also be accomplished through the rectifier, which is referred to as secondary-side control. Distinct from primary-side control, secondary-side control replaces the conventional passive diode rectifier with an active rectifier. Through modulation and control of the active rectifier, power regulation of the system can be achieved. Furthermore, the inverter and active rectifier can be regulated simultaneously to tune the output power [114, 115]. This method is known as dual-side control. Within the dual-side control, both the inverter output voltage and the rectifier input voltage are adjusted, enabling wide power regulation across wide load conditions.

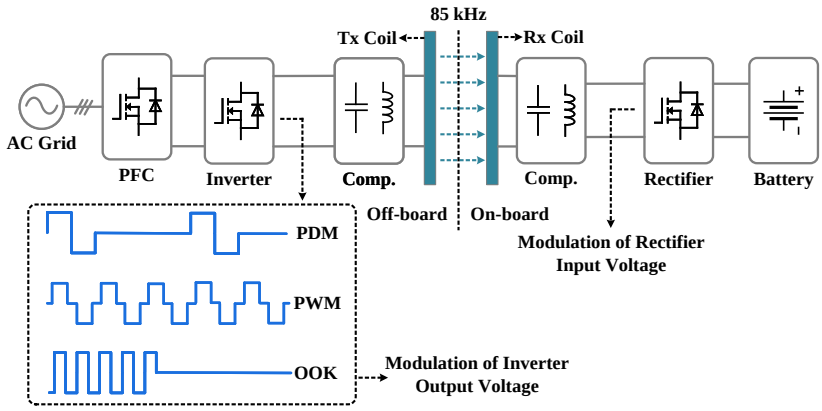

Figure 1.4: Typical modulation techniques for the wireless EV charging systems. Here, the output voltage of the primary-side inverter can be modulated and controlled to tune the system output power. Additionally, by replacing the passive diode rectifier with an active rectifier, the rectifier input voltage can also be adjusted for output power regulation.

On the other hand, within the wireless EV charging systems, mainstream modulation techniques for the inverter and/or rectifier include pulse width modulation (PWM) [116–118], pulse density modulation (PDM) [119, 120], and on-off keying modulation (OOK) [121, 122], as elaborated in Table 1.1.

The PWM, also known as phase shift modulation (PSM), is the most prevalent modulation approach. In the PWM method, the pulse width of the inverter output voltage (or the rectifier input voltage) is adjusted to enable power regulation. Nevertheless, due to the reduced pulse width under load variations, the PWM method is susceptible to the issue of hard switching. Although zero-voltage-switching (ZVS) can be implemented by actively injecting reactive power into the resonant circuits, this approach notably signif-

Table 1.1: Typical modulation techniques for wireless EV charging systems

Modulation	Pros	Cons	References
PWM (or PSM)	• Ease of implementation • Continuous output tuning • Wide tuning range	• Large switching losses • Significant reactive power under load variations	[116–118]
PDM	• Reduced switching losses • Ease of soft-switching	• Limited tuning resolution • Significant voltage/current ripple	[119, 120]
OOK	• Ease of implementation • Continuous output tuning • Ease of soft-switching	• Significant voltage/current ripple • Noticeable surge currents under ON-OFF transients	[121, 122]

icantly increases the circulating reactive currents. (Here, zero-voltage switching (ZVS) refers to switches being turned on when there is zero voltage across them.) These increased reactive currents result in higher power losses, consequently reducing power transmission efficiency [104].

Recently, pulse density modulation (PDM) has been extensively investigated for power regulation in wireless charging systems. In the PDM method, the pulse width of the voltage (either the inverter output voltage or the rectifier input voltage) remains at full duty cycle, whereas adjustments to the voltage are accomplished by tuning the pulse density. As the pulse width is maintained at full duty cycle in the PDM, implementation of ZVS can be facilitated. Moreover, as the PDM method reduces the equivalent switching times of the semiconductor switches, it can also decrease the switching losses for the power switches. Nevertheless, the PDM approach results in irregular pulse distribution, which significantly increases the output voltage ripple and exacerbates current distortions [113].

In addition to the PWM and PDM techniques, the on-off keying modulation (OOK) is also frequently adopted for power regulation. To achieve power delivery across wide-range load variations, the OOK technique introduces the “OFF” state for the converters. During the "OFF" state, the inverter (or the rectifier) is deactivated. Conversely, in the "ON" state, the inverter (or the rectifier) activates, producing square-wave full-duty-cycle AC voltage. Although the OOK method excels in ease of implementation and soft switching capability, it leads to significant surge currents during the transition from the “OFF” state to the “ON” state. Additionally, due to the absence of power injection in the "OFF" state, the OOK technique increases the output voltage ripple of the system [123].

(3) FREQUENCY TUNING

Moreover, tuning the system frequency is also an effective strategy for power regulation. As illustrated in Fig. 1.5, the switching frequency of the inverter output voltage can be adjusted for output tuning. Notably, according to the frequency range defined in SAEJ 2954 (international wireless EV charging standard), the power transfer frequency of the system should be within the range of 79 to 90 kHz.

By adjusting the switching frequency, the output power of the system can be regulated [124]. Additionally, integrating frequency tuning with the PWM method is ef-

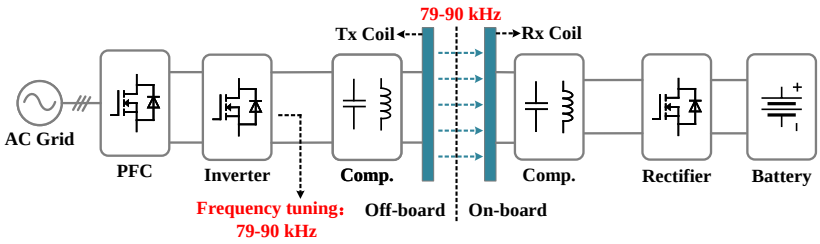

Figure 1.5: Implementation of frequency tuning in wireless EV charging systems. Here, the power transfer frequency is defined as 79-90 kHz in accordance with the SAEJ 2954 standard [1].

fective for achieving wide-range ZVS under load variations [125]. However, tuning the frequency within the wireless charging systems is susceptible to the bifurcation phenomenon [126–128]. As a consequence, existing frequency tuning strategies necessitate careful design of system parameters to prevent the occurrence of bifurcation [129].

1.2.2. TOLERANCE TO PARAMETER DEVIATIONS

In wireless EV charging systems, a notable air gap exists between the Tx and Rx coils. This leads to considerable leakage inductances within the coils and a diminished mutual inductance. The contactless coil architecture essentially forms a loosely coupled transformer. Depending on factors such as spatial distance, alignment precision, and coil dimensions, the wireless EV charging systems typically exhibit a transformer coupling coefficient ranging from 0.1 to 0.4 [1].

To mitigate the significant leakage inductances of the contactless coils, compensation networks are indispensable. By incorporating passive components such as inductors and capacitors, significant leakage inductances can be compensated, allowing the system to operate in a resonant state. However, the parameters of resonant circuits are susceptible to deviations due to coil misalignment and capacitance drift. These parameter deviations result in the detuning of the system, consequently reducing the system efficiency and resulting in a lower power factor [130]. Additionally, significant parameter deviations result in a considerably increased operating range, making it challenging to maintain the desired output power and high efficiency.

Descriptions of coil misalignment and capacitance drift in wireless EV charging applications are demonstrated as follows.

(1) COIL MISALIGNMENT

In wireless EV charging, coil misalignment is prevalent due to the contactless nature between the Tx and Rx coils. Fig. 1.6 illustrates typical misalignment cases in wireless EV charging applications. As it can be observed, coil misalignment occurs in various spatial directions. In addition to horizontal misalignments (including lateral, longitudinal, and rotation directions), vertical misalignment may also occur when different EV models share the same Tx coil. Specifically, according to SAE J2954, EVs should be able to tolerant a certain degree of coil misalignment [1]: vertical: Z1 (100 to 150 mm), Z2 (100 to 210 mm), Z3 (100 to 250 mm); lateral (ΔX: $\pm$ 75mm); longitudinal (ΔY: $\pm$ 100mm). Here,

Z1, Z2, and Z3 are three Z-classes defined in SAEJ2954 to classify the range of ground clearances (the vertical distance between the Tx and Rx coils).

The misalignment between the Tx and Rx coils leads to significant variations in their mutual inductance. Additionally, within the Tx and Rx coils, the metallic shielding plates are commonly utilized to protect human and electronic devices from the stray magnetic field, while magnetic ferrites are employed to improve coil coupling. As these metallic and magnetic materials interfere with the transmission of the magnetic flux, the self-inductances of the coils become sensitive to the coil displacement. Consequently, coil misalignment also results in variations in self-inductances of the coils [131].

(2) CAPACITANCE DRIFT

To mitigate noticeable leak inductances of contactless coils, compensation capacitors are essential in wireless EV charging systems. Nevertheless, the compensation capacitances may deviate from the nominal values in practice [132]. On the one hand, the commercial capacitors in the market usually have several levels of capacitance tolerance, for instance, ±2.5%, ±5%, ±10%, and so on [132, 133]. On the other hand, variations in ambient temperature and aging effects further exacerbate the degree of capacitance drift. For instance, Fig. 1.7 demonstrates typical capacitance drift of ceramic capacitors under temperature variations [2]. As evident from Fig. 1.7, the capacitance of ceramic capacitors experiences significant variations under temperature variations. Consequently, under the combined influences of component tolerances, temperature variations, and aging effects, capacitance drift can be significant in practical EV charging scenarios.

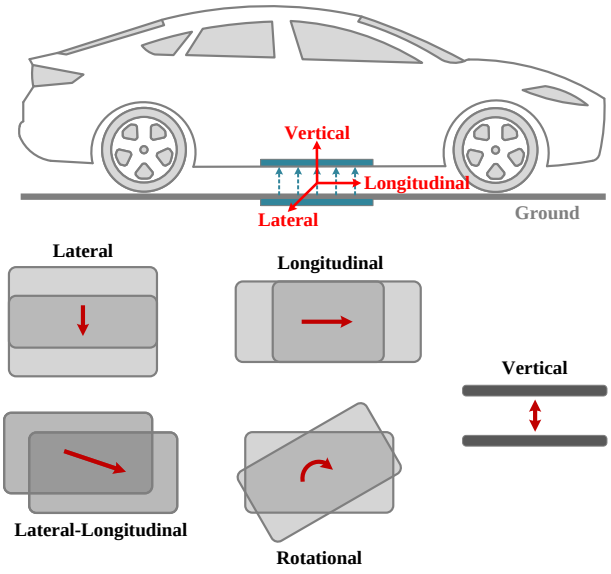

Figure 1.6: Typical cases of coil misalignment in wireless EV charging applications.

1.2.3. INTEROPERABILITY ACROSS DIVERSE EV MODELS

In recent years, the EV market has experienced significant growth, with a wide variety of EV models emerging. To address this trend, it is imperative for wireless charging systems to accommodate the diversity of EV models in the market. However, when considering the interoperability across diverse EV models, several technical challenges emerge. These challenges are elaborated as follows.

(1) VARYING AIR GAPS BETWEEN THE TX AND RX COILS

In the EV market, distinct EV models have varying heights of vehicle chassis, leading to variations in the air gap between the Tx and Rx coils in wireless EV charging systems [1]. As shown in Fig. 1.6, these varying air gaps correspond to vertical coil misalignment. Furthermore, as discussed in Chapter 1.2.2, the self- and mutual inductances of the coils vary due to disparities in the air gap. These deviations in coil inductances result in non-resonance operating of the system, leading to reduced transmission efficiency and lower power factor. Consequently, when accommodating different air gaps among various EV models, challenges arise in maintaining the resonance state under varying coil inductances.

(2) ASYMMETRIC COIL CONFIGURATIONS

In practical wireless EV charging applications, the receiver coil configurations vary across different EV models. This results in inconsistent configurations between the Tx and Rx coils. Under the asymmetric coil configurations, the control variables on the primary side and the secondary side should be adjusted differently to achieve maximum efficiency tracking (also known as optimal load tracking). This presents heightened challenges in achieving dual-side ZVS for both the primary-side inverter and the secondary-side rectifier [134, 135]. Although large reactive power can be injected into resonant circuits for dual-side ZVS implementation, this approach reduces transmission efficiency.

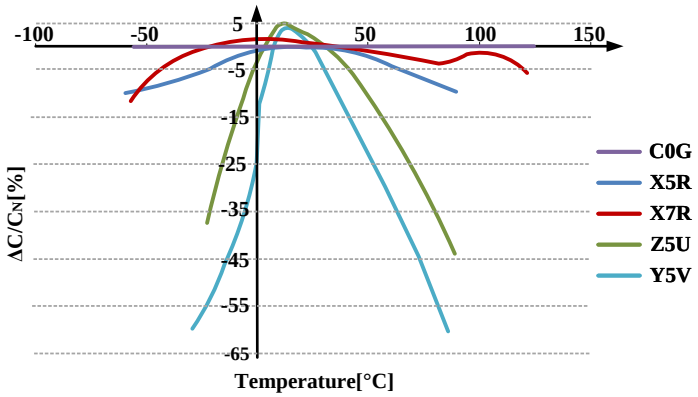

Figure 1.7: Typical capacitance drift of ceramic capacitors under temperature variations [2]. Here, C_N represents the nominal capacitance value, while ΔC indicates the value of capacitance drift. (Source Data: AVX Surface Mount Ceramic Capacitor Products Catalog, v13.10)

To address asymmetric coil configurations, challenges persist in achieving optimal dual-side ZVS while minimizing reactive power within the resonant circuits.

(3) WIDE OUTPUT VOLTAGE VARIATIONS

As more EV models populate the streets, it is evident that their nominal battery voltages vary in a wide range. In accordance with [103], most EV batteries fall into two nominal voltage levels: 400-V and 800-V. Specifically, Table 1.2 illustrates nominal battery voltages of several EV models in the market. As it can be observed, the nominal battery voltages vary significantly across diverse EV models. In this context, achieving wide power regulation while accommodating a wide range of output voltage variations becomes challenging. Moreover, maintaining high efficiency under such a significantly broad operating range is crucially important and poses further challenges.

Table 1.2: Battery voltages of several EV models in the market

Manufacturer	EV model	Battery voltage	Year of Release	Source
Tesla	Cybertruck	816 V	2024	[136]
Tesla	Model S	400 V	2023	[136]
Tesla	Model 3	360 V	2023	[136]
Volkswagen	ID.4	408 V	2023	[136]
Hyundai	IONIQ 6	800 V	2023	[136]
KIA	EV6	697 V	2023	[136]
BMW	i4	398 V	2023	[136]
BMW	i7	376 V	2023	[136]
Porsche	Taycan	800 V	2023	[137]
Mercedes-benz	EQS	500 V	2022	[136]
Mercedes-benz	EQB	420 V	2022	[136]
Audi	e-tron	396 V	2022	[136]

1.2.4. CONCLUSIONS

In this thesis, the above technical challenges are investigated. To address these challenges, corresponding solutions are proposed. Fig. 1.8 demonstrates the technical challenges and the proposed solutions identified in this thesis. Descriptions of the proposed solutions in this thesis are outlined as follows.

Firstly, to address significant battery load variations, hybrid modulation techniques are proposed in Chapters 2 and 3 for achieving wide output power regulation in SS-compensated systems. Furthermore, Chapters 5 and 6 investigate how to enable wide power regulation for double-sided LCC (DLCC) compensated systems.

Secondly, to deal with coil misalignment and capacitance drift, Chapter 4 proposes a parameter identification based impedance tuning method. Additionally, the DLCC com-

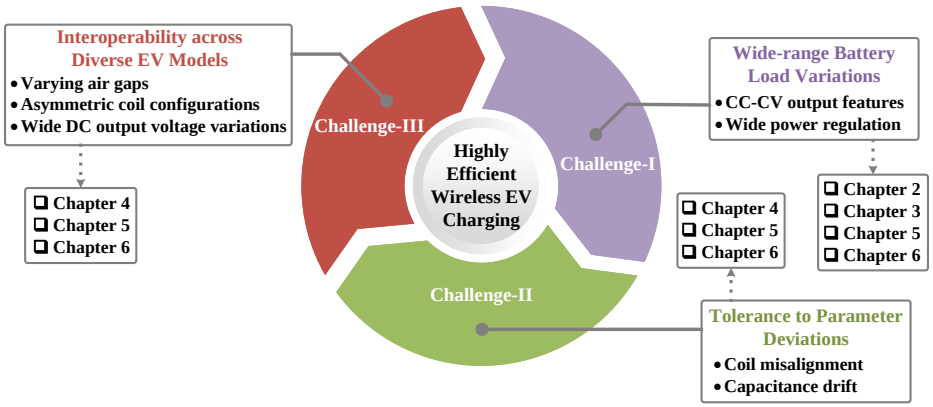

Figure 1.8: Technical challenges and proposed solutions identified in this thesis.

pensation network demonstrated in Chapters 5 and 6 notably enhances the system's robustness against coil misalignment.

Thirdly, several solutions are proposed to improve interoperability across diverse EV models. Specifically, Chapters 5 and 6 investigate the DLCC compensation network to enhance system robustness under varying air gaps, while Chapter 4 demonstrates solutions for identifying unknown coil inductances within different air gap conditions. Moreover, asymmetric coil configurations are investigated in Chapters 5 and 6. Additionally, Chapter 6 highlights achieving high efficiency under wide output voltage variations.

1.3. RESEARCH SCOPE, OBJECTIVE, AND QUESTIONS

1.3.1. RESEARCH SCOPE

This thesis investigates the power conversion stages within static wireless EV charging systems.

As illustrated in Fig. 1.9, the static wireless EV charging system comprises ground assembly (GA) and vehicle assembly (VA) circuits. The GA circuits interface with the AC grid and incorporate a power factor correction (PFC) converter to supply DC input voltage. This voltage is further regulated by a front-end DC-DC converter. Subsequently, a high-frequency inverter converts DC voltage into high-frequency AC voltage (typically within the range of 79-90 kHz). To address significant leakage inductance of the Tx coil, a primary compensation network is integrated between the inverter and the Tx coil. The VA circuits receive magnetic flux via the Rx coil. After passing through a secondary compensation network, the high-frequency AC voltage is rectified into DC voltage using a rectifier. A back-end DC-DC converter can be employed to further adjust the system's output voltage. Notably, the front-end and back-end DC-DC converters are optional in wireless EV charging systems. When these converters are not included, output power regulation of the system can be accomplished through modulation and control of the high-frequency inverter and/or rectifier.

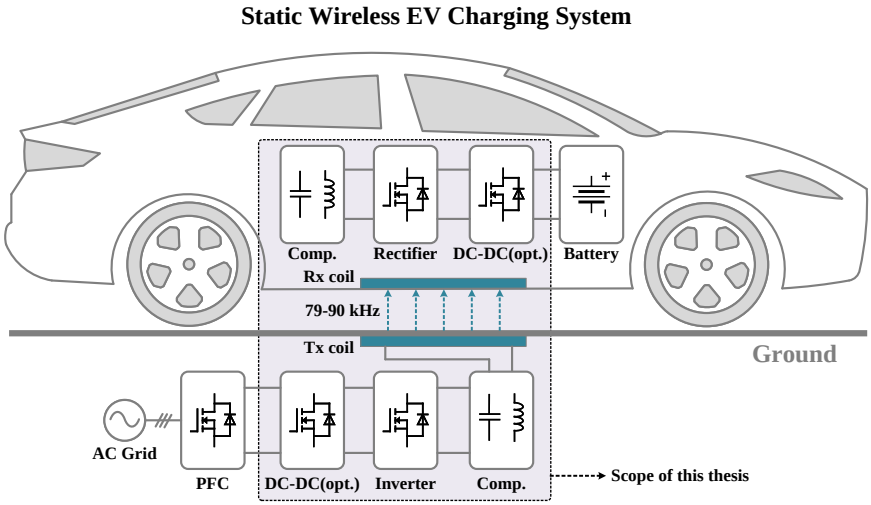

Figure 1.9: Scope of this thesis for wireless EV charging applications.

In this thesis, as indicated by Fig. 1.9, the investigation encompasses the power conversion stages from the PFC output to the battery input.

1.3.2. RESEARCH OBJECTIVE

The overall research objective of this thesis is outlined as follows:

Explore advanced control and modulation techniques for wireless electric vehicle (EV) charging systems, with the goal of achieving robust wide-range output power regulation and sustaining high transmission efficiency despite significant variations in load conditions, output voltages, and parameter deviations.

1.3.3. RESEARCH QUESTIONS

1. How to achieve wide-range output power regulation while maintaining high transmission efficiency under significant battery load variations? (Chapter 2, Chapter 3)

Considering the CC-CV charging profile of EV batteries, it is imperative for wireless EV charging systems to achieve wide-range output power regulation under significant battery load variations. Conventional power regulation methods typically involve the incorporation of front-end and/or back-end DC-DC converters, leading to additional power losses and manufacturing costs. Alternatively, power regulation of the system can be accomplished through the modulation and control of the inverter and/or rectifier without introducing extra DC-DC converters.

This thesis will investigate typical modulation techniques used for the inverter and rectifier. Moreover, it will explore feasible control solutions for achieving wide power regulation, encompassing primary-side control, secondary-side control, and dual-side cooperative control. Building upon existing control solutions and modulation techniques, this thesis will delve into exploring hybrid operating modes for the inverter and recti-

fier aimed at enhancing efficiency under wide-range load variations (Chapter 2). Furthermore, to enable communication-less wide power regulation, the hybrid modulation techniques will be investigated for the secondary-side control (Chapter 3).

2. How to address parameter deviations caused by coil misalignment and capacitance drift in practical EV charging applications? (Chapter 4)

Due to coil misalignment and capacitance drift, parameter deviations are inevitable in wireless EV charging systems. When the parameters of the resonant circuits deviate from their nominal values, the system may operate in a non-resonant state, leading to decreased transmission efficiency and a lower power factor. To address these unpredictable parameter deviations, parameter recognition methods can be utilized. However, when considering significant parameter deviations, existing parameter recognition methods can lead to remarkably higher circulating currents and increased output power.

This thesis will investigate the fundamental principles of existing parameter identification methods. Furthermore, a dynamic frequency-approaching-based parameter recognition strategy will be proposed to accurately identify unknown parameters of resonant circuits. Based on this proposed method, an impedance tuning strategy will be demonstrated to ensure that the system maintains resonance even in the presence of significant coil misalignment and capacitance drift.

3. What strategies can be employed to effectively address asymmetric parameters caused by varying receiver configurations in different EV models? (Chapter 5)

Wireless EV charging systems should ideally support various EV models available in the market. The diversity of EV models results in different configurations of receiver coils, leading to asymmetry in primary and secondary parameters. Under the asymmetric parameters, existing control methods exhibit increased reactive power and reduced system efficiency under varying load conditions.

This thesis will investigate current control strategies and then identify their limitations when applied to asymmetric parameters. Furthermore, an optimal multivariable control strategy will be explored to address these limitations, enabling wide output power regulation and full-range efficiency optimization for wireless EV charging systems operating under asymmetric parameters.

4. How can wide output voltage variations, arising from diverse nominal battery voltages across various EV models, be effectively accommodated? (Chapter 6)

To improve the interoperability of the wireless EV charger, it is important for the system to accommodate diverse nominal battery voltages across various EV models. However, when the system must manage wide output voltage variations, existing methods exhibit notable efficiency drops under load variations.

In this thesis, a dual-side capacitor tuning method based on two switch-controlled capacitors (SCCs) will be proposed to accommodate wide-range output voltage variations. Moreover, a dual-side cooperative control strategy will be presented to achieve wide-range output power regulation and address wide output voltage variations while maintaining high transmission efficiency.

1.4. OUTLINE OF THIS THESIS

This thesis comprises seven chapters, with the first chapter serving as the introduction and the final chapter as the conclusion. The main research content is distributed across

five chapters (Chapter 2 - Chapter 6). These five chapters are categorized into three distinct parts based on their respective topics. Fig. 1.10 outlines the structure of this thesis. Moreover, brief descriptions of each chapter are provided as follows.

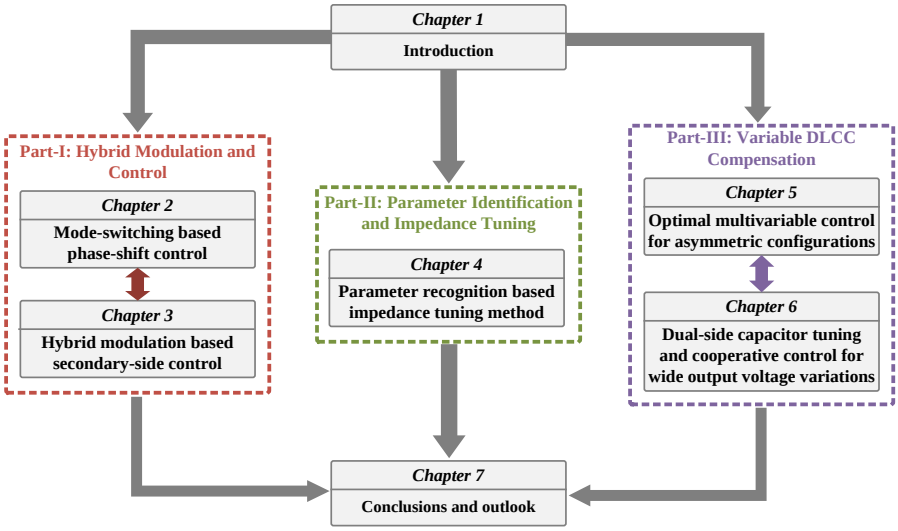

Figure 1.10: Outline of this thesis.

First of all, Chapter 1 provides the introduction to this thesis.

Following the introduction, Part I demonstrates hybrid modulation techniques for achieving wide-range output regulation under significant battery load variations in wireless EV charging. This part consists of Chapter 2 and Chapter 3. Therein, Chapter 2 presents a mode-switching-based phase shift control for dual-side control, while Chapter 3 introduces a hybrid modulation scheme for communication-less secondary-side control.

Subsequently, Part II consists of Chapter 4, demonstrating solutions for addressing parameter deviations caused by coil misalignment and capacitance drift in practical EV charging applications. In Chapter 4, a parameter identification method is proposed to recognize the unknown parameters of the resonant circuits. Furthermore, an impedance tuning method based on the recognized parameters is further demonstrated to ensure that the system consistently operates at resonance even under significant parameter deviations.

Furthermore, Part III, comprising Chapters 5 and 6, demonstrates research efforts based on the variable DLCC compensation network. Specifically, Chapter 5 introduces an optimal multivariable control approach to manage asymmetry in primary and secondary parameters. Moreover, Chapter 6 presents a dual-side capacitor tuning and cooperative control strategy to accommodate wide output voltage variations arising from diverse nominal battery voltages across various EV models.

Finally, Chapter 7 presents the conclusions and outlook of this thesis.

PART I

HYBRID MODULATION AND CONTROL

2

MODE SWITCHING BASED PHASE SHIFT CONTROL

This chapter presents a mode-switching-based phase shift control (MS-PSC) for inductive power transfer (IPT) systems, which is able to achieve power regulation, load matching, and wide ZVS operations simultaneously without using additional DC-DC converters. Based on the mode transitions between the full-bridge, mixed-bridge, and half-bridge modes of both the inverter and the rectifier, the MS-PSC method guarantees a wide-range ZVS with minimized circulation of reactive power. Therefore, the system efficiency is improved over a wider power range compared to the conventional triple-phase-shift (TPS) control and the existing hybrid modulation control. The principles of different operating modes are analyzed. Then, the implementation of the proposed MS-PSC method and the mode selection strategy are presented. Finally, the effectiveness of the proposed MS-PSC method is validated in an IPT prototype. Experimental results show that the proposed MS-PSC method can achieve high overall efficiency in a wide power range. Compared with the conventional TPS control, the MS-PSC method further optimizes the efficiency in 10%-63% of the rated power, with efficiency improvements ranging from 1.5% to 6%. As a result, the system efficiency remains at 93.5%-96.1% in the power range of 1-10 kW, with the transformer coupling coefficient k=0.19.

This chapter is based on:

- G. Zhu, J. Dong, W. Shi, T. B. Soeiro, J. Xu, and P. Bauer, "A mode-switching-based phase shift control for optimized efficiency and wide zvs operations in wireless power transfer systems," *IEEE Transactions on Power Electronics*, vol. 38, no. 4, pp. 5561–5575, Apr. 2023.

2.1. INTRODUCTION

Inductive power transfer (IPT) enables safe, convenient, and automated charging for electric vehicles (EVs) [3, 33, 34, 71, 138–141]. For wireless charging of EVs, batteries act as the load for the IPT systems. Due to the noticeable variation of battery profiles during the charging process, it is vital for IPT systems to achieve accurate power flow control over a wide operating range [139]. Generally, there are three important objectives when designing a controller for IPT systems. Firstly, it is necessary for the controller to provide the desired output based on the load profiles. For EV battery charging, the process is typically divided into two stages: constant current (CC) and constant voltage (CV). Therefore, CC/CV output is the fundamental control target of the IPT systems designed for EVs. Secondly, in order to improve transmission efficiency as well as to reduce electromagnetic interference (EMI) of the system, the implementation of zero-voltage-switching (ZVS) operations across the semiconductors of the typically used resonant converter serves as another important consideration for the controller design [142]. Thirdly, to realize the optimized efficiency, optimal load tracking has become an increasingly important performance indicator in the IPT systems [143, 144]. Thus, it is desired to realize load matching.

In order to realize power regulation and load matching simultaneously, a commonly used approach is to cascade DC /DC converters in the front- and/or back-end of the IPT systems [145, 146]. In [145], Dai *et al.* proposed a maximum efficiency tracking method with two DC-DC converters installed in the front- and back-end of the system, respectively. In this method, a primary-side DC-DC converter is used to provide a stable load voltage, while a secondary-side DC-DC converter is employed for maximum efficiency tracking. In [146], Huang *et al* proposed a control technique based on the perturbation and observation (P&O). The load-side DC-DC converter is responsible for output regulation, while the front-side converter is used to minimize the input power through P&O methods. Although introducing DC-DC converters can realize the control objectives, it also brings extra losses, increased costs, and reduced power density.

Another typical method for power regulation is phase shift control. In [147], phase shift control was implemented in the primary-side inverter for load matching. In this method, the front-end DC-DC converter is avoided by introducing an active control of the inverter. However, the load-side DC-DC converter is still needed to achieve the desired output control metrics, which results in extra power losses and costs. In order to further eliminate the load-side DC-DC converter, an active rectifier can be utilized to regulate the equivalent load impedance [148, 149]. Based on the active rectifier, a dual-phase-shift (DPS) control method was proposed in [150], where the phase shift angles of the inverter and rectifier stages were adjusted cooperatively to achieve power regulation and load matching simultaneously. Nevertheless, the phase difference between the AC port voltages of the inverter and rectifier is maintained at 90° in this method, resulting in hard switching of some power switches. In order to realize wide ZVS operations, a triple-phase-shift (TPS) control method was proposed in [151], where the phase difference of the dual-side AC voltages was served as a new control variable to realize ZVS under a wide output power. However, this approach introduces large reactive power in the resonant tank. This means that higher coil currents are needed to deliver the same amount of power, which increases the power losses of the system. Moreover, some re-

searchers have introduced new control variables to achieve optimal control of the IPT systems. Wang *et al.* [152] proposed a switch-controlled-capacitor-based phase shift modulation (SCC-PSM) to provide the desired output and realize wide ZVS operations. However, the use of SCC leads to additional power losses. In order to avoid additional components, Hu *et al.* [125] proposed a variable frequency phase shift control (VFPSC) to realize ZVS operations under wide load variations. Nevertheless, in this method, the switching frequency needs to be regulated far away from the resonant frequency to ensure wide ZVS operations. This makes the system highly detuned, resulting in reduced overall efficiency.

Recently, some researchers combined the half-bridge (HB) mode and the full-bridge (FB) mode to improve the system efficiency under light load conditions. Li *et al.* [153] proposed a hybrid modulation control (HMC) method to improve the light-load efficiency, where both the inverter and rectifier can operate in the FB and HB modes based on the output power. Compared to the conventional TPS method, the HMC method achieves further efficiency optimization in 16.7%-40% of the rated power. However, due to the limited power transfer capability of the HB mode, the converters still operate in the FB mode at most power levels, and the efficiency optimization range is narrow. Wu *et al.* [154] proposed a dual-sided control strategy based on mode switching (DSC-MS), where the mixed-bridge (MB) mode was utilized to widen the operating range of the inverter. For the MB mode, the inverter operates in the FB and HB modes alternatively in each two switching cycles, which extends the regulation range of the inverter output voltage. In the DSC-MS method, load matching is realized through mode switching of the inverter, while output regulation is achieved by the phase shift control of a semi-active rectifier. Nevertheless, phase shift control of the inverter is missing in this method, and therefore, wide power regulation still relies on the voltage control of the front-stage power factor correction (PFC) converter. Besides, since the MB and HB modes are not considered in the rectifier control, the efficiency under light load conditions is still low. In [154], the system efficiency was only 88.7% at 14.8% of the rated power.

2.1.1. SCOPE AND CONTRIBUTIONS

To fill up the above-mentioned research gaps, this chapter presents a mode-switching-based phase shift control (MS-PSC) for IPT systems. In this method, an active rectifier is adopted, and hybrid modes of both the inverter and rectifier are considered. Both the inverter and rectifier can switch to FB, MB, and HB modes to provide the desired output and achieve load matching. ZVS operations of all power switches are realized under a wide range of power levels. To sum up, the main contributions of the proposed method are listed as follows:

1) Wide power regulation in 10%-100% of the rated power is achieved without using additional DC-DC converters.

2) Thanks to the effective use of the FB, MB, and HB modes and the joint control of the inverter and rectifier, wide ZVS operations are realized with minimized circulation of reactive power. Therefore, an overall efficiency of 93.5%-96.1% is obtained within 10%-100% of the rated power. Compared with the conventional TPS control, the MS-PSC method further optimizes the efficiency in 10%-63% of the rated power, with efficiency improvements ranging from 1.5% to 6%.

3) A mode selection strategy is proposed, which enables the IPT system to switch automatically to the optimal operating mode based on the required output features.

2.1.2. OUTLINE

The rest of this chapter is as follows: Chapter 2.2 demonstrates the conventional triple-phase-shift (TPS) control for the series-series (SS) compensated IPT system. Furthermore, Chapter 2.3 illustrates the working principles of the proposed hybrid operating modes. In this subchapter, the mode selection strategy, as well as the control scheme of the proposed MS-PSC method, are also introduced. In Chapter 2.4, experimental results are presented, demonstrating the effectiveness of the proposed MS-PSC approach. Finally, conclusions are drawn in Chapter 2.5.

2.2. CONVENTIONAL TRIPLE-PHASE-SHIFT CONTROL

2.2.1. SYSTEM MODELING AND ANALYSIS

The circuit diagram of a typical series-series (SS) compensated IPT system is illustrated in Fig. 2.1. In this system, the DC input voltage is denoted by V_{in}, which is typically provided by a front-end power factor correction (PFC) converter. As demonstrated in Fig. 2.1, the DC input voltage V_{in} is converted into a high-frequency AC voltage u_{ab} by a primary-side inverter, and the power switches of the inverter are represented as $S_1 - S_4$. Furthermore, the inverter output voltage u_{ab} excites the resonant tank, with i_P and i_S denoted as the coil currents in the primary and secondary sides, respectively. L_P, C_P, L_S and C_S are the self-inductances and compensation capacitors of the transmitter and receiver coils, while M is the mutual inductance. Moreover, the equivalent resistive losses of the coupling coils and compensation capacitors are denoted by R_P and R_S, respectively. Subsequently, the output AC voltage u_{cd} of the resonant tank is converted to a DC voltage V_{out} by an active rectifier, and the power switches of the rectifier are denoted by $S_5 - S_8$. Finally, to reduce the output voltage ripple of the system, a filter capacitor C_{out} is connected to the equivalent load resistance R_L. The DC output current after the filter capacitor is denoted by I_{out}.

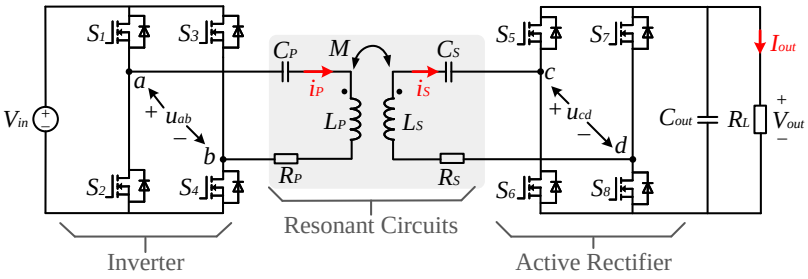

Figure 2.1: Circuit diagram of the SS-compensated IPT system with an active rectifier.

In order to provide the desired output power, phase shift control is typically adopted. The operating waveforms of the IPT system using phase shift control are shown in Fig. 2.2(a). D_P and D_S ($0 < D_P \leq 1$, $0 < D_S \leq 1$) are the duty cycles of u_{ab} and u_{cd}, which can

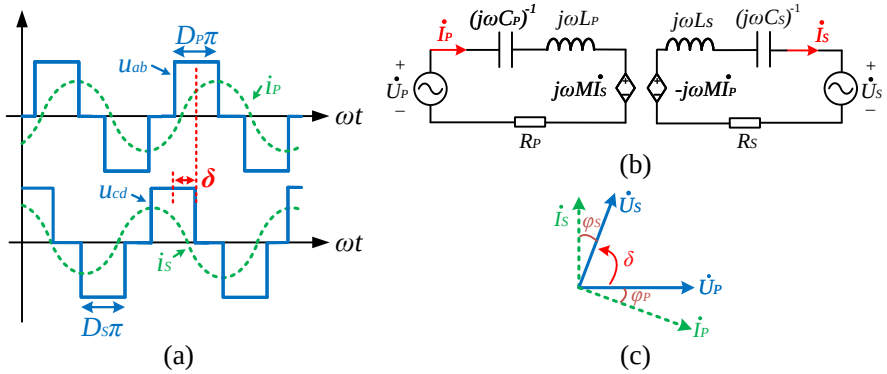

Figure 2.2: (a)Typical waveforms of the IPT system using phase shift control, (b) equivalent circuit model derived by the FHA method, and (c) phasor diagram of the voltages and currents.

be adjusted by changing the phase shift angles of the inverter and rectifier. Moreover, δ is defined as the phase difference between u_{ab} and u_{cd}.

For the SS-compensated IPT system, the compensation capacitors C_P and C_S are designed to be resonant matched with coil inductances L_P and L_S at the resonant switching frequency f_R, and the value of these passive elements satisfy

$$\omega_R = \frac{1}{\sqrt{L_P C_P}} = \frac{1}{\sqrt{L_S C_S}}, \tag{2.1}$$

where $\omega_R = 2\pi f_R$ is the resonant angular frequency.

Moreover, due to the band-pass filtering characteristic of the SS-compensated resonant network, the high-order harmonics of the coil currents are negligible. Therefore, the fundamental harmonic approximation (FHA) method is typically adopted for simplification. The equivalent circuit model of the SS-compensated IPT system derived by the FHA method is shown in Fig. 2.2(b), where $\dot{U}_P$, $\dot{U}_S$, $\dot{I}_P$, and $\dot{I}_S$ are the phasors of fundamental components in u_{ab}, u_{cd}, i_P, and i_S, respectively. Here, ω is the switching frequency of the system. To ensure the system operates at the resonance state, ω is configured as the resonant frequency ($\omega = \omega_R$). Generally, compared with ωM and R_L, the equivalent loss resistances of the resonant network are relatively small. Therefore, R_P and R_S are neglected, and the steady state equation of the system is simplified as

$$\begin{cases} \dot{U}_P & \approx -j\omega M\dot{I}_S \\ \dot{U}_S & \approx j\omega M\dot{I}_P, \end{cases} \tag{2.2}$$

where M can be expressed as

$$M = k\sqrt{L_P L_S}. \tag{2.3}$$

In (2.3), k represents the coupling coefficient of the transformer coils. In accordance with (2.2), the phasor diagram of the voltages and currents is demonstrated in Fig. 2.2(c). As evident from Fig. 2.2(c), the secondary-side current $\dot{I}_S$ lags the primary-side AC voltage $\dot{U}_P$ by 90°, whereas the primary-side current $\dot{I}_P$ leads the secondary-side AC voltage $\dot{U}_S$

by 90°. Consequently, the phase difference between $\dot{U}_P$ and $\dot{I}_P$ (φ_P), as well as the phase difference between $\dot{U}_S$ and $\dot{I}_S$ (φ_S) are given by

$$\begin{cases} \varphi_P = & \pi/2-\delta \\ \varphi_S = & \pi/2-\delta. \end{cases} \tag{2.4}$$

Based on the Fourier series expansion, the phasor forms of the AC voltages on both sides are obtained as

$$\begin{cases} \dot{U}_P = & K_P V_{in} \sin[(D_P\pi)/2]\angle 0 \\ \dot{U}_S = & K_S V_{out} \sin[(D_S\pi)/2]\angle \delta, \end{cases} \tag{2.5}$$

where K_P and K_S denote the DC to AC voltage gains of the inverter and rectifier, respectively. Typically, both the inverter and rectifier operate in the FB mode, and the voltage gain K_P and K_S can be deduced as

$$\begin{cases} K_{P\_FB} = & 2\sqrt{2}/\pi \\ K_{S\_FB} = & 2\sqrt{2}/\pi. \end{cases} \tag{2.6}$$

The subscript FB indicates that the converter operates in the FB mode. Furthermore, substituting (2.5) and (2.6) into (2.2), the amount of output active power P_{out} and circulating reactive power Q_{cir} of the system can be obtained as

$$P_{out} = \mathrm{Re}\{\dot{U}_S \dot{I}_S^*\} = \frac{|\dot{U}_P||\dot{U}_S|\sin(\delta)}{\omega M}, \tag{2.7}$$

$$Q_{cir} = \mathrm{Im}\{\dot{U}_S \dot{I}_S^*\} = -\frac{|\dot{U}_P||\dot{U}_S|\cos(\delta)}{\omega M}. \tag{2.8}$$

As it can be seen from (2.7), the direction of the transferred active power P_{out} is determined by the phase angle δ. The active power flows from the primary side to the secondary side when $0 < \delta < \pi$, while the transfer direction is reversed when $-\pi < \delta < 0$. This chapter only considers the case where the power flows from the primary side to the secondary side, and the phase angle δ should satisfy $0 < \delta < \pi$. Besides, as it can be observed from (2.7) and (2.8), the amount of active power P_{out} is maximized at $\delta = \pi/2$, with the reactive power Q_{cir} under this condition minimized simultaneously. Therefore, it is desired to let the system work in $\delta = \pi/2$ to enhance the power transfer capability of the system as well as to minimize the circulating reactive power in the resonant tank. Moreover, the amplitude of the AC voltages on both sides also determines the amount of transferred active power, which can be regulated by adjusting the duty cycles D_P and D_S.

2.2.2. MAXIMUM EFFICIENCY OF THE RESONANT TANK

The concept of maximum efficiency tracking is important for improving efficiency in IPT systems. To obtain the maximum efficiency point, the power losses of the resonant tank are analyzed. According to the equivalent circuit model shown in Fig. 2.2(b), the power losses of the resonant tank are given by

$$P_{l\_res} = |\dot{I}_P|^2 R_P + |\dot{I}_S|^2 R_S = \frac{|\dot{U}_P|^2 R_S + |\dot{U}_S|^2 R_P}{\omega^2 M^2}. \tag{2.9}$$

Furthermore, the transfer efficiency η_{res} can be approximated as

$$\eta_{res} \approx \frac{P_{out}}{P_{out} + P_{l\_res}}. \tag{2.10}$$

Substituting (2.7) and (2.9) into (2.10), η_{res} is obtained as

$$\eta_{res} \approx \frac{\omega M \sin(\delta)}{R_P T + R_S / G_{AC} + \omega M \sin(\delta)}, \tag{2.11}$$

where G_{AC} is the ratio of the AC voltages on the primary and secondary sides, which can be expressed as

$$G_{AC} = \frac{|\dot{U}_S|}{|\dot{U}_P|} = \frac{K_S V_{out} \sin[(D_P \pi)/2]}{K_P V_{in} \sin[(D_P \pi)/2]}. \tag{2.12}$$

As evident from (2.12), η_{res} varies with the AC voltage ratio (G_{AC}) and the phase difference angle (δ). With the parameters in Table 2.1, the resonant tank efficiency η_{res} with different values of G_{AC} and δ is shown in Fig. 2.3. According to Fig. 2.3, the maximum efficiency is achieved under a certain voltage ratio G_{AC}. The optimal voltage ratio G_{AC_opt}

Table 2.1: Parameters of the investigated IPT system used to verify the proposed MS-PSC method

Symbol	Parameters	Value	Unit
M	Mutual inductance	46	μH
L_P	Primary coil inductance	293.8	μH
L_S	Secondary coil inductance	198.8	μH
C_P	Primary compensation capacitor	12.0	nF
C_S	Secondary compensation capacitor	17.6	nF
R_P	Primary loss resistance	0.21	Ω
R_S	Secondary loss resistance	0.14	Ω
V_{in}	DC input voltage	600	V
V_{out}	DC output voltage	600	V
f	Switching frequency	85	kHz
δ_m	Margin angle	16	°

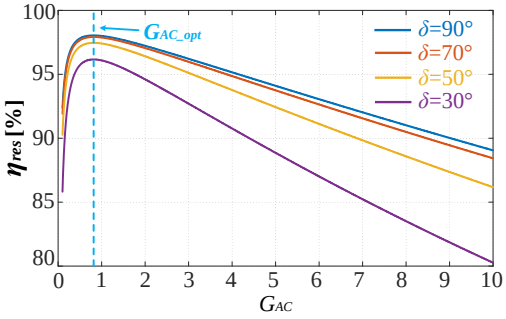

Figure 2.3: Resonant tank efficiency η_{res} under different values of AC voltage gain G_{AC} and phase difference angle δ.

can be deduced by solving the derivative of η_{res} with respect to G_{AC}, which is expressed as

$$\frac{d\eta_{res}}{dG_{AC}} = 0 \Rightarrow G_{AC\_}opt = \sqrt{\frac{R_S}{R_P}}. \tag{2.13}$$

As illustrated in Fig. 2.3, the maximum efficiency of the system is always obtained at $G_{AC\_}opt$ regardless of the variation of δ. It is noteworthy that the concept of optimal voltage ratio is equivalent to the concept of load matching. Apart from the voltage ratio G_{AC}, another important factor that affects η_{res} is the phase difference δ. As evident from Fig. 2.3, when δ deviates from 90°, η_{res} decreases accordingly. Therefore, in order to achieve higher efficiency, the deviation of δ from 90° should be minimized.

2.2.3. IMPLEMENTATION OF ZVS

For the IPT system operating at a high switching frequency, ZVS operations of the power switches are of great importance. In this chapter, MOSFETs are used as the power switches of the converters. In order to realize the ZVS operations for the inverter working in the FB mode, the antiparallel diode of the MOSFET should be conducted before the turn-on instant. This implies that the current i_P should lag the voltage u_{ab}, as shown in Fig. 2.2(a). Specifically, the duty cycle D_P and the phase angle φ_P should satisfy

$$\varphi_P \geq \frac{(1-D_P)\pi}{2}. \tag{2.14}$$

Similarly, for ZVS operations of the rectifier operating in the FB mode, D_S and φ_S should satisfy

$$\varphi_S \geq \frac{(1-D_S)\pi}{2}. \tag{2.15}$$

2.2.4. PROBLEMS UNDER WIDE-RANGE LOAD VARIATIONS

In order to achieve wide ZVS operations for all power switches, the triple-phase-shift (TPS) control was proposed. In this method, the phase angle δ serves as a new control variable to adjust the phase angles φ_P and φ_S for wide ZVS operations. Substituting (2.14) and (2.15) into (2.4), the ZVS condition for all power switches is obtained as

$$\begin{cases} \delta & \leq (D_P\pi)/2 \\ \delta & \leq (D_S\pi)/2. \end{cases} \tag{2.16}$$

To reduce the reactive power in the resonant tank, δ should be as close to 90° as possible, and therefore, δ is selected by

$$\delta = \min\{(D_P\pi)/2, (D_S\pi)/2\} - \delta_m. \tag{2.17}$$

where δ_m is the margin angle to ensure the turn-on current is large enough to charge or discharge the equivalent output capacitor C_{oss} of power switches within the dead time. Although the TPS control is able to realize wide ZVS operations, one problem is that as the desired output power drops, the duty cycles D_P and D_S decrease accordingly, and therefore, the value of δ should be lowered to ensure ZVS operations. This means that a small value of δ is needed when the output power deviates far away from the rated

power. However, according to (2.8), a small value of δ leads to a large amount of reactive power. Therefore, in order to maintain a high overall efficiency, a larger phase angle δ is desired.

2.3. PROPOSED MODE-SWITCHING BASED DUAL-SIDE PHASE-SHIFT CONTROL

According to the analysis in Chapter 2.2.4, the TPS control results in large reactive power under light load conditions. However, if the deviation of δ from 90° can be minimized, the reactive power can be reduced, and a higher transfer efficiency can be obtained. In this subchapter, a mode-switching-based phase-shift control (MS-PSC) method is proposed. In the proposed MS-PSC approach, power regulation, wide ZVS operations, and load matching are realized simultaneously. Besides, this method enables the inverter and rectifier to operate in full-bridge (FB), mixed-bridge (MB), and half-bridge (HB) modes, and thus, the deviation of δ from 90° is minimized.

2.3.1. HYBRID OPERATING MODES

Substituting (2.5) into (2.7), the output power of the system is obtained as

$$P_{out} = \frac{V_{in} V_{out} K_P K_S \sin[(D_P\pi)/2]\sin[(D_S\pi)/2]\sin(\delta)}{\omega M}. \tag{2.18}$$

As illustrated in (2.18), the output power of the system can be regulated by various parameters. However, for a typical IPT system, the DC input voltage V_{in}, the operating angular frequency ω, as well as the mutual inductance M are almost constant during operation. The DC output voltage V_{out} depends on the load profiles, e.g., the battery voltage. Therefore, power regulation is typically achieved by adjusting the duty cycles D_P and D_S. As the desired output power P_{out} drops, D_P and D_S should be decreased accordingly. This means that a smaller δ is needed for ZVS. Nevertheless, further observing (2.18) reveals that the values of K_P and K_S also affect the amount of transferred power, which can be adjusted by switching the working modes of the inverter and rectifier. Thus, lowering K_P and K_S through mode switching can be a feasible way to reduce the drop of D_P and D_S under light- and medium- power levels, which narrows the deviation of δ from 90°.

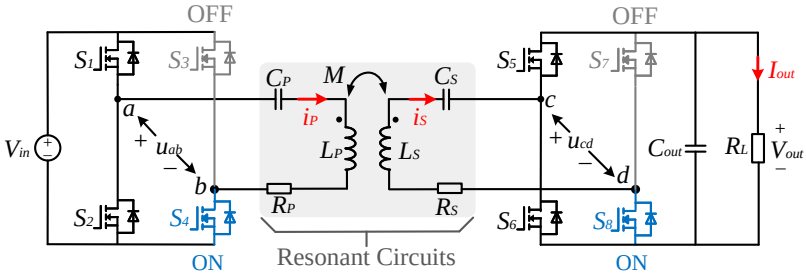

Figure 2.4: Circuit diagram of the IPT system with the inverter and rectifier working in the HB mode.

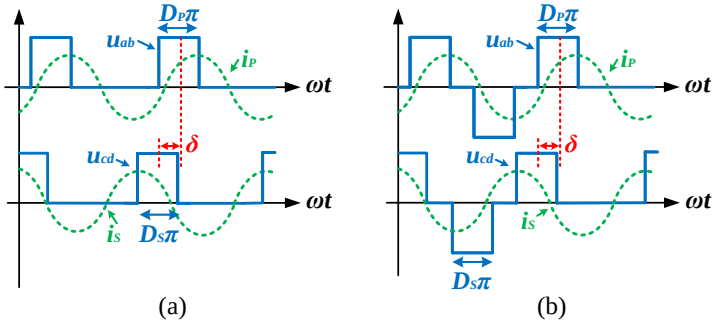

Figure 2.5: Operating waveforms when the inverter and rectifier work in (a) the HB mode and (b) the MB mode.

Based on the hybrid modulation control (HMC) method proposed in [153], both the inverter and rectifier are able to work in the FB and HB modes. The operating principle of the FB mode was already discussed in Chapter 2.2.1 and will not be repeated in this subchapter. For the HB mode, as shown in Fig. 2.4, when the power switch S_3 keeps an "OFF" state while S_4 maintains an "ON" state during the whole operation, the inverter operates in the HB mode. Similarly, when the power switch S_7 keeps an "OFF" state while S_8 maintains an "ON" state all the time, the rectifier operates in the HB mode. The operating waveforms of the IPT system with both the inverter and rectifier working in the HB mode are shown in Fig. 2.5(a). According to the Fourier series expansion, the fundamental components of the AC voltages $\dot{U}_P$ and $\dot{U}_S$ in the HB mode are derived by

$$\begin{cases} \dot{U}_P = & K_{P\_HB} V_{in} \sin[(D_P\pi)/2] \angle 0 \\ \dot{U}_S = & K_{S\_HB} V_{out} \sin[(D_S\pi)/2] \angle \delta, \end{cases} \tag{2.19}$$

where

$$\begin{cases} K_{P\_HB} = & \sqrt{2}/\pi \\ K_{S\_HB} = & \sqrt{2}/\pi. \end{cases} \tag{2.20}$$

Apart from the FB and HB modes, the MB mode is employed in this chapter, where the converter operates alternately in the FB mode and the HB mode. The working waveforms of the system with both the inverter and rectifier operating in the MB mode are depicted in Fig. 2.5(b). As it can be seen from Fig. 2.5(b), in each two switching cycles, the converters operate in the FB mode in one switching cycle and then switch to the HB mode in the other switching cycle. Based on the Fourier series expansion, the fundamental components of $\dot{V}_P$ and $\dot{V}_S$ in the MB mode are derived as

$$\begin{cases} \dot{U}_P = & K_{P\_MB} V_{in} \sin[(D_P\pi)/2] \angle 0 \\ \dot{U}_S = & K_{S\_MB} V_{out} \sin[(D_S\pi)/2] \angle \delta, \end{cases} \tag{2.21}$$

where

$$\begin{cases} K_{P\_MB} = & 3\sqrt{2}/2\pi \\ K_{S\_MB} = & 3\sqrt{2}/2\pi. \end{cases} \tag{2.22}$$

For ZVS operations in the HB and MB modes, as it can be observed in Fig. 2.5(a) and Fig. 2.5(b), the inverter current i_P should lag the inverter voltage u_{ab} at least by

$[(1-D_P)\pi/2]$, while the rectifier current i_S should lead the rectifier voltage u_{cd} at least by $[(1-D_S)\pi/2]$. It should be noted that ZVS constraints in the HB and MB modes are consistent with those in the FB mode. Therefore, (2.14) and (2.15) are still applicable for analyzing ZVS in the HB and MB modes.

On the other hand, as it can be observed from (2.6), (2.20), and (2.22), the voltage gains K_P and K_S decrease accordingly as the converter mode switches from the FB mode to the MB mode and then to the HB mode, i.e., from $2\sqrt{2}/\pi$ to $3\sqrt{2}/2\pi$ and then to $\sqrt{2}/\pi$. This implies that as the output power P_{out} decreases, the converters can switch from the FB mode to the HB mode or the MB mode to narrow the variation of duty cycles D_P and D_S, and thus, a smaller deviation of δ from 90° can be obtained. In this chapter, the proposed MS-PSC method allows both the inverter and rectifier to switch between the above three operating modes, thereby reducing the deviation of δ from 90°. Compared with the conventional TPS control, the proposed MS-PSC method reduces the reactive power at light- and medium-power levels, and the system efficiency is therefore maintained high in a wide power range.

2.3.2. MODE SELECTION STRATEGIES

According to the above analysis, it is preferable to consider the HB and MB modes to reduce the reactive power under light- and medium-load conditions. Nevertheless, the power transfer capability of the system varies as the converters switch between different modes. Therefore, it is of great importance to select an ideal operating mode based on the required output power. To this end, a mode selection strategy is proposed, where the optimal mode of the system is selected with both load matching and ZVS operations taken into consideration. The flowchart of the proposed mode selection strategy is shown in Fig. 2.6.

As discussed in Chapter 2.2.2, in order to realize load matching, an optimal AC voltage ratio $G_{AC\_}opt$ is needed as follows:

$$G_{AC\_}opt = \frac{K_S V_{out}\sin[(D_S\pi)/2]}{K_P V_{in}\sin[(D_P\pi)/2]} = \sqrt{\frac{R_S}{R_P}}. \tag{2.23}$$

Observing (2.23) reveals that there is an optimal ratio between the duty cycles D_P and D_S when load matching is realized. In order to demonstrate the ratio between D_P and D_S, the factor λ is introduced and defined as $\lambda = \sin[(D_S\pi)/2]/\sin[(D_P\pi)/2]$. According to (2.23), the optimal ratio between D_P and D_S under load matching is given by

$$\lambda opt = \frac{\sin[(D_S\pi)/2]}{\sin[(D_P\pi)/2]} = \frac{K_P}{K_S G_{DC}}\sqrt{\frac{R_S}{R_P}}. \tag{2.24}$$

where G_{DC} is the ratio between the DC input voltage V_{in} and the DC output voltage V_{out}, i.e., $G_{DC} = V_{out}/V_{in}$. As illustrated in (2.24), the value of λ_{opt} depends on the voltage gains K_P and K_S. Therefore, λ_{opt} varies as the system switches between different operating modes. Besides, the value of λ_{opt} affects the power transfer capability of the system. Based on the value of λ_{opt}, there are two cases that should be considered.

Case-I ($\boldsymbol{\lambda_{opt} \geq 1}$):

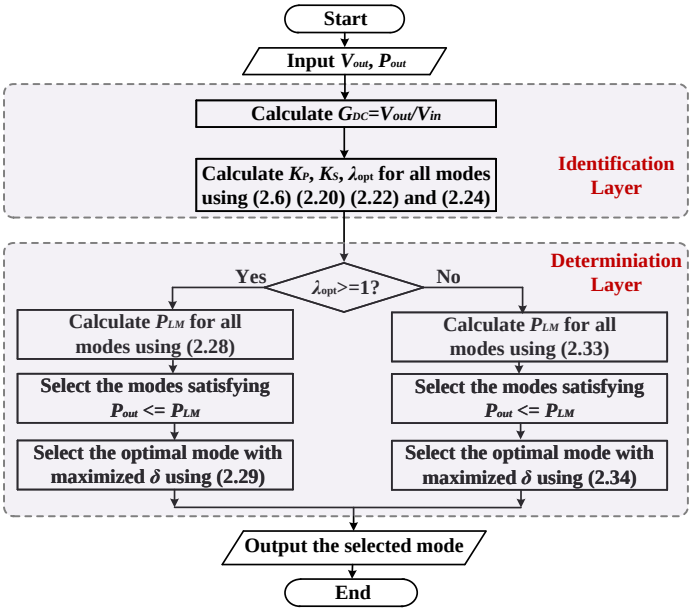

Figure 2.6: Flowchart of the proposed mode selection strategy.

In this case, the optimal ratio between D_P and D_S under load matching is given by

$$\lambda_{opt} = \frac{\sin[(D_S\pi)/2]}{\sin[(D_P\pi)/2]} \geq 1 \Rightarrow D_P \leq D_S. \tag{2.25}$$

As evident from (2.25), D_S is larger than D_P in this case. According to the ZVS constraints described in (2.17), the phase difference δ for ZVS is selected by

$$\delta = (D_P\pi)/2 - \delta_m. \tag{2.26}$$

Substituting (2.24) and (2.26) into (2.18), the output power expression in this case is given by

$$P_{out} = \frac{V_{in}^2 G_{DC} K_P K_S \sin^2[(D_S\pi)/2]}{\lambda_{opt}\omega M}\{\frac{\sin[(D_S\pi)/2]}{\lambda_{opt}}\cos(\delta_m) - \sqrt{1 - \frac{\sin^2[(D_S\pi)/2]}{\lambda_{opt}^2}}\sin(\delta_m)\}. \tag{2.27}$$

As it can be observed in (2.27), the output power P_{out} is a monotonic increasing function of the duty cycle D_S. Considering the upper limit of D_S, the power transfer capability under load matching is obtained as

$$P_{LM} = \frac{V_{in}^2 G_{DC} K_P K_S[\cos(\delta_m) - \sqrt{\lambda_{opt}^2 - 1}\sin(\delta_m)]}{\lambda_{opt}^2 \omega M}. \tag{2.28}$$

As demonstrated in (2.28), the power transfer capability P_{LM} depends on the voltage gains K_P and K_S, which are determined by the working mode of the inverter and rectifier. In other words, P_{LM} can be calculated once the operating mode is selected. For a

selected mode, if the required output power P_{out} satisfies $P_{out} \leq P_{LM}$, it indicates that the power transfer capability of the system is able to meet the load demand. However, there might be several operating modes that can satisfy the load requirement at the same time. Thus, it is necessary to find an optimal mode among all the eligible modes. According to the analysis in Chapter 2.2.1, the phase difference δ should be as large as possible to minimize the reactive power in the resonant tank. Therefore, the operating mode with maximized δ should be selected. Substituting (2.24) and (2.26) into (2.18), the value of δ should satisfy

$$\sin^2(\delta+\delta_m)\sin(\delta) = \frac{\omega M P_{out}}{\lambda_{opt} V_{in}^2 G_{DC} K_P K_S}. \tag{2.29}$$

With given P_{out} and V_{out}, the optimal mode with maximized δ can be selected by solving (2.29).

Case-II ($\lambda_{opt} < 1$):

In this case, the optimal ratio between D_P and D_S under load matching can be expressed as

$$\lambda_{opt} = \frac{\sin[(D_S\pi)/2]}{\sin[(D_P\pi)/2]} < 1 \Rightarrow D_P > D_S. \tag{2.30}$$

According to (2.30), D_P is larger than D_S, and the phase angle δ for ZVS is selected by

$$\delta = (D_S\pi)/2 - \delta_m. \tag{2.31}$$

Then, substituting (2.24) and (2.31) into (2.18), the output power expression of the system is given by

$$\begin{aligned} P_{out} = \quad & \frac{V_{in}^2 G_{DC} K_P K_S \lambda_{opt} \sin^2[(D_P\pi)/2]}{\omega M} \{\lambda_{opt} \sin[(D_P\pi)/2]\cos(\delta_m) \\ & - \sqrt{1-\lambda_{opt}^2 \sin^2[(D_P\pi)/2]}\sin(\delta_m)\}. \end{aligned} \tag{2.32}$$

Considering the upper limit of the duty cycle D_P, the power transfer capability with the load matching is derived by

$$P_{LM} = \frac{V_{in}^2 G_{DC} K_P K_S [\lambda_{opt}\cos(\delta_m) - \sqrt{1-\lambda_{opt}^2}\sin(\delta_m)]}{\omega M}. \tag{2.33}$$

Similarly, substituting (2.24) and (2.31) into (2.18), δ should satisfy

$$\sin^2(\delta+\delta_m)\sin(\delta) = \frac{\lambda_{opt}\omega M P_{out}}{V_{in}^2 G_{DC} K_P K_S}. \tag{2.34}$$

According to (2.34), the optimal mode with maximized δ can be selected in the case of $\lambda_{opt} < 1$.

With the parameters listed in Table 2.1, the selected optimal mode against the desired output power P_{out} is shown in Fig. 2.7. It should be noted that “FB-MB" in Fig. 2.7 means that the inverter operates in the FB mode, while the rectifier works in the MB mode. As illustrated in Fig. 2.7, when the desired output power P_{out} decreases, the converters switch from the FB mode to the MB mode and the HB mode, which narrows the

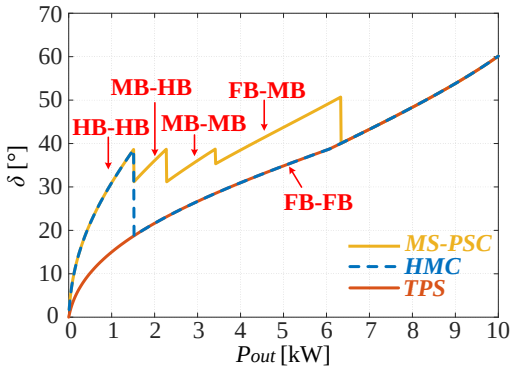

Figure 2.7: Selected operating mode and calculated phase-shift angle δ versus the desired output power P_{out}.

deviation of δ from 90° and reduces the reactive power under light- and medium- loads. Although the “FB-HB" mode and the “HB-FB" mode can be selected based on the HMC method, these two modes are not the optimal mode when the MB mode is considered. Therefore, the “FB-HB" mode and “HB-FB" mode are not selected in this chapter.

In order to demonstrate the improvement in the value of δ, δ versus P_{out} is also plotted in Fig. 2.7. In Fig. 2.7, the results of the conventional TPS method, the HMC method, and the MS-PSC method are benchmarked. As shown in Fig. 2.7, although it is still quite a long way from 90°, the value of δ in the MS-PSC method is improved over the TPS method in the power range of 0-6.3 kW. For the HMC method, although this method can enhance the value of δ under light load conditions, i.e., 0-1.6 kW, the optimization range is narrow due to the limited power transfer capability of the HB mode. With a larger δ obtained in the MS-PSC method, the reactive power in the resonant tank is reduced remarkably, and a higher overall efficiency can be achieved.

2.3.3. REDUCTION OF COIL CURRENTS

The overall power losses of the IPT system mainly include the power losses of the resonant tank and the H-bridge converters. According to the analysis in [155], the power losses of each part are related to the RMS values of coil currents. With the parameters listed in Table 2.1, the RMS values of coil currents I_P and I_S versus the output power P_{out} are plotted in Fig. 2.8, where the results of the TPS method, the HMC method and the proposed MS-PSC method are compared. As it can be seen, when delivering the same amount of power, I_P and I_S are reduced in the MS-PSC method. This is because, compared with TPS and HMC, the reactive power of the MS-PSC is minimized through mode switching, and thus, smaller coil currents can be obtained. With reduced coil currents in the MS-PSC method, the overall power losses of the system are decreased, and higher transmission efficiency can be achieved. Moreover, compared with the FB mode, the switching losses of the MOSFETs are smaller in the MB and HB modes since the equivalent switching times of the MOSFETs are reduced in the MB and HB modes. Thus, the overall power losses of the system can be further reduced using the MS-PSC method.

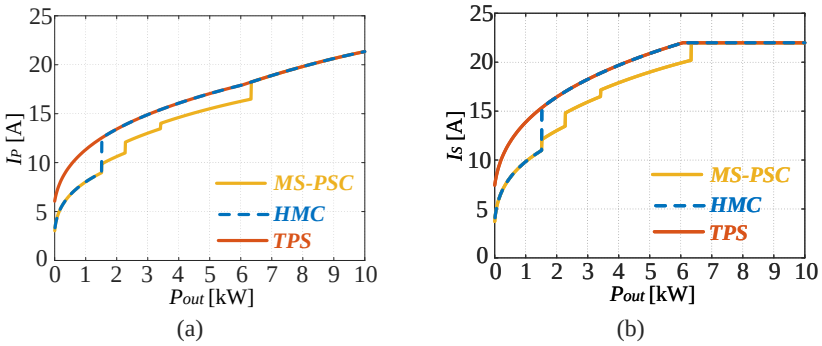

Figure 2.8: RMS values of coil currents versus the desired output power P_{out}: (a) primary coil current I_P, (b) secondary coil current I_S.

2.3.4. CONTROL FRAMEWORK

The block diagram of the proposed MS-PSC method is shown in Fig. 2.9. Generally, the controller of the IPT system is designed for constant voltage (CV) or constant current (CC) output. For the SS-compensated IPT system, the CC output can be realized by reasonable parameter design without regulating control variables. Therefore, CV output is the control objective in this chapter. In the MS-PSC method, the duty cycle D_S is controlled to realize a constant output voltage. Besides, the duty cycle D_P is regulated to realize load matching, whilst δ is adjusted to achieve wide ZVS range.

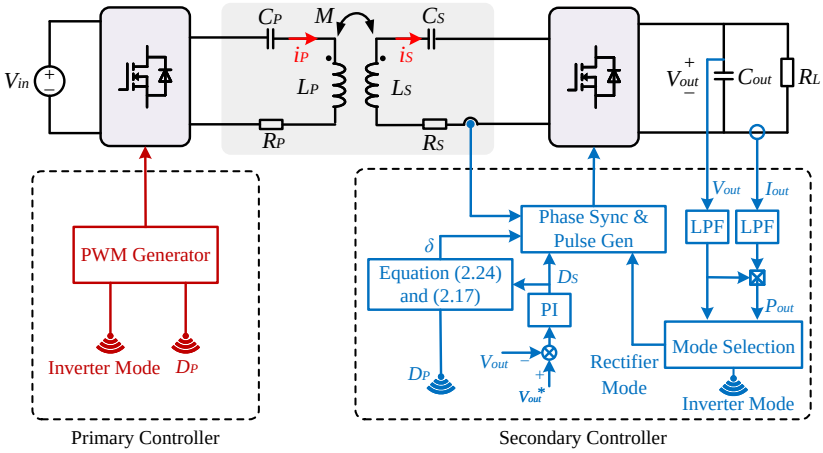

Figure 2.9: Control block diagram of the proposed MS-PSC method.

As illustrated in Fig. 2.9, the DC output voltage V_{out} and current I_{out} are sampled. Two separate low-pass filters (LPFs) are utilized to filter the ripple of V_{out} and I_{out}. Then, the filtered V_{out} and I_{out} are multiplied to obtain the output power P_{out}. The measured output power P_{out}, combined with the filtered V_{out}, are fed to the mode selection module. The operating modes of the inverter and rectifier are then determined based on the

proposed mode selection strategy. A PI controller is adopted to regulate the duty cycle D_S for a constant output voltage. The duty cycle D_P and the phase difference δ are calculated after the value of D_S is determined. When the output power P_{out} is lower than the load matching boundary, the relationship between D_P and D_S should always satisfy (2.21). If P_{out} exceeds the load matching boundary, load matching is sacrificed, and D_P or D_S is regulated to the full duty cycle. To ensure wide ZVS, δ should be selected by (2.14) at all power points. It should be noted that a hysteresis comparator is needed in the mode selection module to avoid switching back and forth when the output power is at the power boundary between two different modes.

2.4. EXPERIMENTAL RESULTS

2.4.1. HARDWARE SETUP

To verify the feasibility of the proposed MS-PSC method, an SS-compensated IPT prototype is established, as shown in Fig. 2.10. A DC source is utilized to provide the required power, with the DC input voltage fixed at 600 V. Another bidirectional DC source, as an electronic load, is connected to the output of the rectifier. In order to measure the DC-to-DC transfer efficiency, a power analyzer (YOKOGAWA WT500) is adopted. The control algorithm and PWM generation are implemented using DSP28379. Three high-voltage parallel-connected SiC MOSFETs IMZ120R030M1H are used as each power switch of the H-bridge converters. The synchronization between the primary and secondary driving signals is realized by the zero-crossing detection technique of the receiver current [142, 156], and the NRF24L01+ module is adopted for the dual-side wireless communication. To ensure ZVS, the margin angle δ_m is set to 16°, and the dead time is configured at 300 ns. More details of the developed system are given in Table 2.1.

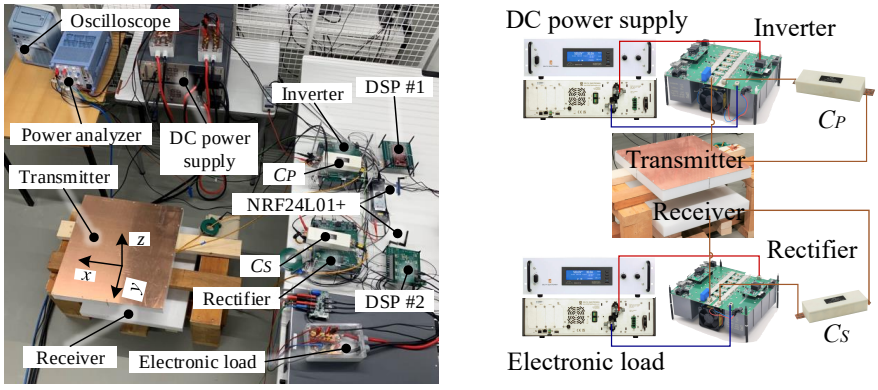

(a) (b)

Figure 2.10: Experimental prototype of the SS-compensated IPT system used to verify the proposed MS-PSC method [3]: (a) overall experimental platform, (b) main circuit of the IPT system.

2.4.2. STEADY-STATE OPERATING WAVEFORM

Experimental results of different operating modes within the proposed MS-PSC method are shown as follows. It should be noted that in these experiments, the DC input and output voltages (V_{in} and V_{out}) are both configured as 600 V.

When delivering 1 kW power, the steady-state waveforms and measured DC-to-DC efficiency of the IPT system working in the HB-HB and FB-FB modes are shown in Fig. 2.11 (a) and (b), respectively. As it can be seen, ZVS operations of all power switches are realized in the HB-HB and FB-FB modes. The duty cycles D_P and D_S of the FB-FB mode, as shown in Fig. 2.11 (b), are 0.44 and 0.36, respectively. To realize ZVS, the phase angle δ is selected as 16° in the FB-FB mode. Compared with the FB-FB mode, D_P and D_S are increased in the HB-HB mode, and therefore, the value of δ is increased to 33°. As a result, the RMS values of the coil currents are reduced in the HB-HB mode, with I_P reduced from 12.3 A to 8.5 A, and I_S reduced from 13.4 A to 9.6 A, respectively. The measured DC to DC efficiency of these two modes is also presented in Fig. 2.11. Compared with the FB-FB mode, the DC to DC efficiency of the HB-HB mode is improved from 87.7% to

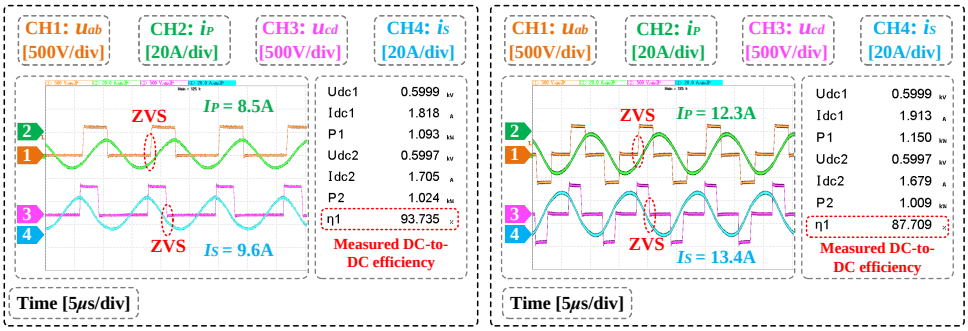

Figure 2.11: Steady-state waveforms and measured DC-to-DC efficiency when delivering 1 kW power: (a) the HB-HB mode, (b) the FB-FB mode.

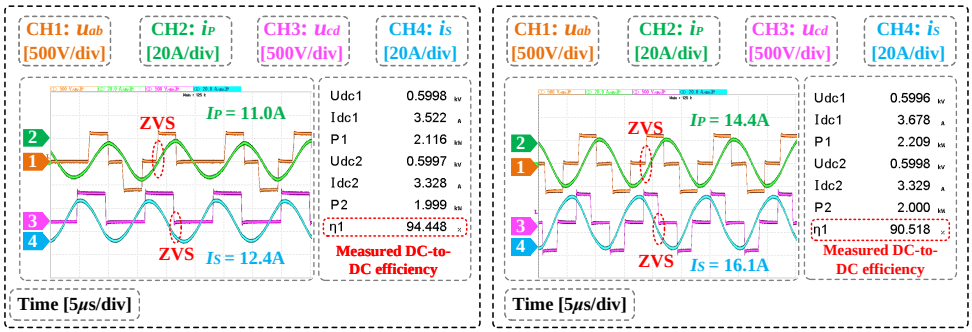

Figure 2.12: Steady-state waveforms and measured DC-to-DC efficiency when delivering 2 kW power: (a) the MB-HB mode, (b) the FB-FB mode.

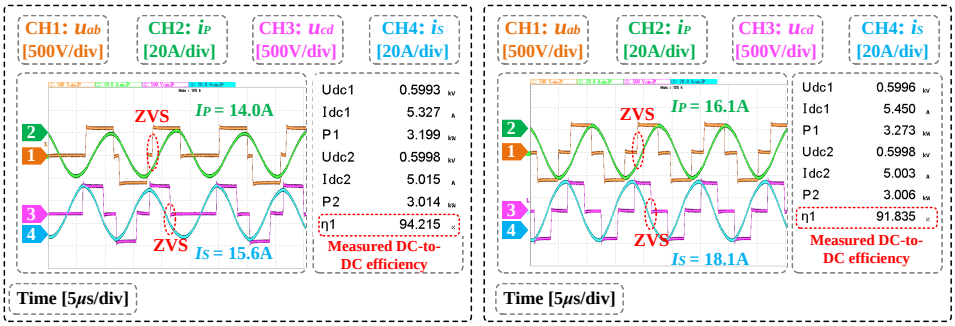

Figure 2.13: Steady-state waveforms and measured DC-to-DC efficiency when delivering 3 kW power: (a) the MB-MB mode, (b) the FB-FB mode.

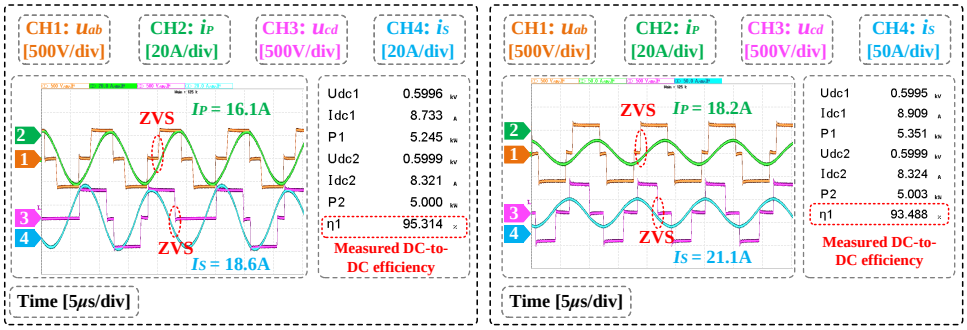

Figure 2.14: Steady-state waveforms and measured DC-to-DC efficiency when delivering 5 kW power: (a) the FB-MB mode, (b) the FB-FB mode.

93.7%, achieving an efficiency enhancement of 6.0%.

Furthermore, experimental results of the MB-HB mode are shown in Fig. 2.12. As it can be observed in Fig. 2.12, when delivering 2 kW power, δ is increased from 22° to 36° with the operating mode switched from the FB-FB mode to the MB-HB mode. Compared with the FB-FB mode, the efficiency of the MB-HB mode is improved from 90.5% to 94.5%, demonstrating an efficiency improvement of 4.0%.

Similar efficiency optimization can also be observed in the MB-MB (Fig. 2.13) and FB-MB (Fig. 2.14) modes, with efficiency improvements of 2.4% and 1.8% when delivering 3 kW and 5 kW power, respectively.

2.4.3. EFFICIENCY OPTIMIZATION

The measured DC to DC transfer efficiency in the power range of 1-10 kW is shown in Fig. 2.15. Compared with the conventional TPS method, the efficiency of the proposed MS-PSC method is greatly improved in the 1-6.3 kW power range, with efficiency improvements ranging from 1.5% to 6%. With the proposed MS-PSC method, the overall

efficiency of the system remains between 93.5% to 96.1%.

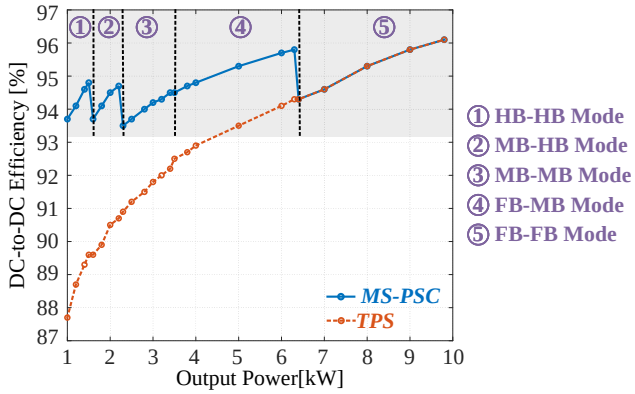

Figure 2.15: Measured overall efficiency improvement of the proposed MS-PSC method.

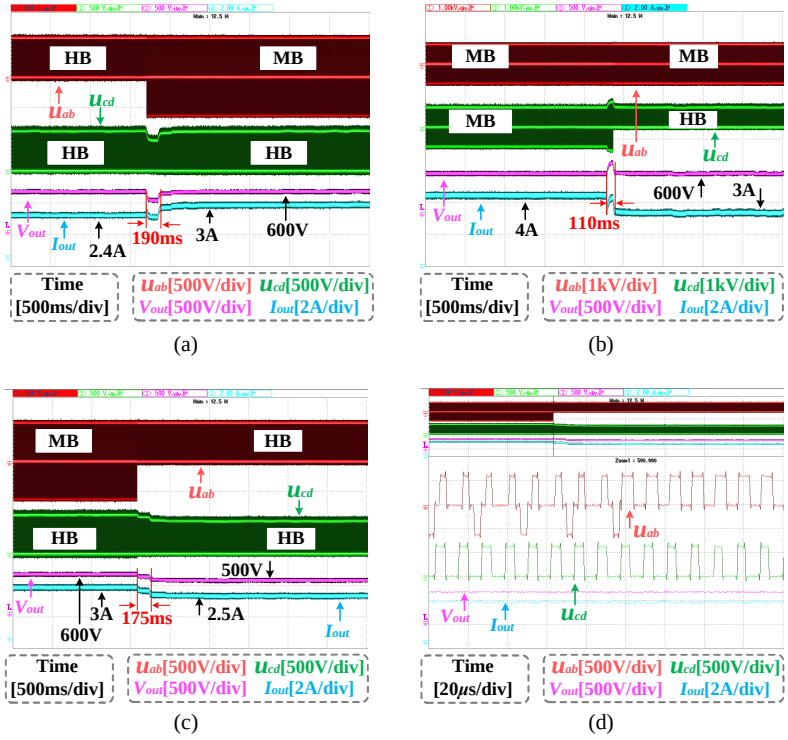

Figure 2.16: Dynamic performance of the proposed MS-PSC method: (a) when the load changes from 250 Ω to 200 Ω, (b) when the load changes from 150 Ω to 200 Ω, (c) when the reference output voltage changes from 600 V to 500 V, (d) enlarged view of Fig. 2.16 (c).

2.4.4. DYNAMIC RESPONSE

To evaluate the dynamic performance of the proposed MS-PSC method, transient response experiments are carried out under different loads and reference voltages. In these experiments, the DC output voltage is tracked through PI control as described in Fig. 2.9, and the mode transition power points are calculated based on the proposed mode selection strategy. In Fig. 2.16 (a), the reference output voltage is set to 600 V, with the load changed from 250 Ω to 200 Ω. As it can be seen, the operating mode changes from the HB-HB mode to the MB-HB mode when the output power is increased from 1.44 kW to 1.8 kW. The DC output voltage is tightly controlled to the reference value, with the dynamic setting time at 190 ms. The dynamic performance of the system with the load changed from 150 Ω to 200 Ω is further presented in Fig. 2.16 (b). As it can be observed, the system switches from the MB-MB mode to the MB-HB mode when the output power is decreased from 2.4 kW to 1.8 kW, with the setting time at 110 ms. In Fig. 2.16 (c), the reference output voltage is suddenly changed from 600 V to 500 V with the load fixed at 200 Ω. The experiment shows that with the proposed MS-PSC method, the system can track the reference output voltage accurately in a response time of 175 ms. An enlarged view of Fig. 2.16 (c) during the mode transition moment is then presented in Fig. 2.16 (d), which shows that the MS-PSC method can realize mode switching seamlessly.

2.5. CONCLUSIONS

In this chapter, an MS-PSC method is presented for ZVS implementation and efficiency optimization in a wide power range. In the proposed method, power regulation, load matching, and wide ZVS operations are realized without using any auxiliary circuits. Moreover, thanks to the effective use of FB, MB, and HB modes, as well as the cooperative operation of the inverter and rectifier, this method can realize wide ZVS operations with minimized reactive power. Compared with conventional TPS control, smaller coil currents are obtained in the MS-PSC method when delivering the same amount of power. As a result, the overall efficiency of the system is enhanced significantly. Experimental results demonstrate that the proposed MS-PSC method can realize an overall efficiency of 93.5%-96.1% in the power range of 1-10 kW.

3

HYBRID MODULATION BASED SECONDARY-SIDE CONTROL

This chapter presents a hybrid modulation (HM) scheme to facilitate secondary-side control in inductive power transfer (IPT) systems. To achieve broad power regulation in IPT systems, the conventional pulse width modulation (PWM) exhibits a significant efficiency drop under light loads, while the existing pulse density modulations (PDMs) lead to considerable current and voltage ripples. To address this issue, an optimal discrete PDM (D-PDM) is first proposed for active rectifier modulation. By symmetrically and uniformly distributing pulses, the proposed optimal D-PDM eliminates even-subharmonics in rectifier input voltage, thereby reducing the current distortions and output voltage ripple while removing the capacitor DC blocking voltages. Moreover, the pulse width regulation is incorporated into the optimal D-PDM, enabling continuous output tuning and further minimizing subharmonics in the voltage. Based on an IPT prototype, the proposed HM is benchmarked with the existing PWM and PDMs. Experimental results show that the proposed HM significantly mitigates current and voltage ripples while facilitating continuous tuning when compared with the existing PDMs. Additionally, when compared to the PWM, the proposed HM demonstrates notable efficiency improvements within the 10%-60% power range, achieving a maximum efficiency enhancement of up to 5.5%.

This chapter is based on:

- G. Zhu, J. Dong, F. Grazian, and P. Bauer, "A hybrid modulation scheme for efficiency optimization and ripple reduction in secondary side controlled wireless power transfer systems," *submitted*.

3.1. INTRODUCTION

To address considerable battery load variations during the EV charging process, achieving wide output power regulation is essential. In addition to the phase shift modulation(PSM), also known as pulse width modulation (PWM), described in Chapter 2, pulse density modulation (PDM) has been extensively investigated for the power regulation in IPT systems as well [113, 119, 157–162]. In [119], PDM was adopted for the HB converters to achieve output power regulation and efficiency optimization. Furthermore, the application of PDM was extended to the FB converters in [157]. Additionally, in [158], the PDM technique was applied to a semi-active rectifier (SAR). However, the conventional PDM in [119, 157, 158] results in significant current distortions and output voltage ripple. To deal with this issue, several improved PDM (iPDM) techniques were proposed. In [159], Sheng et al. proposed an iPDM technique using harmonic analysis. Moreover, Wu et al. presented an iPDM method in [160] based on efficiency analysis and iterative calculation. However, the harmonic analysis in [159] is complicated, while the iterative calculation in [160] requires substantial computational effort. On the other hand, in [161] and [113], the semi-active mode was introduced to optimize the pulse distribution within the iPDM methods. Through evenly distributing the active and semi-active modes, the current and voltage ripples are reduced in [161] and [113]. Although existing iPDMs effectively mitigate current distortions and output voltage ripple compared to the conventional PDM, noticeable current and voltage ripples still exist due to irregular pulse distributions. Additionally, it is challenging to achieve continuous tuning in iPDMs as there are a tremendous number of densities that should be optimized in continuous PDM. Consequently, the tuning resolution of existing iPDMs is limited. In [162], a conditional PDM strategy was proposed to achieve ripple reduction. However, it requires real-time detection of high-frequency coil currents, which notably increases the hardware complexity.

Apart from wide output regulation, another challenge in IPT systems is the implementation of wireless communication. In IPT systems, the primary-side converters cannot acquire load information through a wired feedback system. Consequently, wireless communication is commonly adopted. Nevertheless, the implementation of wireless communication encounters the challenges of communication latency and potential data loss. Therefore, it is preferable to eliminate the wireless communication link in IPT systems [113]. Implementing secondary-side control is an effective method to eliminate wireless communication, and this control can be achieved based on an active rectifier. However, since only one active power conversion stage, i.e., the rectifier, is adopted for wide power tuning, the rectifier modulation ratio needs to be adjusted in a large range. As the modulation ratio decreases, the PWM results in considerable reactive power and decreased efficiency, while the PDMs lead to significant output voltage ripple and current distortions.

3.1.1. SCOPE AND CONTRIBUTIONS

To enable an efficient, communication-less, and wide-range power regulation for IPT systems, this chapter presents a hybrid modulation based secondary-side control (HM-SSC) approach. In the proposed hybrid modulation (HM), the PWM and the optimal discrete PDM (D-PDM) are integrated to regulate the output power in a broad range. The

concept of integrating PWM and optimal D-PDM for wide output tuning in IPT systems, to the best of our knowledge, has not yet been reported in previous studies. Moreover, the main contributions of the proposed HM-SSC method are summarized as follows:

1) The proposed HM-SSC scheme enables communication-less wide output regulation without introducing extra components and DC-DC converters.

2) An optimal D-PDM strategy is proposed. By symmetrically and uniformly distributing pulses, the proposed optimal D-PDM eliminates even-subharmonics in the voltage, thereby significantly reducing current distortions and output voltage ripple. Moreover, the symmetrical pulse distribution eliminates the capacitor DC blocking voltages, thus minimizing the capacitor voltage stresses.

3) An HM technique, which integrates PWM and optimal D-PDM, is further proposed. Compared with the existing PDMs, the proposed HM facilitates continuous tuning by introducing pulse width regulation while minimizing the voltage and current ripples through optimized discrete pulse distributions. On the other hand, when compared to the PWM, the proposed HM diminishes rectifier switching times and minimizes the reactive power under load variations, thereby achieving a notable efficiency enhancement across a broad power range.

3.1.2. OUTLINE

The remainder of this chapter is outlined as follows. Chapter 3.2 illustrates the fundamental working principles of the secondary-side controlled IPT systems. Subsequently, Chapter 3.3 demonstrates the existing pulse density modulation techniques. Furthermore, the proposed HM-SSC method is elaborated in Chapter 3.4, while experimental results are shown in Chapter 3.5. Finally, Chapter 3.6 demonstrates the conclusions.

3.2. COMMUNICATION-LESS SECONDARY-SIDE CONTROL

In the IPT systems, an active rectifier can be utilized for output power regulation while eliminating the need for communication. The circuit topology of the active-rectifier-based IPT system is demonstrated in Fig. 2.1 of Chapter 2.

To investigate the power regulation capability of the secondary-side controlled IPT systems, basic circuit equations of the system are derived as

$$\begin{cases} \dot{U}_P &= (R_P + jX_P)\dot{I}_P - j\omega M\dot{I}_S, \\ \dot{U}_S &= j\omega M\dot{I}_P - (R_S + jX_S)\dot{I}_S, \end{cases} \tag{3.1}$$

where $X_P = \omega L_P - 1/(\omega C_P)$; $X_S = \omega L_S - 1/(\omega C_S)$.

Typically, there are two prevalent modulation techniques for output power regulation in the secondary-side controlled IPT systems. Fig. 3.1(a) demonstrates typical operating waveforms of the secondary-side controlled IPT systems employing the PWM method. As illustrated in Fig. 3.1(a), in the secondary-side controlled IPT systems, the inverter output voltage (u_{ab}) is a full-duty-cycle square wave. Based on the FHA method, the RMS value of $\dot{U}_P$ (Herein, $\dot{U}_P$ denotes the phasor form of the fundamental component in u_{ab}.) is given by

$$|\dot{U}_P| = 2\sqrt{2}V_{in}/\pi \tag{3.2}$$

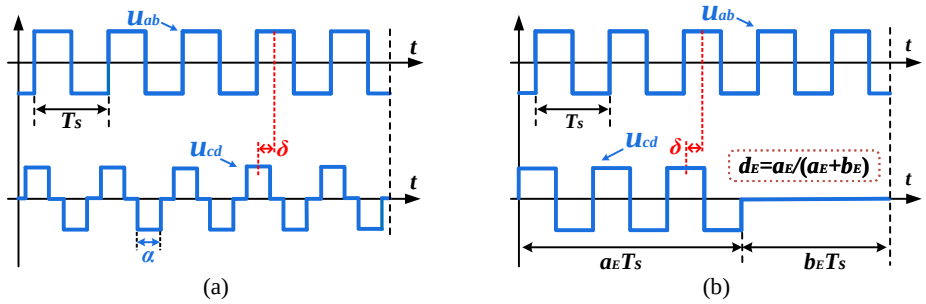

Figure 3.1: Illustration of typical modulation techniques for secondary-side controlled IPT systems: (a) the PWM technique, where α ($\alpha \in [0,\pi]$) indicates the pulse width angle of u_{cd}; (b) the PDM technique, where $a_E T_s$ and $b_E T_s$ denote the time durations of pulse and non-pulse periods within u_{cd}, d_E ($d_E \in [0,1]$) represents the pulse density of u_{cd}. In this figure, T_s denotes the switching cycle, while δ ($\delta \in [0,\pi/2]$) is the phase difference between u_{ab} and u_{cd}.

Moreover, the RMS value of $\dot{U}_S$ (Herein, $\dot{U}_S$ denotes the phasor form of the fundamental component in u_{cd}, and u_{cd} is the input voltage of the active rectifier.) under the PWM is derived as

$$|\dot{U}_S| = 2\sqrt{2}V_{out}/\pi \times \sin(\alpha/2), \tag{3.3}$$

where α is the pulse width angle of u_{cd}. On the other hand, typical operating waveforms of the PDM method are demonstrated in Fig. 3.1(b). In this scenario, the RMS value of $\dot{U}_P$ can be expressed by (3.2) as well. Additionally, the RMS value of $\dot{U}_S$ under the PDM is expressed as

$$|\dot{U}_S| = 2\sqrt{2}V_{out}/\pi \times d_E, \tag{3.4}$$

where d_E is the pulse density of u_{cd}. Furthermore, the output power P_{out} of the system is derived as

$$P_{out} = \mathrm{Re}\{\dot{U}_S \dot{I}_S^*\} = \frac{8V_{in}V_{out}}{\pi^2 \omega M} \times m_S \times \sin(\delta), \tag{3.5}$$

where δ is the phase difference between u_{ab} and u_{cd}; m_S ($m_S \in [0,1]$) is defined as the modulation ratio of the rectifier. Specifically, m_S corresponds to $\sin(\alpha/2)$ within the PWM, whereas it corresponds to d_E under the PDM.

In the secondary-side controlled IPT systems, the rectifier modulation ratio m_S is dynamically adjusted between 0 and 1 for output power regulation. Since the inverter does not actively participate in the power tuning, the secondary-side control imposes greater demands on the rectifier modulation range. Nevertheless, as the value of m_S decreases, the conventional PWM results in remarkable reactive power for ZVS, while the existing PDMs lead to significant current distortions and output voltage ripple.

3.3. EXISTING PULSE DENSITY MODULATIONS

To regulate the output power in the secondary-side controlled IPT systems, the conventional PDM adjusts the pulse density of the rectifier input voltage (u_{cd}). Fig. 3.2(a) illustrates typical operating waveforms of the conventional PDM. Herein, T_s indicates the switching cycle, while T_{PDM} represents the PDM control cycle. As shown in Fig. 3.2(a),

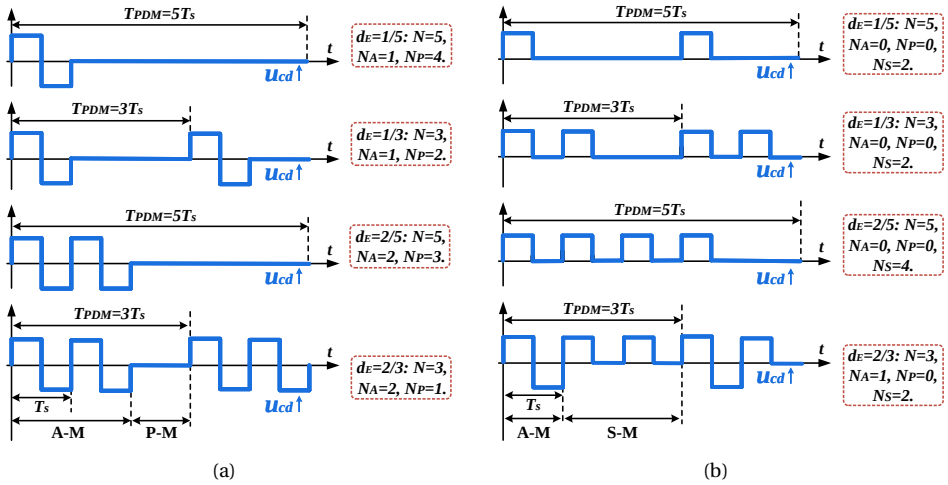

(a) (b)

Figure 3.2: Typical operating waveforms of u_{cd} when employing (a) the conventional PDM, and (b) the iPDM for the secondary-side controlled IPT systems. Here, A-M, P-M, and S-M indicate the active mode, the passive mode, and the semi-active mode, respectively.

there are two operating modes in the conventional PDM, i.e., the active and passive modes. With N_A and N_P representing the number of active and passive modes in one PDM cycle, the pulse density of u_{cd} is given by

$$d_E = \frac{N_A}{N_A + N_P} = \frac{N_A}{N}, \tag{3.6}$$

where $N = N_A + N_P$ is the total number of T_s in one PDM cycle ($T_{PDM} = NT_s$). As evident from (3.4), (3.5), and (3.6), power regulation of the system can be achieved by tuning the value of d_E in the conventional PDM. However, in this method, the number of passive modes N_P increases as the value of d_E decreases, resulting in a long duration time of passive modes. Consequently, significant output voltage ripple and current distortions occur in the conventional PDM under light loads.

To mitigate the voltage and current ripples, the semi-active mode was introduced into the PDM, which is known as improved PDM (iPDM) [113, 161]. Fig. 3.2(b) demonstrates typical operating waveforms of the iPDM. As shown in Fig. 3.2(b), by evenly distributing three operating modes, i.e., the active, semi-active, and passive modes, within a PDM cycle, the iPDM lowers the time duration of passive modes, thereby decreasing the voltage and current ripples. In the iPDM, the pulse density d_E of u_{cd} is

$$d_E = \frac{2N_A + N_S}{2N}, \tag{3.7}$$

where N_S is the number of semi-active modes in a PDM cycle.

3.4. SECONDARY-SIDE CONTROL BASED ON HYBRID MODULATION

3.4.1. PROPOSED OPTIMAL DISCRETE PULSE DENSITY MODULATION

Although the iPDM reduces the voltage and current ripples by introducing the semi-active mode, it leads to the DC component and even-subharmonics in the voltage. The DC blocking voltage across the capacitors enlarges their voltage stresses, while the even subharmonics exacerbate the current distortions and output voltage ripple. To minimize subharmonics in the currents and remove the capacitor DC blocking voltage, the proposed method introduces the reversed semi-active mode into the iPDM. Since only optimal discrete pulse densities are considered, this method is also called optimal D-PDM. The basic principle of the optimal D-PDM is to evenly distribute four different operating modes, i.e., the active, semi-active, reversed semi-active, and passive modes, in a PDM cycle, as demonstrated in Fig. 3.3. The key guidelines for designing the proposed optimal D-PDM are as follows.

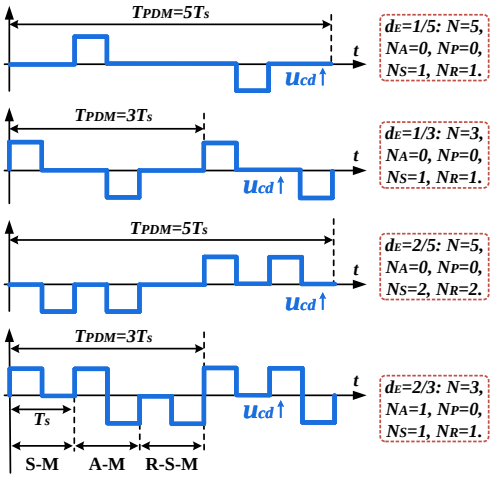

Figure 3.3: Typical operating waveforms of u_{cd} when employing the proposed optimal D-PDM for the secondary-side controlled IPT systems. Here, R-S-M represents the reversed semi-active mode.

Firstly, to remove the DC component and even-subharmonics in the voltage, the semi-active and reversed semi-active modes should be symmetrically distributed, and the numbers of these two modes in one PDM cycle need to be identical. Hence, the pulse density d_E of u_{cd} under the proposed optimal D-PDM is derived as

$$d_E = \frac{2N_A + N_S + N_R}{2N} = \frac{N_A + N_S}{N}, N_S = N_R, \tag{3.8}$$

where N_R denotes the number of reversed semi-active modes in one PDM cycle.

Secondly, the total number of T_s in one PDM cycle, i.e., N, needs to be an odd number. According to the Fourier series expansion, the time-domain expression of $u_{cd}(t)$

under the proposed optimal D-PDM is derived as

$$u_{cd}(t) = \sum_{q} a_q \sin(\frac{q}{N}\omega t + \varphi_k), q = 1,3,5,..., \tag{3.9}$$

where a_q and φ_q represent the amplitude and phase of qth-order subharmonic, respectively; ω is the switching frequency. Due to the symmetrical pulse distribution, the even-subharmonics in u_{cd} are canceled, and q is any positive odd number. In order to excite the series-series (SS) compensated resonant circuits, the fundamental component at the resonant frequency is essential. As evident from (3.9), to obtain the fundamental component at the resonant frequency, there should be a value of q that is exactly equal to N. Since q is odd, N should also be an odd number accordingly.

Thirdly, it is recommended that N be designed as small as possible to minimize subharmonics near the resonant frequency. According to (3.9), as the value of N rises, the subharmonics near the resonant frequency are increased accordingly. Considering the bandpass filtering characteristics of the SS compensation network, the voltage subharmonics near the resonant frequency cannot be effectively attenuated. Therefore, as shown in Fig. 3.3, N is selected as 3 or 5 in the proposed optimal D-PDM for minimizing subharmonics near the resonant frequency.

3.4.2. PROPOSED HYBRID MODULATION

Based on the above analysis, there is a common issue for the PDMs. As evident from (3.6), (3.7), and (3.8), the minimum tuning step d_{E_min} for the conventional PDM and the optimal D-PDM is $1/N$, while it is $1/(2N)$ for the iPDM. As the value of N increases, the pulse density modulated rectifier is able to achieve a wider modulation range and finer tuning resolution. Nevertheless, a higher value of N results in increased subharmonics

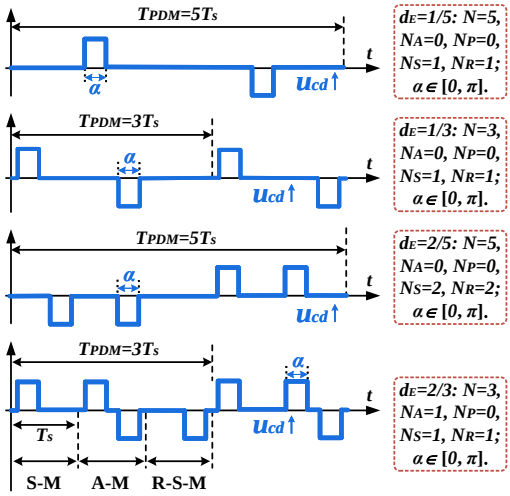

Figure 3.4: Typical operating waveforms of u_{cd} when employing the proposed HM for the secondary-side controlled IPT systems.

in the voltage. As the subharmonics around the resonant frequency cannot be effectively attenuated, this further leads to significant distortions in the currents.

To address this issue, an HM technique, which combines the PWM and the optimal D-PDM, is proposed, as shown in Fig. 3.4. Based on the optimal D-PDM, the proposed HM further adjusts the pulse width to achieve output regulation. As demonstrated in Fig. 3.4, the width of each pulse is identical, and it is represented by the pulse width angle α ($\alpha \in [0,\pi]$). The corresponding time duration of each pulse is given by $\alpha T_s/(2\pi)$. According to the Fourier series expansion, the RMS value of $\dot{U}_S$ under the proposed HM is derived as

$$|\dot{U}_S| = 2\sqrt{2}V_{out}/\pi \times d_E \times \sin(\alpha/2). \tag{3.10}$$

As shown in (3.10), the rectifier modulation ratio m_S can be regulated by varying the pulse density d_E ($d_E \in [0,1]$) and the pulse width angle α simultaneously. In the proposed method, to achieve precise and wide-range power regulation with minimized subharmonics, the optimal d_E is selected as 1, 2/3, 2/5, 1/3, and 1/5, while α is adjusted between 0 and π.

3.4.3. OPTIMAL ZVS TRAJECTORY UNDER HYBRID MODULATION

In IPT systems, the ZVS of the power switches is of great importance. According to the analysis in [153], ZVS can be achieved by tuning the phase difference angle δ ($\delta \in [0,\pi/2]$). Specifically, as the output power decreases, the pulse width angle α diminishes to obtain the required power, and δ can be decreased accordingly to enable ZVS. By reducing δ from $\pi/2$, more reactive power is introduced into the resonant circuits, facilitating ZVS for both the inverter and rectifier. To minimize the reactive power, the optimal relationship between α and δ should be derived under varying power levels. Moreover, as the proposed HM technique introduces subharmonics into the coil currents, it is important to consider the subharmonics when deriving the optimal ZVS trajectory. The detailed derivation of the optimal ZVS trajectory under the proposed HM is elaborated as follows.

Based on the analysis in [153], to guarantee ZVS, a sufficient ZVS current is required to charge or discharge the equivalent output capacitance C_{oss} of the power switches within the dead time. Specifically, as shown in Fig. 3.5, when the pulse density d_E of the rectifier input voltage u_{cd} is configured as 0.2, the following equations should be

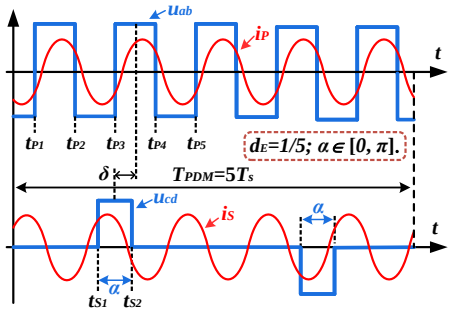

Figure 3.5: Implementation of ZVS when the pulse density d_E of the rectifer input voltage u_{cd} is set as 0.2.

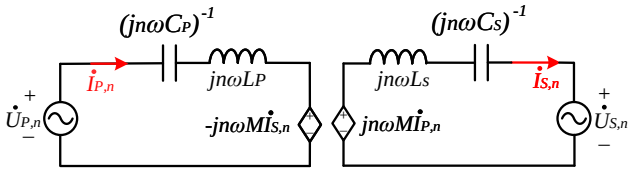

Figure 3.6: Harmonic-considered equivalent circuit model.

satisfied for the inverter and rectifier ZVS:

$$\begin{cases} \min\{|i_P(t_{Pi})|\} & \geq & I_{th}, i = 1,2,3,4,5, \\ \min\{|i_S(t_{Sj})|\} & \geq & I_{th}, j = 1,2, \end{cases} \tag{3.11}$$

where I_{th} is the threshold ZVS current to charge or discharge C_{oss}. It is noteworthy that in (3.11), only half of the PDM cycle needs to be considered due to the symmetrical pulse distribution. Furthermore, based on (3.11), the critical ZVS condition for both the inverter and rectifier is obtained as

$$\min\{|i_P(t_{Pi})|, |i_S(t_{Sj})|\} = I_{th}. \tag{3.12}$$

To derive the above ZVS boundary accurately, subharmonics within $i_P(t)$ and $i_S(t)$ should be considered. Therefore, the harmonic-considered equivalent circuit model is established in Fig. 3.6. Based on the Fourier series expansion, the time-domain expressions of $u_{ab}(t)$ and $u_{cd}(t)$ are given by

$$u_{ab}(t) = \sum_{n=1,3,\ldots} \frac{4V_{in}\sin^2(n\pi/2)}{n\pi}\sin(n\omega t), \tag{3.13}$$

$$u_{cd}(t) = \sum_{n=\frac{1}{5},\frac{3}{5},\ldots} \frac{4V_{out}\sin(n\pi/2)\sin(n\alpha/2)}{n\pi}\sin[n(\omega t+\delta)]. \tag{3.14}$$

Since the PDM control cycle is set as $T_{PDM} = 5T_s$ in the case of $d = 0.2$, subharmonic at the frequency of $\omega/5$ and its odd-integral multiples are considered (n is configured as 1/5, 3/5, ...), as shown in (3.13). Moreover, regarding $\dot{U}_{P,n}$ and $\dot{U}_{S,n}$ as two individual excitation voltage sources and applying the superposition theorem, the phasor-domain expressions of the harmonic-considered coil currents are derived as

$$\begin{cases} \dot{I}_{P\_tot} = \sum\limits_{n=\frac{1}{5},\frac{3}{5},\ldots} \dfrac{j(n-1/n)\hat{X}_S\dot{U}_{P,n} - jn\omega M\dot{U}_{S,n}}{n^2\omega^2M^2 - (n-1/n)^2\hat{X}_P\hat{X}_S}, \\ \dot{I}_{S\_tot} = \sum\limits_{n=\frac{1}{5},\frac{3}{5},\ldots} \dfrac{jn\omega M\dot{U}_{P,n} - j(n-1/n)\hat{X}_S\dot{U}_{S,n}}{n^2\omega^2M^2 - (n-1/n)^2\hat{X}_P\hat{X}_S}, \end{cases} \tag{3.15}$$

where $\hat{X}_P = \omega L_P = 1/(\omega C_P)$; $\hat{X}_S = \omega L_S = 1/(\omega C_S)$; $\dot{I}_{P\_tot}$ and $\dot{I}_{S\_tot}$ are the harmonic-considered coil currents. Combining (3.13), (3.14) and (3.15), the time-domain expressions of $i_{P\_tot}(t)$ and $i_{S\_tot}(t)$ can be derived. Furthermore, substituting $i_{P\_tot}(t)$ and

$i_{S\_tot}(t)$ into (3.12) yields the optimal ZVS trajectory, as shown in Fig. 3.7. Additionally, the power boundary is also demonstrated in Fig. 3.7 based on the calculation of (3.5). As indicated by Fig. 3.7, the intersection point of the power boundary and optimal ZVS trajectory represents the optimal operating point, where the required ZVS can be achieved with minimal reactive power under this power level. In practice, to determine the optimal relationship between α and δ, a look-up table can be established and stored in the microcontrollers.

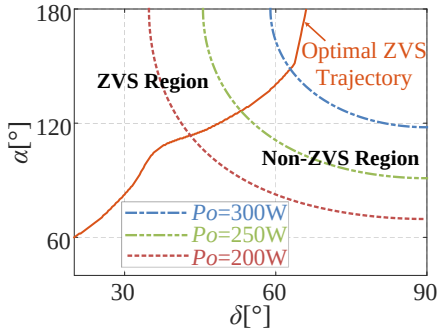

Figure 3.7: Optimal ZVS trajectory and power boundary when the pulse density d_E of u_{cd} is set as 0.2.

The above analysis demonstrates the derivation of optimal ZVS trajectory for the case of $d_E = 0.2$. Similarly, the optimal $\alpha - \delta$ relationship under other discrete values of d_E can be obtained by following the same procedure. The variations of δ, α, and d_E in the whole power range are further demonstrated in Fig. 3.8. As illustrated in Fig. 3.8, the proposed HM introduces the optimal D-PDM for power regulation. As the output power decreases, the proposed HM reduces the pulse density d_E accordingly, thereby significantly reducing the tuning ranges of δ and α. Consequently, the value of δ in the proposed HM is significantly higher than that of the PWM across a wide power range. Based on [153], a higher value of δ results in reduced reactive power, thereby achieving improved efficiency.

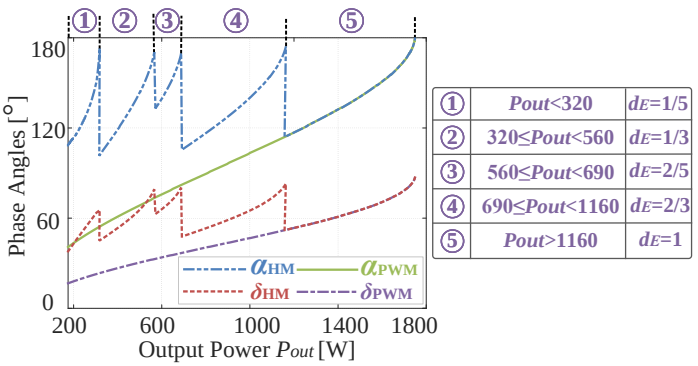

Figure 3.8: Variations of δ, α, and d_E in the whole power range.

3.4.4. CONTROL FRAMEWORK

The control block diagram of the proposed HM-SSC approach is shown in Fig. 3.9. As illustrated in Fig. 3.9, the DC output voltage V_{out} and current I_{out} are firstly measured. By multiplying the measured V_{out} and I_{out}, the output power P_{out} is obtained. Subsequently, P_{out} is fed to the pulse density selection module to determine the optimal pulse density value d_E. As P_{out} decreases during the charging process, d_E is required to be reduced accordingly, as demonstrated in Fig. 3.8. Moreover, a PI controller is utilized for reference tracking, and the controller output is the pulse width angle α. Afterward, according to the optimal $\alpha - \delta$ relationship illustrated in Fig. 3.8, the phase angle δ is obtained by the look-up Table Finally, based on the control outputs d_E, α, and δ, the corresponding driving signals for the rectifier are generated by the pulse generator. On the other hand, the pulse generator of the inverter employs an 85-kHz full-duty-cycle square wave as the modulation signal, and there is no need for wireless communication between the primary and secondary sides.

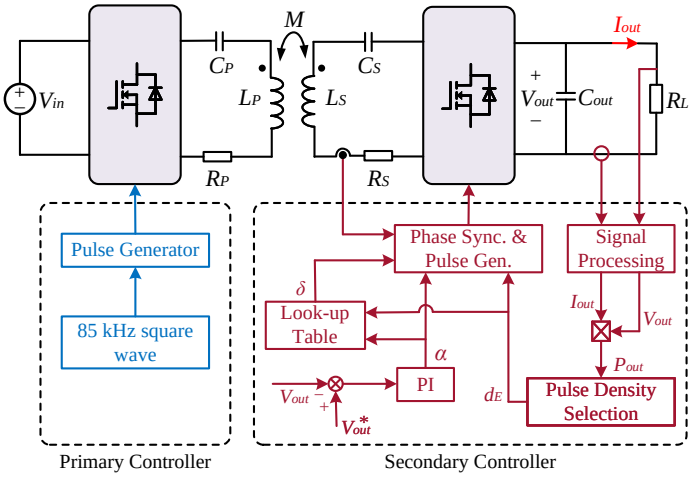

Figure 3.9: Control block diagram of the proposed HM-SSC method.

3.5. EXPERIMENTAL RESULTS

3.5.1. EXPERIMENTAL PROTOTYPE

To evaluate the performance of the proposed HM-SSC method, experiments were carried out based on an IPT prototype, as illustrated in Fig. 3.10. Within this prototype, two H-bridge converters are employed as the inverter and rectifier, respectively. A DC power source is utilized to provide the required power, while rheostats are adopted as the DC load. To compare the proposed HM with other existing modulation schemes, both the HM, PWM and iPDM methods were implemented. The control algorithm and pulse generation for the proposed HM and the conventional PWM were executed based on TI Launchpads F28379D. The iPDM, on the other hand, was implemented utilizing a field programmable gate array (FPGA, Xilinx ZYNQ-7020). Further details about the

Table 3.1: Parameters of the investigated IPT system used to verify the proposed HM-SSC method

Symbol	Parameters	Value	Unit
L_P, L_S, M	Coil inductances	335.8, 220.0, 78.0	μH
C_P, C_S	Compensation capacitances	10.6, 16.1	nF
V_{in}, V_{out}	DC input and output voltages	300, 300	V
f	Switching frequency	85	kHz
P_R	Rated power	1.7	kW

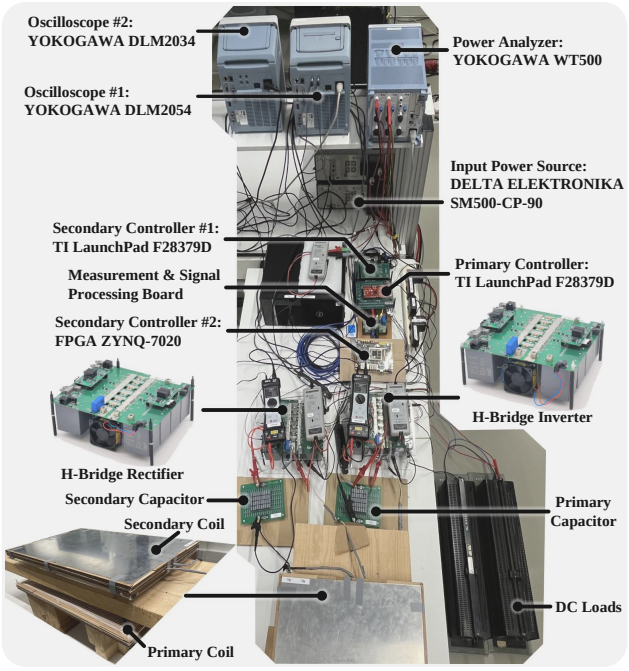

Figure 3.10: Experimental prototype of the SS-compensated IPT system used to verify the proposed HM-SSC method [3, 4].

prototype can be found in Table 3.1.

3.5.2. STEADY-STATE OPERATING WAVEFORMS

Fig. 3.11 demonstrates the steady-state operating waveforms of the proposed HM-SSC method. To enable communication-less control, the inverter output voltage is maintained as an 85-kHz full-duty-cycle square wave. In the proposed HM-SSC method, output regulation is accomplished through the secondary-side active rectifier. As shown in Fig. 3.11, both the pulse width (α) and density (d_E) of the rectifier input voltage are adjusted as the output power varies. With increasing power, the selected pulse density also rises accordingly. Specifically, the optimal pulse density d_E is configured as 1/5, 1/3, 2/5,

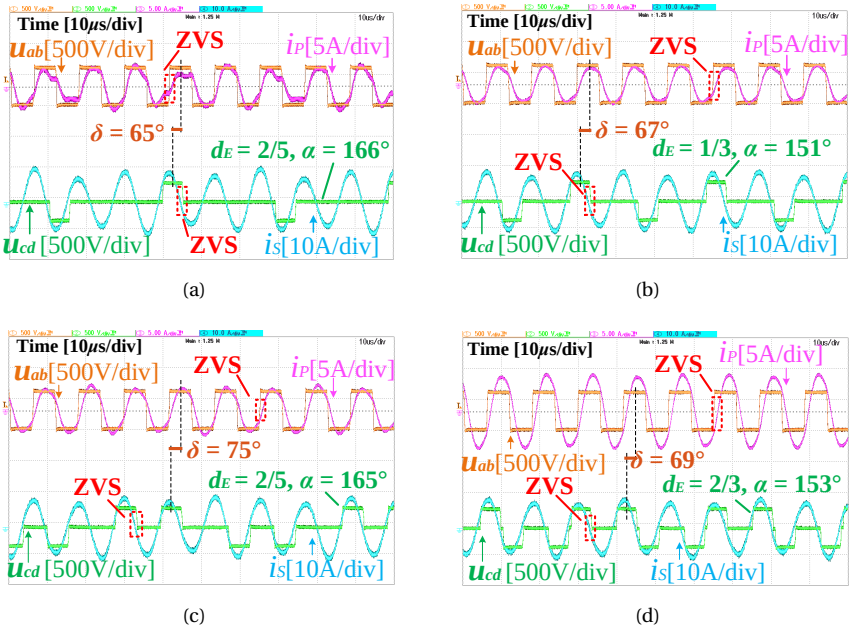

Figure 3.11: Measured operating waveforms of the proposed HM-SSC method when delivering (a) 300 W power at d_E=1/5, (b) 500 W power at d_E=1/3, (c) 650 W power at d_E=2/5, (d) and 1.0 kW power at d_E=2/3.

and 2/3 when delivering 300 W, 500 W, 650 W, and 1 kW power, respectively. Meanwhile, the pulse width angle α is adjusted simultaneously to achieve precise power regulation. Notably, according to the analysis in Chapter 3.4.3, the proposed HM-SSC method implements optimal ZVS tracking through dynamically tuning the phase difference δ, as demonstrated in Fig. 3.11. Consequently, ZVS for both the inverter and rectifier are consistently attained under varying power conditions.

Notably, due to the band-pass filtering characteristics of the SS compensated resonant tank, the harmonic components within the coil currents (i_P and i_S) are considerably small at frequencies above 150 kHz. Since the noise sources of the electromagnetic interference (EMI) arise from frequencies above 150 kHz, the proposed method does not exacerbate the EMI issues.

3.5.3. BENCHMARK WITH EXISTING MODULATION SCHEMES

To benchmark the proposed HM with other existing modulation techniques, experiments were carried out with both the HM, PWM, and iPDM methods. Notably, as iPDM has demonstrated superiority over the conventional PDM in [113], only the iPDM was implemented and compared. The detailed comparisons are elaborated as follows.

(1) Current Ripple: Fig. 3.12 illustrates the measured current ripple when delivering 40% rated power using both the proposed HM and the existing iPDM. In the iPDM, the semi-active mode is incorporated to achieve a modulation ratio of 0.4. However, this approach leads to a significant current ripple, as evident in Fig. 3.12(a). Conversely, the

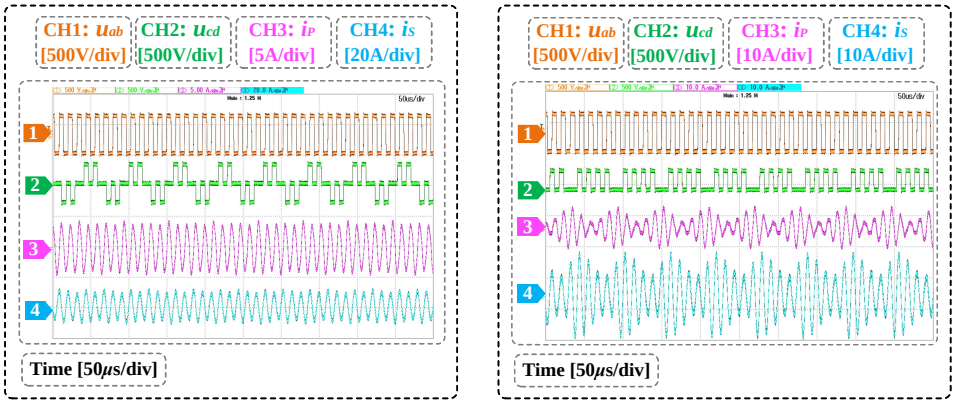

Figure 3.12: Measured current ripple when delivering 40% rated power under (a) the iPDM, and (b) the proposed HM.

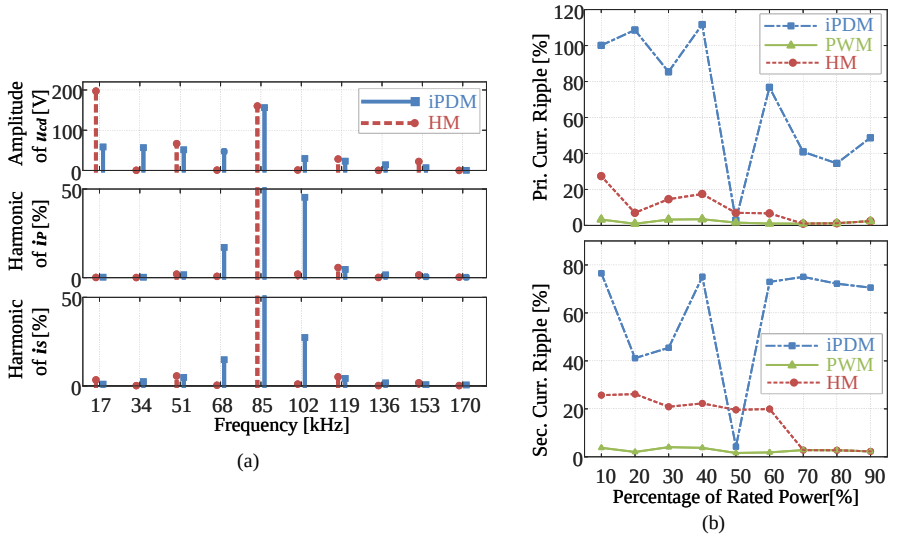

Figure 3.13: (a) The FFT analysis for the measured rectifier input voltage and coil currents when delivering 40% rated power. (b) Measured primary and secondary current ripple under different power levels. Here, the current ripple is quantified as the amplitude difference between the maximum and minimum peak currents, normalized by the rated peak current.

proposed HM introduces both semi-active and reversed semi-active modes. Moreover, through evenly and symmetrically distributing these modes, the HM minimizes the ripple of both the primary and secondary currents, as demonstrated in Fig. 3.12(b).

The fast Fourier transform (FFT) analysis of the above experimental results is further presented in Fig. 3.13(a). As shown in Fig. 3.13(a), implementation of the iPDM intro-

duces noticeable subharmonics near the resonant frequency (85 kHz) into the rectifier input voltage u_{cd}. Due to the bandpass characteristics of the SS compensation, these subharmonics cannot be effectively mitigated. Consequently, in the iPDM, significant subharmonics are observed at 68 kHz and 102 kHz in both the primary and secondary coil currents, i.e., i_P and i_S. In contrast, by symmetrically distributing the pulses, the proposed HM eliminates the even-subharmonics in the voltage, thereby remarkably reducing the current ripple.

In Fig. 3.13(b), a comparison of measured current ripple under various power levels is presented. As indicated by Fig. 3.13(b), the PWM leads to minimal current ripple. Moreover, under the proposed HM, the maximum primary current ripple is 27.4%, while the maximum secondary current ripple is 26.1%. Nevertheless, in the iPDM, the primary current ripple reaches up to 111.7% at 40% rated power, while the secondary current ripple reaches 76.5% at 10% rated power. It is noteworthy that when delivering 50% rated power, the rectifier operates at half-bridge mode in the iPDM, resulting in only integer harmonics in the voltage and decreased current ripple. However, excluding this specific power point, the current ripple of iPDM is significantly higher than that of the proposed HM.

The presence of current ripples may lead to an increase in maximum current stress. According to the experimental results, the proposed HM does not increase the maximum primary current stress compared with the PWM, while it is increased by 26.5% in iPDM. On the other hand, the proposed HM increases the maximum secondary current stress by 13.5%, whereas this figure significantly rises to 49.1% in the iPDM.

(2) Capacitor Voltage Stress: Fig. 3.14 presents the measured capacitor voltage stress when delivering 60% rated power. At this power level, the iPDM employs both the active and semi-active modes to obtain the required power. Conversely, the proposed HM simultaneously incorporates the active, semi-active, and reversed semi-active modes to distribute the voltage pulses evenly and symmetrically. This approach not only mitigates current ripple but also reduces capacitor voltage ripple accordingly. As depicted in Fig. 3.14, the capacitor voltage ripple is significantly diminished in the proposed HM.

According to the experimental results, the proposed HM does not increase the maximum primary capacitor voltage stress compared with the PWM, while the iPDM raises it by 19.1%. Additionally, the proposed HM increases the maximum secondary capacitor voltage stress by 18.4%, whereas this number substantially rises to 53.5% within the iPDM.

(3) Output Voltage Ripple: The output voltage ripple under various power levels is further presented in Fig. 3.15. As indicated by Fig. 3.15, the proposed HM increases the output ripple compared with the PWM. Nevertheless, when compared to the iPDM, the proposed HM achieves a notable reduction in the output voltage ripple.

(4) Efficiency: Fig. 3.16 presents the measured operating waveforms and the DC-to-DC efficiency when delivering 20% rated power under different modulation techniques. As indicated by Fig. 3.16 (a) and (b), both the proposed HM and the PWM achieve inverter and rectifier ZVS. However, compared with the PWM, the proposed HM method notably decreases the primary current. This reduction is attributed to the introduction of optimal D-PDM, which enables a greater phase difference angle δ and reduced reactive power under light loads. The diminished primary current significantly lowers inverter

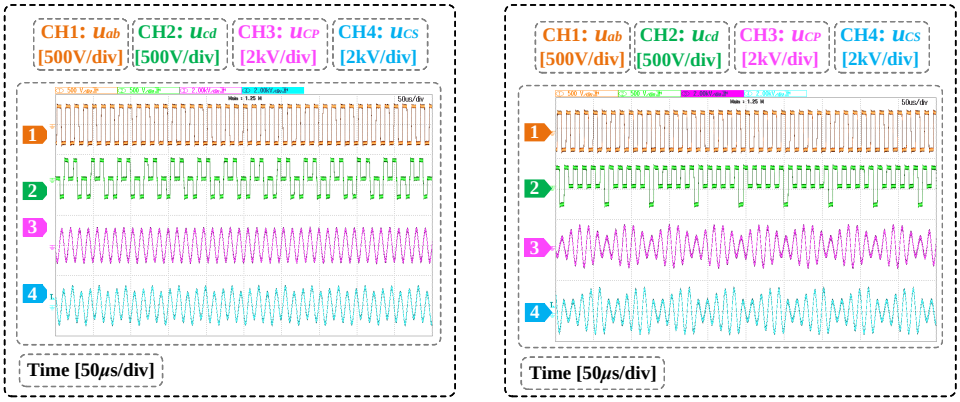

Figure 3.14: Measured capacitor voltage stress when delivering 60% rated power under (a) the iPDM, and (b) the proposed HM.

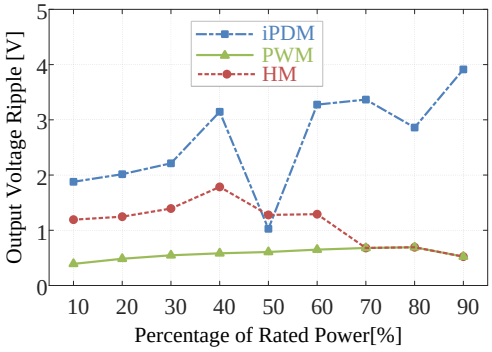

Figure 3.15: Measured output voltage ripple under different power levels.

conduction and turn-OFF losses, as well as primary coil losses. Moreover, as shown in Fig. 3.16(a) and (b), the equivalent switching times of the rectifier are also reduced in the proposed HM, leading to minimized rectifier switching losses. Consequently, the proposed HM notably improves the efficiency from 87.2% to 91.4%, with the efficiency improvement up to 4.2%.

On the other hand, when comparing the proposed HM with the iPDM, as depicted in Fig. 3.16 (a) and (c), the RMS values of the currents are comparable in both methods. Nevertheless, noticeable current distortions are observed in the iPDM, leading to hard switching at some switching points, as illustrated in Fig. 3.16 (c). The hard switching results in substantially increased switching losses. Consequently, the DC-to-DC efficiency of the iPDM was only 84.2%, which is 7.2% lower than the proposed HM.

Fig. 3.16(d) further demonstrates the efficiency comparisons under various power levels. Compared to the PWM, the proposed HM achieves remarkable efficiency im-

provement in the 10% to 60% power range, with the maximum improvement reaching up to 5.5%. On the other hand, when compared with the iPDM method, the proposed HM method enhances efficiency at 10% (+14.6%), 20%(+7.2%), 30%(+3.6%), 40%(+1.7%), 60%(+0.9%), and 90%(+0.5%) rated power, while slightly reducing the efficiency at 50%(-0.3%), 70%(-0.5%), and 80%(-0.2%) rated power. Overall, the proposed HM excels the iPDM in terms of efficiency.

(5) Tuning Resolution: Table 3.2 compares the tuning resolution of different modulation methods. As shown in Table 3.2, the tuning resolution of existing iPDMs is not continuous. This is attributed to the imperative of iPDMs to optimize pulse distribution for each density value. Enhancing tuning resolution necessitates consideration of a greater number of density values, which significantly increases the difficulty of analysis and implementation. Although the incorporation of a Delta-Sigma modulator enables continuous tuning for PDM methods [119], optimizing pulse distribution for each density is still challenging as there are a tremendous number of densities that should be considered in continuous PDM methods.

Conversely, the PWM enables continuous tuning through pulse width adjustment. By incorporating pulse width tuning into the optimal D-PDM, the proposed HM completely leverages the advantages of the PWM in terms of continuous tuning. Since only a limited number of density values are considered, the analysis and implementation of the proposed HM method are much more straightforward than that of the iPDM.

(6) Summary: After a comparative analysis of the proposed HM with existing PWM and iPDM methods, a summary is presented as follows.

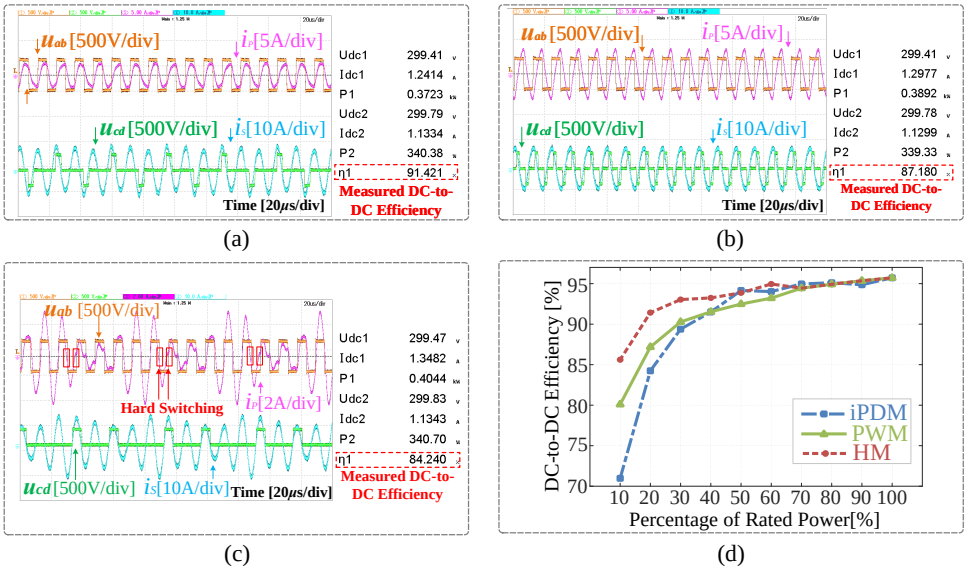

Figure 3.16: Measured waveforms and DC-to-DC efficiency when delivering 20% rated power in (a)the proposed HM, (b) the PWM, and (c) the iPDM. (d) Measured DC-to-DC efficiency under different modulations and power levels.

Table 3.2: Tuning resolution of different modulation schemes

Modulation	iPDM	iPDM	iPDM
Resolution	12.50% [159]	6.25% [113, 161]	5.00% [160]
Modulation	PWM	Proposed HM	
Resolution	Continuous	Continuous	

In comparison to the PWM, the proposed HM leads to increased component stress and output voltage ripple. Fortunately, through optimizing pulse distributions for the adopted discrete pulse densities, this increase is effectively minimized. On the other hand, the proposed HM notably enhances efficiency across a broad power range, with a maximum efficiency improvement of up to 5.5%. This enhancement contributes to the overall efficiency improvement of the system, enabling efficient power transfer under wide load variations.

When compared with the iPDM, the proposed HM achieves a substantial reduction in the component stresses and output voltage ripple. Additionally, the proposed HM facilitates continuous tuning by integrating pulse width regulation. In terms of the overall efficiency, the proposed HM outperforms the iPDM as well.

3.6. CONCLUSIONS

In this chapter, an HM technique is proposed to enable efficient, communication-less, and wide-range output regulation for IPT systems. Through optimizing the pulse distributions and incorporating pulse width regulation, the proposed HM achieves continuous output tuning, minimized voltage and current ripple, as well as improved efficiency. The overall performance of the proposed HM is benchmarked with the existing PWM and iPDM methods in terms of current ripple, capacitor voltage stress, output voltage ripple, efficiency, and tuning resolution. Experimental results demonstrate that the proposed HM substantially reduces the component stresses and output voltage ripple while facilitating continuous tuning when compared to the iPDM. On the other hand, when compared with the PWM, the proposed HM notably enhances the efficiency, enabling efficient power transfer under wide-range load conditions.

PART II

PARAMETER IDENTIFICATION AND IMPEDANCE TUNING

4

PARAMETER IDENTIFICATION BASED IMPEDANCE TUNING METHOD

This chapter presents a parameter identification based impedance tuning method for the impedance mismatch caused by capacitance drift and coil misalignment in inductive power transfer (IPT) systems. First, a parameter identification method is proposed to identify the unknown parameters of the resonant circuits by only measuring the RMS values of the coil currents. No phase detection circuits and auxiliary measurement coils are required. Furthermore, according to the recognized parameters, the reactance on both sides is minimized simultaneously by regulating the system frequency and the phase shift angles of the active rectifier. Compared with the existing methods, the proposed parameter identification method adopts a dynamic frequency approaching strategy to avoid severe system detuning due to the bifurcation phenomenon. Moreover, based on the recognized parameters, the proposed impedance tuning method can simultaneously cope with the parameter deviations caused by capacitance drift and coil misalignment on both sides without using extra circuits and switches. Experimental results show that the unknown parameters of the resonant circuits are recognized accurately, with the average relative errors all less than 3%. Additionally, by implementing the impedance tuning method, the DC-to-DC efficiency of the IPT prototype is improved by 4.3%-15% in the experiments.

This chapter is based on:

- G. Zhu, J. Dong, F. Grazian, and P. Bauer, "A parameter identification based impedance tuning method for ss-compensated wireless power transfer systems," *IEEE Transactions on Power Electronics*, vol. 33, no.11, pp. 13298-13314, Nov. 2023.

4.1. INTRODUCTION

To obtain a higher transmission efficiency for wireless EV charging, various compensation topologies are introduced in IPT systems to cancel the leakage inductance of the loosely coupled coils, where the most widely-used one is the series-series (SS) compensation [108]. In the SS-compensated IPT system, the series capacitors are designed to be resonant with the coils at the nominal resonant frequency. However, due to the component tolerances, temperature variations, and aging effects, the compensation capacitance may deviate from the nominal values [132]. Additionally, in practical IPT applications, the metallic shielding plates are usually used in the transmitter (Tx) and receiver (Rx) coils to protect human and electronic devices from the stray magnetic field, while magnetic ferrites are often employed to improve coil coupling. As a result, the self-inductances of the coils become sensitive to the spatial displacement between the Tx and Rx pads as these metallic and magnetic materials interfere with the transmission of the magnetic flux [131]. The parameter deviations caused by the capacitance drift and coil misalignment lead to the detuning of the system, which reduces the transmission efficiency and results in a lower power factor [130]. Therefore, in order to obtain better transmission performance, it is desirable for the system to consistently operate at the resonance state regardless of the capacitance drift and coil misalignment.

Many works have been done to deal with the impedance mismatch caused by parameter deviations, which can be roughly divided into three categories: 1) using the variable capacitors or inductors [131, 163–167]; 2) tracking the resonant frequency [168, 169]; 3) adopting the active rectifier [116, 149].

A commonly used approach for impedance tuning is to adjust the compensation impedance. In [163], a variable inductor was implemented on the secondary side to tune the receiver circuit dynamically. However, two extra conversion stages, i.e., a diode rectifier and a buck converter, are required in this method, which greatly increases the hardware costs. In [164–166], by introducing the selectable capacitor array, the compensation capacitance is discretely regulated. Nevertheless, the use of numerous switches and capacitors increases the system's volume and costs. Additionally, this method fails to adjust the impedance continuously. To reduce the number of components and realize continuous tuning, controllable capacitors were used in [131] and [167]. In [167], a voltage-controlled capacitor was proposed to achieve dynamic impedance tuning. Nevertheless, the analog amplifier used in this method limits the power transfer capability, and thus, it is only suitable for applications of a few watts. In [131], a pulse-width modulation (PWM) controlled capacitor was proposed to withstand the detuning caused by the Tx inductance variation. This method enables continuous capacitance tuning and is able to cope with high-power applications. However, the introduction of additional power switches in the PWM-controlled capacitors increases the power losses and hardware costs. Additionally, the capacitance drift is not considered in this method.

Another typical method to deal with the impedance mismatch is to track the resonant frequency. In [168], a power-frequency controller was proposed, which implements resonance tracking by synchronizing the switching signals with the resonant current. In [169], a self-oscillating switching technique was adopted, where the switching frequency of the inverter automatically tracks the resonant frequency. However, these methods can only realize zero-phase-angle (ZPA) input, whereas the reactance on the Rx side cannot

be tuned.

To tune the Rx-side reactance, the active control of the rectifier was adopted in some methods. In [149] and [116], by regulating the duty cycle and the phase shift angle of the active rectifier, the equivalent load impedance was regulated to minimize the Rx-side reactance and to realize the maximum efficiency tracking. However, the active rectifier control cannot simultaneously handle the impedance mismatch on both sides.

Recently, some researchers combined the resonant frequency tracking and the active rectifier control to tune the reactance on both the Tx and Rx sides. In [170], an impedance tuning control was proposed to deal with the self-inductance variations caused by coil misalignment, where the switching frequency was controlled to realize ZPA input, and a synchronous switching technique was proposed for the active rectifier to minimize the Rx-side reactance. However, the parameter deviations caused by capacitance drift were not discussed in this method. In [171], an impedance decoupling based method was proposed to minimize the dual-side reactance caused by capacitance drift. Nevertheless, the phase detection circuits and an auxiliary measurement coil are needed to measure the reactance angles on both sides, which increases the hardware costs and complexity.

The phase detection circuits for reactance angle measurements can be avoided by parameter identification. In [172], Dai *et al.* presented a pulse density modulation based parameter identification method to estimate the self-inductance and compensation capacitance on the Rx side simultaneously. However, only the Rx-side reactance is tuned in this method. In [173], a parameter identification based self-tuning method was proposed to address a wide range of coupling coefficient variations, where both the mutual inductance and the self-inductances can be identified without using the phase information and auxiliary measurement coils. However, this method cannot identify the compensation capacitances.

In practice, the impedance mismatch usually involves deviations of multiple parameters, and it is challenging to tune the impedance when considering all of them. Therefore, previous studies mainly focus on parameter deviations in one specific aspect, for instance, only considering the coil misalignment [131, 170, 173–175], the capacitance drift [171], or the impedance mismatch on just one side [172]. To simultaneously tune the dual-side impedance mismatch under capacitance drift and coil misalignment, the parameters of the whole resonant circuit are required to be identified. Although the identification of multiple parameters can be realized by the frequency-sweeping-based front-end monitoring methods [176, 177], these methods generally sweep the frequency around the nominal resonant frequency, which leads to severe system detuning and significant load power ripple, especially under parameter deviations.

4.1.1. SCOPE AND CONTRIBUTIONS

To fill up the above research gaps, this chapter presents a new parameter identification based impedance tuning method. Firstly, a parameter identification method is proposed to identify the unknown parameters of the resonant circuits, and the original features of this method are summarized as follows:

1) Compared to the conventional front-end parameter monitoring methods, the secondary side information is introduced, and therefore, all of the unknown parameters

of the resonant circuits, including the self-inductances, the mutual inductance, and the compensation capacitances, are recognized accurately, without using any phase detection circuits and auxiliary measurement coils.

2) A dynamic frequency approaching strategy is proposed to acquire the required data for parameter identification, which avoids severe system detuning during the traditional frequency-sweep process.

3) The parameter identification is implemented at pre-start-up, with the rectifier output short-circuited during this process, which avoids significant load power fluctuations caused by frequency variations.

4) A simple yet powerful heuristic algorithm called JAYA is introduced to recognize the unknown parameters (the JAYA algorithm will be described in section 4.4.3). Compared with the conventional genetic algorithm (GA) and differential evolution (DE) algorithm, which need to tune the parameters of the differential weight and the crossover rate, the JAYA algorithm is free from algorithm-specific parameters and thereby avoids the difficulty of tuning parameters [178].

Furthermore, based on the recognized parameters, the reactance on both sides is minimized simultaneously by regulating the system frequency and the phase-shift angles of the active rectifier.

4.1.2. OUTLINE

The remaining part of this chapter is organized as follows. Chapter 4.2 investigates the parameter deviations caused by capacitance drift and coil misalignment, while Chapter 4.3 demonstrates the problems of conventional parameter identification methods. Furthermore, in a new parameter identification method is proposed in Chapter 4.4, and the corresponding impedance tuning strategy is illustrated in Chapter 4.5. Experimental results are then provided in Chapter 4.6 to validate the effectiveness of the proposed approach. Finally, Chapter 4.7 presents the conclusions.

4.2. PARAMETER DEVIATIONS

The circuit diagram of the investigated SS-compensated IPT system is illustrated in Fig. 2.1 of Chapter 2. To investigate the parameter deviations within the SS-compensated IPT system, the equivalent circuit model derived by the fundamental harmonic approximation (FHA) method is illustrated in Fig. 4.1. In this figure, Z_E is the equivalent load impedance seen from the input of the active rectifier, while $\dot{U}_P$, $\dot{I}_P$, and $\dot{I}_S$ are the phasor forms of the fundamental components of u_{ab}, i_P, i_S, respectively. According to the

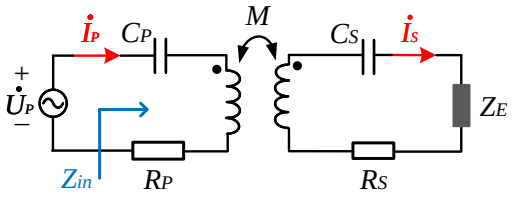

Figure 4.1: Equivalent circuit model of the SS-compensated IPT system.

Kirchhoff's voltage law (KVL), the steady state equation of the system is given by

$$\begin{cases} \dot{U}_P &= Z_P \dot{I}_P - j\omega M \dot{I}_S \\ 0 &= j\omega M \dot{I}_P - (Z_S + Z_E)\dot{I}_S. \end{cases} \tag{4.1}$$

The equivalent impedances of primary and secondary resonant circuits Z_P and Z_S are expressed as

$$Z_i = R_i + jX_i, X_i = \omega L_i - 1/(\omega C_i), \tag{4.2}$$

where the subscript i indicates the primary (P) or the secondary (S) side. Moreover, the equivalent load impedance Z_E is represented by $Z_E = R_E + jX_E$, where R_E and X_E are the equivalent load resistance and reactance, respectively.

Ideally, for the SS-compensated IPT system, the compensation capacitors are designed to be resonant with the coupled coils at the nominal resonant frequency. Nevertheless, in practical applications, the parameters of the resonant circuits may deviate from the nominal values due to coil misalignment and capacitance drift.

4.2.1. PARAMETER DEVIATIONS CAUSED BY COIL MISALIGNMENT

On the one hand, as aluminum shielding sheets and magnetic ferrites are generally used in the Tx and Rx pads, the coil self-inductances vary with the spatial displacement. To demonstrate the impact of coil misalignment, the measured coil inductances under different misalignment directions and air gaps are illustrated in Fig. 4.2 for the charging pads shown in Fig. 4.3. As it can be observed from Fig. 4.2, the coil self-inductances slightly increase as the misalignment in the x- and y- directions increases. More significant inductance variations can be observed under different air gaps. As the air gap D increases from 10 cm to 15 cm, the primary self-inductance L_P drops from 335.5 μH to 327.5 μH, while the secondary self-inductance L_S decreases from 222.7 μH to 216.5 μH. Meanwhile, the increase in the air gap reduces the coupling coefficient k from 0.35 to 0.22. In this thesis, two cases, with the air gap D at 10 cm and 15 cm, are selected as case-A and case-B for theoretical analysis, respectively.

4.2.2. PARAMETER DEVIATIONS CAUSED BY CAPACITANCE DRIFT

On the other hand, due to the ambient temperature variations, the aging effect, and the manufacturing errors, significant capacitance drift may occur in practical applications. Therefore, it is essential to investigate the influence of the capacitance drift. In this thesis, both the primary and secondary capacitance deviations are considered and expressed as

$$C_P = (1 + d_P)C_{P0}, C_S = (1 + d_S)C_{S0}, \tag{4.3}$$

where d_P and d_S indicate the degree of capacitance drift; C_{P0} and C_{S0} are the nominal compensation capacitances. Considering component tolerances of the commercialized capacitors, the aging effects, and the ambient temperature variations, the maximum degree of capacitance drift is set to ±20% to ensure that the proposed IPT system is able to deal with the majority of the capacitance drift cases in practice.

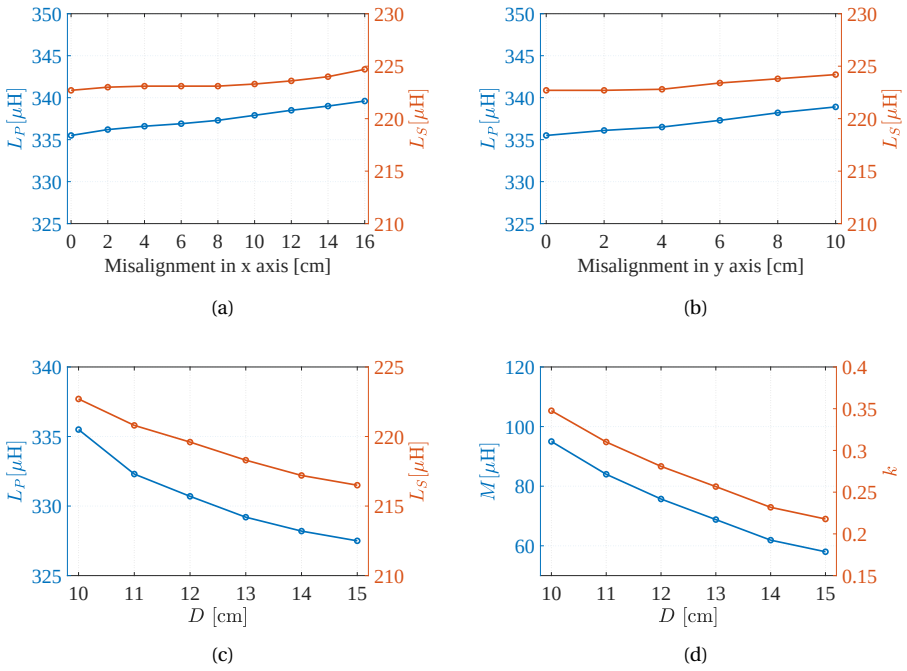

Figure 4.2: Measured coil inductances under different coil misalignment directions and air gaps: (a) self-inductance variations under the x-direction misalignment (D=10 cm), (b) self-inductance variations under the y-direction misalignment (D=10 cm), (c) self-inductance variations under different air gaps, (d) variations in mutual inductance and coupling coefficient under different air gaps.

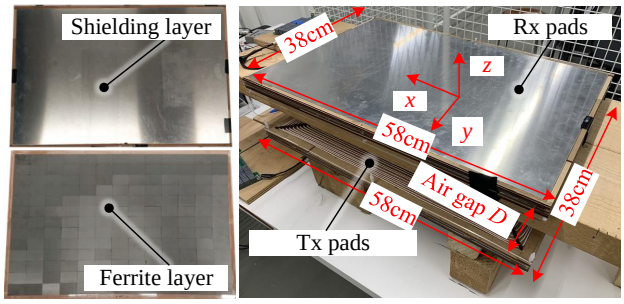

Figure 4.3: Charging pads with the shielding and ferrite layers [4].

4.2.3. IMPACT OF PARAMETER DEVIATIONS

Considering the parameter deviations caused by capacitance drift and coil misalignment, the parameters of the investigated system are listed in Table 4.1. Moreover, the impact of parameter deviations is demonstrated as follows.

(1) Power Transfer Capability: According to [172], the output power of the system

Table 4.1: Parameters of the investigated system used to verify the proposed impedance tuning method

Symbol	Parameters	Value	Unit
L_P	Primary coil inductance	327.5 ~ 335.5	μH
L_S	Secondary coil inductance	216.5 ~ 222.7	μH
k	Coupling coefficient	0.22 ~ 0.35	/
C_{P0}, C_{S0}	Nominal primary and secondary capacitance	10.45, 15.74	nF
d_P, d_S	Degree of capacitance drift	-0.2~0.2	/
R_P, R_S	Primary and secondary loss resistances	0.72, 0.48	Ω
R_L	Load resistance	100	Ω
f	Switching frequency	85	kHz
U_{in}	DC input voltage	200	V

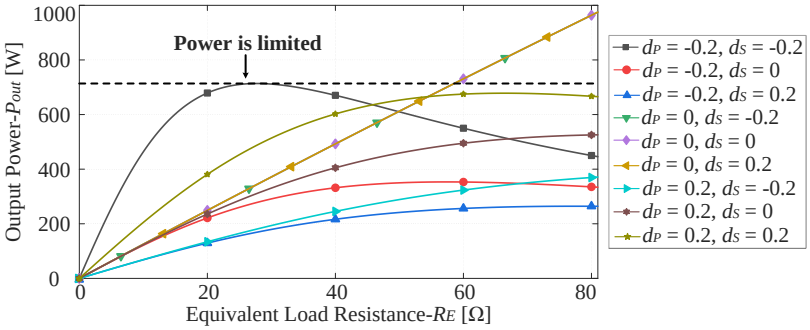

(a)

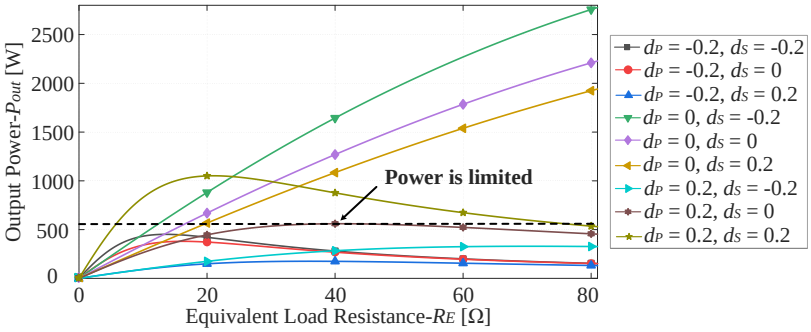

(b)

Figure 4.4: Output power P_{out} versus the equivalent load resistance R_E under parameter deviations: (a) Case-A, (b) Case-B.

is derived by

$$P_{out} = |\dot{I}_S|^2 R_E = \omega^2 M^2 |\dot{U}_P|^2 R_E / D_E, \tag{4.4}$$

where $D_E = (X_P^2 + R_P^2)(R_{ST}^2 + X_{ST}^2) + 2\omega^2 M^2 (R_P R_{ST} - X_P X_{ST}) + \omega^4 M^4$, $R_{ST} = R_S + R_E$, and $X_{ST} = X_S + X_E$. As illustrated in (4.4), the parameter deviations of the coil inductances

and compensation capacitances influence the primary and secondary reactance X_P and X_S, which in turn affects the output power. Assuming the equivalent load reactance $X_E = 0$, the output power P_{out} versus the equivalent load resistance R_E under parameter deviations is shown in Fig. 4.4. As it can be observed in Fig. 4.4(a), the output power curve has a peak point when the degree of capacitance drift is $d_P = d_S = -0.2$. This means that the power transfer capability of the system is limited no matter how the load resistance R_E is adjusted, and therefore, the system may not be able to reach the required output power. Similar power limitations can also be observed in Fig. 4.4(b). Compared with case-A, since the air gap D of case-B is increased from 10 cm to 15 cm, the mutual inductance is correspondingly reduced from 95 μH to 58 μH, and thus, the system can reach more power. However, in some cases, the output power of the system is still limited due to the capacitance drift; for example, in the case of $d_P = 0.2, d_S = 0$.

(2) Transfer Efficiency: Another effect of the parameter deviations is on the transfer efficiency. Based on [172], the transmission efficiency of the resonant tank is obtained as

$$\eta_{res} = \frac{|\dot{I}_S|^2 R_E}{\mathrm{Re}[\dot{U}_P(\dot{I}_P)^*]} = \frac{\omega^2 M^2 R_E}{\omega^2 M^2 R_{ST} + R_P(R_{ST}^2 + X_{ST}^2)}. \tag{4.5}$$

As it can be observed in (4.5), the secondary lumped reactance X_{ST} that exists in the denominator degrades the transfer efficiency, whereas the primary reactance X_P does not directly affect the efficiency. Assuming $X_E = 0$ and $d_P = 0$, the efficiency η_{res} versus the output power P_{out} under parameter deviations is shown in Fig. 4.5. As it can be observed in Fig. 4.5(a), the transfer efficiency of the resonant tank is degraded due to the capacitance drift, and the efficiency drop is more noticeable under light load conditions. Moreover, as shown in Fig. 4.5(b), since the air gap D is increased to 15 cm in case-B, the secondary self-inductance L_S is reduced from 222.7 μH to 216.5 μH. In this case, the secondary reactance X_S becomes larger when the secondary capacitance is also decreased, and thus, remarkable efficiency reduction can be observed when $d_S = -0.2$.

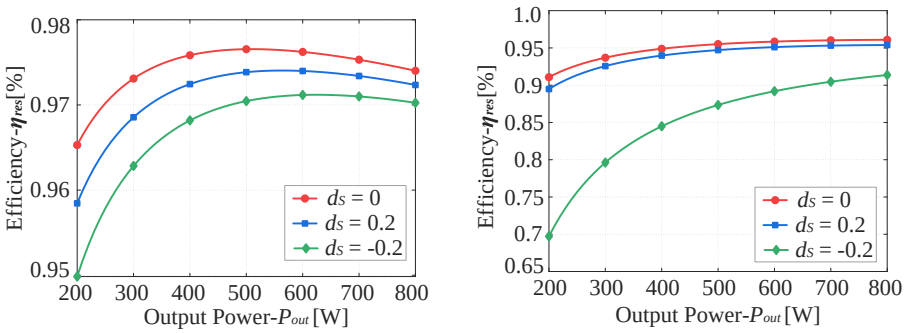

Figure 4.5: Transfer efficiency η_{res} versus the output power P_{out} under parameter deviations: (a) Case-A, (b) Case-B. Here, the equivalent load resistance R_E is adjusted to obtain the same output power under different values of d_S.

According to the above analysis, the parameter deviations caused by coil misalignment and capacitance drift reduce the system transfer efficiency and may result in a failure to obtain the required output power. Therefore, it is desirable to cancel the dual-side reactance caused by parameter deviations so that the system can always operate at the resonance state.

4.3. PROBLEMS OF CONVENTIONAL PARAMETER IDENTIFICATION METHODS

To identify the unknown parameters, conventional parameter identification methods generally sweep the frequency around the nominal resonant frequency [176, 177]. However, for the SS-compensated IPT system, the nominal resonant frequency may split into multiple resonant frequencies due to the parameter deviations, which is the so-called bifurcation phenomenon [126]. Since these resonant frequencies are close to the nominal

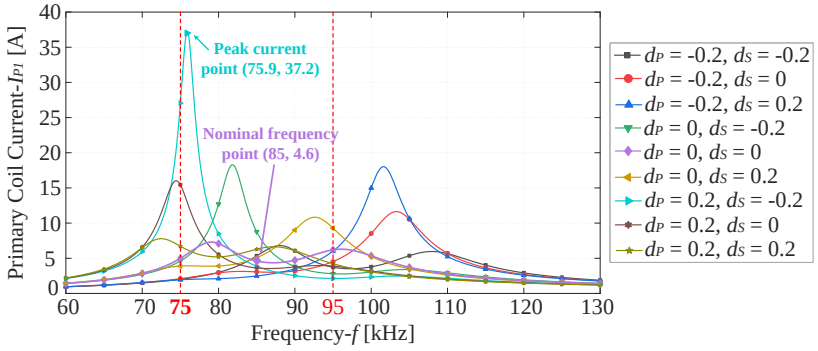

(a)

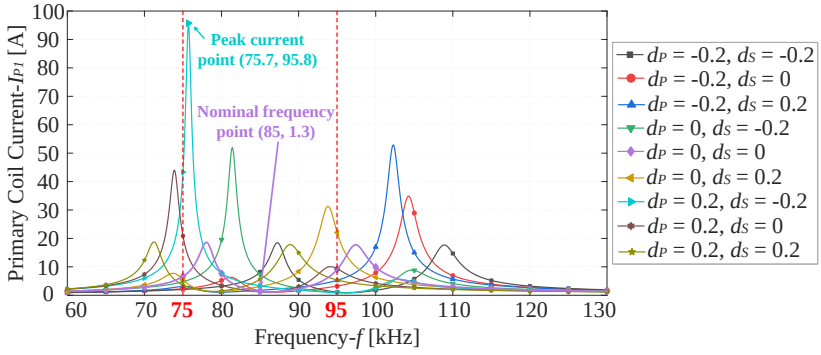

(b)

Figure 4.6: Value of I_{P1} under frequency variations and parameter deviations: (a) $R_E = 24.1\ \Omega$ (case-B), where the output power at the nominal frequency point is 800 W, (b) $R_E = 5.8\ \Omega$ (case-B), where the output power at the nominal frequency point is 200 W. Here, the DC input voltage of the system is 200 V, the nominal switching frequency is 85 kHz, and the inverter output is set to the full duty cycle.

frequency, the traditional frequency-sweep process causes severe system detuning under parameter deviations, which results in enormous coil currents and significant power ripple.

To demonstrate the influence of the system detuning on the coil currents, the RMS value of the fundamental component of the primary coil current I_{P1} under parameter deviations and frequency variations is depicted in Fig. 4.6, where the frequency-sweep band is set to 75~95 kHz to ensure that sufficient frequency points can be collected [176]. In Fig. 4.6, the equivalent load resistance R_E is set to different values to investigate the impact of load variations, while case-B is selected as an example to demonstrate the influence of coil misalignment. Moreover, nine different capacitance drift cases are illustrated with dotted, solid lines in different colors to show the influence of capacitance drift, where the maximum degree of capacitance drift is set to ±20%. As illustrated in Fig. 4.6(a), when the equivalent load resistance R_E is 24.1 Ω under case-B, the output power at the nominal frequency point is 800 W, with the primary coil current at 4.6 A. However, I_{P1} increases to 37.2 A at 75.9 kHz under $d_P = 0.2, d_S = -0.2$. More severe system detuning can be observed under smaller load resistances, as shown in Fig. 4.6(b). When the equivalent load resistance R_E is 5.8 Ω under case-B, the output power at the nominal frequency point is 200 W, with the primary coil current I_{P1} at 1.3 A. Due to the frequency variations and capacitance drift, I_{P1} dramatically increases to 95.8 A at 75.7 kHz under $d_P = 0.2, d_S = -0.2$. It should be noted that in Fig. 4.6, the inverter output is set to the full duty cycle. Although decreasing the inverter duty cycle is able to reduce the coil currents, it results in a remarkable disparity in the current amplitudes under different cases. This poses a great challenge to the measurement accuracy of the coil currents.

Furthermore, observing the current curve in Fig. 4.6 reveals that the peak current point can be derived by sweeping the frequency. Specifically, by sweeping the parameters of the equivalent load resistance R_E and the coil coupling coefficient k, the maximum primary coil current (I_{P1_max}) under load variations and coupling changes is shown in Fig. 4.7. As it can be observed, the value of I_{P1_max} is inversely related to both R_E and k. In other words, when R_E or k is small, more severe system detuning may occur due to frequency variations and parameter deviations. Specifically, the worst case shown in Fig.

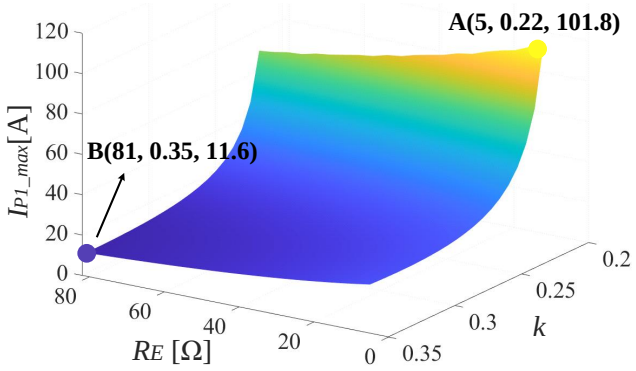

Figure 4.7: Maximum primary coil current (I_{P1_max}) under different values of R_E and k.

4.7 is point A, where the value of I_{P1_max} reaches 101.8 A when $R_E = 5\ \Omega$ and $k = 0.22$, while the best case is the point B, where the value of I_{P1_max} is 11.6 A under $R_E = 81\ \Omega$ and $k = 0.35$.

The increased coil currents not only significantly increase the current stress of the resonant tank, but also potentially damage the semiconductor devices due to the rise of their junction temperature.

Another impact of the system detuning is on the system output power P_{out}. As shown in Fig. 4.8, when the equivalent load resistance R_E is 24.1 Ω under case-B, significant power ripple is observed under frequency variations and parameter deviations. In some cases, the output power of the system may considerably exceed the load tolerance, eventually causing irreparable damage to the load.

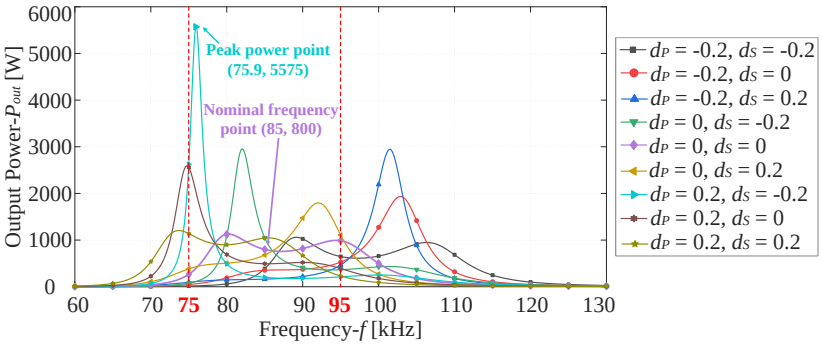

Figure 4.8: System output power P_{out} under frequency variations and parameter deviations when the equivalent load resistance R_E is 24.1 Ω in case-B. Here, the input conditions of the system are the same as those in Fig. 4.6.

According to the above analysis, it can be concluded that the traditional frequency-sweeping-based parameter identification methods may lead to severe system detuning under parameter deviations, resulting in considerable coil currents and significant power ripple. Therefore, to ensure the safe operation of the system, it is essential to avoid wide frequency variations near the nominal resonance point.

4.4. PROPOSED PARAMETER IDENTIFICATION METHOD

A new parameter identification method is proposed to recognize the unknown parameters of the capacitors and coils, i.e., L_P, L_S, C_P, C_S and M, as shown in Fig. 4.9. First, the parameter identification process is carried out at pre-start-up, and the rectifier output is short-circuited during this process. As a result, significant load power ripple during the conventional frequency-sweep process is avoided. Then, the primary and secondary coil currents i_P and i_S are measured and fed to two separate low-pass filters (LPFs). With the LPFs, the fundamental components of i_P and i_S, i.e., i_{P1} and i_{S1}, are extracted. Furthermore, the RMS values of i_{P1} and i_{S1}, i.e., I_{P1} and I_{S1}, are obtained by the RMS value extraction modules. According to the values of I_{P1} and I_{S1}, a dynamic frequency approaching strategy is proposed to determine the selected frequency points. By recording the values of I_{P1} and I_{S1} at different frequency points, multiple sets of $\{\omega_i, I_{P1\_i}, I_{S1\_i}\}$ are

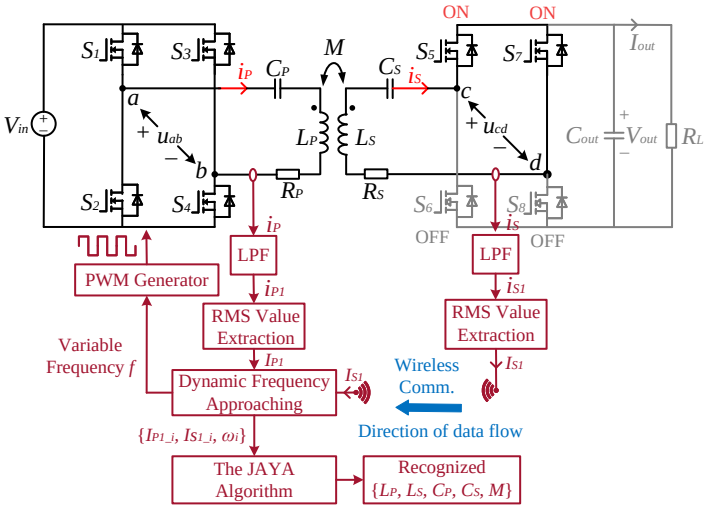

Figure 4.9: Block diagram of the proposed parameter identification method implemented at pre-start-up, where the rectifier output is short-circuited during this process. Here, the measured I_{S1} is transmitted from the secondary controller to the primary controller for parameter identification.

acquired. Finally, based on the acquired data, the unknown parameters are derived by the JAYA algorithm. The implementation details of the proposed method are elaborated as follows.

4.4.1. MATHEMATICAL MODELLING

When the rectifier output is short-circuited, the equivalent input impedance Z_{in} of the SS-compensated system is derived by

$$Z_{in} = R_P + j(\omega L_P - \frac{1}{\omega C_P}) + Z_R, \tag{4.6}$$

where Z_R is the reflected impedance of the secondary resonant circuit, which can be expressed as

$$Z_R = \frac{(\omega M)^2}{R_S + j[\omega L_S - 1/(\omega C_S)]}. \tag{4.7}$$

The amplitude of the equivalent input impedance is denoted by $|Z_{in}|$. If the switching angular frequency ω is switched to another value, a new value of $|Z_{in}|$ can be obtained. Furthermore, by sweeping the switching frequency ω, multiple sets of $\{\omega_i, |Z_{in\_i}|\}$ can be acquired as

$$|Z_{in\_i}| = \frac{U_{P1\_i}}{I_{P1\_i}} = f(R_P, R_S, L_P, L_S, C_P, C_S, M, \omega_i), \tag{4.8}$$

where $\omega_i (i = 1, 2, \cdots, m)$ is the i-th selected frequency point; m is the number of the measured frequency points; U_{P1_i} and I_{P1_i} are the RMS values of u_{P1} and i_{P1} at the i-th frequency point; u_{P1} is the fundamental component of the inverter output voltage u_{ab}.

According to the analysis in [176], assuming R_P and R_S are given, $\{L_P, L_S, C_P, C_S, M\}$ can be estimated by multiple sets of $\{\omega_i, |Z_{in\_i}|\}$.

However, it is difficult to identify $\{L_S, C_S, M\}$ accurately with only the front-end information, as there are countless sets of $\{L_S, C_S, M\}$ that lead to an almost consistent reflected impedance Z_R. Suppose there is a new set of solution $\{L'_S, C'_S, M'\}$ satisfying $L'_S = \lambda L_S$, $C'_S = (1/\lambda)C_S$, $M' = \sqrt{\lambda}M$, where $\{L_S, C_S, M\}$ represents the correct solution and λ is any non-zero positive real number. Generally, when the switching frequency ω is deviated from the secondary resonant frequency ω_S ($\omega_S = 1/\sqrt{L_S C_S}$), X_S is much larger than R_S. Therefore, the reflected impedance Z'_R of the new set of solution satisfies

$$Z'_R \approx \frac{(\omega M')^2}{j[\omega L'_S - 1/(\omega C'_S)]} = \frac{\lambda(\omega M)^2}{j\lambda[\omega L_S - 1/(\omega C_S)]} \approx Z_R. \tag{4.9}$$

Since λ can be any value, there are countless sets of solution $\{L'_S, C'_S, M'\}$ such that the reflected impedance Z'_R is almost identical with the correct reflected impedance Z_R. This means that it is difficult to accurately recognize $\{L_S, C_S, M\}$ with only the primary-side information. Therefore, in this thesis, the secondary coil current i_S is also measured. By introducing the secondary-side information, the relationship between I_{S1} and I_{P1} is established as

$$\frac{I_{P1}}{I_{S1}} = \sqrt{\frac{R_S^2 + [\omega L_S - 1/(\omega C_S)]^2}{(\omega M)^2}} \approx \frac{\omega L_S - 1/(\omega C_S)}{\omega M}. \tag{4.10}$$

Define the ratio of I_{P1} to I_{S1} as T_{ii}, i.e., $T_{ii} = I_{P1}/I_{S1}$. Then, the ratio T'_{ii} of the new set of solution $\{L'_S, C'_S, M'\}$ satisfies

$$T'_{ii} \approx \frac{\omega L'_S - 1/(\omega C'_S)}{\omega M'} = \frac{\lambda[\omega L_S - 1/(\omega C_S)]}{\sqrt{\lambda}\omega M} \approx \sqrt{\lambda} T_{ii}. \tag{4.11}$$

The only solution of λ such that (4.9) and (4.11) hold simultaneously is $\lambda = 1$. This means that by introducing the information of i_S, the correct solution of $\{L_S, C_S, M\}$ is unique, and all the unknown parameters can be estimated accurately.

To introduce the information of i_S into the identification model, the equivalent gain from I_{S1} to U_{P1} is given by

$$|Z_{PS}| = \frac{U_{P1}}{I_{S1}} = |j\omega M - \frac{(R_P + jX_P)(R_S + jX_S)}{j\omega M}|. \tag{4.12}$$

Similarly, by sweeping the switching frequency ω, multiple sets of $\{\omega_i, |Z_{PS\_i}|\}$ can be obtained as

$$|Z_{PS\_}i| = \frac{U_{P1\_i}}{I_{S1\_i}} = g(R_P, R_S, L_P, L_S, C_P, C_S, M, \omega_i). \tag{4.13}$$

Furthermore, with the information on both sides, the identification model for the unknown parameters is derived as

$$\min J = ||\boldsymbol{U_{P1}} - \boldsymbol{U_{P1est}}|| + ||\boldsymbol{U_{P1}} - \hat{\boldsymbol{U}}_{\boldsymbol{P1est}}|| \tag{4.14}$$

s.t. $\boldsymbol{U_{P1est}} = |\boldsymbol{Z_{in}}|\boldsymbol{I_{P1}}$, $\hat{\boldsymbol{U}}_{\boldsymbol{P1est}} = |\boldsymbol{Z_{PS}}|\boldsymbol{I_{S1}}$, $L_{PL} \le L_P \le L_{PH}$, $L_{SL} \le L_S \le L_{SH}$, $C_{PL} \le C_P \le C_{PH}$, $C_{SL} \le C_S \le C_{SH}$, and $M_L \le M \le M_H$, where

$$|\boldsymbol{Z_{in}}| = diag\{|Z_{in\_i}|\}(i = 1, \cdots, m),$$

$$|\boldsymbol{Z_{PS}}| = diag\{|Z_{PS\_i}|\}(i = 1, \cdots, m),$$

$$\boldsymbol{I_{P1}} = [I_{P1\_1}, I_{P1\_2}, \cdots, I_{P1\_m}],$$

$$\boldsymbol{I_{S1}} = [I_{S1\_1}, I_{S1\_2}, \cdots, I_{S1\_m}],$$

$$\boldsymbol{U_{P1est}} = [U_{P1est\_1}, U_{P1est\_2}, \cdots, U_{P1est\_m}],$$

$$\hat{\boldsymbol{U}}_{\boldsymbol{P1est}} = [\hat{U}_{P1est\_1}, \hat{U}_{P1est\_2}, \cdots, \hat{U}_{P1est\_m}],$$

$$\boldsymbol{U_{P1}} = [U_{P1\_1}, U_{P1\_2}, \cdots, U_{P1\_m}].$$

Herein, $\boldsymbol{I_{P1}}$ is the measured RMS values of i_{P1} at multiple frequency points; $\boldsymbol{U_{P1est}}$ is the estimated RMS values of u_{P1} derived by $|\boldsymbol{Z_{in}}|\boldsymbol{I_{P1}}$; $\boldsymbol{I_{S1}}$ is the measured RMS values of i_{S1}; $\hat{\boldsymbol{U}}_{\boldsymbol{P1est}}$ is the estimated RMS values of u_{P1} derived by $|\boldsymbol{Z_{PS}}|\boldsymbol{I_{S1}}$; $\boldsymbol{U_{P1}}$ is the measured RMS values of u_{P1}; $||\boldsymbol{U_{P1}} - \boldsymbol{U_{P1est}}||$ represents the norm of the voltage differences between $\boldsymbol{U_{P1}}$ and $\boldsymbol{U_{P1est}}$; $||\boldsymbol{U_{P1}} - \hat{\boldsymbol{U}}_{\boldsymbol{P1est}}||$ is the norm of the voltage differences between $\boldsymbol{U_{P1}}$ and $\hat{\boldsymbol{U}}_{\boldsymbol{P1est}}$. It should be noted that when the DC input voltage U_{in} and the duty cycle of the inverter AC voltage u_{ab} remain unchanged, the RMS value of u_{P1} does not vary with the switching frequency. In this thesis, the DC input voltage is configured at 200 V, and the inverter output is fixed at the full-duty cycle. This means that the measurement process for the inverter voltage can be avoided. Based on the identification model, the unknown parameters $\{L_P, L_S, C_P, C_S, M\}$ are searched within the empirically selected lower and upper bounds.

4.4.2. DYNAMIC FREQUENCY APPROACHING

Based on the above analysis, it is essential to measure i_P and i_S at multiple frequency points for parameter identification.

However, according to the analysis in Chapter 4.2.3, when the parameters of the capacitors and coils deviate from the nominal values, the frequency variations near the nominal resonance point may lead to severe system detuning, resulting in enormous coil currents. To constrain the coil currents in a safe range, a dynamic frequency approaching strategy is proposed, as shown in Fig. 4.10. In Fig. 4.10, f_L (lower frequency bound of the frequency sweeping process), f_H (upper frequency bound of the frequency sweeping process), I_M (threshold RMS value of the coil currents), as well as the update equations (4.15) and (4.16), are pre-designed based on the system parameters and stored in the microcontrollers in advance. Conversely, the values of I_{P1} and I_{S1} are updated based on the measured results in practical operation. The detailed steps of this strategy are as follows. First, the frequency is swept from the lower bound f_L at various frequency points while I_{P1} and I_{S1} are measured. The frequency-sweeping process is stopped when I_{P1} or I_{S1} exceeds the threshold value I_M. Then, the frequency is swept from the upper bound f_H and is terminated when I_{P1} or I_{S1} is larger than I_M again.

In the proposed method, the current threshold I_M is set as 10 A based on the current capability of the system, while f_L and f_H are set to 65 kHz and 125 kHz. The basic principle of selecting f_L and f_H is to ensure that I_{P1} and I_{S1} at both f_L and f_H are lower than 10 A under any case. Taking case-B as an example, the values of I_{P1} and I_{S1} when the rectifier output is short-circuited are shown in Fig. 4.11. As illustrated in Fig. 4.11(a), f_L is required to be lower than f_{A1} to ensure that the value of I_{P1} is smaller than 10 A at the

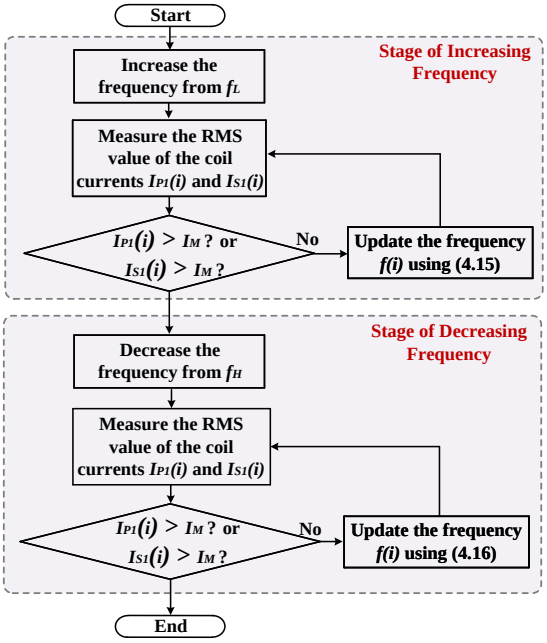

Figure 4.10: Flow chart of the proposed dynamic frequency approaching strategy. Here, f_L and f_H are the lower and upper bound of the frequency sweeping process.

frequency point f_L under any case, while f_H should be higher than f_{B1} to guarantee I_{P1} is always smaller than 10 A at f_H. Similarly, as shown in Fig. 4.11(b), f_L is also required to be less than f_{A2}, and f_H is needed to be greater than f_{B2} to ensure that the value of I_{S1} does not exceed the threshold. Furthermore, define f_{A_min} as the minimum value of f_{A1} and f_{A2}, f_{B_max} as the maximum value of f_{B1} and f_{B2}, the values of f_{A_min} and f_{B_max} under different values of k when the rectifier output is short-circuited is illustrated in Fig. 4.12. To guarantee the coil currents at f_L and f_H are lower than 10 A under any case, as shown in Fig. 4.12, f_L is required to be lower than 65.1 kHz, and f_H should be larger than 121.7 kHz. Therefore, f_L and f_H are set to 65 kHz and 125 kHz, respectively.

Moreover, the interval of the frequency points is not fixed but dynamically adjusted according to the measured current values. The motivations of the dynamic frequency interval are as follows. On the one hand, when the frequency approaches the peak current point, the coil currents rise dramatically. Taking $d_P = d_S = 0.2$ under case-B as an example, as shown in Fig. 4.11(a), I_{P1} is 9.2 A when the frequency is 69 kHz, whereas it rapidly increases to 15.7 A at 70 kHz. As a result, if the frequency interval is large under the high-current frequency points, the coil currents may greatly exceed the threshold, endangering the safe operation of the system. On the other hand, when the frequency is close to f_L and f_H, as illustrated in Fig. 4.11(a), the coil currents might be quite small under some cases, and the measurement errors should be considered in these cases. Therefore, if the frequency interval is small under the low-current frequency points, the measurement errors might be significant in some cases. Besides, a small frequency in-

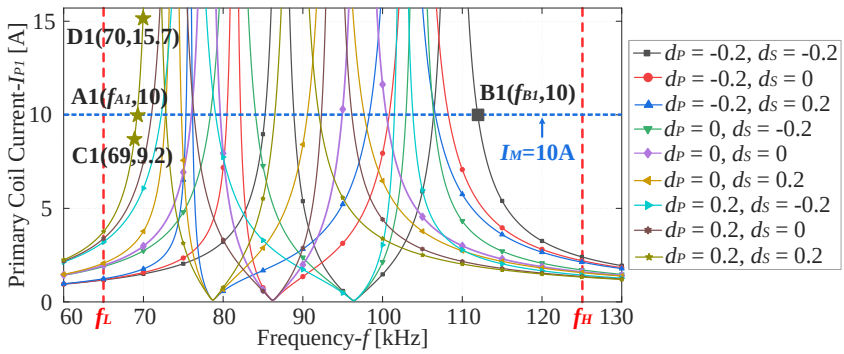

(a)

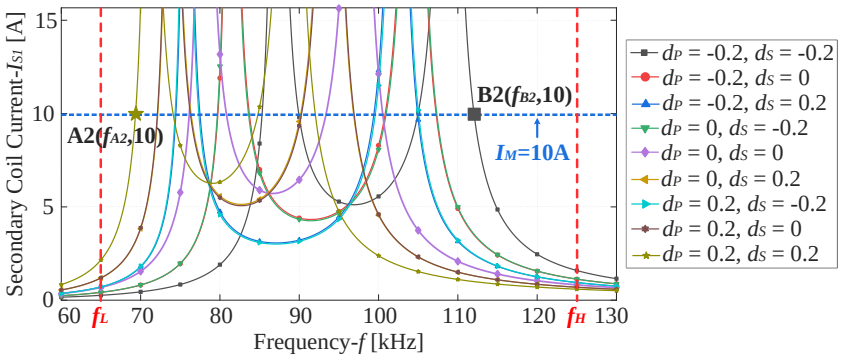

(b)

Figure 4.11: Values of I_{P1} and I_{S1} when the rectifier output is short-circuited under case-B: (a) I_{P1}, (b)I_{S1}. Here, f_{A1}, f_{A2}, f_{B1}, and f_{B2} represent the frequency values at points A1, A2, B1, and B2, respectively.

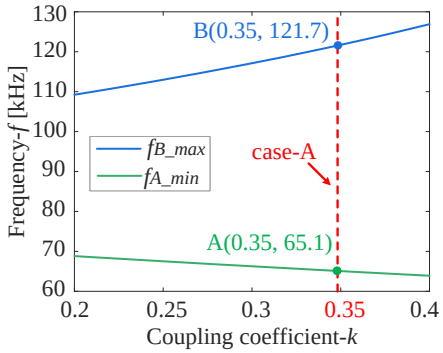

Figure 4.12: Values of f_{A_min} and f_{B_max} under different values of k when the rectifier output is short-circuited.

terval will also make the frequency-sweep process time-consuming. Considering the abovementioned reasons, a dynamic frequency interval is adopted in this thesis. When the frequency is increased from f_L, the update equation is

$$f(i+1) = f(i) + \tau \times ceil[I_M - \max(I_{P1}(i), I_{S1}(i))], \tag{4.15}$$

where $ceil$ is the round-up function; τ is a fixed factor, which is set to 0.2 to ensure that the coil current does not increase dramatically as it approaches the threshold I_M. Similarly, when the frequency is decreased from f_H, the updated equation is

$$f(i+1) = f(i) - \tau \times ceil[I_M - \max(I_{P1}(i), I_{S1}(i))]. \tag{4.16}$$

As shown in (4.15) and (4.16), the frequency interval is dynamically adjusted between 0.2 kHz and 2 kHz according to the RMS values of the coil currents. Based on the above analysis, by using the proposed dynamic frequency approaching strategy, the coil currents are constrained safely, and the required data for parameter identification is acquired efficiently.

4.4.3. THE JAYA ALGORITHM

After the required data is obtained, the optimization problem described in (14) needs to be solved to recognize the unknown parameters. In this thesis, a heuristic algorithm called JAYA is introduced to derive the unknown parameters. Generally, there are two mainstream approaches for solving unknown parameters in IPT systems: the least square approximation (LSA) and the heuristic algorithms. The LSA was implemented in [177] to recognize the mutual inductance and load resistance, while it was used for identifying multiple loads in [177] and the secondary-side reactance in [172]. The heuristic algorithms, which can find optimal solutions more efficiently than the traditional LSA for the multi-variable systems [176], are also usually used, such as the genetic algorithm (GA) in [179], and the adaptive differential evolution (ADE) algorithm in [176]. However, for the conventional GA algorithm and differential evolution (DE) algorithm, various algorithm-specific parameters, including the crossover and mutation rates, need to be tuned. Although the ADE algorithm avoids the difficulty of tuning parameters, the adaptive crossover and mutation rates need to be calculated in each iteration, which increases the complexity of the algorithm. Compared with the GA and ADE algorithms, the JAYA algorithm is free from algorithm-specific parameters (except for two common parameters, i.e., the population size P_{size} and the maximum number of generations Gen_{max}), and only one update equation is required in each generation [178].

The process of the JAYA algorithm is detailed as follows: **[Initialization]** First, a random population $\boldsymbol{x}$ with P_{size} individuals is generated in the search space (within the lower and upper bounds), where $\boldsymbol{x_{p,q}}$ represents the q-th parameter of the p-th individual ($p = 1,2,\cdots,P_{size}$; $q = 1,2,\cdots,N$), and N is the number of the unknown parameters. Specifically, in this thesis, $\boldsymbol{x}$ represents the population with P_{size} (P_{size}=50) individuals, and each individual consists of N (N=7) unknown parameters. The unknown parameters are R_P, R_S, L_P, L_S, C_P, C_S, and M, respectively. **[Fitness]** Then, the fitness value of each individual is calculated based on the cost function described in (14). **[Update]** According to the fitness value of each individual, the best individual

$\boldsymbol{x_{best}} = [x_{best,1}, x_{best,2}, \cdots, x_{best,N}]$ with minimum fitness value and the worst individual $\boldsymbol{x_{worst}} = [x_{worst,1}, x_{worst,2}, \cdots, x_{worst,N}]$ with maximum fitness value are selected, and the population is then updated by

$$x'_{p,q} = x_{p,q} + r_1(x_{best,q} - |x_{p,q}|) - r_2(x_{worst,q} - |x_{p,q}|), \tag{4.17}$$

where $x_{best,q}$ and $x_{worst,q}$ are the q-th parameter of the best and worst individuals, respectively; r_1 and r_2 are two random numbers within [0,1]. In (17), the term $r_1(x_{best,q} - |x_{p,q}|)$ reveals the tendency of approaching the best individual, while $-r_2(x_{worst,q} - |x_{p,q}|)$ indicates the tendency of escaping from the worst individual. **[Selection]** The updated individual $x'_{p,q}$ is accepted if it gives a better fitness value. All the accepted individuals at the end of iteration are retained and become the input of the next generation. **[Termination]** The optimization process is stopped when the termination criteria are satisfied. Here, the termination criteria are the number of iterations that reach Gen_{max}.

4.5. PARAMETER IDENTIFICATION BASED IMPEDANCE TUNING METHOD

Based on the recognized parameters, an impedance tuning method is adopted, as shown in Fig. 4.13. To minimize the primary reactance X_P, the switching frequency ω of the inverter is adjusted to

$$\omega = \frac{1}{\sqrt{L_P C_P}}. \tag{4.18}$$

Additionally, the duty cycle of the inverter AC voltage u_{ab} is maintained at the full duty cycle. Then, the equivalent load impedance Z_E is regulated by the active rectifier to min-

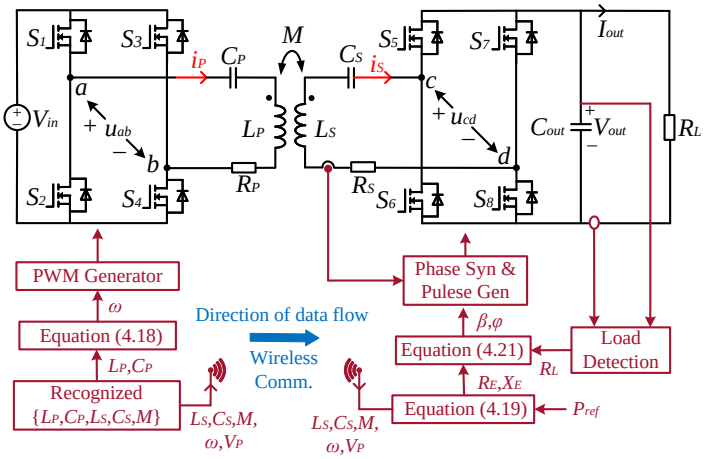

Figure 4.13: Block diagram of the impedance tuning method. Here, the parameters $\{L_S, C_S, M, \omega, U_P\}$ are transmitted from the primary controller to the secondary controller for calculating the required phase shift angles of the active rectifier.

imize the secondary reactance X_S and to obtain the required output power P_{ref}, i.e.,

$$\begin{cases} R_E = \dfrac{\omega^2 M^2 P_{ref}}{U_P^2} \\ X_E = -X_S = -[\omega L_S - 1/(\omega C_S)] \end{cases} \tag{4.19}$$

Herein, it should be noted that the secondary reactance can be slightly overcompensated to realize zero-voltage-switching (ZVS) for the inverter [172]. According to [172], the equivalent load impedance provided by the active rectifier is

$$\begin{cases} R_E = \dfrac{4}{\pi^2} R_L \cos^2(\varphi)(1-\cos(\beta)) \\ X_E = \dfrac{4}{\pi^2} R_L \sin(\varphi)\cos(\varphi)(1-\cos(\beta)) \end{cases} \tag{4.20}$$

where β is the duty-cycle angle of the rectifier input voltage u_{cd}, and φ is the phase shift angle between $\dot{U}_S$ and $\dot{I}_S$. Substituting (20) into (21), β and φ are derived by

$$\begin{cases} \varphi = \arctan(\dfrac{X_E}{R_E}) \\ \beta = \arccos(1 - \dfrac{\pi^2 X_E}{2R_L \sin(2\varphi)}) \end{cases} \tag{4.21}$$

Considering the range of β ($[0,\pi]$) and φ ($[-\pi/2,\pi/2]$), the maximum R_E and X_E that can be provided by the active rectifier are $8R_L/\pi^2$ and $\pm 4R_L/\pi^2$, respectively.

4.6. EXPERIMENTAL RESULTS

4.6.1. EXPERIMENTAL SETUP

To verify the feasibility of the proposed parameter identification based impedance tuning method, experiments are carried out on an SS-compensated IPT prototype using the

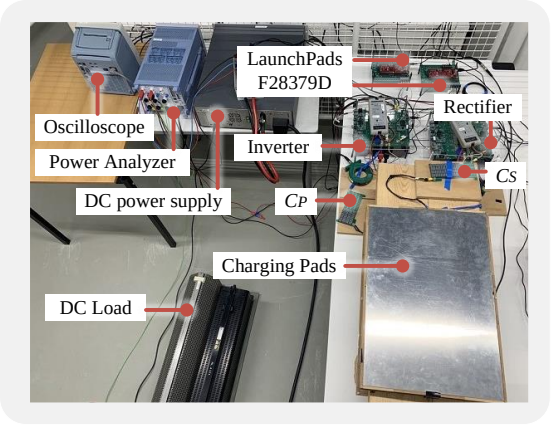

Figure 4.14: Experimental setup of the SS-compensated IPT system used to verify the proposed parameter recognition based impedance tuning method [3, 4].

charging pads in Fig. 4.3, as shown in Fig. 4.14. In this prototype, a DC power supply is utilized to provide the required power, and two rheostats are connected in series as the load resistor. The impedance tuning algorithm and PWM generation are implemented in the LaunchPads F28379D. Two separate H-bridge converters are adopted as the inverter and the active rectifier, respectively. The experimental data and waveforms are recorded by an oscilloscope (YOKOGAWA DLM2054), and the DC to DC efficiency of the system is measured by a power analyzer (YOKOGAWA WT500). More details of the prototype are listed in Table 4.1.

4.6.2. IMPLEMENTATION OF PARAMETER IDENTIFICATION

The accuracy of the proposed parameter identification method is verified in 10 cases of the parameter deviations, as listed in Table 4.2. Here, the parameters of the coil inductances and compensation capacitances are measured by an impedance analyzer (Agilent 4294A).

To acquire the required data for parameter identification, the rectifier output is short-circuited, and the system frequency f is regulated based on the dynamic frequency approaching strategy shown in Fig. 4.10. By dynamically adjusting the system frequency f, the primary and secondary coil currents i_P and i_S are measured at multiple frequency points. The measured data are recorded by the oscilloscope and then extracted to MATLAB for processing. Fig. 4.15 shows the recorded waveforms of case-A1 under different frequency points. It should be noted that when the frequency is increased from f_L (65 kHz), hard switching of the inverter power switches is inevitable due to the capacitive

Table 4.2: Case Study for Parameter identification

No.	L_P[μH]	L_S[μH]	M[μH]	C_P[nF]	C_S[nF]
A1	335.5	222.7	95	9.9	17.32
A2	335.5	222.7	95	11.53	16.5
A3	335.5	222.7	95	11.53	14.88
A4	335.5	222.7	95	9.9	13.21
A5	335.5	222.7	95	9.07	14.88
B1	327.5	216.5	58	9.9	17.32
B2	327.5	216.5	58	11.53	16.5
B3	327.5	216.5	58	11.53	14.88
B4	327.5	216.5	58	9.9	13.21
B5	327.5	216.5	58	9.07	14.88

Table 4.3: Parameters of the JAYA Algorithm

Symbol	Value	Symbol	Value	Symbol	Value	Symbol	Value
L_{PL}	300 μH	L_{PH}	350 μH	L_{SL}	200 μH	L_{SH}	250 μH
M_L	50 μH	M_H	120 μH	C_{PL}	5 nF	C_{PH}	15 nF
C_{SL}	10 nF	C_{SH}	20 nF	R_{PL}	0.5 Ω	R_{PH}	0.9 Ω
R_{SL}	0.3 Ω	R_{SH}	0.7 Ω	P_{size}	50	Gen_{max}	5000

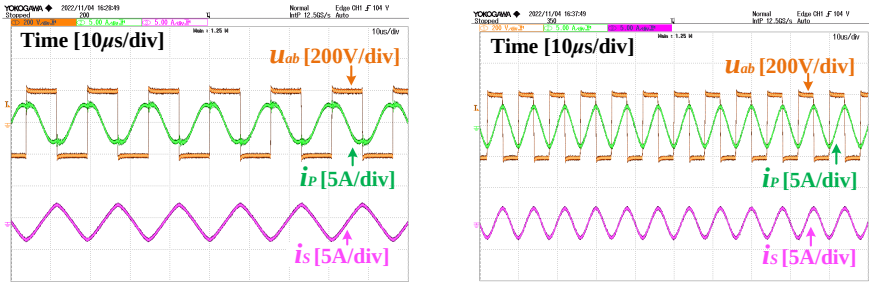

(a) (b)

Figure 4.15: Measured operating waveforms of case-A1 at different frequency points: (a) 65 kHz, (b) 125 kHz.

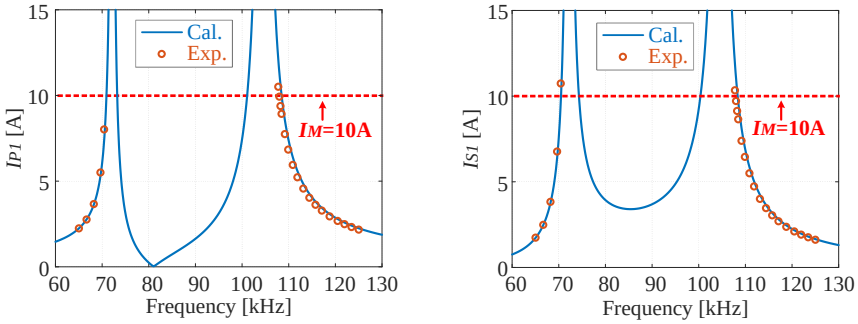

(a) (b)

Figure 4.16: Extracted RMS values of I_{P1} and I_{S1} in case-A1: (a) I_{P1}, (b) I_{S1}.

input impedance Z_{in}. However, since the data acquisition stage only lasts for hundreds of milliseconds (see Chapter 1.6.4), the extra switching loss caused by hard switching during this process can be ignored, and the voltage spikes at the switching transient can also be suppressed by optimizing the resistor-capacitor (RC) snubber circuits in practice [180, 181]. Another noteworthy point is that the extracted coil currents, as shown in Fig. 4.15(a), contain a small amount of 3-rd harmonics when the frequency is increased from f_L (65 kHz). Therefore, a digital second-order LPF is needed to filter out the harmonic components of the coil currents when the frequency is increased from f_L.

After the harmonics are filtered by the LPF, the RMS values of the fundamental components of the coil currents, i.e., I_{P1} and I_{S1}, are then extracted by the rms function of MATLAB. The extracted RMS values of I_{P1} and I_{S1} under case-A1 are illustrated in Fig. 4.16. As it can be observed, by implementing the proposed dynamic frequency approaching method, I_{P1} and I_{S1} are accurately obtained under sufficient frequency points.

Furthermore, based on the values of I_{P1} and I_{S1}, the JAYA algorithm is implemented to recognize the unknown parameters of the resonant circuits. The searching constraints

of the unknown parameters $\{L_P, L_S, M, C_P, C_S\}$ for the JAYA algorithm are listed in Table 4.3. Since the loss resistances R_P and R_S may vary with the system operating conditions, R_P and R_S are considered as the unknown parameters as well. Additionally, the population size P_{size} and the maximum generation numbers Gen_{max} of the JAYA algorithm are also shown in Table 4.3. The parameters are independently recognized by the JAYA algorithm ten times. The JAYA algorithm is implemented in MATLAB on a computer with an Intel(R) Core(TM) i7-1185G7 CPU.

Fig. 4.17 presents the recognized parameters for case-A1 in each identification. As shown in Fig. 4.17, the unknown parameters of case-A1 are recognized accurately, with

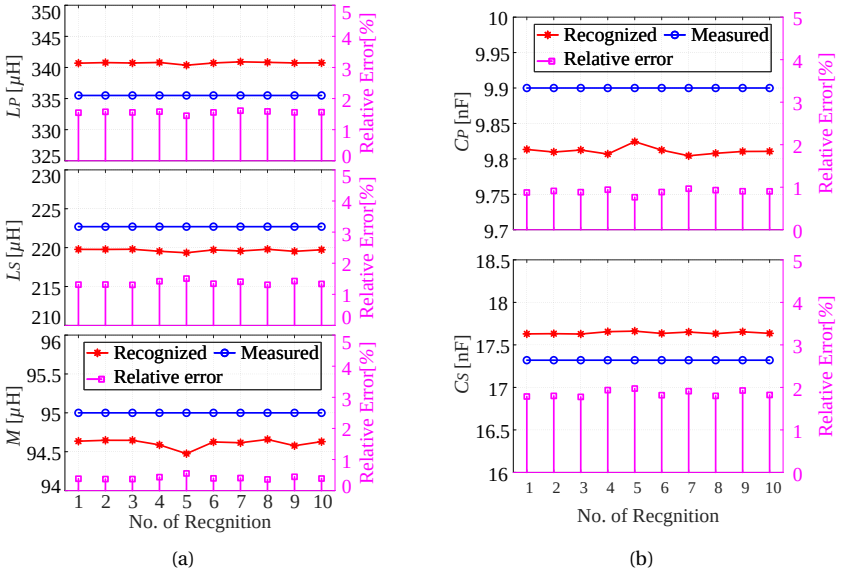

Figure 4.17: Recognized results for case-A1: (a) coil inductances L_P, L_S and M, (b) compensation capacitances C_P and C_S.

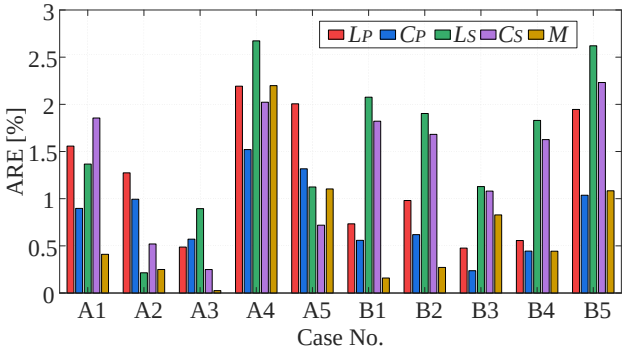

Figure 4.18: Average relative errors (AREs) for the studied 10 cases.

the relative errors in each identification all less than 2%. Besides, as it can be observed, the recognized results of each independent identification are basically consistent, which validates the stability of the JAYA algorithm.

Moreover, all of the 10 cases listed in Table 4.2 are studied. Specifically, the average relative errors (AREs) for the studied 10 cases are presented in Fig. 4.18. As it can be observed, the unknown parameters of the resonant circuits are recognized accurately, with the AREs of all cases less than 3%.

4.6.3. IMPLEMENTATION OF IMPEDANCE TUNING

After the unknown parameters are accurately recognized, the impedance tuning method is implemented to allow the system to operate close to the resonance state. To demonstrate the effectiveness of the impedance tuning method, experiments are carried out in two cases of parameter deviations, i.e., case-A5 and case-B5. For case-A5 and case-B5, the primary and secondary compensation capacitances are 9.07 nF and 14.88 nF, with the degree of capacitance drift at -13.21% and -5.46%, respectively. Besides, compared with case-A5, the air gap of case-B5 is increased from 10 cm to 15 cm, and thus, the coil coupling coefficient k is decreased from 0.35 to 0.22. Due to the abovementioned parameter deviations caused by coil misalignment and capacitance drift, both the primary and secondary resonant circuits are detuned.

Fig. 4.19 presents the measured operating waveforms of case-A5 when delivering 600 W power. Before the impedance tuning, as shown in Fig. 4.19(a), the system frequency is 85 kHz, and the secondary AC voltage u_{cd} and current i_S are in phase. Moreover, due to the system detuning, the primary current i_P leads the primary AC voltage u_{ab}. By implementing the impedance tuning method based on the recognized parameters, the operating frequency is increased to 91 kHz to minimize the primary-side reactance X_P, while the phase shift angle between u_{cd} and i_S, i.e., φ, is regulated to $-22.9°$ to minimize the secondary-side reactance X_S. After the impedance tuning, as illustrated in Fig. 4.19(b), the primary voltage u_{ab} and current i_P are almost in phase (i_P slightly

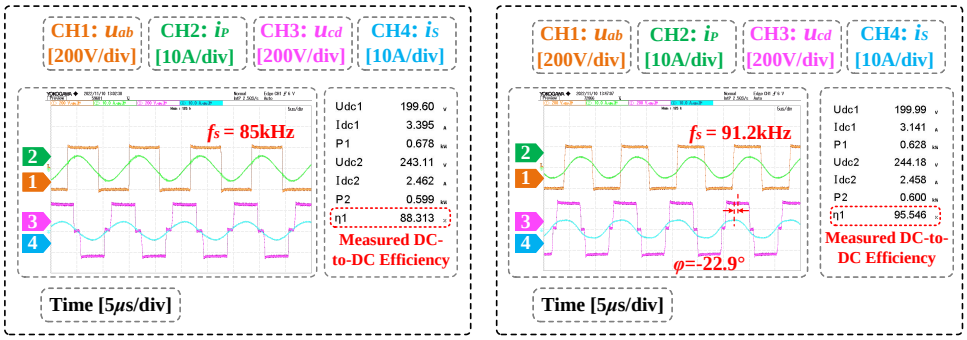

(a) (b)

Figure 4.19: Measured operating waveforms and DC to DC efficiency of case-A5 when delivering 600 W power: (a) operating waveforms and measured DC to DC efficiency before tuning, (b) operating waveforms and measured DC to DC efficiency after tuning.

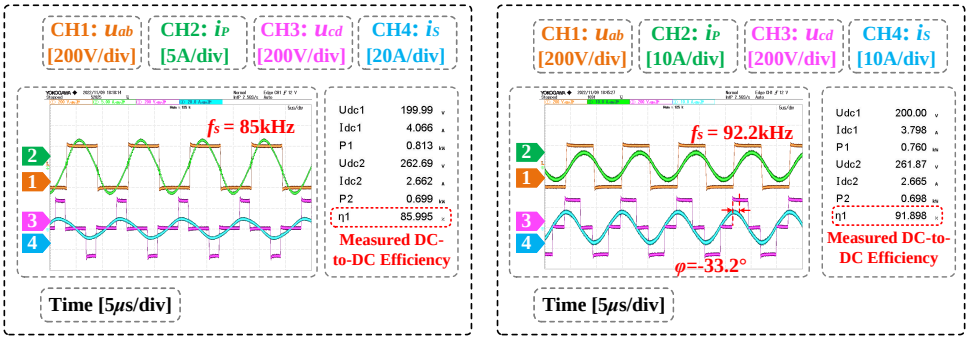

(a) (b)

Figure 4.20: Measured operating waveforms and DC to DC efficiency of case-B5 when delivering 700 W power: (a) operating waveforms and measured DC to DC efficiency before tuning, (b) operating waveforms and measured DC to DC efficiency after tuning.

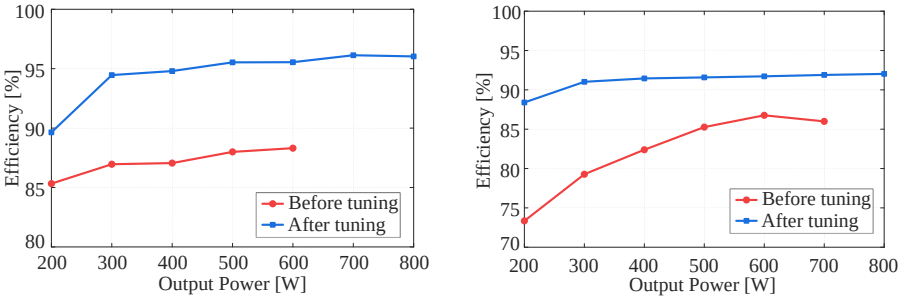

(a) (b)

Figure 4.21: Measured DC to DC efficiency of case-A5 and case-B5 under different power points: (a) case-A5, (b) case-B5.

lags behind u_{ab} to realize ZVS for the inverter). To illustrate the effectiveness of the impedance tuning, the measured DC to DC efficiency of case-A5 before and after tuning is also presented in Fig. 4.19. As it can be observed, when delivering 600 W in case-A5, the DC to DC efficiency of the IPT system is increased from 88.3% to 95.5%.

The measured operating waveforms and efficiency of case-B5 when delivering 700 W power are then demonstrated in Fig. 4.20. Based on the identified parameters and carrying out the impedance tuning, the system frequency is increased from 85 kHz to 92 kHz, and the phase shift angle φ is adjusted to $-33.2°$. The reactance on both sides is minimized simultaneously, and therefore, the DC to DC efficiency of the system is improved from 86% to 91.9%.

Furthermore, the measured DC to DC efficiency of case-A5 and case-B5 under different output power points is shown in Fig. 4.21. By implementing the impedance tuning method, the DC to DC efficiency is significantly improved. As shown in Fig. 4.21(a), the

efficiency is improved by 4.3%-7.7% after achieving impedance tuning in case-A5. More significant efficiency optimization can be observed under case-B5, as illustrated in Fig. 4.21(b). The efficiency improvement after tuning ranges from 5.9% to 15%.

4.6.4. CLOSE-LOOP VERIFICATION

To further verify the feasibility of the proposed method in practice, the closed-loop identification and tuning process is implemented in the TMS320F28379D microcontrollers. Two measurement boards and two signal processing boards are utilized to measure the primary and secondary coil currents, respectively, where the measurement boards are connected to the resonant circuits, and the signal processing boards are installed on top of the LaunchPads. Additionally, the NRF24L01+ modules are employed for the dual-side wireless communication [182].

Based on the above hardware configurations, the close-loop experiments are carried out under case-A5, where the experimental results are demonstrated in Fig. 4.22. As shown in Fig. 4.22(a), the complete implementation of the proposed method includes four different stages, where S1, S2, S3, and S4 represent the pre-start-up stage, the data acquisition stage, the JAYA algorithm execution stage, and the normal charging stage, respectively. After the system starts, it first enters the data acquisition stage, where the rectifier output is short-circuited, and the inverter frequency is adjusted based on the proposed dynamic frequency approaching strategy. During this stage, as shown in Fig. 4.22(b), the inverter frequency f is firstly increased from f_L, and then it is decreased from f_H after the coil currents exceed the threshold I_M. The data acquisition stage stops when the coil currents exceed the threshold again. In the experiments, 20 different frequency points are extracted with the time for each frequency point configured at 20 ms, and therefore, the total time for the whole data acquisition stage is 400 ms. After the data acquisition, the JAYA algorithm is implemented to solve the unknown parameters, which takes around 3.2 s in the experiments.

In the closed-loop tests, the maximum average relative error (ARE) of the recognized

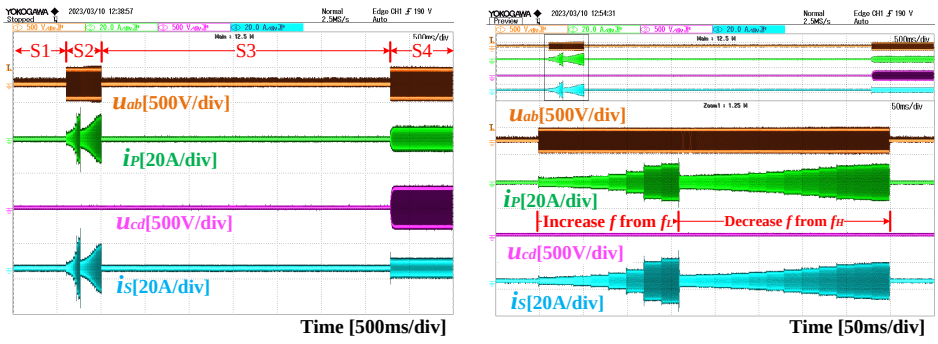

(a) (b)

Figure 4.22: Experimental results of the close-loop experiments under case-A5: (a) complete implementation of the proposed method, (b) enlarged view of the data acquisition stage.

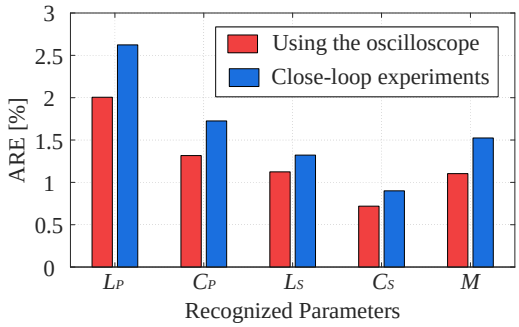

Figure 4.23: Comparisons on the recognized results in the close-loop experiments and those using the oscilloscope. Here, ARE indicates the average relative error.

results for case-A5 is 2.6%, which is slightly larger than that of using the oscilloscope. The identification results in the closed-loop experiments are compared with those using the oscilloscope in Fig. 4.23. The discrepancy in estimated results is attributed to the difference in measurement errors. In the close loop experiments, the current transducer (LAH 50-P) is adopted to measure the coil currents, with the frequency bandwidth at 200 kHz, and the sampling rate of the DSP is configured at 1 MHz. Compared with the 50 MHz bandwidth of the current probe (KEYSIGHT N2782B) and the 12.5 GHz sampling rate of the oscilloscope, the measurement errors in the close-loop experiments are increased due to the limited bandwidth of the adopted measurement system. Consequently, the identification errors in the close-loop experiments are slightly larger than that of using the oscilloscope. In practice, the current sensor with high bandwidth and the analog-to-digital converter (ADC) with a high sampling rate can be employed to further minimize measurement errors, thereby achieving higher identification accuracy. Finally, based on the recognized parameters, the system frequency, as well as the phase shift angles of the rectifier, are regulated to realize the impedance tuning, and the system enters the normal charging stage.

4.7. CONCLUSIONS

In this chapter, a parameter identification based impedance tuning method is proposed for the SS-compensated IPT systems. The proposed parameter identification method is implemented at pre-start-up, with the rectifier output short-circuited during this process. Therefore, the proposed method is more suitable for stationary applications, whereas it is not desirable to be used in dynamic wireless charging cases. Compared with the existing methods, the proposed parameter identification method avoids severe system detuning and significant load power ripple and is able to accurately identify all of the unknown parameters of the resonant circuits. The accuracy of the parameter identification is experimentally validated in 10 cases of parameter deviations, with the relative average errors of the recognized results all less than 3%.

Thanks to the pre-start-up parameter identification, the parameter deviations caused by coil misalignment and capacitance drift on both the primary and secondary sides can

be addressed without adding any extra switches and circuits, which is the main contribution of this proposal. Based on the recognized parameters, an impedance tuning method is carried out to cope with the impedance mismatch caused by parameter deviations. By regulating the system frequency and the phase shift angles of the active rectifier, the reactance on both sides is minimized, and therefore, the DC to DC efficiency of the IPT prototype is enhanced by 4.3% to 15% in the experiments. Closed-loop verification is also implemented to further verify the feasibility of the proposed method in practice, with the time consumption for the whole parameter identification process at around 3.6 s in the experiments.

PART III

VARIABLE DLCC COMPENSATION

5

OPTIMAL MULTIVARIABLE CONTROL FOR ASYMMETRIC SYSTEM CONFIGURATIONS

This chapter presents an optimal multivariable control (OMC) strategy for the inductive power transfer (IPT) systems with asymmetric double-sided LCC (DLCC) compensation network. To mitigate reactive power and achieve higher efficiency, the proposed OMC method incorporates dual-side hybrid modulation and primary-side switch-controlled-capacitor (SCC) tuning into the triple-phase-shift (TPS) control. Firstly, the impact of hybrid modulation and SCC tuning on the system characteristics is investigated. The inverter and rectifier zero-voltage-switching (ZVS) conditions are then analyzed to achieve dual-side ZVS with minimal reactive power. Furthermore, a multivariable optimization problem is established based on the power loss analysis. The solution to this problem provides optimal control variables that minimize the overall system loss. Through collaborative modulation and control of the inverter, rectifier, and SCC, the proposed method reduces the RMS values of the currents and lowers the turn-OFF currents for the converters. As a result, this approach improves efficiency in both light- and heavy-load conditions, enabling wide output regulation and full-range efficiency optimization simultaneously. Finally, the proposed method is benchmarked with the existing TPS method. Experimental results demonstrate that the proposed method achieves higher DC-to-DC efficiency in the power range of 0.2-2.2 kW, with a maximum efficiency improvement of up to 6.3%.

This chapter is based on:

- G. Zhu, J. Dong, G. Yu, W. Shi, C. Riekerk, and P. Bauer, "Optimal multivariable control for wide output regulation and full-range efficiency optimization in lcc-lcc compensated wireless power transfer systems," *IEEE Transactions on Power Electronics*, vol. 39, no. 9, pp. 11834-11848, Sep. 2024.

5.1. INTRODUCTION

To enhance the interoperability of the wireless EV charger, it is preferable for the IPT systems to accommodate different EV models available in the market. The variety of EV models results in distinct receiver configurations, leading to asymmetry in primary and secondary parameters. In order to achieve maximum efficiency tracking (also known as optimal load tracking) under the asymmetric system configurations, the control variables on the primary and secondary sides should be adjusted inconsistently [151]. This poses challenges in achieving dual-side ZVS for both the primary side inverter and the secondary side rectifier. Although considerable reactive power can be injected into resonant circuits for dual-side ZVS implementation, this approach reduces transmission efficiency under load variations [134].

5.1.1. SCOPE AND CONTRIBUTIONS

To fill up the abovementioned technical challenge, this chapter presents an optimal multivariable control (OMC) strategy based on the DLCC compensation network.

There are two important advantages of using DLCC topology for wireless EV charging. Firstly, the DLCC topology provides constant primary and secondary coil currents regardless of coil misalignment [183]. While in the SS topology, significantly increased coil currents can be observed when the mutual inductance is low, leading to a risk of damage to the entire system. Secondly, as described in [183], the DLCC topology offers more design flexibility for the system, where the additional inductances L_{f1} and L_{f2} can work as extra parameters to adjust the output power of the system.

Moreover, the main contributions of this chapter are summarized as follows:

1) The problems of existing triple-phase-shift (TPS) control methods under asymmetric system configurations are identified.

2) A multivariable control method featuring six control variables is proposed. By introducing dual-side hybrid modulation and a primary-side SCC, the proposed method achieves significantly reduced reactive power when compared with the existing TPS control approach.

3) ZVS conditions under hybrid modulation and SCC tuning are investigated for the asymmetric DLCC topology, and the corresponding control variables are derived to implement dual-side optimal ZVS.

4) A multivariable optimization problem is formulated based on the power loss analysis. By solving this problem, optimal control variables are obtained to minimize the overall loss of the system.

5) Through cooperative modulation and control of the inverter, rectifier, and SCC, wide output power regulation is achieved without introducing extra DC-DC converters. More importantly, the proposed method improves efficiency in both light- and heavy-load conditions, thus enabling full-range efficiency optimization for the system.

5.1.2. OUTLINE

The remainder of this chapter is organized as follows. Chapter 5.2 presents the fundamental operating principles of the DLCC-compensated IPT systems and demonstrates the limitations of the existing control methods. Subsequently, Chapter 5.3 elaborates on the design principles and control framework of the proposed OMC method. Experimen-

tal results are further presented in Chapter 5.4. Finally, Chapter 5.5 demonstrates the conclusions.

5.2. DLCC COMPENSATED IPT SYSTEMS

5.2.1. SYSTEM CONFIGURATIONS

Fig. 5.1 presents the circuit topology of the DLCC-compensated IPT system. In this system, an active rectifier is adopted on the secondary side to replace the passive diode rectifier. The DC input voltage is represented by V_{in}, while the battery voltage is denoted by V_{out}. Moreover, the mutual inductance of the contactless coupler is expressed as $M = k\sqrt{L_1 L_2}$, where k is the coupling coefficient; L_1 and L_2 are the primary and secondary self-inductances, respectively.

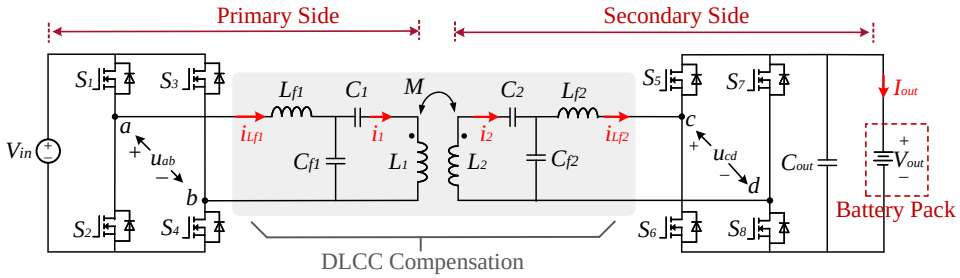

Figure 5.1: Circuit topology of the DLCC compensated IPT system.

To compensate the leakage inductances of the loose coupler, parameters of the DLCC topology are designed as $\omega_R L_{f1} = 1/(\omega_R C_{f1})$, $\omega_R L_{f1} = \omega_R L_1 - 1/(\omega_R C_1)$, $\omega_R L_{f2} = 1/(\omega_R C_{f2})$, $\omega_R L_{f2} = \omega_R L_2 - 1/(\omega_R C_2)$, where ω_R is the resonant frequency [183].

5.2.2. OUTPUT POWER REGULATION

Fig. 5.2 demonstrates the typical operating waveforms of the existing TPS modulation. Here, u_{ab} and u_{cd} are the inverter output voltage and rectifier input voltage; u_P and u_S are the fundamental component of u_{ab} and u_{cd}; D_P and D_S are the duty cycles of u_{ab} and u_{cd}; δ is the phase difference between u_{ab} and u_{cd}. According to the fundamental

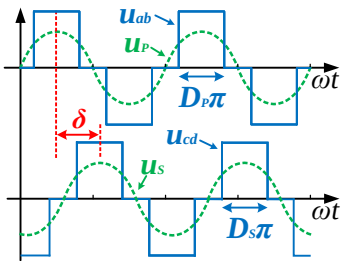

Figure 5.2: Typical operating waveforms of the existing TPS modulation for DLCC compensated IPT systems.

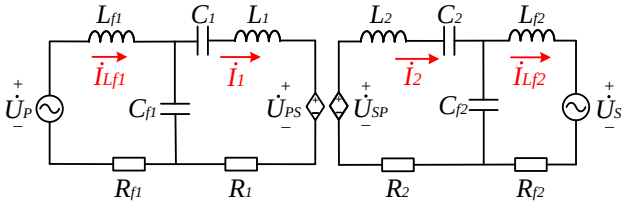

Figure 5.3: Equivalent circuit model of the DLCC compensated system.

harmonic analysis (FHA) method, the equivalent circuit model of the system is derived in Fig. 5.3. In the TPS modulation, the phasor forms of u_P and u_S, denoted as $\dot{U}_P$ and $\dot{U}_S$, are given as

$$\dot{U}_P = \frac{2\sqrt{2}}{\pi} V_{in} \sin(\frac{D_P \pi}{2}) \angle 0, \dot{U}_S = \frac{2\sqrt{2}}{\pi} V_{out} \sin(\frac{D_S \pi}{2}) \angle -\delta. \tag{5.1}$$

Moreover, the induced voltages $\dot{U}_{PS}$ and $\dot{U}_{SP}$ are given by

$$\dot{U}_{PS} = -j\omega M \dot{I}_2, \dot{U}_{SP} = j\omega M \dot{I}_1. \tag{5.2}$$

Assuming that the system parameters are symmetrical and applying Kirchhoff's voltage law (KVL), the output power and circulating reactive power of the system are derived as

$$P_{out} = \mathrm{Re}\{\dot{U}_S \dot{I}_{Lf2}^*\} = \frac{r_L k}{X} |\dot{U}_P||\dot{U}_S| \sin(\delta), \tag{5.3}$$

$$Q_{cir} = \mathrm{Im}\{\dot{U}_S \dot{I}_{Lf2}^*\} = -j\frac{r_L k}{X} |\dot{U}_P||\dot{U}_S| \cos(\delta), \tag{5.4}$$

where $r_L = L_1/L_{f1} = L_2/L_{f2}$; $X = \omega L_1 = \omega L_2$ represents the characteristic reactance of the symmetric resonant circuits. As evident from (5.3) and (5.4), the maximum output power of the system is obtained when δ is $\pi/2$ or $-\pi/2$, where the reactive power of the system is minimized simultaneously.

5.2.3. MAXIMUM EFFICIENCY TRACKING

According to the analysis in [151], when applying the TPS modulation to the symmetrical DLCC topology, the efficiency of the resonant tank is derived as

$$\eta_{res} \approx \frac{r_L k X |\sin(\delta)|}{r_L k X |\sin(\delta)| + a G_{AC} + a/G_{AC}}, \tag{5.5}$$

where $a = r_L^2 k^2 R_{Lf} + R$; $R_{Lf} = R_{Lf1} = R_{Lf2}$ represents the equivalent inductance resistance; $R = R_1 = R_2$ denotes the equivalent coil resistance; $G_{AC} = |\dot{U}_S|/|\dot{U}_P|$ indicates the AC voltage gain of the resonant tank. Observing (5.5) reveals that the maximum efficiency is obtained when $G_{AC} = 1$. Substituting (5.1) into the expression of $G_{AC} = 1$ yields

$$\frac{\sin(D_S \pi/2)}{\sin(D_P \pi/2)} = \frac{V_{in}}{V_{out}}. \tag{5.6}$$

By simultaneously adjusting the duty cycles of the inverter and rectifier according to (5.6), the maximum efficiency tracking of the resonant tank can be achieved.

5.2.4. ZVS IMPLEMENTATION

Moreover, based on [151], the inverter and rectifier ZVS is achieved by tuning the phase difference angle δ in the TPS method. The value of δ can be expressed as $\delta = \pi/2 + \Delta\delta$, where $\Delta\delta$ is the compensation phase angle. As $\Delta\delta$ increases, the deviation between δ and $\pi/2$ increases as well, resulting in a larger reactive power in the resonant tank while facilitating ZVS. Specifically, to realize the inverter ZVS with minimal reactive power, $\Delta\delta$ should be designed as

$$\Delta\delta_1 = \cos^{-1}[\frac{-2\pi X I_{ZVS} + V_{in}(D_P\pi^2 - 8\sin^2(D_P\pi/2))}{8r_L k V_{out}\sin(D_S\pi/2)}] - \frac{D_P\pi}{2}, \tag{5.7}$$

where I_{ZVS} is the threshold ZVS current to charge/discharge the equivalent output capacitance C_{oss} of the power switches within the dead time; $r_L = L_1/L_{f1} = L_2/L_{f2}$; $X = \omega L_1 = \omega L_2$. Similarly, the rectifier ZVS with minimal reactive power can be achieved by designing $\Delta\delta$ as

$$\Delta\delta_2 = \cos^{-1}[\frac{-2\pi X I_{ZVS} + V_{out}(D_S\pi^2 - 8\sin^2(D_S\pi/2))}{8r_L k V_{in}\sin(D_P\pi/2)}] - \frac{D_S\pi}{2}. \tag{5.8}$$

Consequently, to implement ZVS for both the inverter and rectifier in the TPS method, $\Delta\delta$ is configured as

$$\Delta\delta = \max(\Delta\delta_1, \Delta\delta_2). \tag{5.9}$$

5.2.5. EXISTING PROBLEMS UNDER ASYMMETRIC SYSTEM CONFIGURATIONS

Although the existing TPS method is able to achieve maximum efficiency tracking and wide ZVS, it does encounter significant limitations when dealing with non-unity DC voltage gain and asymmetric DLCC networks. The specific limitations of the existing TPS methods are elaborated as follows.

Considering the voltage specifications of the system input and output, it is common practice for the IPT systems to be designed to accommodate non-unity DC voltage gain. Additionally, the diversity of EV models results in distinct receiver coil configurations, leading to asymmetry in the primary and secondary parameters. Therefore, it is preferable to further extend the existing analysis to the asymmetric DLCC networks. In this

Table 5.1: Parameters of the investigated IPT system used to verify the proposed OMC method

Symbol	Parameters	Value	Unit
M	Mutual inductance	94.6	μH
L_1, L_2	Primary and secondary coil inductances	335.6, 224.2	μH
C_1, C_2	Primary and secondary series capacitances	14.8, 25.3	nF
C_{f1}, C_{f2}	Primary and secondary shunt capacitances	33.1, 41.3	nF
L_{f1}, L_{f2}	Primary and secondary compensation inductances	103.8, 83.8	μH
R_1, R_2	Primary and secondary coil resistances	0.45, 0.30	Ω
R_{Lf1}, R_{Lf2}	Primary and secondary inductor resistances	0.20, 0.14	Ω
V_{in}, V_{out}	DC input and output voltage	300, 500	V
f	Switching frequency	85	kHz

chapter, both the non-unity DC voltage gain and the asymmetric network design are considered. The detailed parameters of the investigated IPT system are demonstrated in Table 5.1.

When the asymmetric coil structure is considered, a more general mathematical analysis is essential. Based on the fundamental harmonic analysis (FHA) method and applying KVL, optimal ZVS criteria shown in (5.7) and (5.8) are re-derived as

$$\begin{aligned}\Delta\delta_1 = \quad & \cos^{-1}\{\frac{1}{8MV_{out}\sin(D_S\pi/2)} \times [-2\pi\omega L_{f1}L_{f2}I_{ZVS} \\ & +V_{in}L_{f2}\big(D_P\pi^2-8\sin^2(D_P\pi/2)\big)]\} - D_P\pi/2,\end{aligned} \tag{5.10}$$

$$\begin{aligned}\Delta\delta_2 = \quad & \cos^{-1}\{\frac{1}{8MV_{in}\sin(D_P\pi/2)} \times [-2\pi\omega L_{f1}L_{f2}I_{ZVS} \\ & +V_{out}L_{f1}\big(D_S\pi^2-8\sin^2(D_S\pi/2)\big)]\} - D_S\pi/2.\end{aligned} \tag{5.11}$$

Besides, the efficiency of the resonant tank is re-derived as

$$\begin{aligned}\eta_{res} \approx \quad & \omega ML_{f1}L_{f2}|\sin(\delta)| \times [(R_2L_{f1}^2+M^2R_{Lf1})G_{AC} \\ & +(R_1L_{f2}^2+M^2R_{Lf2})/G_{AC}+\omega ML_{f1}L_{f2}|\sin(\delta)|]^{-1},\end{aligned} \tag{5.12}$$

where $G_{AC} = |\dot{U}_S|/|\dot{U}_P|$ indicates the AC voltage gain of the resonant tank. Here, the derivation of (5.12) follows the analysis in [151] and extends it to the asymmetric networks. According to [151], assumptions are made as follows: a) the converter losses are neglected; b) the power losses of the resonant circuits are modeled with R_1, R_2, R_{Lf1}, and R_{Lf2}, where R_1 and R_2 are the equivalent loss resistances of coil branches, while R_{Lf1} and R_{Lf2} are the equivalent loss resistances of inductor branches; c) the power losses caused by harmonics are neglected, and the FHA method is adopted for loss analysis. As evident from (5.12), the maximum efficiency of the resonant tank is achieved when G_{AC} satisfy

$$G_{AC\_opt} = \sqrt{\frac{bR_1+cR_{Lf2}}{R_2/b+cR_{Lf1}}}, \tag{5.13}$$

where $b = L_{f2}/L_{f1}$, $c = M^2/(L_{f1}L_{f2})$. Further substituting (1) into (9) yields

$$\frac{\sin(D_S\pi/2)}{\sin(D_P\pi/2)} = \frac{V_{in}}{V_{out}}\sqrt{\frac{bR_1+cR_{Lf2}}{R_2/b+cR_{Lf1}}}. \tag{5.14}$$

Due to the asymmetric parameters between the primary and secondary sides, as shown in (5.13), the maximum efficiency of the resonant tank is no longer achieved when $G_{AC} = 1$. Conversely, in the presence of non-unity DC voltage gain and asymmetric network design, the duty cycles D_P and D_S need to be adjusted in an inconsistent manner to realize maximum efficiency tracking, as illustrated in (5.14). To visualize this point of view, the values of D_P and D_S as functions of the output power are depicted in Fig. 5.4(a). As shown in Fig. 5.4(a), there is a considerable disparity between the values of D_P and D_S as the output power varies. Moreover, the asymmetric parameters also result in a distinct difference in the compensation angles $\Delta\delta_1$ and $\Delta\delta_2$, as illustrated in Fig. 5.4(b).

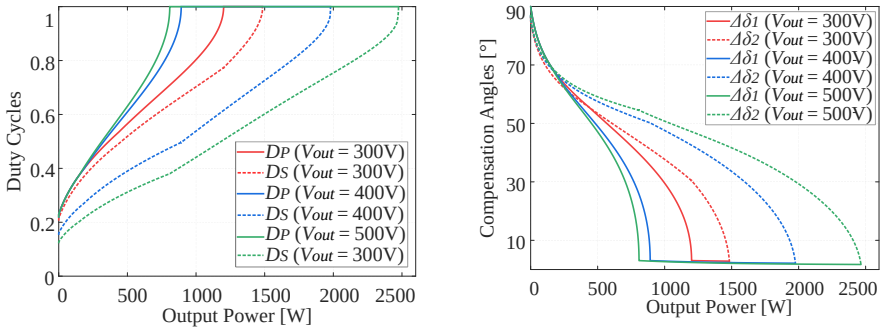

(a) (b)

Figure 5.4: Variations of (a) the duty cycles D_P and D_S, as well as (b) the compensation angle $\Delta\delta$ under various output voltages and power levels. Here, the DC input voltage (V_{in}) is configured as 300 V.

Observing Fig. 5.4 indicates that the existing TPS method exhibits the following two limitations:

(1) As the output power decreases, the duty cycles D_P and D_S are reduced accordingly. Consequently, a significantly increased compensation angle $\Delta\delta$ is required for ZVS, leading to considerable reactive power under light-load conditions.

(2) The compensation angle $\Delta\delta$ is selected as the maximum value of $\Delta\delta_1$ and $\Delta\delta_2$ to guarantee ZVS for both the inverter and rectifier. However, in the cases of asymmetric parameters, significant disparity is observed in $\Delta\delta_1$ and $\Delta\delta_2$. Notably, as the output voltage deviates from the unity value, this difference becomes more pronounced. The substantial gap between $\Delta\delta_1$ and $\Delta\delta_2$ makes it unfeasible to achieve dual-side ZVS with minimal reactive power on both the primary and secondary sides. For instance, considering the scenario of $V_{out} = 500$ V, as depicted by the green curves in Fig. 5.4(b), although the inverter ZVS can be achieved with $\Delta\delta_1$, $\Delta\delta$ has to be selected as $\Delta\delta_2$ ($\Delta\delta_2$ is significantly larger than $\Delta\delta_1$ in most power ranges when $V_{out} = 500$ V) to ensure the rectifier ZVS, leading to a substantial excess of reactive power on the primary side.

5.3. PROPOSED OPTIMAL MULTIVARIABLE CONTROL

In the proposed optimal multivariable control, the abovementioned challenges are addressed from two perspectives. Firstly, the hybrid modes of the converters, including the full-bridge (FB) and half-bridge (HB) modes, are considered to reduce the reactive power under light-load conditions. Here, the inverter operating mode is denoted as K_P, while the rectifier mode is indicated by K_S. Secondly, a primary-side SCC is introduced to facilitate the ZVS control, thus minimizing reactive power on both the primary and secondary sides. The SCC conduction angle is denoted as θ. The introduction of K_P, K_S, and θ into the TPS method forms a multivariable control featuring six degrees of freedom. The objectives of each control variable are demonstrated in Table 5.2, while implementation details of the proposed method are elaborated as follows.

Table 5.2: Control objectives of the proposed OMC method

Variable	Description	Control Objective
D_P	Inverter duty cycle	Maximum efficiency tracking
D_S	Rectifier duty cycle	Wide power regulation
$\Delta\delta$	Compensation phase angle	ZVS for the rectifier
θ	SCC conduction angle	ZVS for the inverter
K_P	Inverter operating mode	Reducing reactive power
K_S	Rectifier operating mode	under light-load conditions

5.3.1. INTRODUCTION OF PRIMARY SCC TUNING

To minimize reactive power, a primary-side SCC is implemented to replace the compensation capacitor C_1, as shown in Fig. 5.5. Within the adopted SCC, the capacitor C_x is connected in parallel with two reverse-connected power switches (S_a and S_b), while C_y is employed to reduce the voltage stress across C_x.

Moreover, Fig. 5.6 demonstrates typical operating waveforms of the adopted SCC. By regulating the conduction angle θ, the equivalent capacitance of the SCC can be adjusted. According to the analysis in [5], the SCC equivalent capacitance is given by

$$C_{1\_eq} = \frac{\pi C_x C_y}{\pi C_x + \pi C_y - \theta C_y - \sin(\theta) C_y}. \tag{5.15}$$

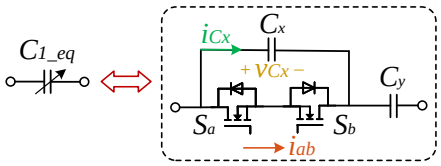

Figure 5.5: Circuit topology of the adopted SCC.

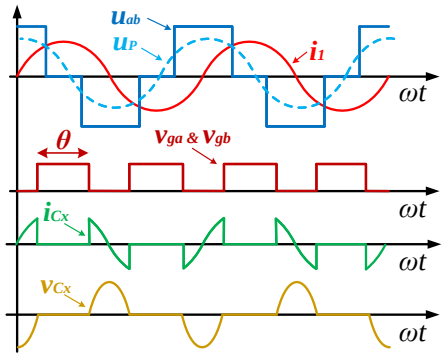

Figure 5.6: Typical operating waveforms of the adopted SCC.

To investigate the impact of SCC tuning, the capacitor tuning factor ε is introduced and defined as

$$\varepsilon = \frac{\omega L_1 - 1/(\omega C_{1\_eq})}{X_1}, \tag{5.16}$$

where $X_1 = \omega L_{f1}$ is the primary characteristic reactance. As evident from (5.15), by regulating the SCC equivalent capacitance, the capacitor tuning factor ε is adjusted accordingly. For ease of analysis, ε will be utilized to indicate the SCC tuning degree in the remainder of this chapter. With the definition of ε and ignoring the loss resistances, the equivalent FHA model of the SCC-based system is simplified in Fig. 5.7(a), while the corresponding phase diagram of voltages and currents is illustrated in Fig. 5.7(b). In this model, $X_2 = \omega L_{f2}$ indicates the secondary characteristic reactance. Moreover, by applying Kirchoff's Voltage Law (KVL) to this model, the influence of SCC tuning on the system characteristics is analyzed.

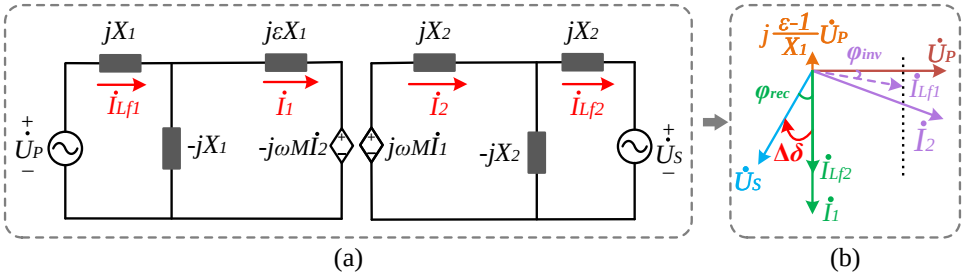

Figure 5.7: (a) Simplified FHA model and (b) phase diagrams of voltages and currents for the SCC-based IPT system.

(1) Coil Currents: Based on the FHA method, the expressions for the coil currents $\dot{I}_1$ and $\dot{I}_2$ are derived as

$$\dot{I}_1 = -j\frac{\dot{U}_P}{X_1}, \dot{I}_2 = j\frac{\dot{U}_S}{X_2}. \tag{5.17}$$

Observing (5.17) reveals that the coil currents $\dot{I}_1$ and $\dot{I}_2$ are only determined by the AC voltages $\dot{U}_P$ and $\dot{U}_S$, remaining unaffected by the SCC tuning.

(2) Inductor Currents: Additionally, the expressions of the inductor currents $\dot{I}_{Lf1}$ and $\dot{I}_{Lf2}$ are derived as

$$\dot{I}_{Lf2} = -j\frac{\omega M}{X_1 X_2}\dot{U}_P, \tag{5.18}$$

$$\dot{I}_{Lf1} = j\frac{\varepsilon - 1}{X_1}\dot{U}_P + j\frac{\omega M}{X_1 X_2}\dot{U}_S. \tag{5.19}$$

As illustrated in (5.18), the SCC tuning does not affect the secondary inductor current $\dot{I}_{Lf2}$. However, further observing (5.19) indicates that both the amplitudes and the phase angles of the primary inductor current $\dot{I}_{Lf1}$ can be adjusted by the SCC tuning. As shown in Fig. 5.7(b), by incorporating the SCC tuning, a new control variable ε is introduced to facilitate the inverter ZVS by dynamically regulating $\dot{I}_{Lf1}$. Furthermore, through simultaneously tuning the SCC and the compensation angle $\Delta\delta$, it is feasible to achieve the

inverter and rectifier ZVS with minimal reactive power on both the primary and secondary sides. Details of how to tune ε and $\Delta\delta$ for achieving dual-side optimal ZVS will be elaborated in Chapter 5.3.2.

(3) Output Power: To investigate the impact of SCC tuning on the power delivery, the output power expression of the SCC-based system is derived by

$$P_{out} = \mathrm{Re}\{\dot{U}_S \dot{I}^*_{Lf2}\} = \frac{M}{\omega L_{f1} L_{f2}} |\dot{U}_P||\dot{U}_S| \sin(\frac{\pi}{2} + \Delta\delta) \tag{5.20}$$

As shown in (5.20), the SCC tuning does not influence the system output power.

5.3.2. OPTIMAL ZVS CONTROL IN MULTIPLE-VARIABLE SCENARIOS

Although it is feasible to simultaneously regulate the SCC tuning factor ε and the compensation angle $\Delta\delta$ to achieve dual-side ZVS, the values of ε and $\Delta\delta$ need to be optimized for minimal reactive power. Moreover, as hybrid modulation is considered to improve efficiency under light loads, it is also essential to analyze ZVS conditions under hybrid modes. Therefore, a detailed description of how to optimize ε and $\Delta\delta$ under the hybrid modes is provided in this subchapter.

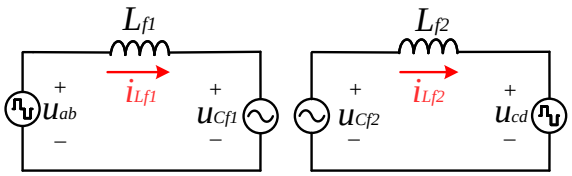

Figure 5.8: Harmonic-considered equivalent circuit model for ZVS analysis.

As the high-order harmonics in i_{Lf1} and i_{Lf2} are notable, it is important to establish a harmonic-considered model to calculate i_{Lf1} and i_{Lf2} for ZVS analysis. Due to the filtering effect of L_{f1}, C_{f1}, L_{f2}, and C_{f2}, the voltages across C_{f1} and C_{f2}, denoted as u_{Cf1} and u_{Cf2}, contain little high-order harmonics. Hence, the high-order harmonics in u_{Cf1} and u_{Cf2} can be ignored [151]. Furthermore, ignoring the loss resistances, the harmonic-considered equivalent circuit model for ZVS analysis is presented in Fig. 5.8. In this model, u_{Cf1} and u_{Cf2} are still approximated as sinusoidal waveforms, while the high-order harmonics in u_{ab} and u_{cd} are considered. Based on this model, ZVS analysis under the hybrid modes is presented as follows. In the following analysis, it is important to clarify that the FB-HB mode represents the inverter operating in FB mode while the rectifier works in HB mode.

(1) The FB-FB Mode: Typical operating waveforms of the FB-FB mode are shown in Fig. 5.9. For the FB-FB mode, the time-domain expressions of $u_{Cf1}(t)$ and $u_{Cf2}(t)$ are

$$u_{Cf1}(t) = \frac{4\varepsilon V_{in}}{\pi} \sin(\frac{D_P \pi}{2}) \sin(\omega t) - \frac{4MV_{out}}{\pi L_{f2}} \sin(\frac{D_S \pi}{2}) \cos(\omega t - \Delta\delta), \tag{5.21}$$

$$u_{Cf2}(t) = \frac{4MV_{in}}{\pi L_{f1}} \sin(\frac{D_P \pi}{2}) \sin(\omega t) - \frac{4V_{out}}{\pi} \sin(\frac{D_S \pi}{2}) \cos(\omega t - \Delta\delta). \tag{5.22}$$

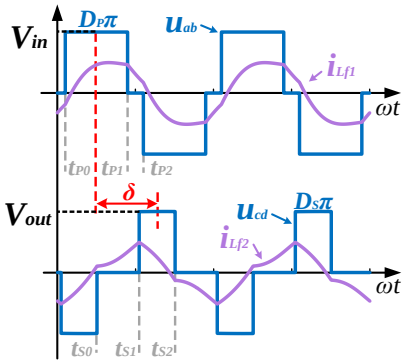

Figure 5.9: Typical operating waveforms of the FB-FB mode.

Moreover, applying KVL to the model shown in Fig. 5.8, the following differential equations are obtained as

$$u_{ab}(t)-u_{Cf1}(t)=L_{f1}\frac{di_{Lf1}(t)}{dt},u_{Cf2}(t)-u_{cd}(t)=L_{f2}\frac{di_{Lf2}(t)}{dt}. \tag{5.23}$$

By solving the above equations, expressions of $i_{Lf1}(t)$ and $i_{Lf2}(t)$ can be derived.

Taking $i_{Lf1}(t)$ as an example, observing Fig. 5.9 indicates that the inverter output voltage $u_{ab}(t)$ remains at V_{in} when $t_{P0}<t<t_{P1}$. Within this time period, the expression of $i_{Lf1}(t)$ is

$$i_{Lf1}(t)=i_{Lf1}(t_{P0})+\frac{1}{L_{f1}}\int_{t_{P0}}^{t}[V_{in}-u_{Cf1}(\tau)]d\tau. \tag{5.24}$$

When $t_{P1}<t<t_{P2}$, it is evident that $u_{ab}(t)=0$, and $i_{Lf1}(t)$ is expressed as

$$i_{Lf1}(t)=i_{Lf1}(t_{P1})+\frac{1}{L_{f1}}\int_{t_{P1}}^{t}[-u_{Cf1}(\tau)]d\tau. \tag{5.25}$$

Considering the symmetric characteristic of $i_{Lf1}(t)$, it is apparent that $i_{Lf1}(t_{P0})=-i_{Lf1}(t_{P2})$. Consequently, $i_{Lf1}(t_{P0})$ is derived as

$$\begin{aligned}i_{Lf1}(t_{P0})=\ &-\frac{V_{in}D_P\pi}{2\omega L_{f1}}+\frac{4\varepsilon V_{in}}{\pi\omega L_{f1}}\sin^2(\frac{D_P\pi}{2})\\&+\frac{4MV_{out}}{\pi\omega L_{f1}L_{f2}}\sin(\frac{D_S\pi}{2})\cos(\frac{D_P\pi}{2}+\Delta\delta).\end{aligned} \tag{5.26}$$

Similarly, $i_{Lf2}(t_{S2})$ is derived as

$$\begin{aligned}i_{Lf2}(t_{S2})=\ &-\frac{V_{out}D_S\pi}{2\omega L_{f2}}+\frac{4V_{out}}{\pi\omega L_{f2}}\sin^2(\frac{D_S\pi}{2})\\&+\frac{4MV_{in}}{\pi\omega L_{f1}L_{f2}}\sin(\frac{D_P\pi}{2})\cos(\frac{D_S\pi}{2}+\Delta\delta).\end{aligned} \tag{5.27}$$

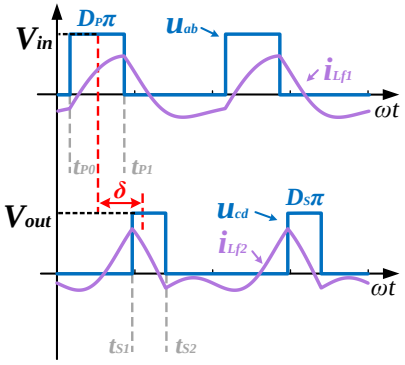

Figure 5.10: Typical operating waveforms of the HB-HB mode.

5

According to [151], to realize the inverter and rectifier ZVS with minimal reactive power on both the primary and secondary sides, the following constraint should be satisfied:

$$i_{Lf1}(t_{P0}) = -I_{ZVS}, i_{Lf2}(t_{S2}) = -I_{ZVS}, \tag{5.28}$$

Apparently, under the asymmetric parameters, only adjusting the compensation angle $\Delta\delta$ is not feasible to simultaneously satisfy these two equations in (5.28). Therefore, a new control variable, i.e., the SCC tuning factor ε, is introduced to facilitate dual-side optimal ZVS. Substituting (5.27) into (5.28) yields the optimal $\Delta\delta_{opt}$, which is expressed as

$$\begin{aligned}\Delta\delta_{opt} = \quad & -D_S\pi/2 + \cos^{-1}\{\Lambda^{-1} \times [-2\pi\omega L_{f1}L_{f2}I_{ZVS} \\ & + V_{out}L_{f1}\left(D_S\pi^2 - 8\sin^2(D_S\pi/2)\right)]\},\end{aligned} \tag{5.29}$$

where $\Lambda = 8MV_{in}\sin(D_P\pi/2)$. Moreover, substituting (5.26) and (5.29) into (5.28) yields the optimal ε_{opt}, which is

$$\begin{aligned}\varepsilon_{opt} = \quad & \Gamma^{-1} \times [-2\pi\omega L_{f1}L_{f2}I_{ZVS} + V_{in}L_{f2}D_P\pi^2 \\ & -8MV_{out}\sin(D_S\pi/2)\cos(D_P\pi/2 + \Delta\delta_{opt})],\end{aligned} \tag{5.30}$$

where $\Gamma = 8V_{in}L_{f2}\sin^2(D_P\pi/2)$.

(2) The HB-HB Mode: Fig. 5.10 presents the typical operating waveforms of the HB-HB mode. For the HB-HB mode, the time-domain expression of $u_{ab}(t)$ is given by

$$\begin{aligned}u_{ab}(t) = \quad & \frac{D_PV_{in}}{2} + \sum_{n=1,2,\ldots}\frac{2V_{in}}{n\pi}\sin(\frac{nD_P\pi}{2})\cos[n(\omega t - \frac{\pi}{2})] \\ = \quad & \frac{D_PV_{in}}{2} + \sum_{n=1,3,\ldots}\frac{2V_{in}}{n\pi}\sin(\frac{nD_P\pi}{2})\sin(\frac{n\pi}{2})\sin(n\omega t) \\ & + \sum_{n=2,4,\ldots}\frac{2V_{in}}{n\pi}\sin(\frac{nD_P\pi}{2})\cos(\frac{n\pi}{2})\cos(n\omega t).\end{aligned} \tag{5.31}$$

Observing (5.31) reveals that u_{ab} consists of three parts: the DC component, the odd-harmonics, and the even-harmonics. The impact of these three parts on i_{Lf1} is analyzed

as follows. Firstly, due to the DC blocking effect of C_{f1} and C_1, the DC component of u_{ab} has no impact on i_{Lf1}. Secondly, the odd-harmonics form a symmetrical full-bridge square waveform, with the DC voltage at $V_{in}/2$ and the duty cycle at D_P. The calculation of $i_{Lf1\_odd}(t)$, which is excited by the odd-harmonics of u_{ab}, can follow the previous analysis for the FB-FB mode. The expression of $i_{Lf1\_odd}(t_{P0})$ is derived as

$$\begin{aligned} i_{Lf1\_odd}(t_{P0}) = & -\frac{V_{in}D_P\pi}{4\omega L_{f1}} + \frac{2\varepsilon V_{in}}{\pi\omega L_{f1}}\sin^2(\frac{D_P\pi}{2}) \\ & + \frac{2MV_{out}}{\pi\omega L_{f1}L_{f2}}\sin(\frac{D_S\pi}{2})\cos(\frac{D_P\pi}{2}+\Delta\delta). \end{aligned} \tag{5.32}$$

Thirdly, regarding the even-harmonics, the time-domain expression of $i_{Lf1\_even}(t)$, which represents the current excited by the even-harmonics, is given by

$$i_{Lf1\_even}(t) = \sum_{n=2,4,\ldots} \frac{2V_{in}\sin(n\omega t)}{n^2\pi\omega L_{f1}}\sin(\frac{nD_P\pi}{2})\cos(\frac{n\pi}{2}). \tag{5.33}$$

Furthermore, $i_{Lf1\_even}(t_{P0})$ is calculated as

$$i_{Lf1\_even}(t_{P0}) = \sum_{n=2,4,\ldots} \frac{-2V_{in}}{n^2\pi\omega L_{f1}}\sin^2(\frac{nD_P\pi}{2}). \tag{5.34}$$

Consequently, $i_{Lf1}(t_{P0})$ in the HB-HB mode is derived as

$$\begin{aligned} i_{Lf1}(t_{P0}) = & -\frac{V_{in}D_P\pi}{4\omega L_{f1}} + \frac{2\varepsilon V_{in}}{\pi\omega L_{f1}}\sin^2(\frac{D_P\pi}{2}) \\ & + \frac{2MV_{out}}{\pi\omega L_{f1}L_{f2}}\sin(\frac{D_S\pi}{2})\cos(\frac{D_P\pi}{2}+\Delta\delta) \\ & - \sum_{n=2,4,\ldots} \frac{2V_{in}}{n^2\pi\omega L_{f1}}\sin^2(\frac{nD_P\pi}{2}). \end{aligned} \tag{5.35}$$

Similarly, $i_{Lf2}(t_{S2})$ under the HB-HB mode is derived as

$$\begin{aligned} i_{Lf2}(t_{S2}) = & -\frac{V_{out}D_S\pi}{4\omega L_{f2}} + \frac{2V_{out}}{\pi\omega L_{f2}}\sin^2(\frac{D_S\pi}{2}) \\ & + \frac{2MV_{in}}{\pi\omega L_{f1}L_{f2}}\sin(\frac{D_P\pi}{2})\cos(\frac{D_S\pi}{2}+\Delta\delta) \\ & - \sum_{n=2,4,\ldots} \frac{2V_{out}}{n^2\pi\omega L_{f2}}\sin^2(\frac{nD_S\pi}{2}). \end{aligned} \tag{5.36}$$

Interestingly, as shown in (5.35) and (5.36), the even-harmonics resulted from the HB mode reduce the values of $i_{Lf1}(t_{P0})$ and $i_{Lf2}(t_{S2})$, which facilitates the implementation of ZVS. Moreover, substituting (5.36) into (5.28) yields the optimal $\Delta\delta_{opt}$ under the HB-HB mode, which is

$$\begin{aligned} \Delta\delta_{opt} = & -D_S\pi/2 + \cos^{-1}\{\Lambda^{-1}\times[-4\pi\omega L_{f1}L_{f2}I_{ZVS} \\ & + V_{out}L_{f1}\big(D_S\pi^2 - 8\sin^2(D_S\pi/2)\big) \\ & + \sum_{n=2,4,\ldots} \frac{8V_{out}L_{f1}}{n^2}\sin^2(\frac{nD_S\pi}{2})]\}. \end{aligned} \tag{5.37}$$

5

Further substituting (5.35) and (5.37) into (5.28) obtains the optimal ε_{opt} under the HB-HB mode, which is expressed as

$$\begin{aligned}\varepsilon_{opt} = \quad & \Gamma^{-1} \times [-4\pi\omega L_{f1} L_{f2} I_{ZVS} + V_{in} L_{f2} D_P \pi^2 \\ & -8MV_{out}\sin(D_S\pi/2)\cos(D_P\pi/2 + \Delta\delta_{opt}) \\ & + \sum_{n=2,4,\ldots} \frac{8V_{in}L_{f2}}{n^2}\sin^2(\frac{nD_P\pi}{2})]\end{aligned} \tag{5.38}$$

(3) The FB-HB and HB-FB Modes: The optimal $\Delta\delta_{opt}$ and ε_{opt} under the FB-HB and the HB-FB modes can be derived in a similar way. Specifically, the optimal $\Delta\delta_{opt}$ and ε_{opt} under the FB-HB mode are derived as

$$\begin{aligned}\Delta\delta_{opt} = \quad & -D_S\pi/2 + \cos^{-1}\{(2\Lambda)^{-1} \times [-4\pi\omega L_{f1} L_{f2} I_{ZVS} \\ & + V_{out} L_{f1}\big(D_S\pi^2 - 8\sin^2(D_S\pi/2)\big) \\ & + \sum_{n=2,4,\ldots} \frac{8V_{out}L_{f1}}{n^2}\sin^2(\frac{nD_S\pi}{2})]\},\end{aligned} \tag{5.39}$$

$$\begin{aligned}\varepsilon_{opt} = \quad & \Gamma^{-1} \times [-2\pi\omega L_{f1} L_{f2} I_{ZVS} + V_{in} L_{f2} D_P \pi^2 \\ & -4MV_{out}\sin(D_S\pi/2)\cos(D_P\pi/2 + \Delta\delta_{opt})].\end{aligned} \tag{5.40}$$

Moreover, the optimal $\Delta\delta_{opt}$ and ε_{opt} under the HB-FB mode are obtained as

$$\begin{aligned}\Delta\delta_{opt} = \quad & -D_S\pi/2 + \cos^{-1}\{(\Lambda/2)^{-1} \times [-2\pi\omega L_{f1} L_{f2} I_{ZVS} \\ & + V_{out} L_{f1}\big(D_S\pi^2 - 8\sin^2(D_S\pi/2)\big)]\},\end{aligned} \tag{5.41}$$

$$\begin{aligned}\varepsilon_{opt} = \quad & \Gamma^{-1} \times [-4\pi\omega L_{f1} L_{f2} I_{ZVS} + V_{in} L_{f2} D_P \pi^2 \\ & -16MV_{out}\sin(D_S\pi/2)\cos(D_P\pi/2 + \Delta\delta_{opt}) \\ & + \sum_{n=2,4,\ldots} \frac{8V_{in}L_{f2}}{n^2}\sin^2(\frac{nD_P\pi}{2})].\end{aligned} \tag{5.42}$$

Based on the above analysis, it is evident that by simultaneously tuning $\Delta\delta$ and ε to $\Delta\delta_{opt}$ and ε_{opt}, both the inverter and rectifier ZVS can be achieved with minimal reactive power.

5.3.3. DERIVATION OF OPTIMAL CONTROL VARIABLES

Distinct from the conventional TPS method, the proposed approach adopts a multivariable control featuring six degrees of freedom, which makes it challenging to derive an explicit expression of the efficiency, especially for the high-order compensation topology. Additionally, it is preferable to consider the overall efficiency of the entire system instead of the efficiency of the resonant tank. Therefore, the traditional approach of identifying the maximum efficiency point by solving the derivative of an explicit efficiency expression is discarded, while it is transformed into an optimization problem with a multivariable input.

The objective of the optimization problem is to minimize the overall losses of the whole system. The power losses of the proposed system comprise the losses incurred by the inverter, the resonant circuits, the SCC, and the rectifier. The power losses of the

inverter mainly consist of the conduction and switching losses of the MOSFETs. Specifically, the conduction losses of the inverter are

$$P_{l\_inv\_con} = 2R_{on}I_{Lf1}^2, \tag{5.43}$$

where R_{on} is the conduction resistance of the power switches. Moreover, the switching losses of the inverter are

$$P_{l\_inv\_sw} = \zeta[i_{Lf1}(t_{P0}) + i_{Lf1}(t_{P1})]V_{in}(\frac{E_{off}}{V_R I_R} + \frac{Q_{RR}}{I_{RD}})f, \tag{5.44}$$

where $\zeta = 2$ corresponds to the FB mode, whereas $\zeta = 1$ corresponds to the HB mode; E_{off} represents the turn-off energy losses of the MOSFET; V_R and I_R denote the reference drain-source voltage and source current of the MOSFET; Q_{RR} and I_{RD} are the reverse recovery charge and the reference current of the body diode [153]. Similarly, the conduction and switching losses of the rectifier are

$$P_{l\_rec\_con} = 2R_{on}I_{Lf2}^2, \tag{5.45}$$

$$P_{l\_rec\_sw} = \zeta[i_{Lf2}(t_{S1}) + i_{Lf2}(t_{S2})]V_{in}(\frac{E_{off}}{V_R I_R} + \frac{Q_{RR}}{I_{RD}})f. \tag{5.46}$$

Additionally, the power losses of the resonant circuits is

$$P_{l\_res} = I_{Lf1}^2 R_{Lf1} + I_{Lf2}^2 R_{Lf2} + I_1^2 R_1 + I_2^2(R_2 + R_{C2}) + I_{Cf1}^2 R_{Cf1} + I_{Cf2}^2 R_{Cf2}, \tag{5.47}$$

where R_{C2}, R_{Cf1}, and R_{Cf2} are the equivalent series resistances (ESRs) of the compensation capacitors C_2, C_{f1}, and C_{f2}, respectively. Moreover, the power losses of the adopted SCC is

$$P_{l\_scc} = 2I_{ab}^2 R_{on} + I_{Cx}^2 R_{Cx} + I_1^2 R_{Cy}, \tag{5.48}$$

where R_{Cx} and R_{Cy} are the ESRs of the compensation capacitors C_x and C_y, respectively; I_{ab} is the RMS current across the power switches S_a and S_b; I_{Cx} is the RMS current across C_x. Consequently, the overall loss of the system is obtained by

$$P_l = P_{l\_inv\_con} + P_{l\_inv\_sw} + P_{l\_rec\_con} + P_{l\_rec\_sw} + P_{l\_res} + P_{l\_scc}. \tag{5.49}$$

With given system parameters and DC voltages, P_l can be expressed as

$$P_l = f(D_P, D_S, \Delta\delta, \varepsilon, K_P, K_S). \tag{5.50}$$

As indicated by (5.50), P_l is a function determined by six control variables. The optimization objective is to find an optimal set of variables $\{D_{P\_opt}, D_{S\_opt}, \Delta\delta_{opt}, \varepsilon_{opt}, K_{P\_opt}, K_{S\_opt}\}$ that minimizes the value of P_l.

The flowchart for deriving the optimal variables is illustrated in Fig. 5.11, and the specific steps are elaborated as follows: **[Initialization]** Firstly, the system parameters, the DC input and output voltages V_{in} and V_{out}, as well as the required output power P_{ref}, are given in the initial stage. **[Mode Selection]** Subsequently, the inverter and rectifier modes K_P and K_S are searched between the FB and HB modes. **[Duty Cycle Selection]** After K_P and K_S are determined, the inverter and rectifier duty cycles D_P and D_S are then

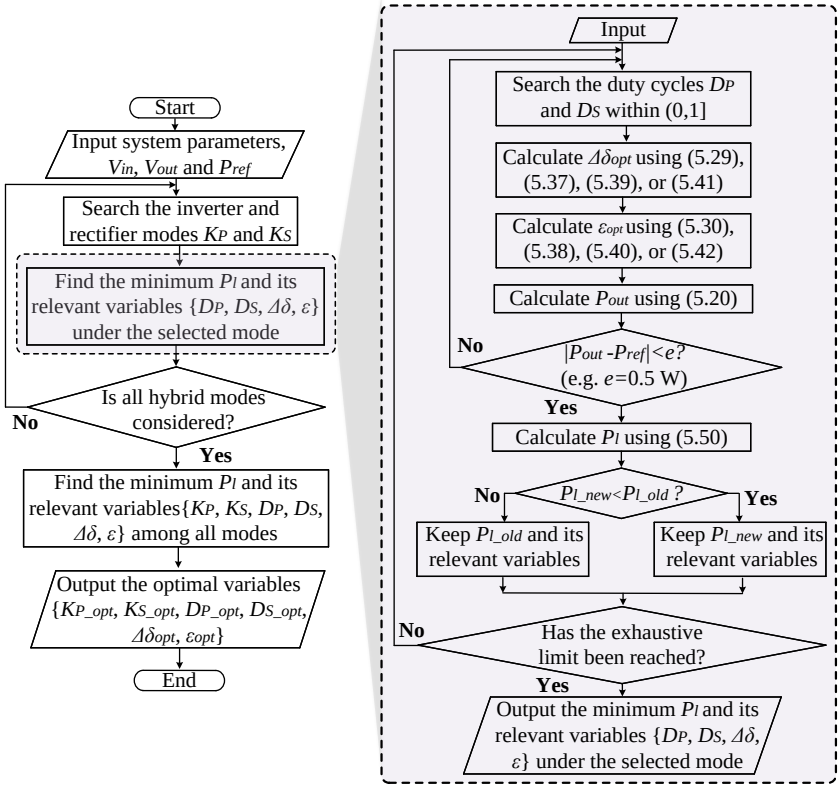

Figure 5.11: Flowchart for deriving the optimal variables to minimize the overall power loss of the system.

searched within the range of (0,1], where the exhaustive method is applied to implement the search of D_P and D_S. **[Optimal ZVS Implementation]** Based on the selected K_P, K_S, D_P, and D_S, the optimal variables $\Delta\delta_{opt}$ and ε_{opt} are calculated according to the analysis in Chapter 5.3.2. **[Power Assessment]** After all of the control variables, i.e., D_P, D_S, $\Delta\delta$, ε, K_P, K_S, are determined, the output power of the system is calculated using (5.20). If the output power P_{out} is consistent with the required power P_{ref}, the currently selected variables are preserved, and the overall power losses P_l is then calculated using (5.50). **[Loss Minimization]** By comparing the power losses P_l obtained from different sets of variables, the optimal set of variables $\{D_{P\_opt}, D_{S\_opt}, \Delta\delta_{opt}, \varepsilon_{opt}, K_{P\_opt}, K_{S\_opt}\}$ that minimizes P_l is identified.

Based on the above approach, the optimal variables are derived with the parameters listed in Table 5.1, as shown in Fig. 5.12. As indicated by Fig. 5.12, the proposed OMC method introduces the HB-HB ($P_{out} \leq 360$ W) and FB-HB (360 W$< P_{out} \leq 1000$ W) modes under light-loads. The introduction of hybrid modes reduces the value of $\Delta\delta$, leading to less reactive power while improving efficiency. As the output power approaches full level, the proposed OMC method operates in the FB-FB mode ($P_{out} > 1000$ W). However, the incorporation of SCC tuning reduces the excessive reactive power caused by

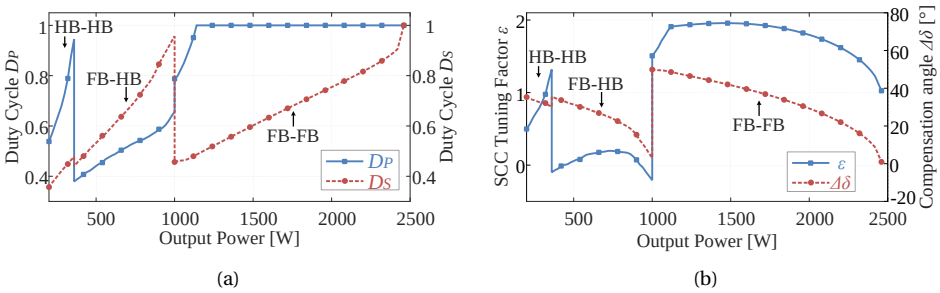

Figure 5.12: Derived optimal control variables: (a) the duty cycles D_P and D_S, (b) the compensation phase angle $\Delta\delta$ and the SCC tuning factor ε.

asymmetric parameters, thereby further enhancing efficiency under heavy-load conditions.

In practical applications, considering the limited computing power of the microcontrollers, it is preferable to implement the abovementioned optimal control variables using a look-up Table It is noteworthy that the value of SCC conduction angle θ instead of the SCC tuning factor ε should be stored as a look-up table in practical implementation.

5.3.4. CONTROL FRAMEWORK

Fig. 5.13 presents the control block diagram of the proposed OMC approach. As illustrated in Fig. 5.13, the DC output voltage V_{out} and current I_{out} are firstly measured. After the signal processing circuits, V_{out} and I_{out} are multiplied to obtain the output power P_{out}. Based on the measured P_{out}, the inverter and rectifier modes K_P and K_S are selected through the mode determination module. Moreover, a PI controller is employed to regulate the rectifier duty cycle D_S for voltage tracking. According to the proposed optimization approach shown in Fig. 5.11, the optimal control variables are calculated

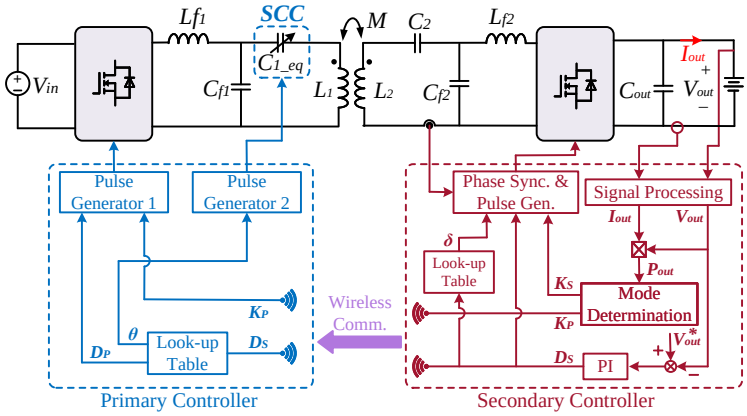

Figure 5.13: Control block diagram of the proposed OMC method.

offline and stored as a look-up table in the microcontrollers. Based on the duty cycle D_S and the look-up table, the corresponding optimal control variables D_P, δ, and θ are obtained. Finally, with the obtained control outputs, the corresponding driving signals for the inverter, the rectifier, as well as the SCC, are generated by the pulse generators.

5.3.5. DESIGN GUIDELINES FOR SCC

(1) Capacitance of C_x and C_y: Based on the optimal variables shown in Fig. 5.12(b), the maximum and minimum SCC tuning factor is: $\varepsilon_{max} = 1.96$, $\varepsilon_{min} = -0.21$. Submitting ε_{max} and ε_{min} into (12) yields the maximum and minimum capacitance of C_{1_eq}, i.e., $C_{1\_eq\_max} = 26.5\ nF$, $C_{1\_eq\_min} = 9.8\ nF$. On the other hand, regarding the tuning range of θ ($0 \le \theta \le \pi$), the equivalent SCC capacitance satisfies: $C_x // C_y \le C_{1\_eq} \le C_y$. To ensure the SCC is able to obtain the required capacitance, the following relationship should be satisfied: $C_y \ge 26.5\ nF$, $C_x // C_y \le 9.8\ nF$. Moreover, as shown in Fig. 5.14, when θ approaches π, the $\theta - \varepsilon$ curve becomes flat. The flattened curve area significantly reduces the SCC tuning sensitivity. Therefore, to prevent encountering this area, it is important to consider sufficient margins when designing C_x and C_y. Consequently, the capacitance of C_x and C_y are designed as 13.0 nF and 31.7 nF, respectively.

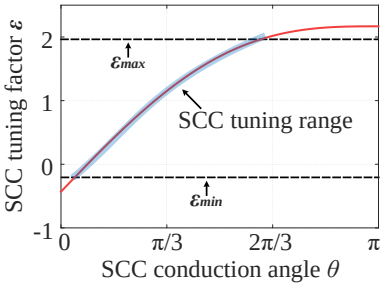

Figure 5.14: Relationship between the SCC conduction angle θ and the capacitor tuning factor ε when C_x = 13.0 nF, C_y = 31.7 nF.

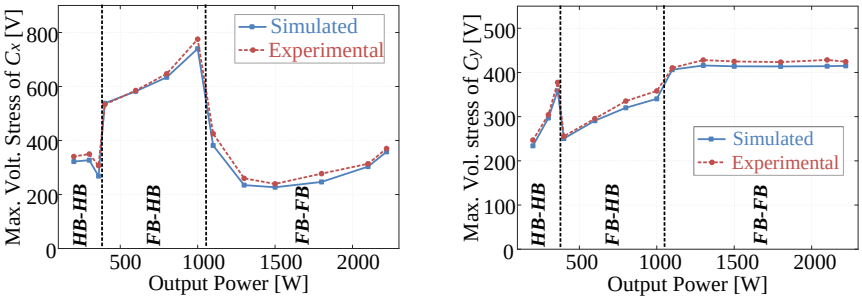

Figure 5.15: Maximum voltage stresses of (a) the capacitor C_x and (b) the capacitor C_y at different power levels.

(2) Voltage stress of SCC: To illustrate the capacitor voltage stresses of the SCC, Fig. 5.15 demonstrates the simulation results of the maximum capacitor voltages at different power levels. As the output power varies, the simulated maximum voltage stresses of C_x and C_y reach up to 740 V and 415 V, respectively. Moreover, the measured maximum voltage stresses of C_x and C_y in the experiments are also presented in Fig. 5.15 for comparisons. As depicted in Fig. 5.15, the experimental results demonstrate good agreement with the simulated results.

Following the above analysis, the selection of SCC MOSFETs can be facilitated. According to the SCC topology, the switches S_a and S_b need to block the voltage of C_x when the switches are turned off. Based on the above simulation analysis for SCC voltage stress, the rated blocking voltage of S_a and S_b should exceed 740 V. It is noteworthy that in practical applications, sufficient margins should be considered when selecting MOSFETs. Therefore, in the proposed system, MOSFETs with a rated voltage of 1.2 kV are selected as the SCC switches.

5.4. EXPERIMENTAL RESULTS

5.4.1. EXPERIMENTAL SETUP

To validate the proposed OMC method, experiments were carried out based on a DLCC compensated IPT prototype, as depicted in Fig. 5.16. Within this prototype, the asymmetric coil structure is investigated, and the inductors L_{f1} and L_{f2} are designed to obtain the required maximum output power. The capacitors C_2, C_{f1}, C_{f2} are designed in accordance with the general principles of the DLCC topology, while the capacitor C_1 is

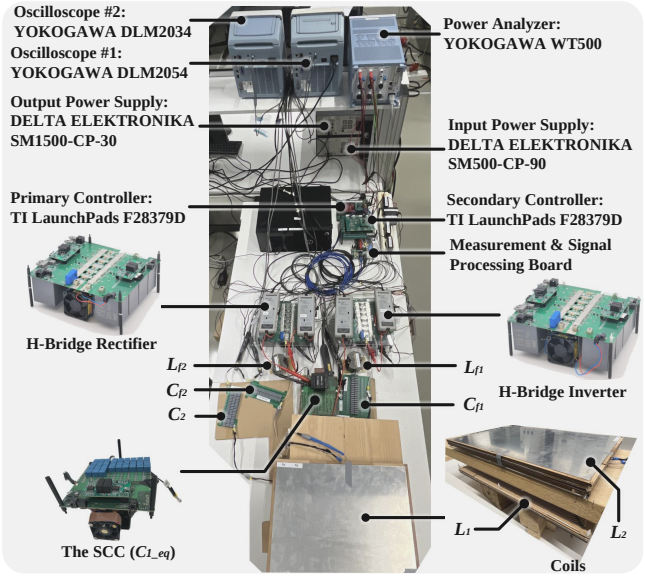

Figure 5.16: Experimental prototype of the DLCC-compensated IPT system used to verify the proposed OMC method [3–5].

replaced by an SCC. The switching frequency is set to the commonly-adopted 85 kHz within IPT systems. Additionally, a non-unity DC voltage gain is considered, with the DC voltages configured as V_{in} = 300 V and V_{out} = 500 V, respectively. Moreover, the proposed control algorithm, as well as the pulse generation for the converters and the SCC, was implemented on the TI LaunchPad F28379D. The synchronization between the primary and secondary sides is achieved by the zero-crossing-detection technique for the secondary coil current. To guarantee ZVS for the inverter and rectifier, the minimum ZVS current of the power switches is designed as 2.0 A. More detailed system parameters of the investigated prototype are elaborated in Table 5.1.

5.4.2. STEADY-STATE OPERATING WAVEFORMS

When delivering 300 W power in the proposed OMC method, as illustrated in Fig. 5.17, the system operates in the HB-HB mode. Moreover, in the proposed method, the SCC

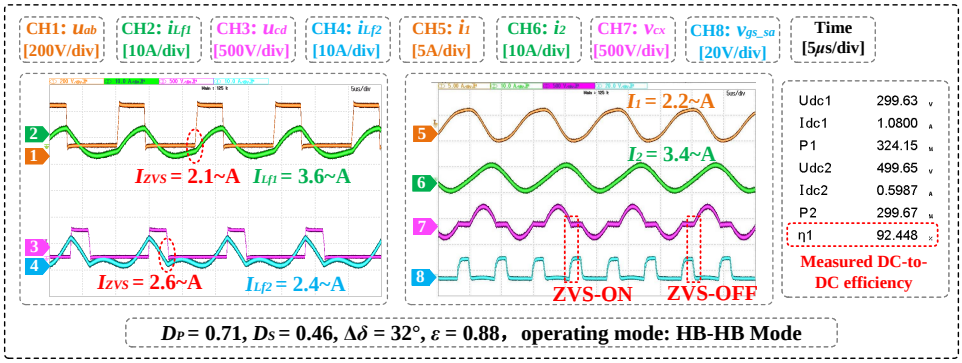

(a)

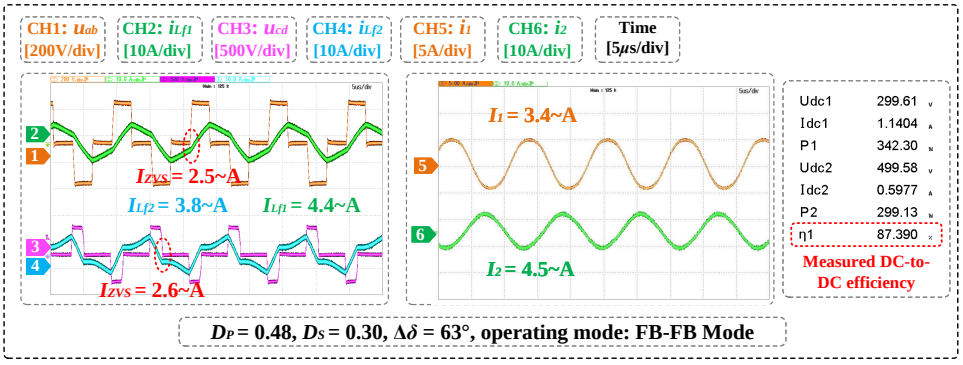

(b)

Figure 5.17: Measured operating waveforms and DC-to-DC efficiency when delivering 300 W power: (a) the proposed OMC method, (b) the existing TPS method. Here, v_{cx} indicates the voltage stress across the SCC capacitor (C_x), while v_{gs_sa} represents the gate-source voltage of the SCC switch (S_a). This description also applies to Fig. 5.19, Fig. 5.20, Fig. 5.23, and Fig. 5.24.

tuning factor ε, as well as the compensation angle $\Delta\delta$, are adjusted to achieve both the inverter and rectifier ZVS while minimizing the reactive power. Specifically, the SCC tuning factor ε is regulated to 0.88, while the compensation angle $\Delta\delta$ is adjusted to 32°. Additionally, as demonstrated in Fig. 5.17, by incorporating the HB-HB mode, the proposed OMC method notably increases the values of D_P and D_S. The incorporation of HB-HB mode and SCC tuning significantly reduces the compensation angle $\Delta\delta$ from 63° to 32° in the proposed method, consequently lowering reactive power within the resonant circuits. The reduction of reactive power contributes to a notable decrease in the RMS values of the inductor and coil currents. In comparison to the TPS method, as demonstrated in Fig. 5.17, the proposed method reduces I_{Lf1} from 4.4 A to 3.6 A, I_{Lf2} from 3.8 A to 2.4 A, I_1 from 3.4 A to 2.2 A, and I_2 from 4.5 A to 3.4 A. The decreased RMS currents not only result in reduced power losses within the resonant circuits, but also minimize conduction losses of the converters. Furthermore, operating the converters in the HB mode halves the equivalent switching times of the power switches, which also significantly reduces the switching losses of the converters. Consequently, as shown in Fig. 5.17, the proposed method improves the DC-to-DC efficiency from 87.4% to 92.4%, achieving an efficiency improvement of 5.0%.

Fig. 5.18 further demonstrates the harmonics analysis for the experiments shown in Fig. 5.17. The introduction of the HB-HB mode, as shown in Fig. 5.18, results in even-harmonics in the AC voltages u_{ab} and u_{cd}, consequently leading to even-harmonics in the inductor currents i_{Lf1} and i_{Lf2}. Although notable harmonics existed within i_{Lf1} and i_{Lf2}, both the inverter and rectifier ZVS were achieved in the proposed method. As illustrated in Fig. 5.17(b), by simultaneously adjusting ε and $\Delta\delta$, the minimum ZVS currents for the inverter and rectifier were 2.1 A and 2.6 A, respectively.

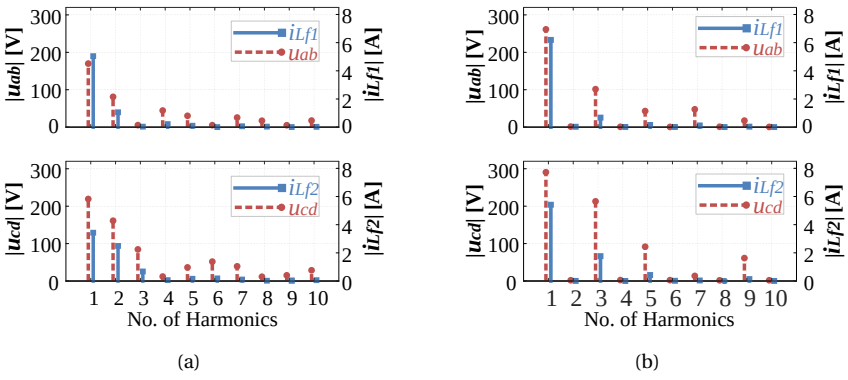

Figure 5.18: Harmonic analysis for the experiments shown in Fig. 5.17: (a) the proposed OMC method, (b) the existing TPS method.

Fig. 5.19 presents the experimental results of the proposed method and the TPS method when delivering 800 W power. When applying the proposed OMC method to deliver 800 W power, the system works in the FB-HB mode. As demonstrated in Fig. 5.19(a), the proposed OMC method adjusts the SCC tuning factor ε to 0.17 to enable the inverter

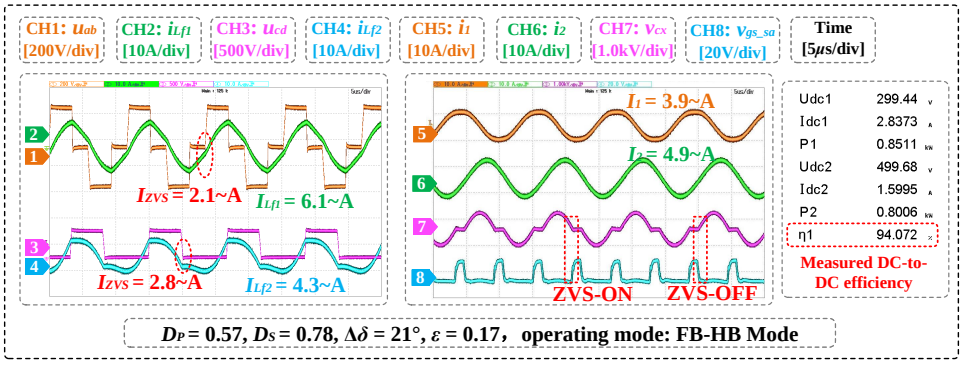

(a)

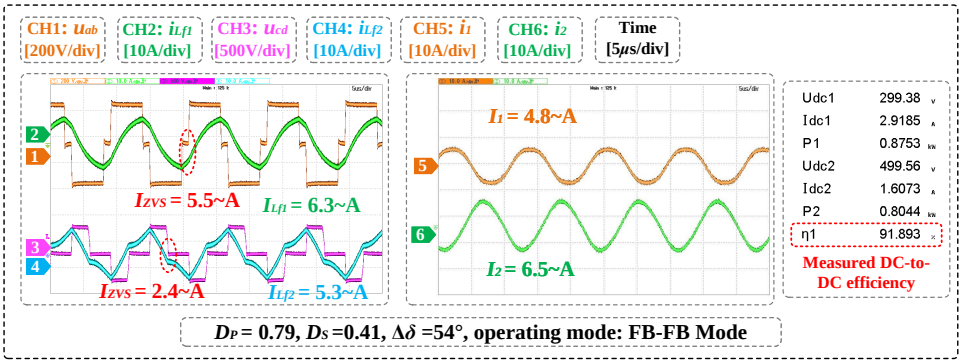

(b)

Figure 5.19: Measured operating waveforms and DC-to-DC efficiency when delivering 800 W power: (a) the proposed OMC method, (b) the existing TPS method.

ZVS. Moreover, the compensation angle $\Delta\delta$ is reduced from 54° to 21° in the proposed OMC method. The introduction of FB-HB mode and SCC tuning reduces I_{Lf1} from 6.3 A to 6.1 A, I_{Lf2} from 5.3 A to 4.3 A, I_1 from 4.8 A to 3.9 A, and I_2 from 6.5 A to 4.9 A. More importantly, by adjusting the SCC, the proposed method reduces the minimum inverter ZVS current from 5.5 A to 2.1 A, resulting in a decrease in inverter turn-OFF losses. When delivering 800 W, the proposed method enhances the efficiency from 91.9% to 94.1%, leading to an efficiency improvement of 2.2%.

Fig. 5.20 demonstrates the experimental results when delivering 1500 W power. When delivering 1.5 kW power in the proposed method, as shown in Fig. 5.20, both the proposed OMC method and the TPS method operate in the FB-FB mode. In both methods, the duty cycles D_P and D_S, as well as the compensation angle $\Delta\delta$, are similar. However, in the proposed OMC method, the SCC tuning factor ε is regulated to 1.95 to facilitate the optimal inverter ZVS. As illustrated in Fig. 5.20, the proposed method dramatically reduces the minimum ZVS current of the inverter from 10.8 A to 2.8 A, leading to a substantial reduction in the inverter turn-OFF losses. Moreover, I_{Lf1} is also decreased from

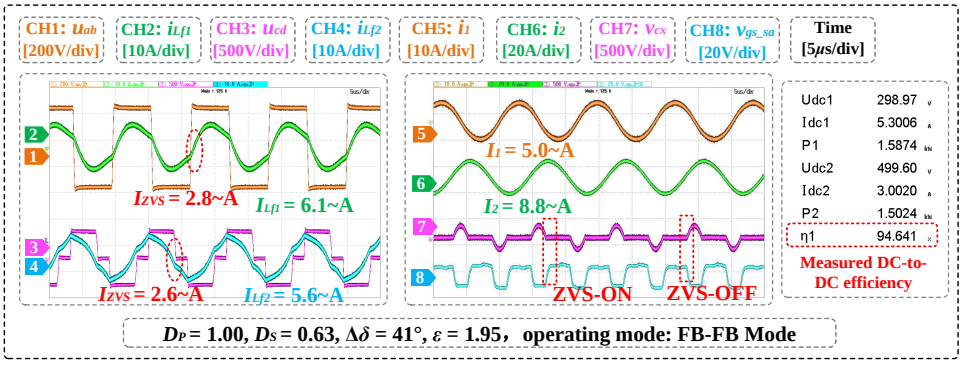

(a)

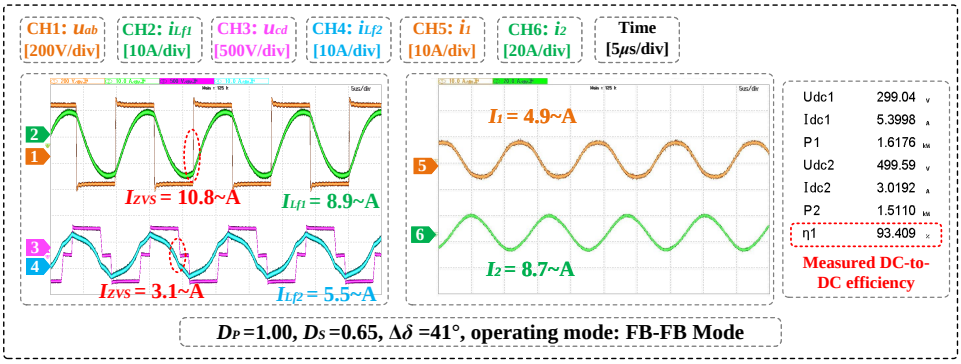

(b)

Figure 5.20: Measured operating waveforms and DC-to-DC efficiency when delivering 1500 W power: (a) the proposed OMC method, (b) the existing TPS method.

8.9 A to 6.1 A, which lowers the inverter conduction losses and the primary inductor losses. Compared with the TPS method, the proposed method achieves an efficiency improvement of 1.2 %, with the efficiency improved from 93.4 % to 94.6 %.

5.4.3. POWER LOSS ANALYSIS AND EFFICIENCY COMPARISONS

Fig. 5.21 demonstrates the calculated power loss distributions for the above experiments. As illustrated in Fig. 5.21, owing to the introduction of hybrid modulation and SCC tuning, the losses in the converters, inductors, capacitors, and coils are all reduced when delivering 300 W and 800 W power in the proposed method. Moreover, when delivering 1.5 kW power, the incorporation of SCC reduces the primary inductor current and the inverter turn-OFF current, contributing to a significant reduction in the inverter and inductor losses. It is noteworthy that the implementation of ZVS turn-ON and turn-OFF for the SCC (as shown in Fig. 5.17, 5.19 and 5.20) effectively minimizes the SCC switching losses, and extra losses caused by the SCC are insignificant.

Furthermore, Fig. 5.22 demonstrates the measured DC-to-DC efficiency of the pro-

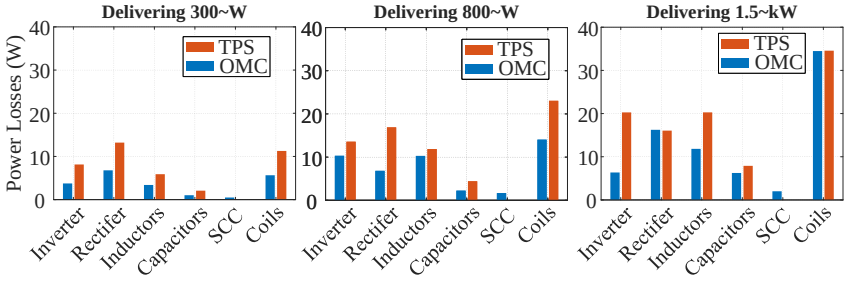

Figure 5.21: Calculated power loss distributions for the experiments presented in Fig. 5.17, 5.19 and 5.20.

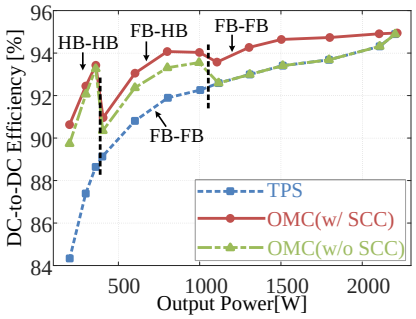

Figure 5.22: Measured DC-to-DC efficiency of the proposed OMC method and the TPS method at different output power levels.

posed OMC method with the TPS method at different output power levels. As illustrated in Fig. 5.22, the introduction of hybrid modulation and SCC tuning significantly enhances the efficiency under light-load conditions, resulting in a maximum efficiency improvement of up to 6.3%. The maximum efficiency improvement is observed at 200 W, where the efficiency is improved from 84.3% to 90.6%. In addition to the enhanced efficiency under light-load conditions, the proposed approach further improves efficiency as the output power approaches the full level through the implementation of SCC tuning. Consequently, the proposed OMC method enables full-range efficiency optimization, with the efficiency consistently exceeding 90% in the power range of 0.2-2.2 kW.

5.4.4. BENCHMARK WITH AND WITHOUT SCC TUNING

To demonstrate the benefits of SCC tuning, Fig. 5.23 presents the experimental results when delivering 200 W power in the HB-HB mode, comparing cases with and without SCC. As shown in Fig. 5.23(b), only adjusting the compensation angle $\Delta\delta$ fails to achieve dual-side optimal ZVS. To guarantee dual-side ZVS without SCC, $\Delta\delta$ is adjusted to 49°, and the minimum rectifier ZVS current reaches 4.1 A. Conversely, introducing SCC enables both the inverter and rectifier to achieve ZVS with minimized ZVS currents. Furthermore, SCC tuning reduces $\Delta\delta$ from 49° to 35°, resulting in diminished reactive power within the resonant circuits. As demonstrated in Fig. 5.23, SCC tuning decreases I_{Lf2} from 2.5 A to 2.0 A, I_1 from 2.1 A to 1.8 A, I_2 from 3.5 A to 3.0 A, achieving an efficiency

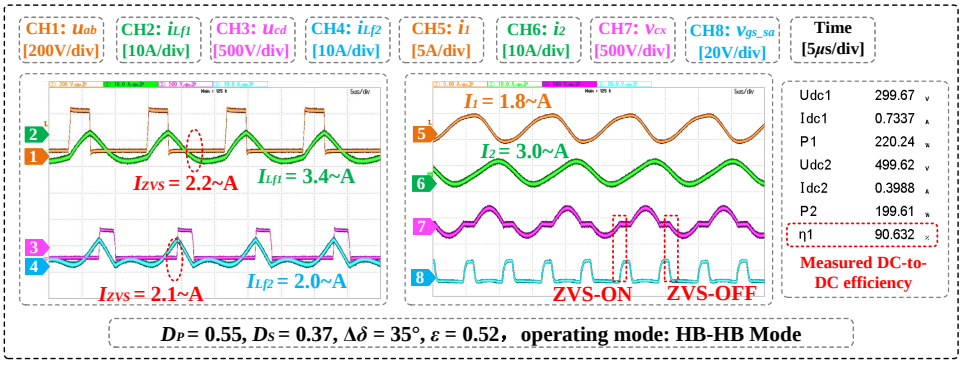

(a)

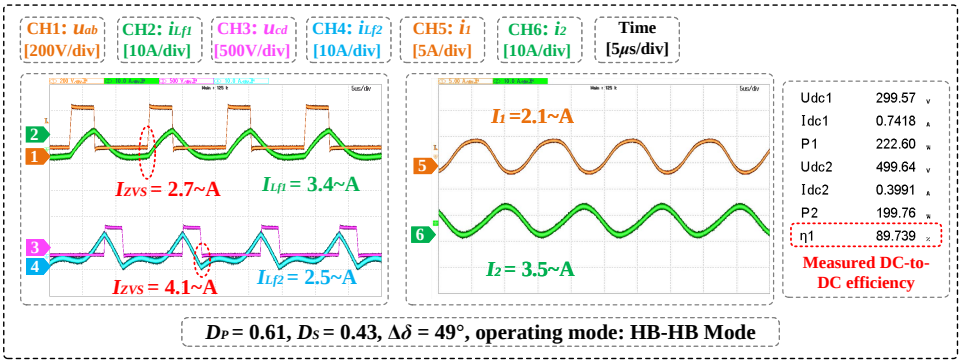

(b)

Figure 5.23: Measured operating waveforms and DC-to-DC efficiency when delivering 200 W power in the proposed OMC method: (a) with SCC, (b) without SCC.

improvement of 0.9%.

Additionally, Fig. 5.24 compares experimental results for 600 W power delivery in the FB-HB mode with and without SCC. As shown in Fig. 5.24, introducing SCC lowers the minimum rectifier ZVS current from 4.6 A to 2.3 A and decreases $\Delta\delta$ from 46° to 31°. Moreover, it reduces I_{Lf2} from 4.3 A to 3.7 A, I_1 from 3.8 A to 3.3 A, and I_2 from 5.3 A to 4.5 A, leading to an efficiency enhancement of 0.7%.

The DC-to-DC efficiency with and without SCC tuning under different power levels is also compared in Fig. 5.22. As demonstrated in Fig. 5.22, the introduction of SCC improves the efficiency across the entire power range, encompassing HB-HB, FB-HB, and FB-FB modes.

5.4.5. DYNAMIC PERFORMANCE

To assess the dynamic performance of the proposed OMC method, the experimental prototype was tested under transient load changes. A measurement and signal processing board was designed to monitor the DC output voltage and current in real time. Addi-

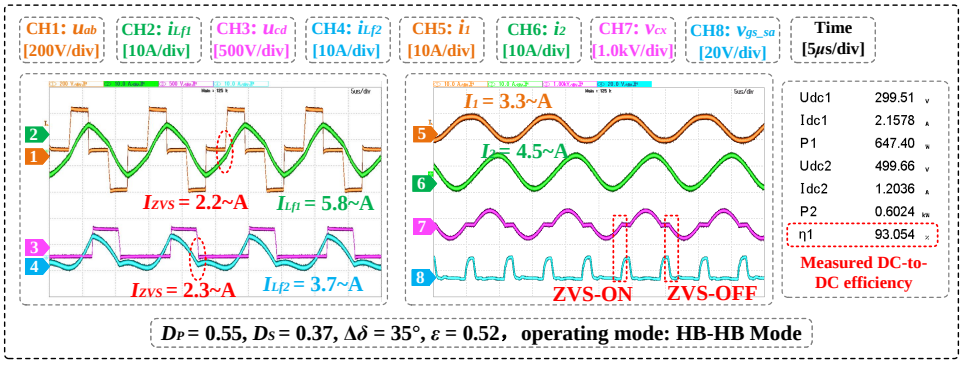

(a)

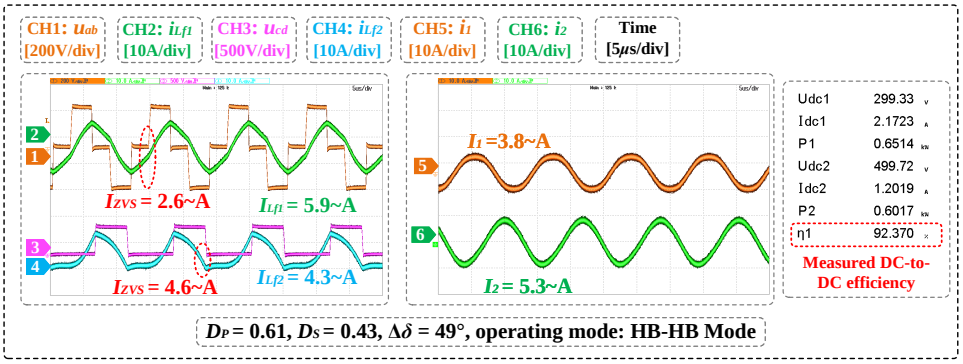

(b)

Figure 5.24: Measured operating waveforms and DC-to-DC efficiency when delivering 600 W power in the proposed OMC method: (a) with SCC, (b) without SCC.

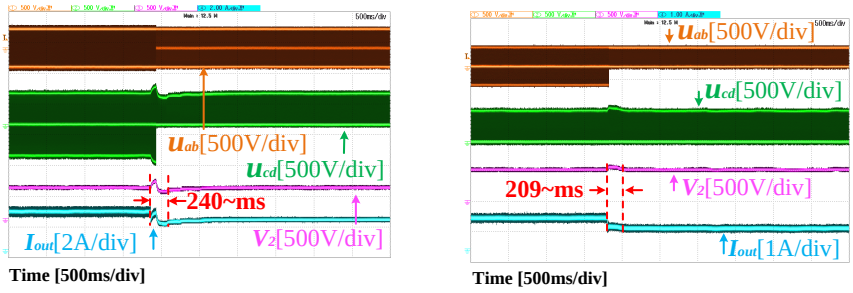

(a) (b)

Figure 5.25: Dynamic performance of the proposed OMC method: (a) when the DC load is changed from 200 Ω to 250 Ω, with the output power decreased from 1.25 kW to 1 kW; (b) when the DC load is changed from 500 Ω to 750 Ω, with the output power decreased from 500 W to 333.3 W.

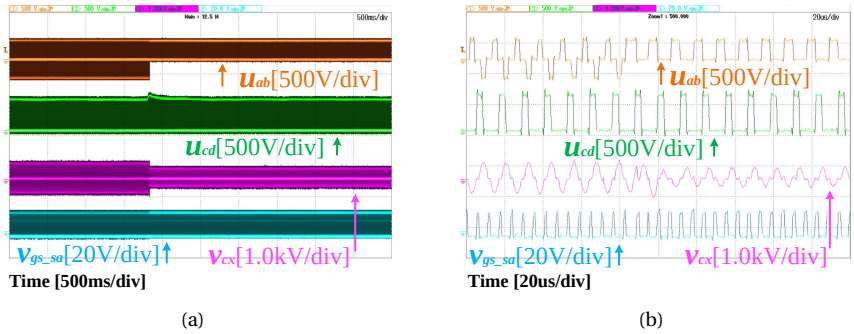

(a) (b)

Figure 5.26: (a) Dynamic performance of SCC, and (b) enlarged view of Fig. 5.26(a) when the DC load is altered from 500 Ω to 750 Ω.

tionally, a PI controller was implemented in the TI launchpads to achieve voltage tracking under load changes.

The dynamic experimental results are demonstrated in Fig. 5.25. As shown in Fig. 5.25(a), when the DC load suddenly changes from 200 Ω to 250 Ω, the operating mode of the system shifts from the FB-FB mode to the FB-HB mode. The DC output voltage is restored to 500 V within 240 ms, with the output power decreased from 1.25 kW to 1.0 kW. As the output power further decreases, the system operating mode switches from the FB-HB mode to the HB-HB mode, as demonstrated in Fig. 5.25(b). Experiments reveal that when the DC load is abruptly changed from 500 Ω to 750 Ω, the proposed method effectively restores the output voltage to the reference value within 209 ms, with the output power decreased from 500 W to 333.3 W.

Moreover, Fig. 5.26 presents the dynamic performance of the SCC when the DC load is altered from 500 Ω to 750 Ω. As illustrated in Fig. 5.26, by adjusting the SCC conduction angle, the proposed method achieves dynamic SCC tuning under load changes.

5.5. CONCLUSIONS

To facilitate wide output power regulation while improving efficiency for the IPT systems, this chapter presents an optimal multivariable control strategy by incorporating SCC tuning and hybrid modulation into the TPS method. By simultaneously adjusting the converter phase-shift angles and the SCC conduction angle, the proposed approach achieves inverter and rectifier ZVS with minimized reactive power on both the primary and secondary sides. Moreover, the integration of hybrid modulation reduces reactive power under light-load conditions. The reduction in reactive power leads to decreased RMS currents, as well as reduced turn-OFF currents, consequently minimizing power losses within the system. Experimental results confirm that the proposed method effectively achieves wide output regulation and full-range efficiency optimization for a DLCC-compensated IPT prototype.

6

DUAL-SIDE CAPACITOR TUNING AND COOPERATIVE CONTROL FOR WIDE OUTPUT VOLTAGE VARIATIONS

This chapter presents a dual-side capacitor tuning and cooperative control strategy for wireless electric vehicle (EV) charging. To improve the efficiency of wireless EV charging across broad output voltages and wide-range load variations, this chapter first introduces a reconfigurable IPT system by incorporating two switch-controlled-capacitors (SCCs) into the double-sided LCC (DLCC) compensation network. Based on the analytical model of the system, optimal capacitor tuning factors are derived to reduce the RMS values of the inductor currents and to minimize the turn-OFF currents across the semiconductors. Furthermore, a dual-side cooperative control strategy is proposed. Through the collaborative control of the inverter, rectifier, and SCCs, the proposed method achieves dual-side optimal zero-voltage-switching (ZVS), wide power regulation, and maximum efficiency tracking simultaneously. Compared with the existing triple-phase-shift (TPS) method, the proposed approach improves the system efficiency across a wide range of DC output voltages and power levels. Experimental results demonstrate that the proposed method achieves a maximum efficiency improvement of up to 1.8% in the boost mode and 1.9% in the buck mode, respectively.

This chapter is based on:

- G. Zhu, J. Dong, T.B. Soeiro, H. Vahedi, and P. Bauer, "Dual-side capacitor tuning and cooperative control for efficiency-optimized wide output voltages in wireless ev charging," *IEEE Transactions on Industrial Electronics*, Early Access, 2024.

6.1. INTRODUCTION

As increasing EV models populate the streets, it is apparent that their nominal battery voltages vary in a broad range. According to [103], most EV batteries fall into two nominal voltage levels: 400-V and 800-V. In this thesis, Table 1.2 (see Chapter 1) demonstrates nominal battery voltages of several EV models in the market. As evident from Table 1.2, the nominal battery voltages vary in a notably wide range due to the variety of EV models. In this context, achieving wide power regulation while accommodating a wide range of output voltage variations is challenging. Moreover, maintaining high transmission efficiency under such a significantly broad operating range is crucially important and poses further challenges.

An intuitive strategy for accommodating wide output voltage variations is to incorporate DC-DC converters in the front- and/or back-end of the system [184, 185]. However, the introduction of DC-DC converters leads to increased losses, higher costs, and reduced power density [185].

Another effective method for addressing wide output voltage variations involves optimizing modulation and control strategies for the inverter and/or rectifier of the system. Existing control strategies for the IPT system can be roughly categorized into three groups: primary-side control [186], secondary-side control [113], and dual-side cooperative control [115]. Compared with single-side control, dual-side control significantly expands the operating range by replacing the passive diode rectifier with an active rectifier. To enable wide output power regulation while ensuring ZVS operations of power switches, triple-phase-shift (TPS) control is widely adopted in existing research [104, 151, 153]. However, the existing TPS methods lead to a notable efficiency drop when the output voltage varies significantly. Existing dual-side control methods lack effective measures to simultaneously address wide power regulation and wide output voltage variations while maintaining high efficiency.

6.1.1. SCOPE AND CONTRIBUTIONS

To fill up the above research gap, this chapter proposes a dual-side cooperative control strategy based on a reconfigurable double-sided LCC (DLCC) compensation network. The DLCC topology achieves load-independent constant-current (CC) output and provides increased design flexibility, which has been widely investigated in wireless EV charging [187–189]. Based on the DLCC network, this chapter incorporates two separate switched-controlled capacitors (SCCs) on the primary and secondary sides, respectively. The SCC technique has been extensively studied for IPT systems. To deal with the inductance variations caused by substantial coil misalignment, the SCC technique proves effective by dynamically compensating the varying inductances [174, 175, 190]. Additionally, the SCC method is also frequently employed to achieve wide ZVS. In [152], a primary-side SCC was integrated into the LCC-S topology to achieve wide inverter ZVS. Moreover, Zhou et al. integrated a secondary-side SCC for the DLCC topology to minimize the input current of the rectifier [191]. It is noteworthy that the methods presented in [152] and [191] only consider the primary-side control. Nevertheless, the operating range of the primary-side control is limited. To extend the operating scope, Fu et al. further implemented the secondary-side SCC with dual-side control [134]. Although the operating range is effectively expanded, this approach only improves the efficiency in the

buck mode, and therefore, the efficiency-optimized output voltage range is constrained.

Considering the limitations of previous research, a dual-side cooperative control strategy is proposed, and the main contributions of this work are as follows:

1)A reconfigurable DLCC topology is introduced, featuring two SCCs integrated on the primary and secondary sides, respectively. Moreover, detailed system characteristics under dual-side capacitor tuning are investigated.

2) An analytical model for the reconfigurable DLCC topology is established. Based on this model, optimal capacitor tuning factors are derived to lower the reactive power, thereby reducing the inductor RMS currents and minimizing the turn-OFF currents for the H-bridge converters.

3) A dual-side capacitor tuning and cooperative control strategy is proposed. Through the cooperative control of the inverter, rectifier, and SCCs, the proposed strategy achieves dual-side optimal ZVS, wide output power regulation, and maximum efficiency tracking simultaneously. Notably, the proposed approach improves efficiency in both the buck and boost modes, enabling efficient charging for a broad range of output power and accommodating significant output voltage variations.

6.1.2. OUTLINE

The rest of this chapter is organized as follows. Chapter 6.2 demonstrates the limitations of conventional methods under wide output voltage applications. Subsequently, Chapter 6.3 presents the proposed reconfigurable DLCC topology with dual-side SCCs. Furthermore, detailed strategies for dual-side capacitor tuning and cooperative control are shown in Chapter 6.4, while experimental results are presented in Chapter 6.5. Finally, conclusions are made in Chapter 6.6.

6.2. WIDE OUTPUT VOLTAGES IN WIRELESS EV CHARGING APPLICATIONS

6.2.1. SYSTEM CHARACTERISTICS

Fig. 6.1 presents the equivalent circuit model for the conventional DLCC-compensated IPT system. In this diagram, u_{ab} and u_{cd} represent the AC voltages generated by the inverter and rectifier, respectively. Additionally, i_1 and i_2 represent the primary and secondary coil currents, while i_{Lf1} and i_{Lf2} indicate the currents flowing through the primary and secondary inductors, respectively. Moreover, the contactless coils are regarded as a loosely coupled transformer (LCT), where L_1 is the primary self-inductance, L_2 is the

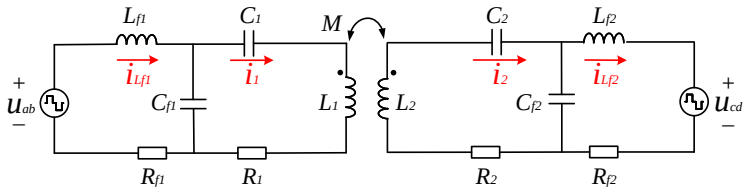

Figure 6.1: Equivalent model of the traditional DLCC compensated system.

secondary self-inductance, and M is the mutual inductance. To enhance the power factor of the system, both the primary and secondary sides of the LCT are compensated using the LCC networks. The DLCC topology is designed as $L_{f1}C_{f1} = 1/\omega_n^2$, $L_{f2}C_{f2} = 1/\omega_n^2$, $L_1 - L_{f1} = 1/(\omega_n^2 C_1)$, $L_2 - L_{f2} = 1/(\omega_n^2 C_2)$, where ω_n represents the nominal resonant frequency.

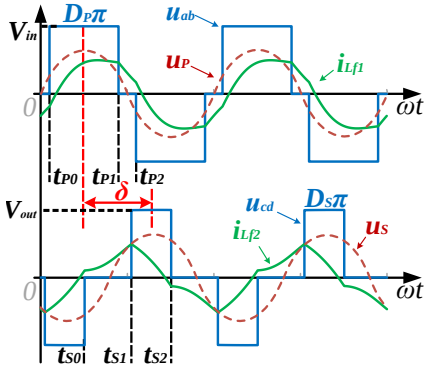

Figure 6.2: Typical operating waveforms of the conventional TPS control.

6

Furthermore, to achieve power regulation and implement ZVS, the TPS control is commonly adopted. Fig. 6.2 presents the typical operating waveforms of the existing TPS method. In Fig. 6.2, V_{in} and V_{out} are the DC input and output voltages, while u_P and u_S represent the fundamental components of u_{ab} and u_{cd}, respectively. Additionally, the inverter and rectifier duty cycles are denoted by D_P and D_S, while the phase difference between u_P and u_S is indicated by δ. According to [151], when employing the TPS control, the transfer efficiency of the resonant circuits is derived as

$$\begin{aligned}\eta_{res} \approx \quad & \omega M L_{f1} L_{f2} |\sin(\delta)| \times [(R_2 L_{f1}^2 + M^2 R_{Lf1}) G_{AC} \\ & + (R_1 L_{f2}^2 + M^2 R_{Lf2})/G_{AC} + \omega M L_{f1} L_{f2} |\sin(\delta)|]^{-1},\end{aligned} \tag{6.1}$$

where $G_{AC} = |u_S|/|u_P|$ represents the AC voltage gain of the resonant circuits; $|u_P| = 2\sqrt{2}V_{in}\sin(D_P\pi/2)/\pi$; $|u_S| = 2\sqrt{2}V_{out}\sin(D_S\pi/2)/\pi$. As evident from (6.1), to realize maximum efficiency tracking for the resonant circuits, the inverter and rectifier duty cycles should be adjusted as

$$\frac{\sin(D_S\pi/2)}{\sin(D_P\pi/2)} = \frac{V_{in}}{V_{out}} \sqrt{\frac{bR_1 + cR_{Lf2}}{R_2/b + cR_{Lf1}}}, \tag{6.2}$$

where $b = L_{f2}/L_{f1}$, $c = M^2/(L_{f1}L_{f2})$.

Moreover, to achieve ZVS in the TPS control, the phase angle δ needs to be modified away from $\pi/2$. For convenience of analysis, the phase angle δ is expressed as $\delta = \pi/2 + \Delta\delta$, where $\Delta\delta$ represents the compensation angle for enabling ZVS. Increasing $\Delta\delta$ allows for greater injection of reactive power into the resonant circuits, consequently achieving ZVS for the inverter and rectifier. Specifically, the minimum value of $\Delta\delta$ for achieving the

inverter ZVS is determined as

$$\begin{aligned}\Delta\delta_1 = \quad & \arccos\{\frac{1}{8MV_{out}\sin(D_S\pi/2)} \times [-2\pi\omega L_{f1}L_{f2}I_{ZVS} \\ & + V_{in}L_{f2}\big(D_P\pi^2 - 8\sin^2(D_P\pi/2)\big)]\} - D_P\pi/2.\end{aligned} \tag{6.3}$$

where I_{ZVS} is the threshold current for charging/discharging C_{oss} of the power switches within the dead time. Similarly, the minimum value of $\Delta\delta$ for the rectifier ZVS is

$$\begin{aligned}\Delta\delta_2 = \quad & \arccos\{\frac{1}{8MV_{in}\sin(D_P\pi/2)} \times [-2\pi\omega L_{f1}L_{f2}I_{ZVS} \\ & + V_{out}L_{f1}\big(D_S\pi^2 - 8\sin^2(D_S\pi/2)\big)]\} - D_S\pi/2.\end{aligned} \tag{6.4}$$

Finally, to ensure ZVS for both the inverter and rectifier, the compensation angle $\Delta\delta$ is selected as

$$\Delta\delta = \max(\Delta\delta_1, \Delta\delta_2). \tag{6.5}$$

6.2.2. EXISTING PROBLEMS UNDER WIDE OUTPUT VOLTAGE VARIATIONS

To accommodate diverse EV models in the market, it is advantageous for the IPT system to efficiently manage broad output voltages. However, the existing TPS method exhibits significant limitations when the output voltage varies.

Table 6.1: Parameters of the investigated IPT system used to verify the proposed dual-side capacitor tuning and cooperative control method

Symbol	Parameters	Value	Unit
M	Mutual inductance	95.0	μH
L_1, L_2	Coil inductances	335.8, 224.7	μH
C_1, C_2	Series capacitances	14.8, 25.3	nF
C_{f1}, C_{f2}	Parallel capacitances	33.1, 41.3	nF
L_{f1}, L_{f2}	Compensation inductances	103.8, 83.8	μH
R_1, R_2	Coil resistances	0.45, 0.30	Ω
R_{Lf1}, R_{Lf2}	Inductor resistances	0.20, 0.14	Ω
V_{in}	DC input voltage	300	V
V_{out}	DC output voltage	150-450	V
f	Switching frequency	85	kHz

When the system needs to manage wide output voltages, as indicated in (6.2), it becomes necessary to regulate the duty cycles D_P and D_S in an inconsistent manner for achieving maximum efficiency tracking. Further observing (6.3) and (6.4) reveals that the difference between the compensation angles $\Delta\delta_1$ and $\Delta\delta_2$ also undergoes significant variations as the output voltage and power change. With the system parameters listed in Table 6.1, the distinction between $\Delta\delta_1$ and $\Delta\delta_2$ under various output power and voltages is illustrated in Fig. 6.3. Therein, the disparity between $\Delta\delta_1$ and $\Delta\delta_2$ initially rises with increasing output power and subsequently exhibits a decrease as the power approaches the rated level. Another notable point is that this difference becomes more pronounced as the DC voltage gain deviates from the unity value.

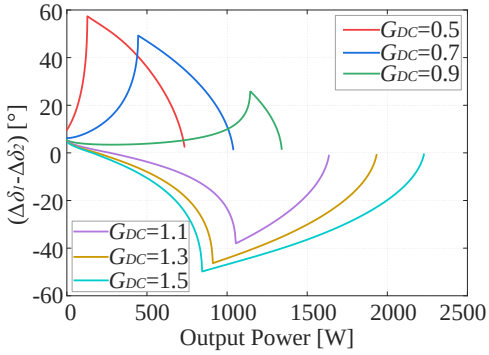

Figure 6.3: Difference between $\Delta\delta_1$ and $\Delta\delta_2$ under various output power and voltages. Here, $G_{DC} = V_{out}/V_{in}$ is the DC voltage gain of the system.

As described in (6.5), the existing TPS control selects the maximum value of $\Delta\delta_1$ and $\Delta\delta_2$ to guarantee ZVS for both the inverter and rectifier. However, when the difference between $\Delta\delta_1$ and $\Delta\delta_2$ becomes significant, this approach results in increased reactive power. Taking G_{DC}=0.5 as an example, the value of $\Delta\delta_1$ exceeds that of $\Delta\delta_2$, and this difference becomes significant under power variations. This implies that even though ZVS for the rectifier can be achieved at $\Delta\delta = \Delta\delta_2$, the compensation angle $\Delta\delta$ must be selected as $\Delta\delta_1$ to ensure ZVS for the inverter, which leads to extra reactive power on the secondary side. The presence of this excessive reactive power results in increased currents, consequently reducing the system's efficiency.

6.3. RECONFIGURABLE DLCC COMPENSATION NETWORKS

To reduce the above-mentioned additional reactive power, a reconfigurable DLCC-compensated IPT system is introduced, as shown in Fig. 6.4. This system incorporates two separate SCCs, one configured on the primary side and the other on the secondary side.

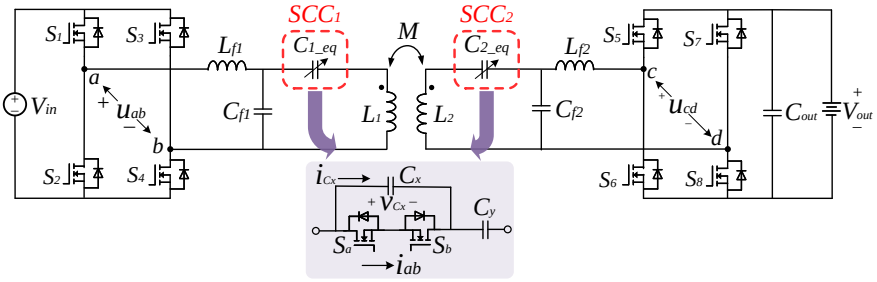

Figure 6.4: Topology of the proposed reconfigurable DLCC compensated system with dual-side SCCs. Here, C_{1_eq} and C_{2_eq} represent the equivalent capacitances of the primary and secondary SCCs, respectively.

The implementation of dual-side SCCs allows for continuous tuning for the equivalent capacitances of C_{1_eq} and C_{2_eq}. Distinct from the conventional DLCC network,

the proposed system operates at detuned conditions, and the detuning factors for the primary (ε_1) and secondary (ε_2) resonant circuits are denoted by

$$\varepsilon_1 = \frac{\omega L_1 - 1/(\omega C_{1\_eq})}{X_1}, \varepsilon_2 = \frac{\omega L_2 - 1/(\omega C_{2\_eq})}{X_2}. \tag{6.6}$$

where $X_1 = \omega L_{f1}$ indicates the primary characteristic reactance, while $X_2 = \omega L_{f2}$ represents the secondary characteristic reactance. Furthermore, using the fundamental harmonic analysis (FHA) method and ignoring the loss resistances, the circuit model of the proposed system is simplified, as shown in Fig. 6.5. Here, $\dot{U}_P$, $\dot{U}_S$, $\dot{I}_1$, $\dot{I}_2$, $\dot{I}_{Lf1}$, and $\dot{I}_{Lf2}$ are the phase forms of the fundamental components of u_{ab}, u_{cd}, i_1, i_2, i_{Lf1} and i_{Lf2}, respectively. Based on this simplified model, the basic characteristics of the proposed system are analyzed as follows.

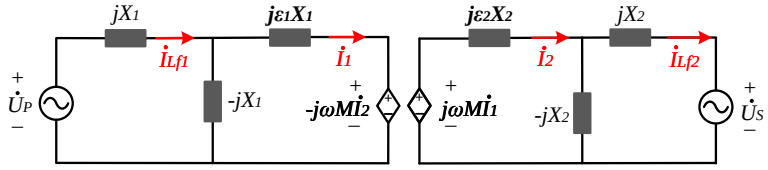

Figure 6.5: Simplified equivalent circuit model of the proposed system.

6.3.1. CIRCULATING COIL AND INDUCTOR CURRENTS

Based on Fig. 6.5 and applying Kirchhoff's Voltage Law (KVL), expressions of $\dot{I}_1$ and $\dot{I}_2$ are derived as

$$\dot{I}_1 = -j\frac{\dot{U}_P}{X_1}, \dot{I}_2 = j\frac{\dot{U}_S}{X_2}. \tag{6.7}$$

As evident from (6.7), the coil currents $\dot{I}_1$ and $\dot{I}_2$ are only determined by the excited AC voltages $\dot{U}_P$ and $\dot{U}_S$, as well as the characteristic reactance X_1 and X_2. Adjusting the detuning factors ε_1 and ε_2 does not influence the coil currents.

Moreover, the inductor currents $\dot{I}_{Lf1}$ and $\dot{I}_{Lf2}$ are derived as

$$\dot{I}_{Lf1} = j\frac{\varepsilon_1 - 1}{X_1}\dot{U}_P + j\frac{\omega M}{X_1 X_2}\dot{U}_S, \tag{6.8}$$

$$\dot{I}_{Lf2} = -j\frac{\varepsilon_2 - 1}{X_2}\dot{U}_S - j\frac{\omega M}{X_1 X_2}\dot{U}_P. \tag{6.9}$$

As indicated by (6.8) and (6.9), both the amplitudes and the phase angles of $\dot{I}_{Lf1}$ and $\dot{I}_{Lf2}$ can be adjusted by modifying ε_1 and ε_2. It is noteworthy that tuning ε_1 solely influences $\dot{I}_{Lf1}$, whereas adjusting ε_2 exclusively impacts $\dot{I}_{Lf2}$. This unique characteristic allows for independent control of $\dot{I}_{Lf1}$ and $\dot{I}_{Lf2}$ through separate adjustments of ε_1 and ε_2.

6.3.2. OUTPUT POWER OF THE SYSTEM

The output power of the proposed system is derived as

$$P_{out} = \mathrm{Re}\{\dot{U}_S \dot{I}^*_{Lf2}\} = \frac{M}{\omega L_{f1} L_{f2}} |\dot{U}_P||\dot{U}_S| \sin(\delta). \tag{6.10}$$

As shown in (6.10), the system output power remains unaffected by the values of ε_1 and ε_2, indicating that dual-side capacitor tuning has little impact on the output power.

6.3.3. ZVS ANALYSIS

To investigate how to achieve ZVS, the phase diagrams of the voltages and currents under dual-side SCC tuning are illustrated in Fig. 6.6. Here, φ_{inv} is the phase difference between $\dot{U}_P$ and $\dot{I}_{Lf1}$, while φ_{rec} is the phase difference between $\dot{U}_S$ and $\dot{I}_{Lf2}$. As shown in Fig. 6.6, with the compensation angle $\Delta\delta$ raises, the phase angles φ_{inv} and φ_{rec} increase accordingly, facilitating ZVS for both the inverter and rectifier. Nonetheless, based on the analysis in Chapter 6.2.2, this approach leads to excessive reactive power at wide output voltages. Fortunately, as indicated by Fig. 6.6, adjusting ε_1 and ε_2 allows for the reduction of φ_{inv} and φ_{rec}, as well as I_{Lf1} and I_{Lf2}. Consequently, when $\Delta\delta$ is selected as the maximum value of $\Delta\delta_1$ and $\Delta\delta_2$ for dual-side ZVS, it is feasible to further regulate ε_1 or ε_2 to minimize excessive reactive power. Details on how to optimize the values of ε_1 and ε_2 are shown in Chapter 6.4.1.

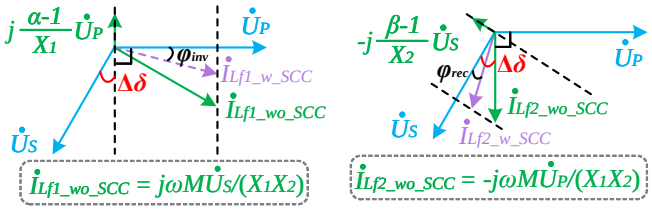

(a) (b)

Figure 6.6: Impact of (a) primary and (b) secondary SCC tuning on ZVS. Here, $\dot{I}_{Lf1\_w\_SCC}$ and $\dot{I}_{Lf1\_wo\_SCC}$ indicate the primary inductor current with and without SCC tuning, while $\dot{I}_{Lf2\_w\_SCC}$ and $\dot{I}_{Lf2\_wo\_SCC}$ represent the secondary inductor current with and without SCC tuning.

6.4. DUAL-SIDE CAPACITOR TUNING AND COOPERATIVE CONTROL

6.4.1. DUAL-SIDE OPTIMAL ZVS

According to [151], to achieve ZVS while minimizing reactive power, the following conditions should be satisfied:

$$i_{Lf1}(t_{P0}) = -I_{ZVS}, i_{Lf2}(t_{S2}) = -I_{ZVS}. \tag{6.11}$$

As shown in (6.11), to achieve optimal ZVS, it is imperative to derive the time-domain expressions for the inductor currents i_{Lf1} and i_{Lf2}. Although the FHA method is accurate

for power calculations, it introduces a notable error in ZVS analysis due to the high-order harmonics. Therefore, it is important to consider the high-order harmonics in i_{Lf1} and i_{Lf2}. Owing to the filtering effects of L_{f1}, C_{f1}, L_{f2} and C_{f1}, the voltages across C_{f1} and C_{f2} (denoted as u_{Cf1} and u_{Cf2}) contain little high-order harmonics [151]. Hence, the calculations of u_{Cf1} and u_{Cf2} can still be achieved using the FHA method, which is expressed as

$$u_{Cf1}(t) = \frac{4\varepsilon_1 V_{in}}{\pi}\sin(\frac{D_P\pi}{2})\sin(\omega t) + \frac{4MV_{out}}{\pi L_{f2}}\sin(\frac{D_S\pi}{2})\sin(\omega t - \frac{\pi}{2} - \Delta\delta), \tag{6.12}$$

$$u_{Cf2}(t) = \frac{4MV_{in}}{\pi L_{f1}}\sin(\frac{D_P\pi}{2})\sin(\omega t) + \frac{4\varepsilon_2 V_{out}}{\pi}\sin(\frac{D_S\pi}{2})\sin(\omega t - \frac{\pi}{2} - \Delta\delta). \tag{6.13}$$

Applying KVL based on Fig. 6.1 and ignoring the loss resistances, the following differential equations are obtained as

$$u_{ab}(t) - u_{Cf1}(t) = L_{f1}\frac{di_{Lf1}(t)}{dt}, u_{Cf2}(t) - u_{cd}(t) = L_{f2}\frac{di_{Lf2}(t)}{dt}. \tag{6.14}$$

By solving (6.14), the time-domain expressions for $i_{Lf1}(t)$ and $i_{Lf2}(t)$ can be obtained.

Using $i_{Lf1}(t)$ as an illustrative example, observing Fig. 6.2 reveals that the inverter output voltage $u_{ab}(t)$ remains constant at V_{in} during the time interval $t_{P0} < t < t_{P1}$, and within this interval, the expression for $i_{Lf1}(t)$ can be derived as follows:

$$i_{Lf1}(t) = i_{Lf1}(t_{P0}) + \frac{1}{L_{f1}}\int_{t_{P0}}^{t}[V_{in} - u_{Cf1}(\tau)]d\tau. \tag{6.15}$$

Moreover, $u_{ab}(t)$ remains at 0 during the period $t_{P1} < t < t_{P2}$, within which the expression for $i_{Lf1}(t)$ can be derived as

$$i_{Lf1}(t) = i_{Lf1}(t_{P1}) + \frac{1}{L_{f1}}\int_{t_{P1}}^{t}[-u_{Cf1}(\tau)]d\tau. \tag{6.16}$$

Given the symmetrical characteristics of the current waveforms, it is apparent that $i_{Lf1}(t_{P0}) = -i_{Lf1}(t_{P2})$. Consequently, the derivation of $i_{Lf1}(t_{P0})$ is as follows:

$$\begin{aligned} i_{Lf1}(t_{P0}) = \quad & -\frac{V_{in}D_P\pi}{2\omega L_{f1}} + \frac{4\varepsilon_1 V_{in}}{\pi\omega L_{f1}}\sin^2(\frac{D_P\pi}{2}) \\ & + \frac{4MV_{out}}{\pi\omega L_{f1}L_{f2}}\sin(\frac{D_S\pi}{2})\cos(\frac{D_P\pi}{2} + \Delta\delta). \end{aligned} \tag{6.17}$$

The derivation of $i_{Lf2}(t_{S2})$ can be accomplished in a similar way, and it is expressed as

$$\begin{aligned} i_{Lf2}(t_{S2}) = \quad & -\frac{V_{out}D_S\pi}{2\omega L_{f2}} + \frac{4\varepsilon_2 V_{out}}{\pi\omega L_{f2}}\sin^2(\frac{D_S\pi}{2}) \\ & + \frac{4MV_{in}}{\pi\omega L_{f1}L_{f2}}\sin(\frac{D_P\pi}{2})\cos(\frac{D_S\pi}{2} + \Delta\delta). \end{aligned} \tag{6.18}$$

Furthermore, substituting (6.17) into (6.11) yields the optimal ε_{1_opt} for achieving the inverter ZVS, which is expressed as

$$\begin{aligned}\varepsilon_{1\_opt} = \quad & \Gamma^{-1} \times [-2\pi\omega L_{f1} L_{f2} I_{ZVS} + V_{in} L_{f2} D_P \pi^2 \\ & -8MV_{out}\sin(D_S\pi/2)\cos(D_P\pi/2+\Delta\delta)],\end{aligned} \tag{6.19}$$

where $\Gamma = 8V_{in}L_{f2}\sin^2(D_P\pi/2)$. Similarly, substituting (6.18) into (6.11) obtains the optimal ε_{2_opt} for rectifier ZVS, which is

$$\begin{aligned}\varepsilon_{2\_opt} = \quad & \Lambda^{-1} \times [-2\pi\omega L_{f1} L_{f2} I_{ZVS} + V_{out} L_{f1} D_S \pi^2 \\ & -8MV_{in}\sin(D_P\pi/2)\cos(D_S\pi/2+\Delta\delta)],\end{aligned} \tag{6.20}$$

where $\Lambda = 8V_{out}L_{f1}\sin^2(D_S\pi/2)$.

Based on the above analysis, it is evident that by dynamically adjusting ε_1 and ε_2 to ε_{1_opt} and ε_{2_opt}, optimal ZVS for both the inverter and rectifier can be achieved with minimal reactive power.

6.4.2. DUAL-SIDE COOPERATIVE CONTROL

To determine the maximum efficiency point for the proposed system, the efficiency of the resonant circuits is derived as

$$\eta_{res} \approx \frac{\omega M L_{f1} L_{f2} |\sin(\delta)|}{AG_{AC} + B/G_{AC} + C}, \tag{6.21}$$

where

$$\begin{cases} A &= [(\varepsilon_2-1)^2 R_{Lf2} + R_2] L_{f1}^2 + R_{Lf1} M^2, \\ B &= [(\varepsilon_1-1)^2 R_{Lf1} + R_1] L_{f2}^2 + R_{Lf2} M^2, \\ C &= 2M\sin(\Delta\delta)[(1-\varepsilon_1)R_{Lf1}L_{f2} + (1-\varepsilon_2)R_{Lf2}L_{f1}] + \omega M L_{f1} L_{f2} |\sin(\delta)|. \end{cases}$$

Observing (6.21) illustrates that the maximum efficiency of the resonant circuits is achieved when G_{AC} satisfy

$$G_{AC\_opt} = \frac{V_{out}\sin(D_S\pi/2)}{V_{in}\sin(D_P\pi/2)} = \sqrt{\frac{[(\varepsilon_1-1)^2 R_{Lf1} + R_1] L_{f2}^2 + R_{Lf2} M^2}{[(\varepsilon_2-1)^2 R_{Lf2} + R_2] L_{f1}^2 + R_{Lf1} M^2}}. \tag{6.22}$$

According to (6.22), there is an optimal relationship between D_P and D_S for maximum efficiency tracking. However, due to the limited computing power of microcontrollers, solving the optimal interrelationship between D_P and D_S in real time is difficult. Therefore, this chapter employs the approach of polynomial fitting to establish the optimal relationship between D_P and D_S, thereby achieving the maximum efficiency tracking.

With the parameters listed in Table 6.1, the optimal relationship between D_P and D_S is constructed in Fig. 6.7. Within Fig. 6.7, the calculated outcomes are derived from (6.22), while the fitted results are generated through polynomial fitting applied to the calculated results. To ensure a satisfactory level of fitting accuracy, a third-order polynomial fit is adopted. It should be noted that when the IPT system operates in the boost mode

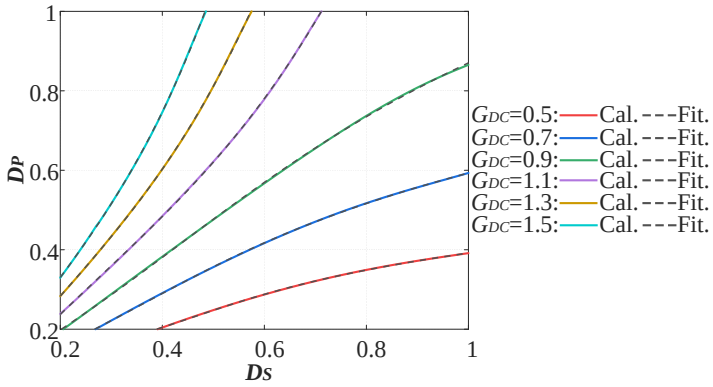

Figure 6.7: Optimal relationship between D_P and D_S for maximum efficiency tracking.

($G_{DC} > 1$), the duty cycle D_P exceeds D_S over the whole power range. To prevent output saturation of the controller, it is preferable to consider D_S as the independent variable in the boost mode, while regarding D_P as the dependent variable. The corresponding fitting relationship for the boost mode is

$$D_P = h_1 D_S^3 + h_2 D_S^2 + h_3 D_S + h_4. \tag{6.23}$$

Conversely, when the system works in the buck mode ($G_{DC} < 1$), the duty cycle D_S is always greater than D_P. Hence, the fitting expression for the buck mode can be given by

$$D_S = h_1 D_P^3 + h_2 D_P^2 + h_3 D_P + h_4. \tag{6.24}$$

6.4.3. REDUCTION OF THE INDUCTOR CURRENTS

To illustrate the effectiveness of the proposed method at wide output voltages, Fig. 6.8 presents its performance in the buck mode with the DC voltage gain at $G_{DC} = 0.5$. In

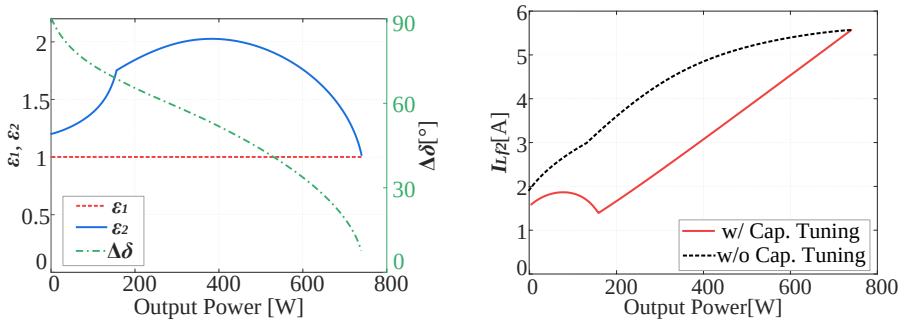

Figure 6.8: Performance of the proposed method in the buck mode ($G_{DC} = 0.5$): (a) variations of ε_1, ε_2 and $\Delta\delta$, (b) comparison of I_{Lf2} with and without capacitor tuning.

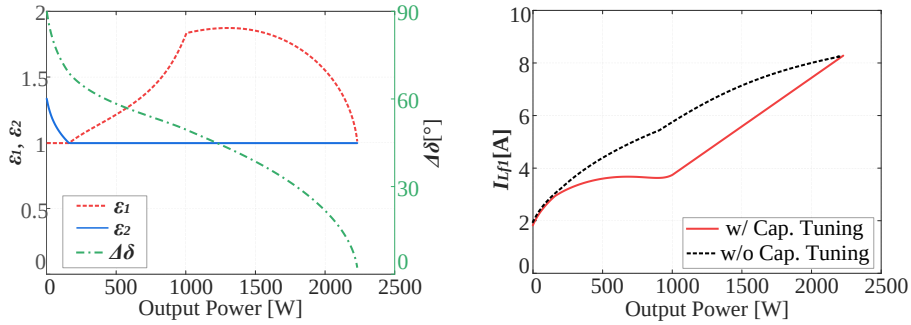

Figure 6.9: Performance of the proposed method in the boost mode (G_{DC} = 1.5): (a) variations of ε_1, ε_2 and $\Delta\delta$, (b) comparison of I_{Lf1} with and without capacitor tuning.

order to achieve dual-side ZVS, the compensation angle $\Delta\delta$ is selected as the maximum value of $\Delta\delta_1$ and $\Delta\delta_2$. Additionally, as shown in Fig. 6.8(a), the value of ε_2 is adjusted as the output power varies. The dynamic tuning of the secondary-side SCC minimizes excessive reactive power caused by the compensation angle $\Delta\delta$, thereby reducing the RMS value of the i_{Lf2}. Fig. 6.8(b) compares the RMS value of i_{Lf2} with and without capacitor tuning. As evident from Fig. 6.8(b), the introduction of SCC tuning contributes to a notable reduction in I_{Lf2}. This reduction not only decreases power losses in the inductor L_{f2}, but also lowers the conduction and turn-off losses for the rectifier, thus improving the overall efficiency.

Furthermore, Fig. 6.9 demonstrates the performance of the proposed approach in the boost mode with the DC voltage gain at G_{DC} = 1.5. By dynamically tuning ε_1 in the boost mode, as shown in Fig. 6.9, the RMS value of i_{Lf2} is reduced within a wide power range, leading to decreased power losses in the inductor L_{f1} as well as reduced conduction and turn-off losses for the inverter.

6.4.4. DESIGN OF DUAL-SIDE SCCS

The operating waveforms of the adopted SCCs are shown in Fig. 6.10. According to [5], the equivalent capacitance of the adopted SCCs can be derived as

$$C_{eq} = \frac{\pi C_x C_y}{\pi C_x + [\pi - \theta - \sin(\theta)] C_y}. \tag{6.25}$$

Considering the tuning range of ε_1 and ε_2, the compensation capacitances C_{x1} and C_{y1} of the primary SCC are designed as 36.3 nF and 24.9 nF, while C_{x2} and C_{y2} of secondary SCC are designed as 36.3 nF and 78 nF, respectively. With the designed parameters, the relationship between ε_1 and θ_P, as well as the relationship between ε_2 and θ_S, can be obtained by combining (6.6) and (6.25).

Moreover, according to the simulation results, the maximum current and voltage stresses across the SCC switches are 13.1 A and 662.9 V, respectively. Notably, when selecting the current and voltage ratings for the SCC switches, sufficient margins should

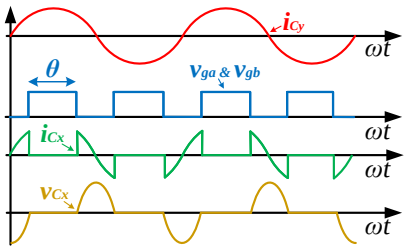

Figure 6.10: Typical operating waveforms of the adopted SCCs.

be considered in practice.

Additionally, based on the measured maximum coil current (13.4 A) in the experiments and the ON-resistance (20 $m\Omega$) of the adopted SCC MOSFETs, the maximum voltage drop caused by the SCC switches is calculated as 0.54 V. Compared with the voltage stresses of inductors and capacitors within the resonant circuits, which can reach hundreds of volts, the maximum voltage drop of 0.54 V is negligible.

It is noteworthy that although introducing SCC increases hardware costs, it notably improves the overall system efficiency. The improved efficiency not only conserves energy but also alleviates thermal stress on the converters and inductors. Hence, for applications demanding high energy efficiency, the proposed method is beneficial.

6

6.4.5. CONTROL FRAMEWORK

Fig. 6.11 presents the control block diagram of the proposed IPT system. Firstly, the DC output voltage is measured by a voltage sensor. Subsequently, a PI controller is employed for voltage tracking. The output of the PI controller depends on the input-to-output DC voltage gain of the system. When the system operates in the boost mode, the output of the PI controller defines the rectifier duty cycle D_S, while the inverter duty cycle D_P is calculated by (6.23). Conversely, if the system works in the buck mode, the PI controller

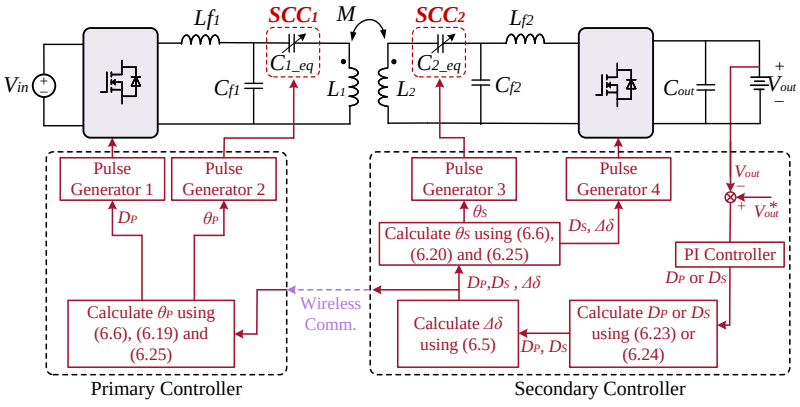

Figure 6.11: Block diagram of the proposed dual-side capacitor tuning and cooperative control method.

generates D_P, with D_S determined by (6.24). After the duty cycles D_P and D_S are obtained, the compensation angle $\Delta\delta$ is calculated by (6.11) to implement ZVS for both the inverter and rectifier. Additionally, the SCC control angles θ_P and θ_S are also derived and applied to the dual-side SCCs to enable dynamic capacitor tuning, thereby reducing the inductor currents and minimizing turn-OFF currents for the converters.

6.5. EXPERIMENTAL RESULTS

6.5.1. EXPERIMENTAL PROTOTYPE

To demonstrate the effectiveness of the proposed method, a 2.0 kW scale-down IPT prototype with a reconfigurable DLCC topology was developed, as shown in Fig. 6.12. The configurations of DC voltages and rated power of the scale-down prototype are based on the reference design recommended in SAEJ 2954 standard [1], as illustrated in Table 6.2. For the reference design, the 600 V DC input voltage can be provided by a front-end

Table 6.2: Specifications of the reference design and the scale-down prototype

Symbol	Specifications	Reference design [1]	Scale-down prototype
P_R	Rated power	7.7 [kW]	2.0 [kW]
V_{in}	DC input voltage	600 [V]	300 [V]
V_{out}	DC output voltage	300-900 [V]	150-450 [V]
I_R	Rated charging current	9.0 [A]	4.5 [A]
f	Switching frequency	85 [kHz]	85 [kHz]

1 The reference design is based on the SAE J2954 standard [1].

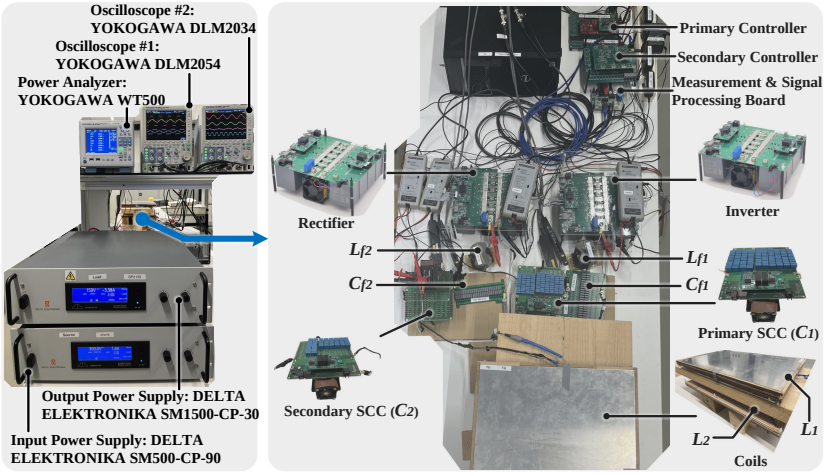

Figure 6.12: Experimental setup of the DLCC-compensated IPT system used to verify the proposed dual-side capacitor tuning and cooperative control method [3–5].

power factor correction (PFC) converter, while the 300-900 V DC output voltage accommodates most EV battery voltages. Based on the reference design, the DC voltages of the developed prototype are scaled down by a factor of 0.5. Notably, the application of the proposed method is suited for residential wireless EV charging, where the battery charging current is relatively low, and the thermal issue of batteries is not a significant concern. Moreover, this prototype utilizes two H-bridge converters as the inverter and rectifier stages, with two separate SCCs on the primary and secondary sides, respectively. The entire system was powered by a constant 300 V DC source, with a bidirectional DC power supply serving as an electronic load. The control algorithm and pulse generation were implemented through TI Launchpads F28379D. To achieve ZVS for the power switches, the designed minimum ZVS current was set to 2 A. It is noteworthy that in the proposed method, the control variables need to be transmitted from the secondary to the primary. Additionally, the primary circuit parameters may need to be transmitted to the secondary controller in practice. Hence, wireless communication between the primary and secondary sides is essential. In the prototype, the nRF24L01+ module is used to achieve dual-side information exchange. More parameters are shown in Table 6.1.

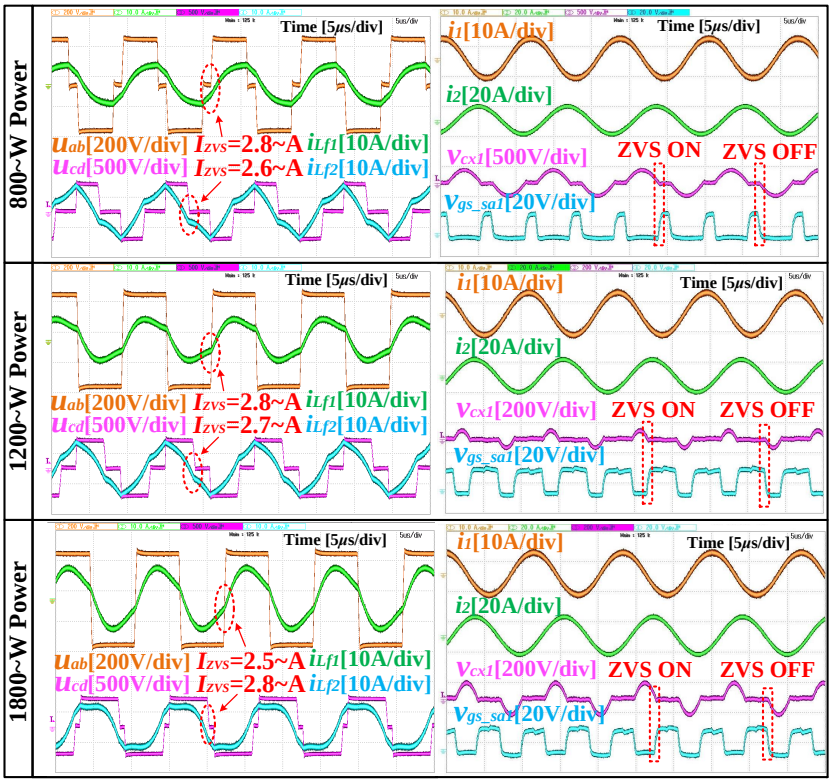

Figure 6.13: Steady-state operating waveforms of the proposed method when delivering various power in boost mode (V_{out} =450 V, G_{DC}=1.5). Here, v_{cx1} indicates the voltage stress across the capacitor (C_{x1}) within the primary SCC, while v_{gs_sa1} denotes the gate-source voltage across the power switch (S_{a1}) in the primary SCC.

6.5.2. STEADY-STATE OPERATING WAVEFORMS

Fig. 6.13 presents the steady-state operating waveforms of the proposed method in the boost mode. Here, the output voltage is adjusted at 450 V with a DC voltage gain of G_{DC}=1.5. As demonstrated in Fig. 6.13, the proposed method simultaneously adjusts the inverter and rectifier duty cycles (D_P and D_S), as well as the phase difference between u_{ab} and u_{cd} (δ), to achieve power regulation, ZVS operations, and maximum efficiency tracking under load variations. More importantly, the primary-side SCC is dynamically regulated in the boost mode. Fig. 6.13 also displays the operating waveforms of the primary-side SCC (see the waveforms of v_{cx1} and v_{gs_sa1}). As it can be observed, the SCC consistently achieves ZVS turn-ON and turn-OFF under power variations, thus reducing the switching losses of the SCC MOSFETs. Additionally, thanks to the dynamic capacitor tuning, the ZVS of both the inverter and rectifier is achieved with minimized ZVS current. As illustrated in Fig. 6.13, the minimum ZVS currents for both the inverter and rectifier are regulated at around the designed value of 2 A.

Moreover, the steady-state operating waveforms of the proposed method in the buck

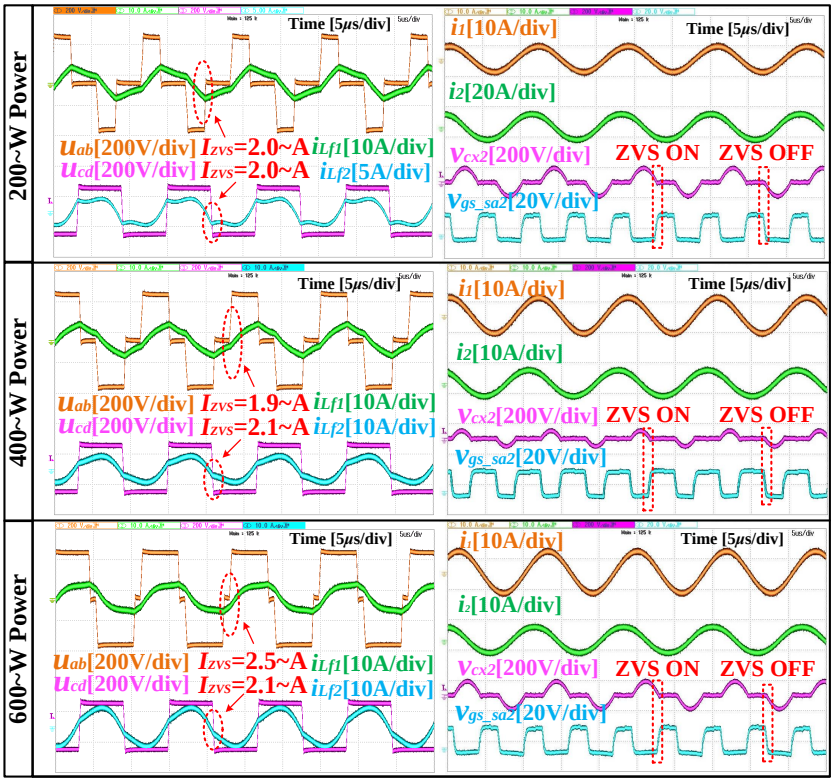

Figure 6.14: Steady-state operating waveforms of the proposed method when delivering various power in buck mode (V_{out} =150 V, G_{DC}=0.5). Here, v_{cx2} indicates the voltage stress across the capacitor (C_{x2}) in the secondary SCC, while v_{gs_sa2} is the gate-source voltage across the power switch (S_{a2}) in the secondary SCC.

mode, where the output voltage is regulated to 150 V with a DC voltage gain at G_{DC}=0.5, is further demonstrated in Fig. 6.14. To minimize the reactive power in the buck mode, the secondary-side SCC is dynamically adjusted. The secondary-side SCC achieves ZVS turn-ON and turn-OFF to lower the SCC switching losses as well. Meanwhile, the minimum ZVS current for both the inverter and rectifier is also tuned to approximately 2 A.

6.5.3. BENCHMARK WITH TPS

To illustrate the enhanced efficiency achieved by the proposed method, the operating waveforms and measured DC-to-DC efficiency of the proposed method are benchmarked with the existing TPS method, as shown in Fig. 6.15 and Fig. 6.16.

When delivering 1 kW power in the boost mode (V_{out}=450 V, G_{DC}=1.5), as shown in Fig. 6.15(a), the RMS value of i_{Lf1} reaches 6.5 A under the TPS control, while the minimum ZVS current of the inverter reaches up to 9.2 A. However, owing to the dynamic tuning of the primary-side SCC, as shown in Fig. 6.15(b), the RMS value of i_{Lf1} is reduced from 6.5 A to 4.2 A in the proposed method, and the minimum ZVS current of the inverter is decreased from 9.2 A to 2.8 A. Consequently, the efficiency is improved from 92.7 % to 94.5 % in the proposed method, resulting in an efficiency improvement of up to 1.8 %. Fig. 6.16 further presents the comparisons in the buck mode (V_{out}=150 V, G_{DC}=0.5). With active tuning of the secondary-side SCC, the proposed method reduces the RMS value of i_{Lf2} from 4.5 A to 2.4 A when delivering 300 W, and also decreases the minimum rectifier

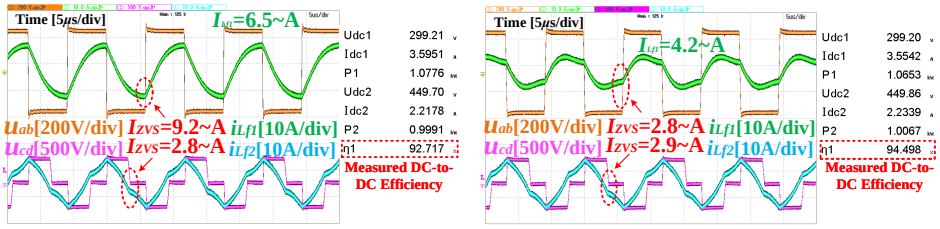

(a) (b)

Figure 6.15: Benchmark when delivering 1 kW power in the boost mode (V_{out}=450 V, G_{DC}=1.5): operating waveforms and measured DC-to-DC efficiency of (a) the TPS method, and (b) the proposed method.

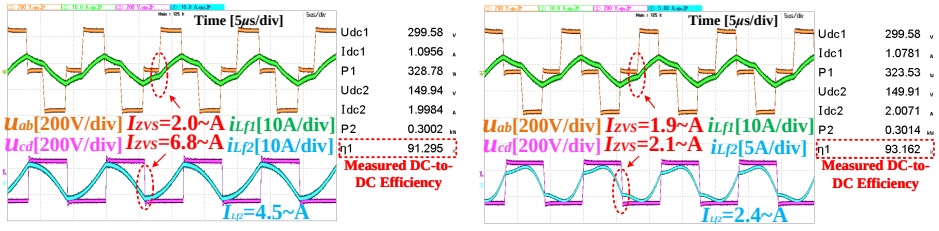

(a) (b)

Figure 6.16: Benchmark when delivering 300 W power in the boost mode (V_{out}=150 V, G_{DC}=0.5): operating waveforms and measured DC-to-DC efficiency of (a) the TPS method, and (b) the proposed method.

ZVS current from 6.8 A to 2.1 A. This results in an efficiency improvement of up to 1.9 %, with the efficiency improved from 91.3 % to 93.2 %.

6.5.4. POWER LOSS BREAKDOWN AND EFFICIENCY COMPARISONS

Moreover, Fig. 6.17 demonstrates the calculated power loss breakdown for the above experiments. As shown in Fig. 6.17(a), when operating in the boost mode, the proposed method significantly reduces both the inverter and inductor losses. These loss reductions result from the decreased primary inductor current and inverter turn-off currents. Meanwhile, the losses of the rectifier, capacitors, and coils exhibit similar performance in both methods. Conversely, as shown in Fig. 6.17(b), the proposed method notably decreases the rectifier and inductor losses by reducing the secondary inductor current and rectifier turn-OFF currents in the buck mode. In this case, the losses of the inverter, capacitors, and coils are similar.

Notably, considering the low ON-resistance of SCC MOSFETs, the conduction losses caused by SCC MOSFETs are not significant. Moreover, the SCC switching losses are

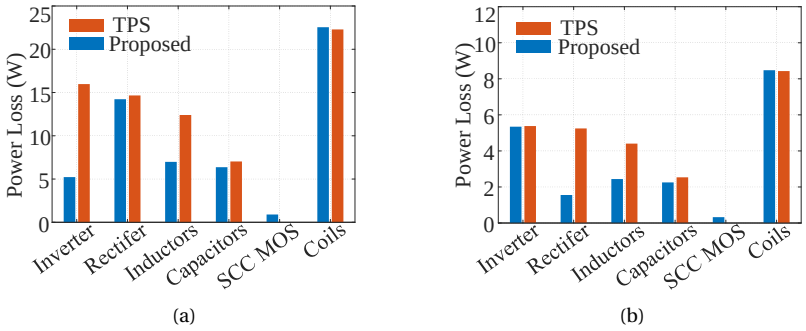

Figure 6.17: Calculated power loss breakdown for the proposed method and the conventional TPS method: (a) when delivering 1 kW in the boost mode; (b) when delivering 300 W in the buck mode.

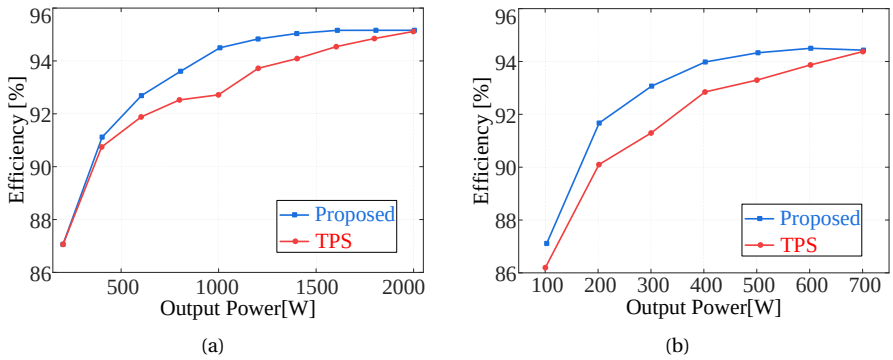

Figure 6.18: Efficiency comparisons between the proposed method and the TPS method under various output power levels: (a) in the boost mode (V_{out}=450 V, G_{DC}=1.5), and (b) in the buck mode (V_{out}=150 V, G_{DC}=0.5).

minimized through the implementation of zero-voltage turn-ON and zero-voltage turn-OFF. Therefore, the extra losses caused by the SCC MOSFETs are not significant in both the boost and buck modes.

Furthermore, the efficiency of the proposed scheme is evaluated in comparison with the TPS method across various output power levels, as visualized in Fig. 6.18. It demonstrates that the proposed method enhances the efficiency over a broad output power, achieving a maximum efficiency improvement of 1.8 % in the boost mode and 1.9 % in the buck mode.

6.5.5. IMPLEMENTATION OF CC-CV CHARGING

To validate the feasibility of the proposed approach for EV battery charging, experiments are further carried out under constant current (CC) and constant voltage (CV) modes. As shown in Fig. 6.19, the proposed approach is able to implement CC and CV charging profiles under both the boost and buck modes, achieving a peak efficiency of 95.16% (in the boost mode) and 94.5 % (in the buck mode), respectively.

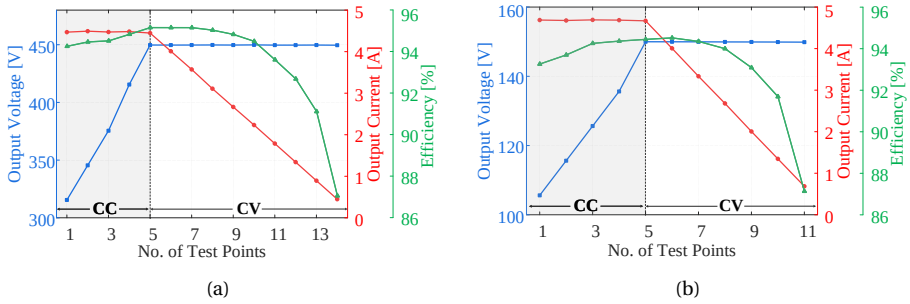

Figure 6.19: Implementation of CC-CV charging profile in the experiments: measured DC output voltage, DC output current, and DC-to-DC efficiency in (a) the boost mode, and (b) the buck mode.

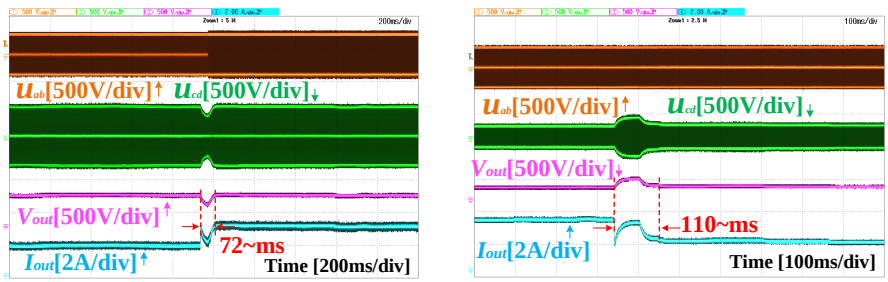

Figure 6.20: Transient response of the proposed method: (a) when the equivalent DC load is increased from 250 Ω to 150 Ω (V_{out}=450 V), (b) when the equivalent DC load is reduced from 50 Ω to 100 Ω (V_{out}=150 V).

6.5.6. TRANSIENT RESPONSE

To demonstrate the feasibility of the proposed method in practical EV charging applications, the transient response capability of this method is evaluated. Here, the DC output voltage is measured utilizing a signal measurement & processing board, while a PI controller is employed for constant voltage tracking.

Fig. 6.20(a) shows the dynamic performance of the proposed method when the equivalent DC load is increased from 250 Ω to 150 Ω in the boost mode. As it can be observed, the output voltage is reliably controlled at 450 V under load changes, with the response time at 72 ms. Moreover, Fig. 6.20(b) presents the dynamic performance in the buck mode. Experiments reveal that the proposed method restores the output voltage within 110 ms when the equivalent DC load is reduced from 50 Ω to 100 Ω.

6.6. CONCLUSIONS

In this chapter, a dual-side cooperative control strategy is proposed to optimize efficiency over a wide output voltage range in wireless EV charging applications. To mitigate the increased reactive power when the DC output voltage varies significantly, the proposed method integrates two separate SCCs into the DLCC topology. Based on the dual-side capacitor tuning, this approach notably reduces the inductor RMS currents and minimizes turn-OFF currents for the converters, thereby improving efficiency across broad output power levels and output voltages. Experimental results are presented, demonstrating that the proposed method achieves a notably higher efficiency compared with the existing TPS method in both the buck and boost modes.

7

CONCLUSION

This thesis investigates inductive power transfer (IPT) technologies for achieving highly efficient wireless charging of electric vehicles (EVs). To achieve wide-range output power regulation and maintain high transfer efficiency across a broad operating range, modulation and control techniques for power converters and compensation networks are explored. The research begins by addressing several key technical challenges in wireless EV charging. Based on these challenges, four research questions are proposed. Subsequently, the thesis is divided into three parts (encompassing five chapters in total) to address these questions, focusing on hybrid modulation and control, parameter identification and impedance tuning, and variable DLCC compensation.

7.1. REGARDING THE RESEARCH QUESTIONS

1. How to achieve wide-range output power regulation while maintaining high transmission efficiency under significant battery load variations?

The CC-CV charging profile of EV batteries necessitates wide output power regulation capability of wireless EV charging systems. However, existing power regulation methods result in notable efficiency drops under considerable load variations.

To maintain high efficiency at light-load conditions, Chapter 2 presents a mode-switching based phase shift control (MS-PSC) for achieving wide output power regulation. In the proposed MS-PSC method, both the inverter and active rectifier are modulated and controlled to implement wide power regulation, maximum efficiency tracking (also known as optimal load tracking), and wide ZVS operations simultaneously. In the proposed system, the front-end and back-end DC-DC converters in conventional IPT systems are eliminated, allowing power to be directly transferred from the PFC output to the battery. More importantly, hybrid operating modes, including the half-bridge (HB), mixed-bridge (MB), and full-bridge (FB) modes, are implemented. Based on the mode transitions of both the inverter and the rectifier, the proposed MS-PSC method guarantees a wide-range ZVS with minimized circulation of reactive power. The effectiveness of the proposed MS-PSC method is experimentally validated, demonstrating notable ef-

ficiency improvement over the conventional triple-phase-shift (TPS) method. Specifically, the proposed MS-PSC method enhances efficiency in the 10%-63% rated power range, with efficiency improvements from 1.5% to 6%. Consequently, the proposed system demonstrates DC-to-DC efficiency between 93.5% and 96.1% in the 1-10 kW power range.

Furthermore, in Chapter 3, a hybrid modulation (HM) technique is proposed to facilitate secondary-side control in wireless EV charging systems. The secondary-side control technique enables communication-less power regulation, thereby significantly reducing control complexity. To achieve broad power regulation in secondary-side controlled IPT systems, the conventional phase shift modulation (PSM), also known as pulse width modulation (PWM), exhibits significant efficiency drop under light loads, whereas the existing pulse density modulations (PDMs) lead to considerable current and voltage ripples. To address this challenge, an optimal discrete PDM (DPDM) is first proposed for active rectifier modulation. By symmetrically and uniformly distributing pulses, the proposed optimal D-PDM eliminates even-subharmonics in rectifier input voltage, thereby reducing the current distortions and output voltage ripple while removing the capacitor DC blocking voltages. Moreover, the pulse width regulation is incorporated into the optimal D-PDM, enabling continuous output tuning and further minimizing subharmonics in the voltage. Experiments are carried out, demonstrating that the proposed HM significantly mitigates current and voltage ripples while facilitating continuous tuning when compared with the existing PDMs. Additionally, when compared to the PWM, the proposed HM demonstrates notable efficiency improvements within the 10%-60% power range, achieving a maximum efficiency enhancement of up to 5.5%.

2. How to address parameter deviations caused by coil misalignment and capacitance drift in practical EV charging applications?

Due to coil misalignment and capacitance drift, parameter deviations are inevitable in practical wireless EV charging applications. The parameter deviations within the resonant circuits result in non-resonant operating conditions, leading to decreased transmission efficiency and a lower power factor.

To address significant parameter deviations, Chapter 4 proposes a parameter identification method to identify the unknown parameters of the resonant circuits. The proposed approach is achieved by only measuring the RMS values of the coil currents, and there is no need for phase detection circuits and auxiliary measurement coils. Furthermore, according to the identified parameters, an impedance tuning method is proposed to address the issue of system detuning caused by parameter deviations. Therein, the undesirable reactance of the resonant circuits is minimized by adjusting the system frequency and the phase shift angles of the active rectifier. Experimental results demonstrate that the unknown parameters of the resonant circuits are recognized accurately in the proposed parameter identification approach, with the average relative errors all less than 3%. Moreover, by implementing the proposed impedance tuning method, the DC to DC efficiency of the IPT system is improved by 4.3%-15% in the experiments.

3. What strategies can be employed to effectively address asymmetric parameters caused by varying receiver configurations in different EV models?

To enhance the interoperability of the wireless EV charger, it is preferable for the IPT system to accommodate diverse EV models available in the market. The diversity of EV models leads to distinct configurations of receiver coils, leading to asymmetry in primary and secondary parameters.

To manage asymmetric parameters of the IPT system, Chapter 5 presents an optimal multivariable control (OMC) strategy for a double-sided LCC (DLCC) compensation network. The DLCC network is investigated as it provides constant coil currents under poor coupling conditions, thus significantly improving the robustness of the system under varying air gaps and coil misalignment. Within Chapter 5, the limitations of existing methods under asymmetric parameters are firstly identified: under the asymmetric parameters, existing control methods exhibit increased reactive power and reduced system efficiency under varying load conditions. Subsequently, to mitigate reactive power and achieve higher efficiency, the proposed OMC method incorporates dual-side hybrid modulation and primary-side switch-controlled-capacitor (SCC) tuning into the triple-phase-shift (TPS) control. Through collaborative modulation and control of the inverter, rectifier, and SCC, the proposed OMC method reduces the RMS values of the circulating currents and lowers the turn-OFF currents for the converters. As a result, this approach improves efficiency in both light- and heavy-load conditions, enabling wide output regulation and full-range efficiency optimization simultaneously. Finally, experimental results are presented, demonstrating the superiority of the proposed OMC method. Compared with the existing TPS methods, the proposed method achieves higher DC-to-DC efficiency in the power range of 0.2-2.2 kW, with a maximum efficiency improvement of up to 6.3%.

4. How can wide output voltage variations arising from diverse nominal battery voltages across various EV models be effectively accommodated?

The public wireless EV chargers should ideally accommodate distinct nominal battery voltages across various EV models. Nevertheless, when the system must manage wide output voltage variations, existing methods exhibit notable efficiency drops under load variations.

To manage wide output voltage variations while maintaining high overall efficiency, Chapter 6 proposes a dual-side capacitor tuning and cooperative control strategy. Within Chapter 6, a reconfigurable DLCC compensation network is first proposed by incorporating two switch-controlled capacitors (SCCs) on the primary and secondary sides, respectively. Subsequently, optimal capacitor tuning factors are derived to reduce the RMS values of the inductor currents and to minimize the turn-OFF currents across the semiconductors. Furthermore, a dual-side cooperative control strategy is proposed. Through the collaborative control of the inverter, rectifier, and SCCs, the proposed approach achieves dual-side optimal zero-voltage-switching (ZVS), wide power regulation, and maximum efficiency tracking simultaneously. Experimental results demonstrate that the proposed method achieves notable efficiency improvement over a wide input-to-output DC voltage gain (0.5-1.5) without requiring additional DC-DC converters, with a maximum efficiency improvement of up to 1.9%.

7.2. OUTLOOK

Following this research, several potential research directions are demonstrated as follows.

(1) COMMERCIALIZATION OF THE PROPOSED SOLUTIONS

While this thesis verifies the effectiveness of the proposed solutions using laboratory prototypes, a range of additional factors must be addressed for commercialization. Future work should focus on real-world production challenges such as ensuring electromagnetic compatibility (EMC), adhering to human safety standards, and optimizing manufacturing costs. Additionally, considerations around reliability, robustness in various operational environments, and scalability for mass production are critical to facilitate a smooth transition from prototype to market-ready products.

(2) MULTI-PORT WIRELESS EV CHARGING SYSTEMS

This thesis presents several solutions aimed at enhancing system interoperability for public wireless EV charging applications. However, these solutions are developed for a single IPT system. In real-world public EV charging scenarios, simultaneous charging of multiple EVs is essential. Therefore, extending the proposed solutions from this thesis to address multi-port wireless EV charging systems would provide valuable research insights.

(3) HIGH-POWER AND HIGH-FREQUENCY IPT TECHNOLOGIES FOR FAST EV CHARGING

In this thesis, the charging power of the systems is tailored for light-duty EV charging, achieving a maximum power of 10 kW in experimental setups. However, light-duty EVs are capable of handling DC fast charging up to hundreds of kW. Therefore, exploring high-power wireless fast charging for EVs is valuable. Given the limited space available in light-duty EVs, optimizing the power density of the high-power charging systems is indispensable. While industry standards have identified a frequency range of 79-90 kHz, investigating higher frequencies (above 100 kHz) for achieving higher power density presents an intriguing topic for academic exploration.

(4) POTENTIAL INDUSTRY APPLICATIONS BEYOND EV CHARGING

Although this thesis primarily investigates IPT technologies for EV charging applications, there are additional application scenarios that warrant exploration. For example, wireless charging for maritime vehicles could benefit from galvanic isolation in challenging environments. Another application could involve using IPT systems to electrify robotic devices, leveraging the flexibility and automation of wireless charging.

BIBLIOGRAPHY

BIBLIOGRAPHY

[1] SAE J2954 standard, Wireless power transfer for light-duty plug-in/electric vehicles and alignment methodology. [Online]. Available: www.sae.org/standards/content/j2954_202010/

[2] Por rick wiens, What is a capacitor and what are the different types, 2023. [Online]. Available: https://www.digikey.com/es/articles/what-is-a-capacitor-and-what-are-the-different-types

[3] W. Shi, J. Dong, T. B. Soeiro, C. Riekerk, F. Grazian, G. Yu, and P. Bauer, "Design of a highly efficient 20-kw inductive power transfer system with improved misalignment performance," *IEEE Transactions on Transportation Electrification*, vol. 8, no. 2, pp. 2384–2399, 2021.

[4] F. Grazian, T. B. Soeiro, and P. Bauer, "Design trade-offs between the coupled coils' inductance and the series-series compensation capacitance for ev wireless charging systems," in *2022 International Symposium on Power Electronics, Electrical Drives, Automation and Motion (SPEEDAM)*. IEEE, 2022, pp. 270–276.

[5] ——, "Inductive power transfer based on variable compensation capacitance to achieve an ev charging profile with constant optimum load," *IEEE Journal of Emerging and Selected Topics in Power Electronics*, vol. 11, no. 1, pp. 1230–1244, 2022.

[6] A. Kurs, A. Karalis, R. Moffatt, J. D. Joannopoulos, P. Fisher, and M. Soljacic, "Wireless power transfer via strongly coupled magnetic resonances," *science*, vol. 317, no. 5834, pp. 83–86, 2007.

[7] M. Song, P. Jayathurathnage, E. Zanganeh, M. Krasikova, P. Smirnov, P. Belov, P. Kapitanova, C. Simovski, S. Tretyakov, and A. Krasnok, "Wireless power transfer based on novel physical concepts," *Nature Electronics*, vol. 4, no. 10, pp. 707–716, 2021.

[8] S. Y. R. Hui, W. Zhong, and C. K. Lee, "A critical review of recent progress in mid-range wireless power transfer," *IEEE Transactions on Power Electronics*, vol. 29, no. 9, pp. 4500–4511, 2013.

[9] B. Wang, W. Yerazunis, and K. H. Teo, "Wireless power transfer: Metamaterials and array of coupled resonators," *Proceedings of the IEEE*, vol. 101, no. 6, pp. 1359–1368, 2013.

[10] L. Xie, Y. Shi, Y. T. Hou, and A. Lou, "Wireless power transfer and applications to sensor networks," *IEEE Wireless Communications*, vol. 20, no. 4, pp. 140–145, 2013.

[11] C. J. Stevens, "Magnetoinductive waves and wireless power transfer," *IEEE Transactions on Power Electronics*, vol. 30, no. 11, pp. 6182–6190, 2014.

[12] Y. Zeng, B. Clerckx, and R. Zhang, "Communications and signals design for wireless power transmission," *IEEE Transactions on Communications*, vol. 65, no. 5, pp. 2264–2290, 2017.

[13] K. Huang and V. K. Lau, "Enabling wireless power transfer in cellular networks: Architecture, modeling and deployment," *IEEE Transactions on Wireless Communications*, vol. 13, no. 2, pp. 902–912, 2014.

[14] T. Fujita, T. Yasuda, and H. Akagi, "A dynamic wireless power transfer system applicable to a stationary system," *IEEE Transactions on Industry Applications*, vol. 53, no. 4, pp. 3748–3757, 2017.

[15] Z. N. Low, R. A. Chinga, R. Tseng, and J. Lin, "Design and test of a high-power high-efficiency loosely coupled planar wireless power transfer system," *IEEE transactions on industrial electronics*, vol. 56, no. 5, pp. 1801–1812, 2008.

[16] M. Xia and S. Aissa, "On the efficiency of far-field wireless power transfer," *IEEE transactions on signal processing*, vol. 63, no. 11, pp. 2835–2847, 2015.

[17] W. Zhong, C. K. Lee, and S. R. Hui, "General analysis on the use of tesla's resonators in domino forms for wireless power transfer," *IEEE transactions on industrial electronics*, vol. 60, no. 1, pp. 261–270, 2011.

[18] J. Garnica, R. A. Chinga, and J. Lin, "Wireless power transmission: From far field to near field," *Proceedings of the IEEE*, vol. 101, no. 6, pp. 1321–1331, 2013.

[19] M. Wagih, A. S. Weddell, and S. Beeby, "Rectennas for radio-frequency energy harvesting and wireless power transfer: A review of antenna design [antenna applications corner]," *IEEE Antennas and Propagation Magazine*, vol. 62, no. 5, pp. 95–107, 2020.

[20] J. Huang, Y. Zhou, Z. Ning, and H. Gharavi, "Wireless power transfer and energy harvesting: Current status and future prospects," *IEEE wireless communications*, vol. 26, no. 4, pp. 163–169, 2019.

[21] C. T. Rodenbeck, P. I. Jaffe, B. H. Strassner II, P. E. Hausgen, J. O. McSpadden, H. Kazemi, N. Shinohara, B. B. Tierney, C. B. DePuma, and A. P. Self, "Microwave and millimeter wave power beaming," *IEEE Journal of Microwaves*, vol. 1, no. 1, pp. 229–259, 2021.

[22] K. Jin and W. Zhou, "Wireless laser power transmission: A review of recent progress," *IEEE Transactions on Power Electronics*, vol. 34, no. 4, pp. 3842–3859, 2018.

[23] S. Roy, A. W. Azad, S. Baidya, M. K. Alam, and F. Khan, "Powering solutions for biomedical sensors and implants inside the human body: A comprehensive review on energy harvesting units, energy storage, and wireless power transfer techniques," *IEEE Transactions on Power Electronics*, vol. 37, no. 10, pp. 12 237–12 263, 2022.

[24] X. Lu, P. Wang, D. Niyato, D. I. Kim, and Z. Han, "Wireless charging technologies: Fundamentals, standards, and network applications," *IEEE communications surveys & tutorials*, vol. 18, no. 2, pp. 1413–1452, 2015.

[25] H.-J. Kim, H. Hirayama, S. Kim, K. J. Han, R. Zhang, and J.-W. Choi, "Review of near-field wireless power and communication for biomedical applications," *IEEE Access*, vol. 5, pp. 21 264–21 285, 2017.

[26] K. Dautov, M. Hashmi, G. Nauryzbayev, and N. Nasimuddin, "Recent advancements in defected ground structure-based near-field wireless power transfer systems," *IEEE access*, vol. 8, pp. 81 298–81 309, 2020.

[27] J. Park, Y. Tak, Y. Kim, Y. Kim, and S. Nam, "Investigation of adaptive matching methods for near-field wireless power transfer," *IEEE Transactions on Antennas and Propagation*, vol. 59, no. 5, pp. 1769–1773, 2011.

[28] K. Zhang, C. Liu, Z. H. Jiang, Y. Zhang, X. Liu, H. Guo, and X. Yang, "Near-field wireless power transfer to deep-tissue implants for biomedical applications," *IEEE Transactions on Antennas and Propagation*, vol. 68, no. 2, pp. 1098–1106, 2019.

[29] B. Luo, T. Long, L. Guo, R. Dai, R. Mai, and Z. He, "Analysis and design of inductive and capacitive hybrid wireless power transfer system for railway application," *IEEE Transactions on Industry Applications*, vol. 56, no. 3, pp. 3034–3042, 2020.

[30] X. Li, C. Tang, X. Dai, P. Deng, and Y. Su, "An inductive and capacitive combined parallel transmission of power and data for wireless power transfer systems," *IEEE Transactions on Power Electronics*, vol. 33, no. 6, pp. 4980–4991, 2017.

[31] F. Lu, H. Zhang, H. Hofmann, and C. C. Mi, "An inductive and capacitive combined wireless power transfer system with lc-compensated topology," *IEEE Transactions on Power Electronics*, vol. 31, no. 12, pp. 8471–8482, 2016.

[32] J. Dai and D. C. Ludois, "A survey of wireless power transfer and a critical comparison of inductive and capacitive coupling for small gap applications," *IEEE Transactions on Power Electronics*, vol. 30, no. 11, pp. 6017–6029, 2015.

[33] Z. Zhang, H. Pang, A. Georgiadis, and C. Cecati, "Wireless power transfer—an overview," *IEEE transactions on industrial electronics*, vol. 66, no. 2, pp. 1044–1058, 2018.

[34] A. Ahmad, M. S. Alam, and R. Chabaan, "A comprehensive review of wireless charging technologies for electric vehicles," *IEEE transactions on transportation electrification*, vol. 4, no. 1, pp. 38–63, 2017.

[35] D. Patil, M. K. McDonough, J. M. Miller, B. Fahimi, and P. T. Balsara, "Wireless power transfer for vehicular applications: Overview and challenges," *IEEE Transactions on Transportation Electrification*, vol. 4, no. 1, pp. 3–37, 2017.

[36] M. Schormans, V. Valente, and A. Demosthenous, "Practical inductive link design for biomedical wireless power transfer: A tutorial," *IEEE Transactions on Biomedical Circuits and Systems*, vol. 12, no. 5, pp. 1112–1130, 2018.

[37] J. H. Kim, B.-S. Lee, J.-H. Lee, S.-H. Lee, C.-B. Park, S.-M. Jung, S.-G. Lee, K.-P. Yi, and J. Baek, "Development of 1-mw inductive power transfer system for a high-speed train," *IEEE Transactions on Industrial Electronics*, vol. 62, no. 10, pp. 6242–6250, 2015.

[38] S.-H. Lee, B.-S. Lee, and J.-H. Lee, "A new design methodology for a 300-kw, low flux density, large air gap, online wireless power transfer system," *IEEE Transactions on Industry Applications*, vol. 52, no. 5, pp. 4234–4242, 2016.

[39] J. Shin, S. Shin, Y. Kim, S. Ahn, S. Lee, G. Jung, S.-J. Jeon, and D.-H. Cho, "Design and implementation of shaped magnetic-resonance-based wireless power transfer system for roadway-powered moving electric vehicles," *IEEE Transactions on Industrial electronics*, vol. 61, no. 3, pp. 1179–1192, 2013.

[40] S. Sinha, A. Kumar, B. Regensburger, and K. K. Afridi, "A new design approach to mitigating the effect of parasitics in capacitive wireless power transfer systems for electric vehicle charging," *IEEE Transactions on Transportation Electrification*, vol. 5, no. 4, pp. 1040–1059, 2019.

[41] S. Hui, "Planar wireless charging technology for portable electronic products and qi," *Proceedings of the IEEE*, vol. 101, no. 6, pp. 1290–1301, 2013.

[42] Y. Wang, Z. Sun, Y. Guan, and D. Xu, "Overview of megahertz wireless power transfer," *Proceedings of the IEEE*, 2023.

[43] R. Guida, E. Demirors, N. Dave, and T. Melodia, "Underwater ultrasonic wireless power transfer: A battery-less platform for the internet of underwater things," *IEEE Transactions on Mobile Computing*, vol. 21, no. 5, pp. 1861–1873, 2020.

[44] O. Lucia, P. Maussion, E. J. Dede, and J. M. Burdío, "Induction heating technology and its applications: past developments, current technology, and future challenges," *IEEE Transactions on industrial electronics*, vol. 61, no. 5, pp. 2509–2520, 2013.

[45] P. E. Glaser, "Power from the sun: Its future," *Science*, vol. 162, no. 3856, pp. 857–861, 1968.

[46] D. C. Ludois, J. K. Reed, and K. Hanson, "Capacitive power transfer for rotor field current in synchronous machines," *IEEE Transactions on Power Electronics*, vol. 27, no. 11, pp. 4638–4645, 2012.

[47] J. Moore, S. Castellanos, S. Xu, B. Wood, H. Ren, and Z. T. H. Tse, "Applications of wireless power transfer in medicine: State-of-the-art reviews," *Annals of biomedical engineering*, vol. 47, pp. 22–38, 2019.

[48] M. Song, P. Belov, and P. Kapitanova, "Wireless power transfer inspired by the modern trends in electromagnetics," *Applied physics reviews*, vol. 4, no. 2, 2017.

[49] C. T. Rim and C. Mi, *Wireless power transfer for electric vehicles and mobile devices*. John Wiley & Sons, 2017.

[50] M. Tavana, M. Ozger, A. Baltaci, B. Schleicher, D. Schupke, and C. Cavdar, "Wireless power transfer for aircraft iot applications: System design and measurements," *IEEE Internet of Things Journal*, vol. 8, no. 15, pp. 11 834–11 846, 2021.

[51] K. Agarwal, R. Jegadeesan, Y.-X. Guo, and N. V. Thakor, "Wireless power transfer strategies for implantable bioelectronics," *IEEE reviews in biomedical engineering*, vol. 10, pp. 136–161, 2017.

[52] F. Lu, H. Zhang, and C. Mi, "A two-plate capacitive wireless power transfer system for electric vehicle charging applications," *IEEE Transactions on Power Electronics*, vol. 33, no. 2, pp. 964–969, 2017.

[53] L. Li, H. Liu, H. Zhang, and W. Xue, "Efficient wireless power transfer system integrating with metasurface for biological applications," *IEEE Transactions on Industrial Electronics*, vol. 65, no. 4, pp. 3230–3239, 2017.

[54] N. Shinohara, "History and innovation of wireless power transfer via microwaves," *IEEE journal of microwaves*, vol. 1, no. 1, pp. 218–228, 2021.

[55] T. Yilmaz, N. Hasan, R. Zane, and Z. Pantic, "Multi-objective optimization of circular magnetic couplers for wireless power transfer applications," *IEEE Transactions on Magnetics*, vol. 53, no. 8, pp. 1–12, 2017.

[56] H. Shoki, "Issues and initiatives for practical deployment of wireless power transfer technologies in japan," *Proceedings of the IEEE*, vol. 101, no. 6, pp. 1312–1320, 2013.

[57] S.-Y. R. Hui, Y. Yang, and C. Zhang, "Wireless power transfer: a paradigm shift for the next generation," *IEEE Journal of Emerging and Selected Topics in Power Electronics*, 2023.

[58] J. Park, D. Kim, K. Hwang, H. H. Park, S. I. Kwak, J. H. Kwon, and S. Ahn, "A resonant reactive shielding for planar wireless power transfer system in smartphone application," *IEEE Transactions on Electromagnetic Compatibility*, vol. 59, no. 2, pp. 695–703, 2017.

[59] A. A. Mohamed, A. Marim, and O. Mohammed, "Magnetic design considerations of bidirectional inductive wireless power transfer system for ev applications," *IEEE Transactions on Magnetics*, vol. 53, no. 6, pp. 1–5, 2017.

[60] B. M. Badr, R. Somogyi-Csizmazia, P. Leslie, K. R. Delaney, and N. Dechev, "Design of a wireless measurement system for use in wireless power transfer applications for implants," *Wireless Power Transfer*, vol. 4, no. 1, pp. 21–32, 2017.

[61] V. Bana, M. Kerber, G. Anderson, J. D. Rockway, and A. Phipps, "Underwater wireless power transfer for maritime applications," in *2015 IEEE Wireless Power Transfer Conference (WPTC)*. IEEE, 2015, pp. 1–4.

[62] N. Van Thuan, S. H. Kang, J. H. Choi, and C. W. Jung, "Magnetic resonance wireless power transfer using three-coil system with single planar receiver for laptop applications," *IEEE Transactions on Consumer Electronics*, vol. 61, no. 2, pp. 160–166, 2015.

[63] International Energy Agency, "Global EV Outlook 2024", 2024. [Online]. Available: https://iea.blob.core.windows.net/assets/a9e3544b-0b12-4e15-b407-65f5c8ce1b5f/GlobalEVOutlook2024.pdf

[64] A. Khaligh and S. Dusmez, "Comprehensive topological analysis of conductive and inductive charging solutions for plug-in electric vehicles," *IEEE Transactions on Vehicular Technology*, vol. 61, no. 8, pp. 3475–3489, 2012.

[65] S. Rivera, S. M. Goetz, S. Kouro, P. W. Lehn, M. Pathmanathan, P. Bauer, and R. A. Mastromauro, "Charging infrastructure and grid integration for electromobility," *Proceedings of the IEEE*, vol. 111, no. 4, pp. 371–396, 2022.

[66] H. Feng, R. Tavakoli, O. C. Onar, and Z. Pantic, "Advances in high-power wireless charging systems: Overview and design considerations," *IEEE Transactions on Transportation Electrification*, vol. 6, no. 3, pp. 886–919, 2020.

[67] G. Buja, C.-T. Rim, and C. C. Mi, "Dynamic charging of electric vehicles by wireless power transfer," *IEEE Transactions on Industrial Electronics*, vol. 63, no. 10, pp. 6530–6532, 2016.

[68] S. Li and C. C. Mi, "Wireless power transfer for electric vehicle applications," *IEEE journal of emerging and selected topics in power electronics*, vol. 3, no. 1, pp. 4–17, 2014.

[69] V.-D. Doan, H. Fujimoto, T. Koseki, T. Yasuda, H. Kishi, and T. Fujita, "Simultaneous optimization of speed profile and allocation of wireless power transfer system for autonomous driving electric vehicles," *IEEJ Journal of Industry Applications*, vol. 7, no. 2, pp. 189–201, 2018.

[70] J. Zhang, T.-Q. Tang, Y. Yan, and X. Qu, "Eco-driving control for connected and automated electric vehicles at signalized intersections with wireless charging," *Applied Energy*, vol. 282, p. 116215, 2021.

[71] P. Machura and Q. Li, "A critical review on wireless charging for electric vehicles," *Renewable and Sustainable Energy Reviews*, vol. 104, pp. 209–234, 2019.

[72] S. Y. Choi, B. W. Gu, S. Y. Jeong, and C. T. Rim, "Advances in wireless power transfer systems for roadway-powered electric vehicles," *IEEE Journal of emerging and selected topics in power electronics*, vol. 3, no. 1, pp. 18–36, 2014.

[73] C. C. Mi, G. Buja, S. Y. Choi, and C. T. Rim, "Modern advances in wireless power transfer systems for roadway powered electric vehicles," *IEEE Transactions on Industrial Electronics*, vol. 63, no. 10, pp. 6533–6545, 2016.

[74] Y. Do Chung, E. Y. Park *et al.*, "Impact investigations and characteristics by strong electromagnetic field of wireless power charging system for electric vehicle under air and water exposure indexes," *IEEE Transactions on Applied Superconductivity*, vol. 28, no. 3, pp. 1–5, 2018.

[75] S. D. Manshadi, M. E. Khodayar, K. Abdelghany, and H. Üster, "Wireless charging of electric vehicles in electricity and transportation networks," *IEEE Transactions on Smart Grid*, vol. 9, no. 5, pp. 4503–4512, 2017.

[76] M. Bojarski, E. Asa, K. Colak, and D. Czarkowski, "Analysis and control of multiphase inductively coupled resonant converter for wireless electric vehicle charger applications," *IEEE transactions on transportation electrification*, vol. 3, no. 2, pp. 312–320, 2016.

[77] Y.-C. Hsieh, Z.-R. Lin, M.-C. Chen, H.-C. Hsieh, Y.-C. Liu, and H.-J. Chiu, "High-efficiency wireless power transfer system for electric vehicle applications," *IEEE Transactions on Circuits and Systems II: Express Briefs*, vol. 64, no. 8, pp. 942–946, 2016.

[78] C.-C. Huang, C.-L. Lin, and Y.-K. Wu, "Simultaneous wireless power/data transfer for electric vehicle charging," *IEEE Transactions on Industrial Electronics*, vol. 64, no. 1, pp. 682–690, 2016.

[79] A. N. Azad, A. Echols, V. A. Kulyukin, R. Zane, and Z. Pantic, "Analysis, optimization, and demonstration of a vehicular detection system intended for dynamic wireless charging applications," *IEEE Transactions on Transportation Electrification*, vol. 5, no. 1, pp. 147–161, 2018.

[80] Y. D. Ko and Y. J. Jang, "The optimal system design of the online electric vehicle utilizing wireless power transmission technology," *IEEE Transactions on intelligent transportation systems*, vol. 14, no. 3, pp. 1255–1265, 2013.

[81] Q. Wang, W. Li, J. Kang, and Y. Wang, "Electromagnetic safety evaluation and protection methods for a wireless charging system in an electric vehicle," *IEEE Transactions on Electromagnetic Compatibility*, vol. 61, no. 6, pp. 1913–1925, 2018.

[82] S. Jeong, Y. J. Jang, and D. Kum, "Economic analysis of the dynamic charging electric vehicle," *IEEE Transactions on Power Electronics*, vol. 30, no. 11, pp. 6368–6377, 2015.

[83] Z. Bi, T. Kan, C. C. Mi, Y. Zhang, Z. Zhao, and G. A. Keoleian, "A review of wireless power transfer for electric vehicles: Prospects to enhance sustainable mobility," *Applied energy*, vol. 179, pp. 413–425, 2016.

[84] C. Park, S. Lee, S. Y. Jeong, G.-H. Cho, and C. T. Rim, "Uniform power i-type inductive power transfer system with dq-power supply rails for on-line electric vehicles," *IEEE Transactions on Power Electronics*, vol. 30, no. 11, pp. 6446–6455, 2015.

[85] U. K. Madawala and D. J. Thrimawithana, "A bidirectional inductive power interface for electric vehicles in v2g systems," *IEEE Transactions on Industrial Electronics*, vol. 58, no. 10, pp. 4789–4796, 2011.

[86] V. Z. Barsari, D. J. Thrimawithana, and G. A. Covic, "An inductive coupler array for in-motion wireless charging of electric vehicles," *IEEE Transactions on Power Electronics*, vol. 36, no. 9, pp. 9854–9863, 2021.

[87] M. Budhia, J. T. Boys, G. A. Covic, and C.-Y. Huang, "Development of a single-sided flux magnetic coupler for electric vehicle ipt charging systems," *IEEE Transactions on Industrial Electronics*, vol. 60, no. 1, pp. 318–328, 2011.

[88] G. A. Covic and J. T. Boys, "Modern trends in inductive power transfer for transportation applications," *IEEE Journal of Emerging and Selected topics in power electronics*, vol. 1, no. 1, pp. 28–41, 2013.

[89] C.-S. Wang, O. H. Stielau, and G. A. Covic, "Design considerations for a contactless electric vehicle battery charger," *IEEE Transactions on industrial electronics*, vol. 52, no. 5, pp. 1308–1314, 2005.

[90] S. Ruddell, U. K. Madawala, and D. J. Thrimawithana, "A wireless ev charging topology with integrated energy storage," *IEEE Transactions on Power Electronics*, vol. 35, no. 9, pp. 8965–8972, 2020.

[91] G. A. Covic and J. T. Boys, "Inductive power transfer," *Proceedings of the IEEE*, vol. 101, no. 6, pp. 1276–1289, 2013.

[92] J. M. Miller, O. C. Onar, and M. Chinthavali, "Primary-side power flow control of wireless power transfer for electric vehicle charging," *IEEE journal of Emerging and selected topics in power electronics*, vol. 3, no. 1, pp. 147–162, 2014.

[93] E. Aydin, H. Barua, A. Aktas, M. Mohammad, O. C. Onar, and B. Ozpineci, "Thermal analysis of a 100 kw polyphase wireless power transfer system," in *2024 IEEE Applied Power Electronics Conference and Exposition (APEC)*. IEEE, 2024, pp. 1927–1931.

[94] J. M. Miller, P. T. Jones, J.-M. Li, and O. C. Onar, "Ornl experience and challenges facing dynamic wireless power charging of ev's," *IEEE cIrcuIts and systEms magazInE*, vol. 15, no. 2, pp. 40–53, 2015.

[95] J. Kim, J. Kim, S. Kong, H. Kim, I.-S. Suh, N. P. Suh, D.-H. Cho, J. Kim, and S. Ahn, "Coil design and shielding methods for a magnetic resonant wireless power transfer system," *Proceedings of the IEEE*, vol. 101, no. 6, pp. 1332–1342, 2013.

[96] J. Huh, S. W. Lee, W. Y. Lee, G. H. Cho, and C. T. Rim, "Narrow-width inductive power transfer system for online electrical vehicles," *IEEE Transactions on Power Electronics*, vol. 26, no. 12, pp. 3666–3679, 2011.

[97] S. Y. Choi, S. Y. Jeong, B. W. Gu, G. C. Lim, and C. T. Rim, "Ultraslim s-type power supply rails for roadway-powered electric vehicles," *IEEE Transactions on Power Electronics*, vol. 30, no. 11, pp. 6456–6468, 2015.

[98] R. Bosshard, U. Iruretagoyena, and J. W. Kolar, "Comprehensive evaluation of rectangular and double-d coil geometry for 50 kw/85 khz ipt system," *IEEE Journal of Emerging and Selected Topics in Power Electronics*, vol. 4, no. 4, pp. 1406–1415, 2016.

[99] R. Bosshard and J. W. Kolar, "Multi-objective optimization of 50 kw/85 khz ipt system for public transport," *IEEE Journal of Emerging and Selected Topics in Power Electronics*, vol. 4, no. 4, pp. 1370–1382, 2016.

[100] O. Knecht and J. W. Kolar, "Performance evaluation of series-compensated ipt systems for transcutaneous energy transfer," *IEEE Transactions on Power Electronics*, vol. 34, no. 1, pp. 438–451, 2018.

[101] S. Chopra and P. Bauer, "Driving range extension of ev with on-road contactless power transfer—a case study," *IEEE transactions on industrial electronics*, vol. 60, no. 1, pp. 329–338, 2011.

[102] S. Bandyopadhyay, P. Venugopal, J. Dong, and P. Bauer, "Comparison of magnetic couplers for ipt-based ev charging using multi-objective optimization," *IEEE Transactions on Vehicular Technology*, vol. 68, no. 6, pp. 5416–5429, 2019.

[103] F. Grazian, T. B. Soeiro, and P. Bauer, "Voltage/current doubler converter for an efficient wireless charging of electric vehicles with 400-v and 800-v battery voltages," *IEEE Transactions on Industrial Electronics*, vol. 70, no. 8, pp. 7891–7903, 2022.

[104] G. Zhu, J. Dong, W. Shi, T. B. Soeiro, J. Xu, and P. Bauer, "A mode-switching-based phase shift control for optimized efficiency and wide zvs operations in wireless power transfer systems," *IEEE Transactions on Power Electronics*, vol. 38, no. 4, pp. 5561–5575, 2022.

[105] Tesla Wireless Charging, Swap And Robots—How Will Robotaxis Recharge? [Online]. Available: www.forbes.com/sites/bradtempleton/2024/10/22/tesla-wireless-charging-swap-robotshow-will-robotaxis-recharge/

[106] F. Grazian, W. Shi, J. Dong, P. van Duijsen, T. B. Soeiro, and P. Bauer, "Survey on standards and regulations for wireless charging of electric vehicles," in *2019 AEIT International Conference of Electrical and Electronic Technologies for Automotive (AEIT AUTOMOTIVE)*. IEEE, 2019, pp. 1–5.

[107] W. Zhang, J. C. White, A. M. Abraham, and C. C. Mi, "Loosely coupled transformer structure and interoperability study for ev wireless charging systems," *IEEE Transactions on Power Electronics*, vol. 30, no. 11, pp. 6356–6367, 2015.

[108] W. Zhang and C. C. Mi, "Compensation topologies of high-power wireless power transfer systems," *IEEE Transactions on Vehicular Technology*, vol. 65, no. 6, pp. 4768–4778, 2015.

[109] F. Liu, K. Chen, Z. Zhao, K. Li, and L. Yuan, "Transmitter-side control of both the cc and cv modes for the wireless ev charging system with the weak communication," *IEEE Journal of Emerging and Selected Topics in Power Electronics*, vol. 6, no. 2, pp. 955–965, 2017.

[110] M. Fu, C. Ma, and X. Zhu, "A cascaded boost–buck converter for high-efficiency wireless power transfer systems," *IEEE Transactions on industrial informatics*, vol. 10, no. 3, pp. 1972–1980, 2013.

[111] Z. Li, H. Liu, Y. Tian, and Y. Liu, "Constant current/voltage charging for primary-side controlled wireless charging system without using dual-side communication," *IEEE Transactions on Power Electronics*, vol. 36, no. 12, pp. 13 562–13 577, 2021.

[112] Z. Liu, L. Wang, Y. Guo, and S. Li, "Primary-side linear control for constant current/voltage charging of the wireless power transfer system based on the lcc-n compensation topology," *IEEE Transactions on Industrial Electronics*, vol. 69, no. 9, pp. 8895–8904, 2021.

[113] V. Yenil and S. Cetin, "An improved pulse density modulation control for secondary side controlled wireless power transfer system using lcc-s compensation," *IEEE Transactions on Industrial Electronics*, vol. 69, no. 12, pp. 12 762–12 772, 2021.

[114] K. Song, R. Wei, G. Yang, H. Zhang, Z. Li, X. Huang, J. Jiang, C. Zhu, and Z. Du, "Constant current charging and maximum system efficiency tracking for wireless charging systems employing dual-side control," *IEEE Transactions on Industry Applications*, vol. 56, no. 1, pp. 622–634, 2019.

[115] S. Chen, H. Li, and Y. Tang, "Extending the operating region of inductive power transfer systems through dual-side cooperative control," *IEEE Transactions on Industrial Electronics*, vol. 67, no. 11, pp. 9302–9312, 2019.

[116] A. Berger, M. Agostinelli, S. Vesti, J. A. Oliver, J. A. Cobos, and M. Huemer, "A wireless charging system applying phase-shift and amplitude control to maximize efficiency and extractable power," *IEEE Transactions on Power Electronics*, vol. 30, no. 11, pp. 6338–6348, 2015.

[117] Y. Zhang, S. Chen, X. Li, and Y. Tang, "Dual-side phase-shift control of wireless power transfer implemented on primary side based on driving windings," *IEEE Transactions on Industrial Electronics*, vol. 68, no. 9, pp. 8999–9002, 2020.

[118] K. Colak, E. Asa, M. Bojarski, D. Czarkowski, and O. C. Onar, "A novel phase-shift control of semibridgeless active rectifier for wireless power transfer," *IEEE Transactions on Power Electronics*, vol. 30, no. 11, pp. 6288–6297, 2015.

[119] H. Li, J. Fang, S. Chen, K. Wang, and Y. Tang, "Pulse density modulation for maximum efficiency point tracking of wireless power transfer systems," *IEEE Transactions on Power Electronics*, vol. 33, no. 6, pp. 5492–5501, 2017.

[120] H. Li, K. Wang, J. Fang, and Y. Tang, "Pulse density modulated zvs full-bridge converters for wireless power transfer systems," *IEEE Transactions on Power Electronics*, vol. 34, no. 1, pp. 369–377, 2018.

[121] W. Zhong and S. Hui, "Maximum energy efficiency operation of series-series resonant wireless power transfer systems using on-off keying modulation," *IEEE Transactions on Power Electronics*, vol. 33, no. 4, pp. 3595–3603, 2017.

[122] Y. Li, X. Cui, J. Chen, Y. Liu, S. Liu, J. Hu, and Z. He, "Enhanced on-off keying modulation for wireless power transfer systems to improve efficiency over a wide load range," *IEEE Transactions on Vehicular Technology*, 2023.

[123] W. Zhong, H. Li, S. Hui, and M. D. Xu, "Current overshoot suppression of wireless power transfer systems with on–off keying modulation," *IEEE Transactions on Power Electronics*, vol. 36, no. 3, pp. 2676–2684, 2020.

[124] A. Mostafa, Y. Wang, H. Zhang, C. Zhu, Y. Mei, N. Jiao, and F. Lu, "Output power regulation of a series-series inductive power transfer system based on hybrid voltage and frequency tuning method for electric vehicle charging," *IEEE Transactions on Industrial Electronics*, vol. 69, no. 10, pp. 9927–9937, 2021.

[125] H. Hu, T. Cai, S. Duan, X. Zhang, J. Niu, and H. Feng, "An optimal variable frequency phase shift control strategy for zvs operation within wide power range in ipt systems," *IEEE Transactions on Power Electronics*, vol. 35, no. 5, pp. 5517–5530, 2019.

[126] C.-S. Wang, G. A. Covic, and O. H. Stielau, "Power transfer capability and bifurcation phenomena of loosely coupled inductive power transfer systems," *IEEE transactions on industrial electronics*, vol. 51, no. 1, pp. 148–157, 2004.

[127] G. Zhu, J. Dong, and P. Bauer, "A dynamic frequency sweeping based parameter estimation method for wireless power transfer," in *IECON 2023-49th Annual Conference of the IEEE Industrial Electronics Society*. IEEE, 2023, pp. 1–6.

[128] G. Zhu, J. Dong, F. Grazian, and P. Bauer, "A parameter recognition based impedance tuning method for ss-compensated wireless power transfer systems," *IEEE Transactions on Power Electronics*, 2023.

[129] K. Aditya and S. S. Williamson, "Design guidelines to avoid bifurcation in a series–series compensated inductive power transfer system," *IEEE Transactions on Industrial Electronics*, vol. 66, no. 5, pp. 3973–3982, 2018.

[130] L. Shi, P. Alou, J. Á. Oliver, J. C. Rodriguez, A. Delgado, and J. A. Cobos, "A self-adaptive wireless power transfer system to cancel the reactance," *IEEE Transactions on Industrial Electronics*, vol. 68, no. 12, pp. 12 141–12 151, 2020.

[131] D.-H. Kim and D. Ahn, "Self-tuning lcc inverter using pwm-controlled switched capacitor for inductive wireless power transfer," *IEEE Transactions on Industrial Electronics*, vol. 66, no. 5, pp. 3983–3992, 2018.

[132] Y. Wang, Z. Yang, and F. Lin, "Design and implementation of wireless power transfer systems with improved capacitor error tolerance," *IEEE Transactions on Industrial Electronics*, vol. 69, no. 5, pp. 4707–4717, 2021.

[133] Polypropylene pulse/high frequency capacitors r76, double metallized polypropylene film, radial, dc and pulse applications (automotive grade), 2022. [Online]. Available: https://content.kemet.com/datasheets/KEM_F3034_R76.pdf

[134] N. Fu, J. Deng, Z. Wang, and D. Chen, "An lcc–lcc compensated wpt system with switch-controlled capacitor for improving efficiency at wide output voltages," *IEEE Transactions on Power Electronics*, 2023.

[135] G. Zhu, J. Dong, G. Yu, W. Shi, C. Riekerk, and P. Bauer, "Optimal multivariable control for wide output regulation and full-range efficiency optimization in lcc-lcc compensated wireless power transfer systems," *IEEE Transactions on Power Electronics*, 2024.

[136] EVSpecifications, Accessed: April 9, 2024. [Online]. Available: www.evspecifications.com

[137] Sophisticated thermal management, up to 800-volt system voltage, Accessed: April 9, 2024. [Online]. Available: media.porsche.com/mediakit/taycan/en/porsche-taycan/die-batterie

[138] A. A. Mohamed, A. A. Shaier, H. Metwally, and S. I. Selem, "A comprehensive overview of inductive pad in electric vehicles stationary charging," *Applied Energy*, vol. 262, p. 114584, 2020.

[139] W. V. Wang, D. J. Thrimawithana, and M. Neuburger, "An si mosfet-based high-power wireless ev charger with a wide zvs operating range," *IEEE Transactions on Power Electronics*, vol. 36, no. 10, pp. 11 163–11 173, 2021.

[140] M. Kim, D.-M. Joo, and B. K. Lee, "Design and control of inductive power transfer system for electric vehicles considering wide variation of output voltage and coupling coefficient," *IEEE Transactions on Power Electronics*, vol. 34, no. 2, pp. 1197–1208, 2018.

[141] A. C. Bagchi, A. Kamineni, R. A. Zane, and R. Carlson, "Review and comparative analysis of topologies and control methods in dynamic wireless charging of electric vehicles," *IEEE Journal of Emerging and Selected Topics in Power Electronics*, vol. 9, no. 4, pp. 4947–4962, 2021.

[142] Y. Jiang, L. Wang, Y. Wang, J. Liu, X. Li, and G. Ning, "Analysis, design, and implementation of accurate zvs angle control for ev battery charging in wireless high-power transfer," *IEEE Transactions on Industrial Electronics*, vol. 66, no. 5, pp. 4075–4085, 2018.

[143] M. Fu, H. Yin, X. Zhu, and C. Ma, "Analysis and tracking of optimal load in wireless power transfer systems," *IEEE Transactions on Power Electronics*, vol. 30, no. 7, pp. 3952–3963, 2014.

[144] T. Zhang, M. Fu, C. Ma, and X. Zhu, "Optimal load analysis for a two-receiver wireless power transfer system," in *2014 IEEE Wireless Power Transfer Conference*. IEEE, 2014, pp. 84–87.

[145] X. Dai, X. Li, Y. Li, and A. P. Hu, "Maximum efficiency tracking for wireless power transfer systems with dynamic coupling coefficient estimation," *IEEE Transactions on Power Electronics*, vol. 33, no. 6, pp. 5005–5015, 2017.

[146] Z. Huang, S.-C. Wong, and K. T. Chi, "Control design for optimizing efficiency in inductive power transfer systems," *IEEE Transactions on Power Electronics*, vol. 33, no. 5, pp. 4523–4534, 2017.

[147] W. X. Zhong and S. Hui, "Maximum energy efficiency tracking for wireless power transfer systems," *IEEE Transactions on Power Electronics*, vol. 30, no. 7, pp. 4025–4034, 2014.

[148] T. Diekhans and R. W. De Doncker, "A dual-side controlled inductive power transfer system optimized for large coupling factor variations and partial load," *IEEE Transactions on Power Electronics*, vol. 30, no. 11, pp. 6320–6328, 2015.

[149] R. Mai, Y. Liu, Y. Li, P. Yue, G. Cao, and Z. He, "An active-rectifier-based maximum efficiency tracking method using an additional measurement coil for wireless power transfer," *IEEE Transactions on Power Electronics*, vol. 33, no. 1, pp. 716–728, 2017.

[150] Y. Li, J. Hu, F. Chen, Z. Li, Z. He, and R. Mai, "Dual-phase-shift control scheme with current-stress and efficiency optimization for wireless power transfer systems," *IEEE Transactions on Circuits and Systems I: Regular Papers*, vol. 65, no. 9, pp. 3110–3121, 2018.

[151] X. Zhang, T. Cai, S. Duan, H. Feng, H. Hu, J. Niu, and C. Chen, "A control strategy for efficiency optimization and wide zvs operation range in bidirectional inductive power transfer system," *IEEE Transactions on Industrial Electronics*, vol. 66, no. 8, pp. 5958–5969, 2018.

[152] X. Wang, J. Xu, M. Leng, H. Ma, and S. He, "A hybrid control strategy of lcc-s compensated wpt system for wide output voltage and zvs range with minimized reactive current," *IEEE Transactions on Industrial Electronics*, vol. 68, no. 9, pp. 7908–7920, 2020.

[153] Y. Li, W. Sun, X. Zhu, and J. Hu, "A hybrid modulation control for wireless power transfer systems to improve efficiency under light-load conditions," *IEEE Transactions on Industrial Electronics*, vol. 69, no. 7, pp. 6870–6880, 2021.

[154] M. Wu, X. Yang, W. Chen, L. Wang, Y. Jiang, C. Zhao, and Z. Yan, "A dual-sided control strategy based on mode switching for efficiency optimization in wireless power transfer system," *IEEE Transactions on Power Electronics*, vol. 36, no. 8, pp. 8835–8848, 2021.

[155] B. X. Nguyen, D. M. Vilathgamuwa, G. H. B. Foo, P. Wang, A. Ong, U. K. Madawala, and T. D. Nguyen, "An efficiency optimization scheme for bidirectional inductive power transfer systems," *IEEE Transactions on Power Electronics*, vol. 30, no. 11, pp. 6310–6319, 2014.

[156] Y. Jiang, L. Wang, Y. Wang, M. Wu, Z. Zeng, Y. Liu, and J. Sun, "Phase-locked loop combined with chained trigger mode used for impedance matching in wireless high power transfer," *IEEE Transactions on Power Electronics*, vol. 35, no. 4, pp. 4272–4285, 2019.

[157] H. Li, S. Chen, J. Fang, Y. Tang, and M. A. de Rooij, "A low-subharmonic, full-range, and rapid pulse density modulation strategy for zvs full-bridge converters," *IEEE Transactions on Power Electronics*, vol. 34, no. 9, pp. 8871–8881, 2018.

[158] I.-W. Iam, C.-K. Choi, C.-S. Lam, P.-I. Mak, and R. P. Martins, "A constant-power and optimal-transfer-efficiency wireless inductive power transfer converter for battery charger," *IEEE Transactions on Industrial Electronics*, 2023.

[159] X. Sheng and L. Shi, "An improved pulse density modulation strategy based on harmonics for icpt system," *IEEE Transactions on Power Electronics*, vol. 35, no. 7, pp. 6810–6819, 2019.

[160] D. Wu, R. Mai, W. Zhou, Y. Liu, F. Peng, S. Zhao, and Q. Zhou, "An improved pulse density modulator in inductive power transfer system," *IEEE Transactions on Power Electronics*, vol. 37, no. 10, pp. 12 805–12 813, 2021.

[161] M. Fan, L. Shi, Z. Yin, L. Jiang, and F. Zhang, "Improved pulse density modulation for semi-bridgeless active rectifier in inductive power transfer system," *IEEE Transactions on Power Electronics*, vol. 34, no. 6, pp. 5893–5902, 2018.

[162] J. Zhou, G. Guidi, S. Chen, Y. Tang, and J. A. Suul, "Conditional pulse density modulation for inductive power transfer systems," *IEEE Transactions on Power Electronics*, 2023.

[163] R. Mai, P. Yue, Y. Liu, Y. Zhang, and Z. He, "A dynamic tuning method utilizing inductor paralleled with load for inductive power transfer," *IEEE Transactions on Power Electronics*, vol. 33, no. 12, pp. 10 924–10 934, 2018.

[164] Y. Lim, H. Tang, S. Lim, and J. Park, "An adaptive impedance-matching network based on a novel capacitor matrix for wireless power transfer," *IEEE Transactions on Power Electronics*, vol. 29, no. 8, pp. 4403–4413, 2013.

[165] T. C. Beh, M. Kato, T. Imura, S. Oh, and Y. Hori, "Automated impedance matching system for robust wireless power transfer via magnetic resonance coupling," *IEEE Transactions on Industrial Electronics*, vol. 60, no. 9, pp. 3689–3698, 2012.

[166] J. Kim, D.-H. Kim, and Y.-J. Park, "Free-positioning wireless power transfer to multiple devices using a planar transmitting coil and switchable impedance matching networks," *IEEE Transactions on Microwave Theory and Techniques*, vol. 64, no. 11, pp. 3714–3722, 2016.

[167] R. W. Porto, V. J. Brusamarello, L. A. Pereira, and F. R. de Sousa, "Fine tuning of an inductive link through a voltage-controlled capacitance," *IEEE Transactions on Power Electronics*, vol. 32, no. 5, pp. 4115–4124, 2016.

[168] M. Moghaddami, A. Sundararajan, and A. I. Sarwat, "A power-frequency controller with resonance frequency tracking capability for inductive power transfer systems," *IEEE Transactions on Industry Applications*, vol. 54, no. 2, pp. 1773–1783, 2017.

[169] A. Namadmalan, "Self-oscillating tuning loops for series resonant inductive power transfer systems," *IEEE Transactions on Power Electronics*, vol. 31, no. 10, pp. 7320–7327, 2015.

[170] S. Ann and B. K. Lee, "Analysis of impedance tuning control and synchronous switching technique for a semibridgeless active rectifier in inductive power transfer systems for electric vehicles," *IEEE Transactions on Power Electronics*, vol. 36, no. 8, pp. 8786–8798, 2021.

[171] K. Song, G. Yang, H. Zhang, X. Huang, J. Jiang, Y. Lan, X. Huang, J. Li, and C. Zhu, "An impedance decoupling-based tuning scheme for wireless power transfer system under dual-side capacitance drift," *IEEE Transactions on Power Electronics*, vol. 36, no. 7, pp. 7526–7536, 2020.

[172] R. Dai, R. Mai, and W. Zhou, "A pulse density modulation based receiver reactance identification method for wireless power transfer system," *IEEE Transactions on Power Electronics*, vol. 37, no. 9, pp. 11 394–11 405, 2022.

[173] W. Li, G. Wei, C. Cui, X. Zhang, and Q. Zhang, "A double-side self-tuning lcc/s system using a variable switched capacitor based on parameter recognition," *IEEE Transactions on Industrial Electronics*, vol. 68, no. 4, pp. 3069–3078, 2020.

[174] Z. Luo, Y. Zhao, M. Xiong, X. Wei, and H. Dai, "A self-tuning lcc/lcc system based on switch-controlled capacitors for constant-power wireless electric vehicle charging," *IEEE Transactions on Industrial Electronics*, vol. 70, no. 1, pp. 709–720, 2022.

[175] W. Li, Q. Zhang, C. Cui, and G. Wei, "A self-tuning s/s compensation wpt system without parameter recognition," *IEEE Transactions on Industrial Electronics*, vol. 69, no. 7, pp. 6741–6750, 2021.

[176] Y. Yang, S.-C. Tan, and S. Y. R. Hui, "Front-end parameter monitoring method based on two-layer adaptive differential evolution for ss-compensated wireless power transfer systems," *IEEE Transactions on Industrial Informatics*, vol. 15, no. 11, pp. 6101–6113, 2019.

[177] J. Yin, D. Lin, C. K. Lee, T. Parisini, and S. Hui, "Front-end monitoring of multiple loads in wireless power transfer systems without wireless communication systems," *IEEE Transactions on Power Electronics*, vol. 31, no. 3, pp. 2510–2517, 2015.

[178] R. Rao, "Jaya: A simple and new optimization algorithm for solving constrained and unconstrained optimization problems," *International Journal of Industrial Engineering Computations*, vol. 7, no. 1, pp. 19–34, 2016.

[179] D. Lin, J. Yin, and S. R. Hui, "Parameter identification of wireless power transfer systems using input voltage and current," in *2014 IEEE energy conversion congress and exposition (ECCE)*. IEEE, 2014, pp. 832–836.

[180] Toshiba Electronic Devices and Storage Corporation, "Power mosfet selecting mosfets and consideration for circuit design", 2018. [Online]. Available: https://toshiba.semicon-storage.com/info/application_note_en_20180726_AKX00064.pdf?did=13416

[181] Fairchild Semiconductor, "Resistor-capacitor (rc) snubber design for power switches", 2014. [Online]. Available: https://www.digikey.com/en/articles/resistor-capacitor-rc-snubber-design-for-power-switches

[182] Nordic Semiconductor, "nRF24L01 single chip 2.4 GHz radio transceiver", 2006. [Online]. Available: https://www.sparkfun.com/datasheets/Components/nRF24L01_prelim_prod_spec_1_2.pdf

[183] S. Li, W. Li, J. Deng, T. D. Nguyen, and C. C. Mi, "A double-sided lcc compensation network and its tuning method for wireless power transfer," *IEEE transactions on Vehicular Technology*, vol. 64, no. 6, pp. 2261–2273, 2014.

[184] Z. Zhou, L. Zhang, Z. Liu, Q. Chen, R. Long, and H. Su, "Model predictive control for the receiving-side dc–dc converter of dynamic wireless power transfer," *IEEE Transactions on Power Electronics*, vol. 35, no. 9, pp. 8985–8997, 2020.

[185] G. Yu, J. Dong, T. B. Soeiro, G. Zhu, Y. Yao, and P. Bauer, "Three-mode variable-frequency zvs modulation for four-switch buck+ boost converters with ultra-high efficiency," *IEEE Transactions on Power Electronics*, 2022.

[186] Z. Hua, K. Chau, W. Han, W. Liu, and T. W. Ching, "Output-controllable efficiency-optimized wireless power transfer using hybrid modulation," *IEEE Transactions on Industrial Electronics*, vol. 69, no. 5, pp. 4627–4636, 2021.

[187] X. Zhang, J. Li, and X. Tong, "A unique design approach of double-sided lcc compensated ipt system for misalignment-tolerant characteristic," *IEEE Transactions on Power Electronics*, vol. 38, no. 1, pp. 1288–1300, 2022.

[188] S. Luo, Z. Yao, Z. Zhang, X. Zhang, and H. Ma, "Balanced dual-side lcc compensation in ipt systems implementing unity power factor for wide load range and misalignment tolerance," *IEEE Transactions on Industrial Electronics*, vol. 70, no. 8, pp. 7796–7809, 2022.

[189] J. Huang, X. He, P. Huo, and R. Xu, "A hybrid modulation strategy for lcc-lcc compensated bidirectional wireless power transfer system to achieve high efficiency in the whole operating range," *IEEE Transactions on Industrial Electronics*, 2023.

[190] R. Matsumoto, T. Fujita, and H. Fujimoto, "Communication-less reactance compensation using pwm-controlled switched capacitors for wireless power transfer," *IEEE Transactions on Power Electronics*, 2023.

[191] L. Zhou, R. Mai, S. Liu, J. Yu, Y. Li, and L. Fu, "Minimizing input current of the rectifier of lcc–lcc compensated ipt systems by switch-controlled capacitor for improving efficiency," *IEEE Transactions on Industry Applications*, vol. 58, no. 1, pp. 1010–1021, 2021.

CURRICULUM VITÆ

Gangwei ZHU

09-03-1997 Born in Changsha, China.

EDUCATION

2021–2024 Ph.D. candidate
Delft University of Technology (TU Delft), the Netherlands

2018–2021 MSc in Electrical Engineering
Shanghai Jiao Tong University, China

2014–2018 BSc in Electrical Engineering
Central South University, China

LIST OF PUBLICATIONS

JOURNAL PAPERS

1. **G. Zhu**, J. Dong, W. Shi, T. B. Soeiro, J. Xu, and P. Bauer, "A mode-switching-based phase shift control for optimized efficiency and wide zvs operations in wireless power transfer systems," *IEEE Transactions on Power Electronics*, vol. 38, no. 4, pp. 5561–5575, Apr. 2023.

2. **G. Zhu**, J. Dong, F. Grazian, and P. Bauer, "A hybrid modulation scheme for efficiency optimization and ripple reduction in secondary side controlled wireless power transfer systems," *submitted*.

3. **G. Zhu**, J. Dong, F. Grazian, and P. Bauer, "A parameter identification based impedance tuning method for ss-compensated wireless power transfer systems," *IEEE Transactions on Power Electronics*, vol. 33, no.11, pp. 13298-13314, Nov. 2023.

4. **G. Zhu**, J. Dong, G. Yu, W. Shi, C. Riekerk, and P. Bauer, "Optimal multivariable control for wide output regulation and full-range efficiency optimization in lcc-lcc compensated wireless power transfer systems," *IEEE Transactions on Power Electronics*, vol. 39, no. 9, pp. 11834-11848, Sep. 2024.

5. **G. Zhu**, J. Dong, T.B. Soeiro, H. Vahedi, and P. Bauer, "Dual-side capacitor tuning and cooperative control for efficiency-optimized wide output voltages in wireless ev charging," *IEEE Transactions on Industrial Electronics*, Early Access, 2024.

As a co-author

1. G. Yu, J. Dong, T. B. Soeiro, **G. Zhu**, Y. Yao, and P. Bauer, "Three-mode variable-frequency zvs modulation for four-switch buck+boost converters with ultra-high efficiency," *IEEE Transactions on Power Electronics*, vol. 38, no. 4, pp. 4805–4819, Apr. 2023.

CONFERENCE PAPERS

1. **G. Zhu**, J. Dong, and P. Bauer, "A dynamic frequency sweeping based parameter estimation method for wireless power transfer," in *IECON 2023-49th Annual Conference of the IEEE Industrial Electronics Society*. IEEE, 2023, pp. 1–6.

2. **G. Zhu**, J. Dong, J. Wang, Z. Deng, Y. Li, and P. Bauer, "Implementation of variable capacitance to improve efficiency for asymmetric lcc-lcc compensated wireless power transfer systems," in *ECCE Europe 2024 (accepted)*. IEEE, 2024, pp. 1–6.

3. **G. Zhu**, J. Dong, and P. Bauer, "A hybrid rectifier mode control for communication-free wireless power transfer," in *ECCE USA 2024 (accepted)*. IEEE, 2024, pp. 1–6.

ACKNOWLEDGEMENTS

I would like to thank the people who have supported me throughout my PhD. Your encouragement, guidance, and companionship have been invaluable to me during this incredible journey. Without your support, this thesis would not have been possible.

First of all, I would like to thank my promotor, Prof. Bauer, for giving me the opportunity to join the DCE&S group and for the insightful guidance that helped me develop my research. Your expertise, wisdom, and unwavering support have been instrumental in shaping my academic path. Your encouragement during challenging times and your constructive feedback were crucial in refining my work. Your leadership and dedication to advancing the field have been a constant source of inspiration for me, and I am profoundly grateful for your mentorship.

I was fortunate to have Jianning as my daily supervisor. I learned a lot from you, both technically and philosophically. I benefited immensely from your way of conducting good research as well as being a good researcher. Your patience, profound knowledge, and constant encouragement have deeply influenced my academic growth. Thank you for being my supervisor and friend. You are always ready to provide support and share your wisdom. Your ability to guide me through complex problems and your readiness to engage in meaningful discussions have been invaluable.

I want to thank Thiago, Hani, Wenli, Zian, and Aditya, who were always ready to answer my questions and solve problems. I enjoyed every cooperation and discussion with you. Your dedication, meticulous approach, and innovative thinking were truly inspiring. I was impressed by your experience, knowledge, and passion for research, which set a high standard for me to aspire to. I feel honored to have worked with you and learned so much from our collaborations. Your insights and practical solutions greatly enhanced the quality of my work.

I also want to thank the other assistant professors: Sebastián, Gautham, and Laura, who were always ready to answer my questions and engage in meaningful conversations. Your insights, encouragement, and willingness to help have been invaluable to my research journey. Each of you brought unique perspectives and expertise that enriched my understanding and broadened my horizons.

I would like to thank Sharmila for your kindness and help with my endless requests. Your organizational skills, patience, and positive attitude made a significant difference. Your support extended beyond academic matters, bringing warmth and balance to my life. Your ability to manage everything so efficiently and your friendly nature has been a great comfort.

Thank you to the lab managers Hitesh, Mladen, Joris, Bart, and Harrie, who helped me with hardware issues and building the professional movable platform. Your technical expertise, problem-solving abilities, and dedication ensured that my experiments ran smoothly. Your assistance was crucial in overcoming many practical challenges. Your

commitment to maintaining the lab's functionality and your readiness to assist at any time was truly remarkable.

I want to say thanks to my office mates who fought together in the PhD journey to be good researchers. Thank you Junjie, Faezeh, and Miad. Your camaraderie, support, and shared experiences made the challenging journey more manageable and enjoyable. We have grown together both personally and professionally. The shared laughs, debates, and mutual support made the office a second home.

I also want to thank other electromagnetic teammates, Wenli, Francesca, Calvin, Guangyao, Jundong, Zichen, and Yongpeng. We helped each other and had inspiring discussions about wireless charging and electromagnetic research. Your collaboration and shared enthusiasm for our research field were a great source of motivation and insight. The teamwork and mutual encouragement significantly advanced our projects and made the research process rewarding.

The DCE&S group is a big family where everyone tries to give care and help. I am very happy to be part of this lovely group. Thanks Zhengzhao, Lu, Yang, Sachin, Fan, Yunhe, Tianming, Weichuan, Ruijun, Reza, Yawen, Dingsihao, Rohan, Ibrahim, Gautam, Joel, István, Felipe, Nikos, Carina, Heshi, Koen, Alvaro, Margo, Farshid, Bagas, Julian, Robin, Manfredo, Leila, Siddhesh, Sourabh, Darío, Christian. Your friendship, support, and collective spirit created a nurturing and inspiring environment. The group's welcoming atmosphere and collaborative spirit were crucial to my academic and personal development.

I could not have completed this long journey without the unconditional love and support of my family. I would like to thank my father, Mr. Shusheng Zhu, and my mother, Mrs. Qinyan Zhang. Your unwavering belief in me, sacrifices, and constant encouragement have been my constant source of inspiration and strength. Also, my senior sister, Mrs. Jinrong Zhu, for always being there for me. And to my wife, Mrs. Chuanhao Hu, your love, patience, and understanding have been my pillar of strength. Your support made this journey possible. Your belief in my potential and your unending support were the foundations upon which this thesis was built.

Thank you all from the bottom of my heart. Your contributions have been vital to my success, and I will always cherish the memories of our time together.

Gangwei Zhu

Delft, The Netherlands, May 2024